



**NASA-CONVAIR ACS SPACE SHUTTLE STUDY
AT MACH NUMBER 8.0**

W. T. Strike, Jr. and J. T. Best, Jr.

ARO, Inc.

May 1973

Approved for public release; distribution unlimited.

**VON KÁRMÁN GAS DYNAMICS FACILITY
ARNOLD ENGINEERING DEVELOPMENT CENTER
AIR FORCE SYSTEMS COMMAND
ARNOLD AIR FORCE STATION, TENNESSEE**

NOTICES

When U. S. Government drawings specifications, or other data are used for any purpose other than a definitely related Government procurement operation, the Government thereby incurs no responsibility nor any obligation whatsoever, and the fact that the Government may have formulated, furnished, or in any way supplied the said drawings, specifications, or other data, is not to be regarded by implication or otherwise, or in any manner licensing the holder or any other person or corporation, or conveying any rights or permission to manufacture, use, or sell any patented invention that may in any way be related thereto.

Qualified users may obtain copies of this report from the Defense Documentation Center.

References to named commercial products in this report are not to be considered in any sense as an endorsement of the product by the United States Air Force or the Government.

**NASA-CONVAIR ACS SPACE SHUTTLE STUDY
AT MACH NUMBER 8.0**

**W. T. Strike, Jr. and J. T. Best, Jr.
ARO, Inc.**

Approved for public release; distribution unlimited.

FOREWORD

The work presented in this report was conducted at the Arnold Engineering Development Center (AEDC) and was sponsored by the Marshall Space Flight Center (MSFC) of the National Aeronautics and Space Administration (NASA) for the General Dynamics/Convair Division of San Diego, California, under Program Element 921E-2.

The results of the test were obtained by ARO, Inc. (a subsidiary of Sverdrup & Parcel and Associates, Inc.), contract operator of the AEDC, Air Force Systems Command (AFSC), Arnold Air Force Station, Tennessee. The test program was conducted under ARO Project No. VA023-43BA (formerly VB1264); the data were obtained from May 10 to 17, 1972, and the final data package was completed on June 30, 1972. The manuscript was submitted for publication on August 29, 1972.

The special computer programs for the data reduction, including the online numerical integration of the pressure data, were provided by Mr. M. B. Krauth of the Data Reduction Section, Instrument Branch of the von Kármán Gas Dynamics Facility (VKF).

This technical report has been reviewed and is approved.

JIMMY W. MULLINS
Lt Colonel, USAF
Chief Air Force Test Director, VKF
Directorate of Test

A. L. COAPMAN
Colonel, USAF
Director of Test

ABSTRACT

Some aerothermodynamic design problems of the Space Shuttle attitude control system (ACS) were experimentally studied in a series of tests conducted at Mach number 8, at Reynolds numbers of 1×10^6 and 5×10^6 , using a flat plate containing interchangeable, flush-mounted nozzle cavities and lateral jet nozzles. The ACS configurations considered in this test program were a single supersonic nozzle and a cluster of four symmetrically located supersonic nozzles. Also, some preliminary results were obtained with nozzles similar to those on the flat plate used to simulate the yaw controls on a 2-percent-scaled nose section of the Convair Aerospace B-9U booster. The test data consist of pressure measurements, integrated pressure data to provide estimates of the jet interaction loading, heat-transfer-rate gage measurements, phase-change paint data, interferograms, and schlieren photographs. The flat plate was used to simulate the wing panel of a space shuttle vehicle. Interchangeable circular, contoured, nozzle cavities (no flow) of various sizes were mounted in the flat plate to determine the pressure and thermal loading generated within and around these cavities as the flat plate was inclined to the free-stream flow at angles of inclination from zero to nominally 30 deg. Small amounts of gas bled into the cavity from the plenum were found to have adverse effect on the thermal input to the cavity at zero angle of attack when the boundary layer passing over the cavity was laminar and a favorable effect with the plate inclined 30 deg and a turbulent boundary layer passing over the cavity. Supersonic nozzles mounted in the flat plate for the purpose of simulating the aerodynamic interference between a lateral jet and the external stream were found not only to increase the pressure loading, but also, in some cases, to increase the heat-transfer rates around the nozzle. The thermal input to the flat plate produced by the jet interaction was found to vary as the ratio of the jet gas specific enthalpy to the local or free-stream specific enthalpy. Heated air and room temperature helium gas were used to produce the lateral jet.

CONTENTS

	<u>Page</u>
ABSTRACT	iii
NOMENCLATURE	vii
I. INTRODUCTION	1
II. TEST EQUIPMENT	
2.1 Wind Tunnel	2
2.2 Models	2
2.3 Instrumentation and Precision	8
III. PROCEDURE	
3.1 Test Procedure	9
3.2 Numerical Integrations and Reference Values	10
3.3 Test Conditions	16
IV. RESULTS	
4.1 Flat Plate Characteristics	18
4.2 Flat Plate Cavity Results	19
4.3 Flat Plate Jet Interference Results	29
4.4 Booster Nose Jet Interference Results	51
V. SUMMARY OF RESULTS	56
REFERENCES	58

ILLUSTRATIONS

Figure

1. Flat Plate (2-D) Model and Nozzle Inserts	3
2. Flat Plate with Silicone Rubber Insert and a Melted Coating of Phase-Change Paint	5
3. 3-D Model (B-9U Booster Nose Section)	6
4. 3-D Model Installation with Silicone Rubber Insert	7
5. Undisturbed Flat Plate Heat-Transfer-Rate Distributions	18
6. Influence of Cavity Bleed on the Pressure Distribution at $Re_g = 5 \times 10^6$	20
7. Cavity Size, Reynolds Number, Boundary Layer, and Angle-of-Attack Effects on the Pressure Distribution Around a Cavity	21
8. Influence of Cavity Bleed on the Heat-Transfer-Rate Distribution at $Re_g = 5 \times 10^6$	23
9. Cavity Size, Reynolds Number, Boundary Layer, and Angle-of-Attack Effects on the Thermal Loading Within and Around the Cavity in a Flat Plate	25
10. Correlation of the Heat-Transfer-Rate Distributions Along the Reattachment Surface of a Cavity ($\theta = 0$) in a Flat Plate	26
11. Heat-Transfer-Rate Distribution Along the Separation Surface of the Cavity ($\theta = 160$ to 180 deg) in a Flat Plate	29

<u>Figure</u>	<u>Page</u>
12. Typical Pressure Distributions Around a Single Supersonic Air Jet Flush Mounted in a Flat Plate, $\alpha = 0$	30
13. Supersonic Lateral Air Jet Interaction Effects on a Flat Plate at $\alpha = 0$, $M_\infty = 8.0$ and $Re_\ell = 5 \times 10^6$ (Single Nozzle, $M_j = 2.84$, $d_j = 0.50$ in.)	31
14. Angle-of-Attack Effect on the Pressure Distribution Around a Single Supersonic Air Jet, $p_{o,j}/q_\infty \cong 60$, $T_{o,j}/T_{o,\infty} = 0.4$, $M_\infty = 8.0$, and $Re_\ell = 5 \times 10^6$	33
15. Helium and Air Gas Jet Effects on the Pressure Distributions Around a Single Supersonic Nozzle, $\alpha = 0$	34
16. Comparison of Helium and Air Jet Plume Interference Effects on a Flat Plate at $\alpha = 11$ deg, Supersonic Nozzle (Area Ratio of 2.73), $d_j = 0.50$ in., $p_{o,j}/q_\infty \cong 58$, $M_\infty = 8.0$ and $Re_\ell = 5 \times 10^6$	35
17. Comparison of Cluster Nozzle with Single Nozzle Flat Plate Pressure Distributions, Air Jet, $p_{o,j}/q_\infty \cong 60$, $T_{o,j}/T_{o,\infty} = 0.4$, $\alpha = 0$, and $Re_\ell = 5 \times 10^6$	36
18. Comparison of the Single Supersonic Nozzle and a Cluster of Four Supersonic Nozzles Flow Field Disturbances on a Flat Plate at $\alpha = 0$, $M_\infty = 8.0$, and $Re_\ell = 5 \times 10^6$	37
19. Angle-of-Attack Effects on the Circumferential Loading Around a Single Conical Nozzle Air Jet Disturbance	38
20. Correlation of the Supersonic Lateral Air Jet Augmentation Factors	40
21. Location of the Initial Lateral Air Jet Disturbance on the Flat Plate	42
22. Typical Phase-Changing Paint Photographs of Heat-Transfer-Rate Distribution on a Flat Plate in the Presence of a Laminar Boundary Layer at $\alpha = 0$ with a Supersonic Air Jet ($T_{o,j}/T_{o,\infty} = 0.47$)	43
23. Comparison of Phase-Changing Paint Data with the Heat Gage Data Obtained on a Flat Plate at $\alpha = 0$, $M_\infty = 8.0$, and $Re_\ell = 5 \times 10^6$	45
24. Phase-Changing Paint Heat-Transfer-Rate Results Obtained on a Flat Plate at $\alpha = 30$ deg in the Presence of a Turbulent Boundary Layer with a Supersonic Air Jet, $M_j = 2.54$, $d_j = 0.50$ in., $p_{o,j}/q_\infty \cong 60.0$, and $T_{o,j}/T_{o,\infty} = 0.44$	47
25. Air Jet Stagnation Pressure and Temperature Effects on the Heat- Transfer-Rate Distribution on a Flat Plate, ($\alpha = 0$) Around a Supersonic Nozzle, $M_j = 2.54$, $d_j = 0.50$ in., $M_\infty = 8.0$, and $Re_\ell = 5 \times 10^6$	48
26. Angle-of-Attack Effects on the Heat-Transfer Rates on a Flat Plate Around an Air Jet from a Supersonic Nozzle, $M_j = 2.54$, $p_{o,j}/q_\infty \cong 60$, $T_{o,j}/T_{o,\infty} = 0.41$, $M_\infty = 8.0$, and $Re_\ell = 5 \times 10^6$	49

<u>Figure</u>	<u>Page</u>
27. Helium and Air Gas Jet Effects on the Heat-Transfer-Rate Distributions Around a Supersonic Nozzle, $\alpha = 0$	50
28. Loading Produced by a Yaw Control Jet with an Exit Mach Number of 2.54 on the Convair Aerospace B-9U Booster Nose Section, $M_\infty = 8.0$ and $Re_\eta = 1.9 \times 10^6$	51
29. Heat-Transfer-Rate Distributions on the 3-D Body with a Single Supersonic Nozzle Air Jet at $p_{o,j}/q_\infty = 58.0$, $T_{o,j}/T_{o,\infty} = 0.44$, $\alpha = 0$, $M_\infty = 8.0$, and $Re_\eta = 1.9 \times 10^6$	53
30. Angle-of-Attack Effects on the Heat-Transfer-Rate Distributions Produced by a Single Supersonic Nozzle Air Jet at $p_{o,j}/q_\infty \cong 60.0$, $T_{o,j}/T_{o,\infty} = 0.44$, $M_\infty = 8.0$, and $Re_\eta = 1.9 \times 10^6$	54
31. Heat-Transfer-Rate Distribution Around a Cluster of Four Supersonic Nozzle Air Jets on the 3-D Model at $\alpha = 0$, $p_{o,j}/q_\infty \cong 64.0$, $T_{o,j}/T_{o,\infty} \cong 0.45$, $M_\infty = 8.0$, and $Re_\eta = 1.9 \times 10^6$	55
32. Heat-Transfer-Rate Distribution Through the Lateral Air Jet Interference Region on the 3-D Model at $\alpha = 0$, Single Supersonic Nozzle Air Jet at $p_{o,j}/q_\infty \cong 58.0$, $T_{o,j}/T_{o,\infty} = 0.44$, $M_\infty = 8.0$, and $Re_\eta = 1.9 \times 10^6$	56

APPENDIXES

I. GRAPHICAL PRESENTATION OF PRESSURE AND HEAT-TRANSFER- RATE DISTRIBUTIONS AND PRESSURE LOADING ON A FLAT PLATE AROUND SUPERSONIC NOZZLES	59
II. GRAPHICAL PRESENTATION OF PRESSURE AND HEAT-TRANSFER- RATE DISTRIBUTIONS ON THE 3-D BODY (B-9U BOOSTER NOSE SECTION) AROUND SUPERSONIC NOZZLES	135

NOMENCLATURE

A_b	3-D model base area, $(4.320)^2 \pi$, in.
A_j	Nozzle or cavity exit area, in. ²
CP	Center of pressure of the net interference loading, in.
c_p	Specific heat at constant pressure
d_j	Nozzle exit or cavity diameter, in.
d_{jt}	Throat diameter, in.
F_j	Jet reaction force of a sonic nozzle with an exit equal to the supersonic nozzle throat diameter, lb _f

f_m	Local pitching moment about the jet nozzle (see Section 3.2), in.-lb _f /radian
\bar{f}_m	Normalized local pitching moment about the jet nozzle (see Section 3.2), per radian
\bar{f}_N	Normalized interference loading (see Section 3.2), per radian
F_N, F_Y	Net surface loading produced by the jet interference in the normal and side force planes, respectively, lb _f
f_N	Local interference loading (see Section 3.2), lb _f /(in. ² -radian)
f_j	Radially distributed thrust loading of the jet, lb _f /(in. ² -radian)
H_{T_o}	Film heat-transfer coefficient, $\dot{q}/(T_o - T_w)$, Btu/ft ² -sec - °R
H_{REF}	Reference film heat-transfer coefficient, $\dot{q}_{REF}/(T_o - T_w)$, Btu/ft ² -sec - °R
h	Displacement from cavity exit into the cavity, in.
ℓ	Reference length, flat plate $\ell = 16.0$ in. and 3-D model $\ell = 6.0$ in.
M	Mach number
p	Static pressure, lb _f /in. ²
p_o	Reservoir pressure, lb _f /in. ²
q	Dynamic pressure, $\rho u^2/2$, lb _f /in. ²
\dot{q}	Heat-transfer rate, Btu/(ft ² -sec)
Re_ℓ	Reynolds number based on the reference length
Re_x	Reynolds number based on the local length x
r	Local body or nozzle cavity radius, in.
r_o	Radius of the 3-D model base, 4.320 in.
St_∞	Stanton number defined as $H_{T_o}/(\rho_\infty u_\infty C_p)$
T_o	Reservoir temperature, °R
T_{pc}	Phase-change paint melt temperature, °R

T_w	Local model wall temperature, °R
t	Time model is exposed to wind tunnel stream, sec
u	Velocity, ft/sec
x	Axial displacement from model leading edge or nose, in.
x_{cp}	Center of pressure of the local loading along a radial element emanating from the nozzle center, in.
x_R	Radial distance on the flat plate from the center of the nozzle or cluster of nozzles, in.
\bar{x}_R	Normalized radial coordinate, $(2x_R/d_j)\bar{x}_{R_0}$
\bar{x}_{R_0}	Normalizing parameter based on the free-stream properties, $\sqrt{p_\infty/(\gamma p_j M_j^2)}$
\bar{x}_{SEP}	Normalized radial coordinate of the length of separated flow along $\theta = 180$ deg, $(2x_{SEP}/d_j)\bar{x}_{R_0}$
α	Angle of attack, positive on the flat plate when the instrumented section is windward, deg
β	Mach number parameter, $\sqrt{M^2-1}$
γ	Ratio of specific heats
ΔC_A	Change in axial-force coefficient due to the jet interference, change in axial force/ $(q_\infty A_b)$
Δc_A	Local change in axial-force coefficients (see Section 3.2), per radian
ΔC_m	Change in pitching moment/ $(q_\infty A_b r_b)$ or $/(q_\infty A_j d_j/2)$
Δc_m	Local change in the pitching-moment coefficients (see Section 3.2), per radian
ΔC_N	Change in normal force/ $(q_\infty A_b)$ or $/(q_\infty A_j)$
Δc_N	Local change in the normal-force coefficient (see Section 3.2), per inch
ΔC_n	Change in yawing moment/ $(q_\infty A_b r_b)$
ΔC_y	Change in side force/ $(q_\infty A_b)$
Δc_y	Local change in the side-force coefficient (see Section 3.2), per inch

Δp	Change in pressure produced by the jet interference or cavity, lb _f /in. ²
θ	Angular orientation of the instrument rays around the nozzle (cavity) on the flat plate or circumferential stations on the 3-D model, deg
κ	Relative energy coefficient, ratio of lateral jet stream to the local stream energies per unit mass
λ	Ratio of bleed rate at the nozzle exit to the free-stream mass flow rate, $\rho_j u_j / (\rho_\infty u_\infty)$
λ_o	Ratio of the jet stream mass flow rate at the nozzle throat to the free-stream mass flow rate, $\rho_{jt} u_{jt} / (\rho_\infty u_\infty)$
ρ	Density
Φ	Correlation parameter, $[p_{oj}/(p_\infty M_\infty^2)] [\kappa \lambda_t]^{-3/4} \sqrt{d_{jt}/(\ell/\beta)}$

SUBSCRIPTS

j	Jet exit property
t	Property at the nozzle throat
REF	Undisturbed or theoretical value
∞	Free-stream property

SUPERSCRIPT

*	Undisturbed flat plate angle-of-attack property
---	---

SECTION I INTRODUCTION

Attitude control systems (ACS) of the Space Shuttle orbiter will include small secondary thrusters flush-mounted in some cases in the vehicle's nose and wing tip panels. During reentry, the orbiter will pass through the hypersonic flight regime and will be exposed to a severe aerothermodynamic environment which will generate high local pressure and thermal inputs to the surface in the vicinity of the ACS jet nozzles. The purpose of this test was to provide some preliminary design data to be used in developing an adequate thermal protection system (TPS) for the ACS.

With the ACS off, the external stream passing over the nozzle cavity can generate high heating rates within and immediately downstream of the nozzle. Therefore, one aspect of the present test program involved the measurement of the heat-transfer rates and the pressure distribution within and around a three-dimensional, axisymmetric, contoured nozzle cavity flush mounted in a flat plate. The local stream properties in the vicinity of the cavity were varied by varying the free-stream Reynolds number and the model angle of attack. The effect of bleeding a small amount of gas into the cavity was also evaluated.

With the ACS operating, that is, with the lateral jets on, high heating rates and pressure loadings are generated by the interference between the expanding jet plume from the ACS and the enveloping external flow field over the model surface. Therefore, another phase of the test program involved the measurement of the pressure loading and heat-transfer rates produced by a lateral jet from a supersonic nozzle flush mounted in a flat plate and also in a 3-D model representing the two-percent-scale nose section of the Convair Aerospace B-9U booster. The flat plate with the flush-mounted nozzles represented a wing panel with an ACS. The effects of jet gas pressure and total temperature on the aerodynamics over the model surface in the vicinity of the jet controls were experimentally evaluated in this study. Also, an ACS configuration consisting of a cluster of four symmetrically located supersonic nozzles was compared to the results obtained from a single supersonic nozzle. In all cases, the supersonic nozzles were conical and had a nominal area ratio of 2.73. Both helium and heated air were used in generating the lateral jet effects.

The tests were conducted at a nominal Mach number of 8 at free-stream Reynolds numbers of 1×10^6 and 5×10^6 (based on a flat plate reference length of 16-in.) in the 50-in. Hypersonic Wind Tunnel (B) of the von Kármán Gas Dynamics Facility (VKF). The flat plate angle of attack was varied from zero to about 30 deg with the nozzles installed on the compression surface. The 3-D model was tested at zero- and 27-deg angle of attack with the nozzles located in the yaw plane of the model. The test data consisted of model surface pressure measurements, heat-transfer-rate gage measurements, phase-change Tempilaq® paint data, interferograms reconstructed from double-plate, single-exposure holograms, and conventional schlieren pictures.

This report contains a brief summary of the more significant experimental results obtained with the cavity and with the lateral jet from a circular supersonic nozzle. The

model surface pressure distributions around the supersonic jet disturbance were numerically integrated and these results are compared to previously recorded sonic lateral jet force measurements. Appendixes containing most of the pressure and heat-transfer-rate data are also included in the report.

A complete analysis of test data will be published by the General Dynamics/Convair Aerospace Division of San Diego, California, under NASA Contract NA8-27683.

SECTION II TEST EQUIPMENT

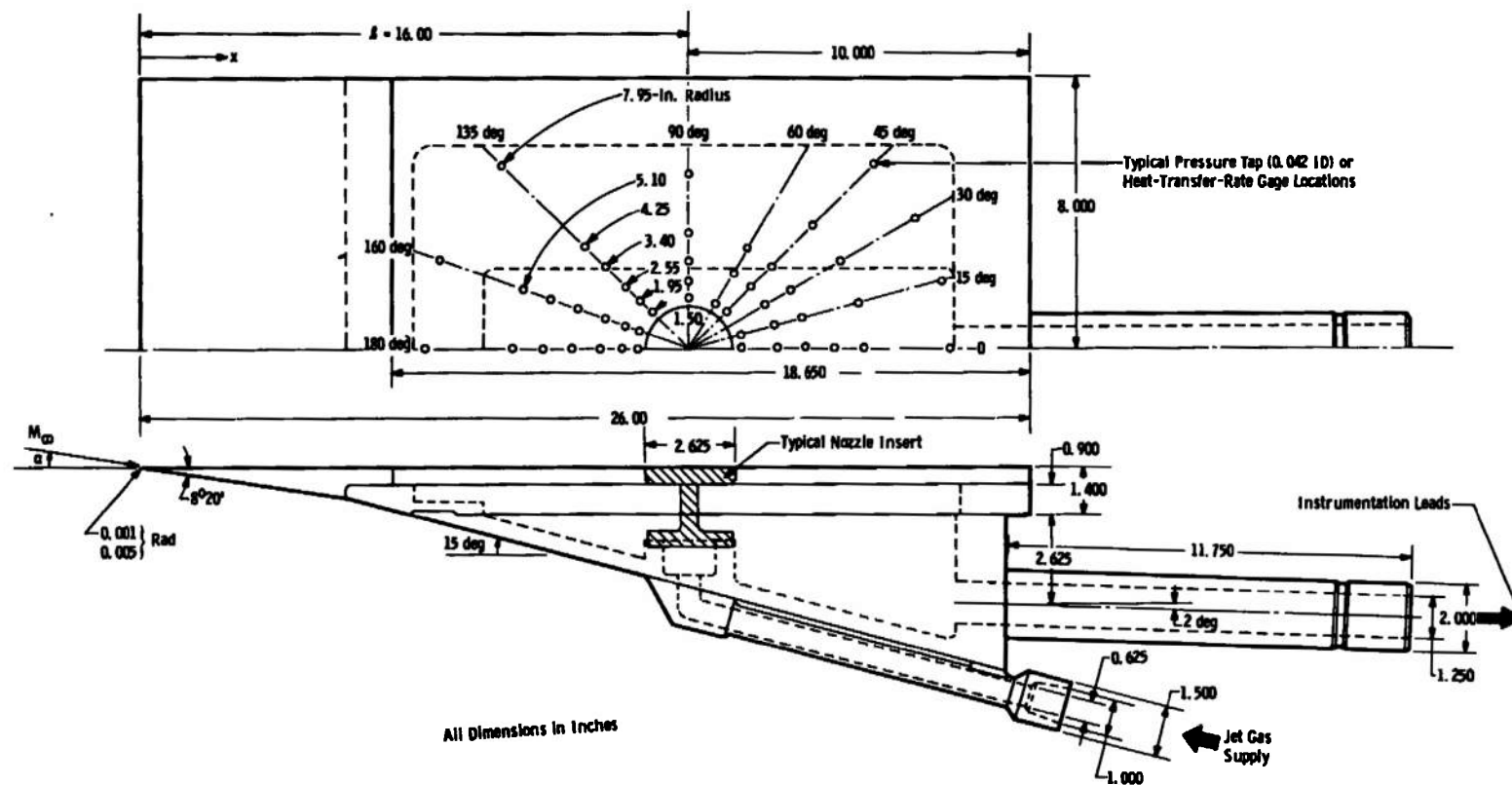
2.1 WIND TUNNEL

Tunnel B is a continuous, closed-circuit, variable density wind tunnel with an axisymmetric contoured nozzle and a 50-in.-diam test section. The tunnel can be operated at a nominal Mach number of 6 or 8 at stagnation pressures from 20 to 300 psia or 50 to 900 psia, respectively, and at stagnation pressures up to 1350°R. The model may be injected into the tunnel for a test run and then retracted for model cooling or model changes without interrupting the tunnel flow.

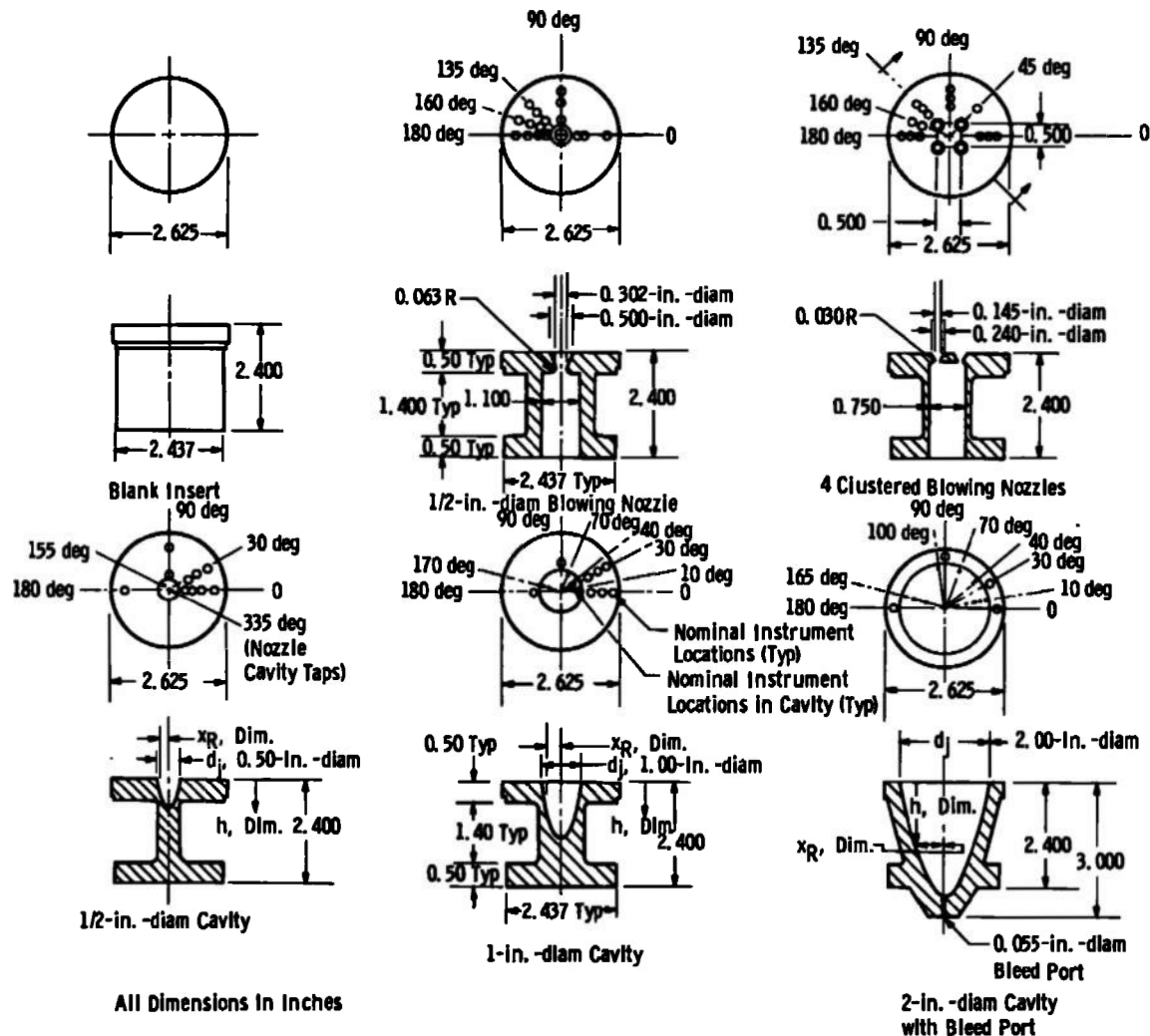
2.2 MODELS

The flat plate model, Fig. 1, furnished by the General Dynamics/Convair Division, was fitted with three interchangeable instrumented sections. The three instrumented sections were as follows: one with pressure taps, one with heat-transfer-rate gages, and another of silicone rubber (General Electric RTV[®] 60) which was nominally 0.75 in. thick for the phase-change paint tests. The locations of the pressure taps and the heat gages were identical and are given in Fig. 1a for the flat plate inserts and in Fig. 1b for the nozzle inserts. A grid was embedded in the silicone rubber flat plate insert as a reference for interpreting the paint data. The reference grid intersections as shown in the model photograph, Fig. 2, corresponded to the pressure tap and heat-transfer-gage locations. This figure also includes typical paint melt lines which were used to determine heat-transfer-rate distributions over the flat plate.

All three flat plate sections were fitted for the nozzle inserts shown in Fig. 1b. There were two sets of five nozzle inserts; one set was instrumented with pressure taps and the other set with heat-transfer gages. One blank uninstrumented nozzle insert was fabricated for use in both the pressure and heat-transfer-rate model configurations and another blank insert was fabricated and coated with a silicone rubber surface for the phase-change paint tests. A set of five nozzle inserts consisted of a 0.5-in.-diam and a 1.0-in.-diam cavity, a 2.0-in.-diam cavity with a 0.055-in.-diam bleed port in the cavity base, a single supersonic conical nozzle with a 0.5-in.-diam exit, and a cluster of four supersonic conical nozzles with 0.25-in.-diam exits. All the supersonic conical nozzles had an exit to throat area ratio of 2.737. Another 2-in.-diam cavity was fabricated of silicone rubber with an internal grid for use with the flat plate rubber insert phase-change paint model.



a. Basic Flat Plate Model and Nominal Instrumentation Locations
Fig. 1 Flat Plate (2-D) Model and Nozzle Inserts



Contour for
Nozzle Cavities

$2h/d_i$	$2x_R/d_i$
0	1.000
0.156	0.977
0.313	0.950
0.469	0.921
0.625	0.888
0.781	0.853
0.938	0.814
1.094	0.763
1.250	0.728
1.406	0.681
1.563	0.628
1.719	0.574
1.875	0.514
2.031	0.446
2.188	0.371
2.344	0.285
2.422	0.238
2.461	0.212
2.500	0.176
2.539	0.129
2.578	0

b. Blank, Blowing Conical Nozzles, and Contoured (Non-Blowing) Cavity Inserts
Fig. 1 Concluded

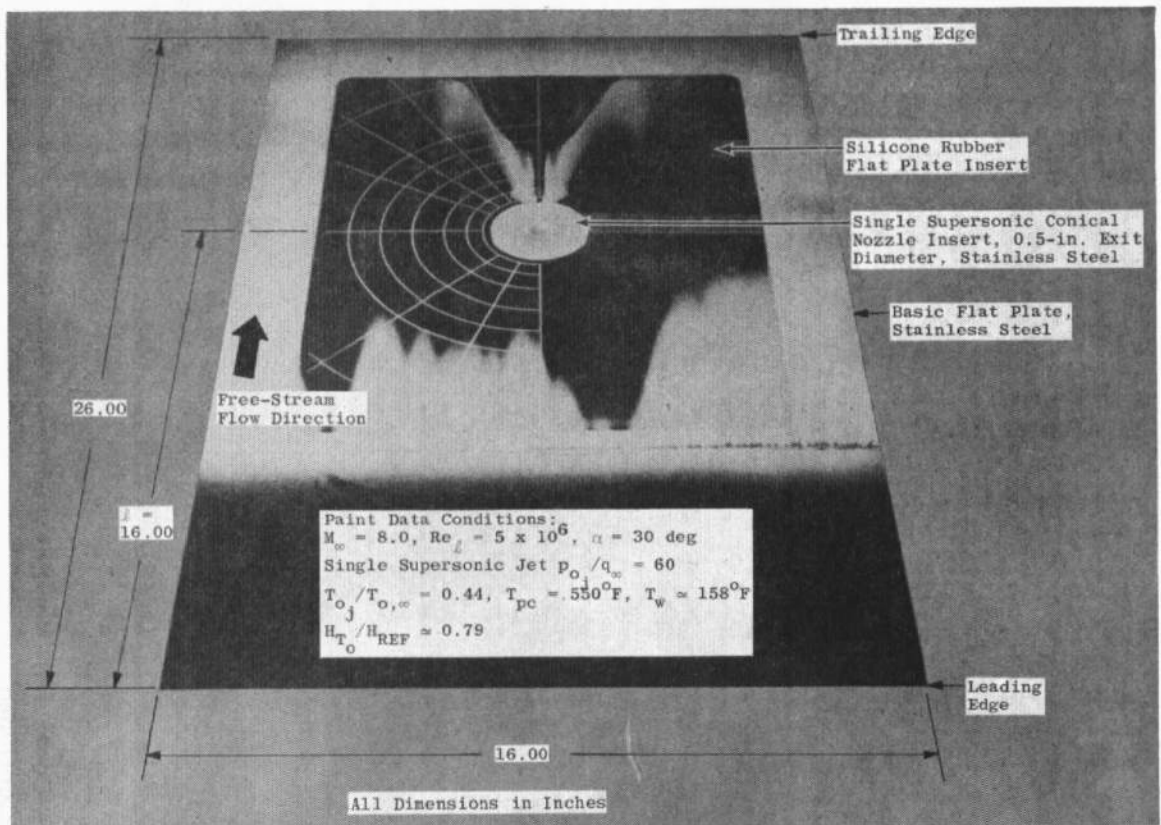
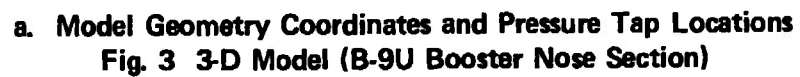
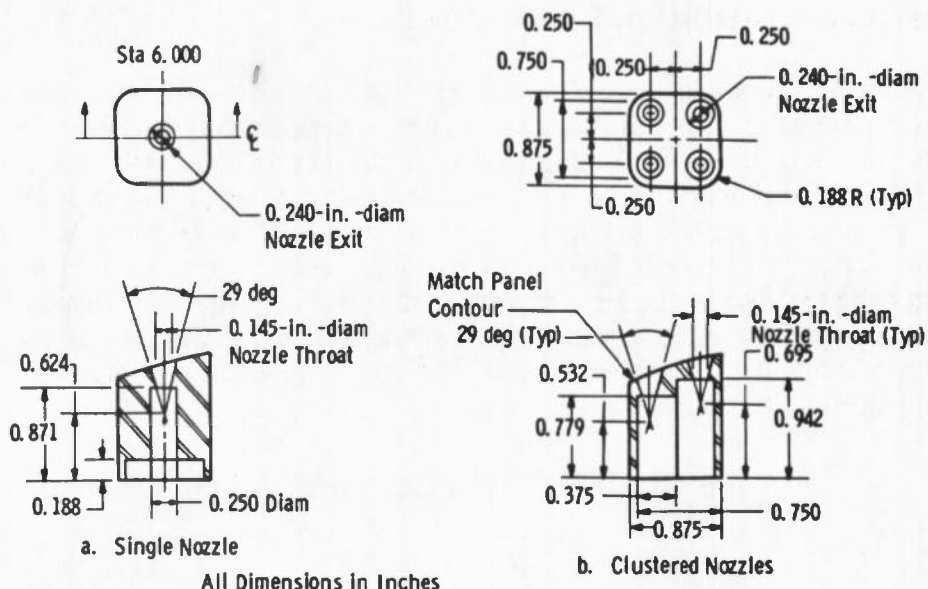


Fig. 2 Flat Plate with Silicone Rubber Insert and a Melted Coating of Phase-Change Paint

The axisymmetric model (Fig. 3) representing a 2-percent-scale version of the B-9U booster nose section was also furnished by General Dynamics and fabricated with two interchangeable instrumented sections. One section contained pressure taps and the other was fabricated with a 0.25-in.-thick silicone rubber shell. The location of the pressure taps shown in Fig. 3 corresponded to the intersection of the grid reference lines embedded in the silicone rubber model insert. This model was fitted with two interchangeable nozzle inserts, a single supersonic conical nozzle insert and an insert containing a cluster of four supersonic nozzles as shown in Figs. 3b and Fig. 4. There was no instrumentation on these nozzle inserts. The basic material of all model components other than the silicone rubber inserts was stainless steel. An illustration of the silicone rubber insert 3-D model is shown in Fig. 4 with a coating of phase-change paint and typical melt lines on the model surface.





b. Nozzle Inserts for the 3-D Model Configuration
Fig. 3 Concluded

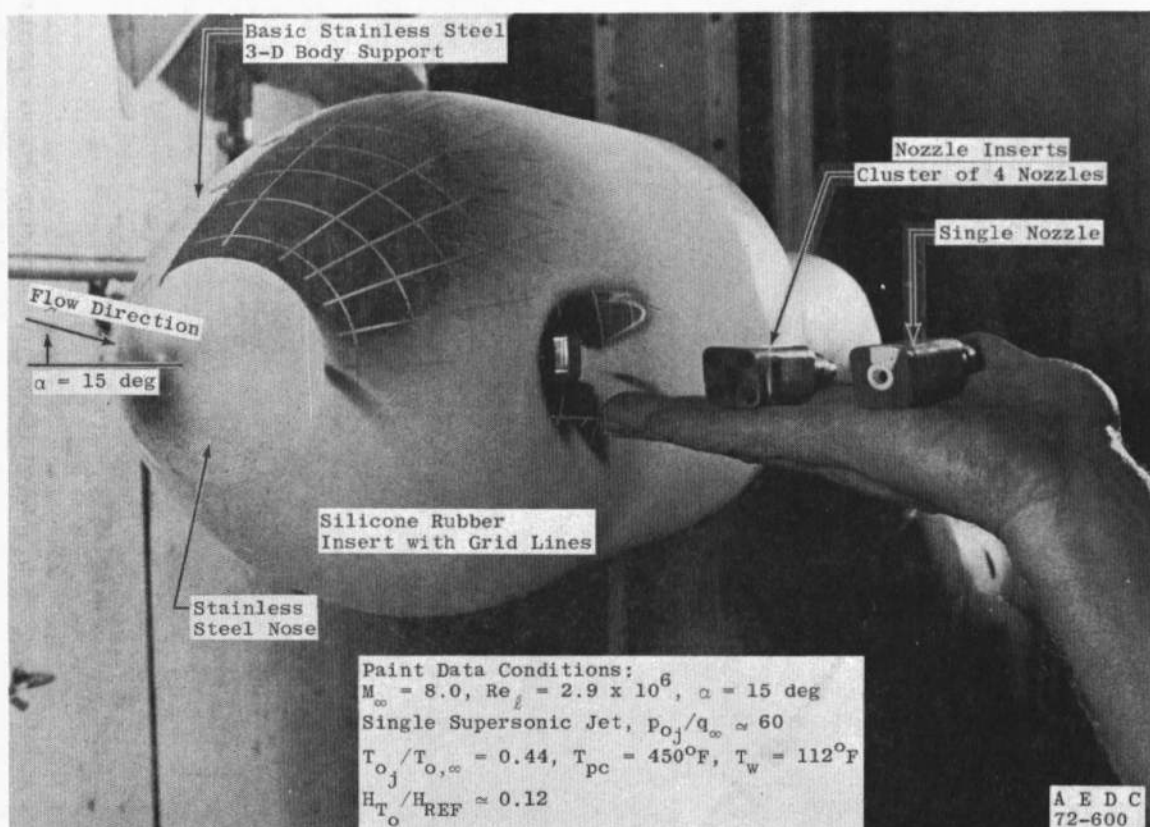


Fig. 4 3-D Model Installation with Silicone Rubber Insert

2.3 INSTRUMENTATION AND PRECISION

The Tunnel B stilling chamber pressure is measured with 100- and 1000-psid transducers referenced to a near vacuum. Based on periodic comparisons with secondary standards, the uncertainty (a bandwidth which includes 95 percent of the residuals) of the transducers is estimated to be ± 0.2 percent of the calibrated range. Stilling chamber temperature measurements are obtained with Chromel®-Alumel® thermocouples which have an uncertainty of ± 0.75 percent of the reading based on the thermocouple wire manufacturer's specifications. These uncertainties, along with the calibrated uniformity of the Mach number 8 tunnel test section flow, were used to estimate, by means of the Taylor series method of error propagation, the corresponding uncertainties in evaluating the following free-stream properties:

Free-Stream Uncertainties, percent

Basic Values:	<u>M_∞</u>	<u>p_o</u>	<u>T_o</u>	
	± 0.15	± 0.20	± 0.75	
Computed Values:	<u>p_∞</u>	<u>q_∞</u>	<u>$\rho_\infty u_\infty$</u>	<u>Re_ℓ</u>
	± 1.0	± 0.7	± 0.8	± 1.2

The model surface pressures were measured with 15-psid transducers calibrated for ranges of 10 and 0.5 psia. When the measured pressure exceeds 0.75 psia, the 10-psia calibration was used giving an uncertainty of ± 0.010 psia. If the pressure was less than 0.75 psia, the 0.5-psia calibration was used giving an uncertainty of ± 0.002 psia. The uncertainty in the ratio of the measured pressure to the free-stream static pressure based on the Taylor series propagation of errors is as follows for the selected test conditions:

Uncertainty in Model Surface Pressure Ratios, percent

<u>Nominal Ratio</u>		
<u>p/p_∞</u>	<u>$Re_\ell = 5 \times 10^6$</u>	<u>$Re_\ell = 1 \times 10^6$</u>
1.0	± 2.5	± 14.3
10.0	± 1.5	± 1.7
30.0	± 1.1	± 1.1

The model heat-transfer rates were recorded by high sensitivity transducers which were developed at VKF and derive their basic principle of operation from the Gardon® gage, but have a sensitivity to the incident heat flux which is more than an order of

magnitude higher. Three gage sizes were used, namely gages with 0.25-, 0.1875-, and 0.125-in. OD, and because of material considerations, they are limited to a maximum service temperature of less than 350°F. Absolute accuracy of the heat flux calibrations is believed to be within ± 5 percent, and the repeatability and the linearity are ± 3 percent. The wall temperature measurements were recorded on selected gages by Iron-Constantan and Chromel-Alumel thermocouples. The uncertainty in these readings is about ± 0.75 percent of the reading based on the thermocouple wire manufacturer's specifications. Using the error propagation method, the uncertainty of the film heat-transfer ratio, H_{T_o} , is ± 5.18 percent and of the Stanton number, St_{∞} , is ± 5.25 percent.

The total mass flow rate through the nozzles was obtained from measurements of the total pressure and temperature in the nozzle chamber. Depending on the measured pressure, a 500-, 100-, or a 50-psid transducer calibrated full scale was used. The uncertainty of these transducer measurements is nominally ± 0.2 percent of the full-scale calibration. The propagated uncertainty in the mass flow measurement, by use of the Taylor series method of error propagation, is as follows for the three nozzles and the 2.0-in.-diam cavity with the bleed port.

Mass Flow Rate Uncertainties, percent

<u>d_j, in.</u>	<u>P_{o_j}</u>	<u>T_{o_j}</u>	<u>\dot{m}_j</u>	<u>λ or λ_o</u>
0.055 (cavity)	± 0.2	± 0.75	± 3.7	± 3.8
0.145	± 0.2	± 0.75	± 1.4	± 1.6
0.302	± 0.2	± 0.75	± 0.8	± 1.1

The model pitch angle near zero, based on repeat calibrations of the sector pitching mechanism, is known to within ± 0.05 deg. At zero angle of attack, the model attitude was checked and set optically to within a few one-hundredths of one degree of zero. Model support deflections at the higher angles of attack increased this angle-of-attack error and the model angle of attack was measured from the schlieren photographs to within ± 0.25 deg.

Shadowgraph, schlieren and double-plate, single exposure holographic photographs were made of the flow field. The holograms were later reconstructed to produce conventional shadowgraph, interferogram, and infinite fringe interferogram photographs.

SECTION III PROCEDURE

3.1 TEST PROCEDURE

During the test, pressure distributions, heat-transfer-rate distributions, and Tempilaq (phase change) paint data were recorded. The test, consisting of five phases, was conducted with two basic model configurations with 3 cavity inserts and 2 nozzle inserts in the following sequence:

OVERALL TEST PLAN

<u>Phase</u>	<u>Model</u>	<u>Number of Nozzle Inserts</u>	<u>Type of Data</u>
1	2-D, Flat Plate	5	Pressure, Schlieren, Shadowgraph
2	2-D, Flat Plate	5	Heat Gage, Holograms
3	2-D, Flat Plate	2	Phase-Change Paint
4	3-D, B-9U Booster Nose	2	Pressure
5	3-D, B-9U Booster Nose	3	Phase-Change Paint

As shown above, no useful shadowgraph or schlieren photograph of the flow field over the 3-D model were obtained.

The model was injected into the stream at the desired angle of attack and a set of reference data was obtained with no flow passing through the nozzle cavity. At each model attitude, the mass flow through the nozzle was varied by changing the nozzle chamber pressure and then holding the chamber pressure constant; the nozzle chamber gas temperature was increased from 550 to about 1050°R. The effects of lateral jet gas temperature on the pressure and heat-transfer-rate distribution on the flat plate were recorded as the gas temperature was increased. During the pressure and heat-transfer-rate tests on the flat plate, the jet gas was changed from air to helium, and a few selected test points were obtained. No helium gas jet results were obtained with the 3-D model (the B-9U booster nose shape). The lateral jet on the 3-D model was always located in the yaw plane, that is, it produced a reaction force in the yaw plane of the 3-D model as the model was pitched from 0 to 27 deg.

3.2 NUMERICAL INTEGRATIONS AND REFERENCE VALUES

The primary purpose of this test program was to evaluate the pressure loading existing in the region adjacent to and within the nozzle cavity of an auxiliary control system (ACS). An attempt was also made to integrate these radial surface pressure distributions around the nozzle and examine the distribution of the local loading generated around the nozzle by the lateral jet disturbance. In addition, the net loading produced by the jet on the flat plate was evaluated and compared to the theoretical thrust of the lateral jet. These numerical evaluations were made while the test program was in progress.

The following assumptions and numerical techniques were adopted and programmed to integrate the pressure distributions. Each flat plate radial distribution was divided into three integration intervals, so that a special formula was used to estimate the initial and

final portion of the distribution. Two points were arbitrarily added to the pressure distribution so that at the nozzle rim ($x_R = d_j/2$) and at the edge of the flat plate, the incremental change in pressure, Δp , and the pressure gradient, $d(\Delta p)/dx_R$, were set equal to zero. These conditions or boundaries tended to provide a consistent and more realistic curve fit to the pressure distribution. The initial and final portions of the integration consisted of the first three and last three points in the distribution, respectively, and included the arbitrarily defined boundary points. The curve fit of these portions of the pressure distribution can be described analytically as follows:

$$\Delta p = a_0 + a_1 x_R + a_2 x_R^2 + a_3 x_R^3 \quad (1)$$

where, from the boundary conditions

$$a_0 = a_2 x_R^2(k) + 2a_3 x_R^3(k)$$

$$a_1 = -\{2a_2 x_R(k) + 3a_3 x_R^2(k)\}$$

and, using the other two points in the interval

$$a_2 = (N_1 D_3 - N_2 D_1) / (D_2 D_3 - D_1^2)$$

$$a_3 = (N_2 D_2 - N_1 D_1) / (D_2 D_3 - D_1^2)$$

$$D_1 = \sum_k^{k+1} x_1(k) x_2(k)$$

$$D_2 = \sum_k^{k+1} x_1^2(k) \quad \text{and} \quad D_3 = \sum_k^{k+1} x_2^2(k)$$

$$N_1 = \sum_k^{k+1} \Delta p(k) x_1(k)$$

$$N_2 = \sum_k^{k+1} \Delta p(k) x_2(k)$$

$$x_1(k) = [x_R(\ell) - x_R(k)]^2$$

$$x_2(k) = 2x_R^3(\ell) - 3x_R^2(\ell) x_R(k) + x_R^2(k)$$

The term $x_R(\ell)$ refers to either $x_R(1)$ or $x_R(m)$, the arbitrarily defined first or last coordinate in the distribution, that is, the nozzle exit radius and the edge of the flat plate. This procedure tends to force the analytical curve fit of the data to more closely approach a zero asymptote at the inner and outer limits of the radial pressure distribution. The integration is only performed over the first two and last two points, in the initial and final portions of the distribution, respectively. Letting k be either the first point in the distribution for the initial interval or the $m-1$ point for the final interval, the integration of the two intervals can be written as follows:

$$1/2 \int_{x_R(k)}^{x_R(k+1)} \Delta p \times dx_R^2 = \sum_{n=2}^5 a_{n-2} x_R^{n/n} \quad (2)$$

The region between the inner and outer estimates of the pressure integration is obtained by using a simple three-point, unequally spaced, numerical integration subroutine. This numerical scheme is based on an expression formulated from a Lagrange curve fit of three unequally spaced points. The integration is evaluated from the first point to the intermediate point of the group of three points. The next group of three points is selected, beginning with the intermediate point and using the next two points, and the integration scheme is reapplied. The process is completed over the whole interior interval of the pressure distribution. This numerical scheme is outlined below.

$$1/2 \int_{x_R(2)}^{x_R(m-2)} \Delta p \times dx_R^2 = 1/2 \sum_{n=2}^{m-2} \int_{x_R(n)}^{x_R(n+1)} \Delta p \times dx_R^2 \quad (3a)$$

and

$$\int_{x_R(n)}^{x_R(n+1)} \Delta p \times dx_R^2 = \frac{H_1}{6} \left[\left(\frac{2H_1 + 3H_2}{H} \right) \Delta p_n + \left(\frac{H_1 + 3H_2}{H_2} \right) \Delta p_{n+1} - \frac{H_1^2}{H(H_2)} \Delta p_{n+2} \right] \quad (3b)$$

where

$$H = x_R^{2(n+2)} - x_R^{2(n)}$$

$$H_1 = x_R^{2(n+1)} - x_R^{2(n)}$$

$$H_2 = H - H_1 = x_R^{2(n+2)} - x_R^{2(n+1)}$$

This numerical technique is reapplied throughout the data reduction procedure to obtain estimates of the resultant load and moments produced by the lateral jet disturbance on the flat plate and also on the 3-D model. Of course, the variable of integration and the function of the integral must be modified to meet a particular application, but the numerical scheme is the same.

3.2.1 Flat Plate Integrations

As previously suggested, the loading along each ray emanating from the center of the nozzle was integrated to determine the interference load produced by the lateral jet disturbance. The coordinates of the distribution were normalized, before the results were integrated, as follows:

$$\bar{f}_N = \frac{f_N}{p_\infty} \times x_{R_o}^2 = 1/2 \int_{\bar{x}_R(1)}^{\bar{x}_R(m)} \left(\frac{\Delta p}{p_\infty} \right) d(\bar{x}_R^2) \quad (4)$$

where at $\alpha = 0$, $\Delta p = p - p_\infty$

$$\bar{x}_R = (2x_R/d_j) \times x_{R_0} \quad (5)$$

$$x_{R_0} = \sqrt{p_\infty/(\gamma_j p_j M_j^2)} \quad (6)$$

The lower limit of the integral is \bar{x}_R at the nozzle exit and the upper limit, $\bar{x}_R(m)$, is \bar{x}_R at the edge of the plate. If $\alpha \neq 0$, then p_∞ is replaced by oblique shock static pressure, p^* , corresponding to the angle of attack of the flat plate. The local moment, f_m , and corresponding center of the load, x_{cp} , relative to the jet is obtained in the following manner.

$$(2x_{cp}/d_j) = (\bar{f}_m/\bar{f}_N)/x_{R_0} \quad (7)$$

where

$$\bar{f}_m = \frac{x_{R_0}^3}{p_\infty} f_m = 1/3 \int_{\bar{x}_R(1)}^{\bar{x}_R(m)} \frac{\Delta p}{p_\infty} \times d(\bar{x}_R^3) \quad (8)$$

The resultant surface loading coefficient and moment coefficient about the nozzle is given as follows:

$$\Delta C_N = 2k \int_0^\pi \bar{f}_N \times d\theta \quad (9a)$$

where

$$k = 2p_j M_j^2 / (\gamma p_\infty M_\infty^2) / \pi \quad (9b)$$

In essence, $\Delta C_N = \text{change in loading}/(q_\infty A_j)$

$$\Delta C_m = 2k/x_{R_0} \int_0^\pi \bar{f}_m \cos \theta d\theta \quad (10a)$$

where

$$\Delta C_m = \text{change in pitching moment}/(q_\infty A_j d_j/2) \quad (10b)$$

The effective center of pressure of the change in the interference loading is simply defined as

$$CP = \Delta C_m / \Delta C_N \quad (11)$$

The corresponding jet reaction coefficients can be evaluated as follows:

For a supersonic jet, the normalized radial thrust element is

$$\frac{f_j}{p_\infty} \times x_{R_o}^2 = 1/2[1 - \gamma_j M_j^2] \quad (12)$$

For a supersonic jet, the change in the normal force coefficient is

$$\Delta C_{N,j} = (p_j/q_\infty)(1 + \gamma_j M_j^2) - p_\infty/q \quad (13)$$

or for a sonic jet with the same throat diameter as the supersonic jet the change in normal force would be

$$\Delta C_{N,j}(M_j = 1) = \frac{p_{o,j}}{q_\infty} \left\{ 2 \left(\frac{2}{\gamma_j + 1} \right)^{\frac{1}{\gamma_j - 1}} - p_\infty/p_{o,j} \right\} \frac{A^*}{A_j} \quad (14)$$

3.2.2 3-D Model Integrations

In these integrations, the base diameter of the body was selected as a reference area and the reference length was set equal to the model base radius of 4.320 in. Also, the integrations of the change in surface loading extended from model station 2.0 in. to 14.0 in. and over the surface angles (θ) from 0 to 180 deg.

The changes in the local normal-force coefficient, c_N , and the net changes in normal force and pitching-moment coefficient produced by the normal component jet interference on the 3-D model were obtained as follows:

$$\Delta c_N = -k \int_0^\pi \left(\frac{\Delta p}{p_\infty} \right) r \cos \theta \, d\theta \quad (15)$$

where

$$\Delta p = p - p_\infty \quad \text{and} \quad k = 2/(\gamma M_\infty^2 \pi r_b^2)$$

$$\Delta C_N = \int_{2.0}^{14.0} \Delta c_N \times dx \quad (16)$$

$$\Delta C_m(N) = \int_{2.0}^{14.0} \Delta c_N (6.00 - x)/r_b \times dx \quad (17)$$

The letter, N, in brackets of $\Delta C_m(N)$ simply indicates that the normal component of the jet interference was used to evaluate the change in the pitching-moment coefficient. In subsequent definitions, the letters Y and A are used to define changes in moment

coefficients produced by, respectively, the side force and axial-force components of the jet interference loading. In each integral, the numerical scheme used is given in Section 3.2 by Equation (2). The side force and yawing moment components were defined as follows:

$$\Delta c_y = -k \int_0^{\pi} \left(\frac{\Delta p}{p_\infty} \right) r \sin \theta d\theta \quad (18)$$

$$\Delta C_y = \int_{2.0}^{14.0} \Delta c_y \times dx \quad (19)$$

$$\Delta C_n(Y) = \int_{2.0}^{14.0} \Delta c_y (6.00 - x)/r_b \times dx \quad (20)$$

The jet is located in the yaw plane; therefore, the maximum change in the coefficients occurred with the side force and yawing-moment components. The change in axial force and the change in pitching- and yawing-moment loading produced by the axial loading are given, respectively, as follows:

$$\Delta c_A = k/2 \int_{(1.813)^2}^{(4.320)^2} \left(\frac{\Delta p}{p_\infty} \right) d(r^2) \quad (21)$$

$$\Delta C_A = \int_0^{\pi} \Delta c_A \times d\theta \quad (22)$$

$$\Delta c_m(A) = (k/r_b) \int_{1.813}^{4.320} \frac{\Delta p}{p_\infty} r^2 dr \quad (23)$$

For the change in the pitching-moment coefficient resulting from the axial component of the jet interference loading

$$\Delta C_m(A) = - \int_0^{\pi} \Delta c_m(A) \cos \theta d\theta \quad (24)$$

For the change in the yawing-moment coefficient resulting from the axial component of the jet interference loading

$$\Delta C_n(A) = \int_0^{\pi} \Delta c_m(A) \sin \theta d\theta \quad (25)$$

The resultant change in pitching-moment and yawing-moment coefficients are defined, respectively, as follows:

$$\Delta C_m = \Delta C_m(N) + \Delta C_m(A) \quad (26)$$

$$\Delta C_n = \Delta C_n(Y) + \Delta C_n(A) \quad (27)$$

Since these coefficients represent the loading over a portion of the 9-BU booster nose, these values are meaningless unless the coefficients obtained with the jet-off are subtracted from the jet-on values to provide an estimate of the change in coefficients produced by the jet interference. This change in the aerodynamic coefficients must be increased by the force and moment coefficient associated to the thrust of the jet. In this case, for example, the side force coefficient would increase by the following amount:

$$\Delta C_{y,j} = [(p_j/q_\infty)(1 + \gamma_j M_j^2) - p^*/q_\infty] \frac{A_j}{A_b} \quad (28)$$

3.3 TEST CONDITIONS

The tests were conducted at a nominal Mach number of 8 at the free-stream conditions listed below.

Nominal Test Conditions

Mach Number	p_o , psia	T_o , °R	$Re/ft \times 10^{-6}$	p_∞ , psia	T_∞ , °K
8.00	866	1350	3.75	0.089	97
7.92	130	1130	0.75	0.014	84

The flat plate model configuration with the pressure tap insert plate and the heat-transfer-rate gage insert plate were tested at the maximum and minimum free-stream Reynolds number. At the maximum Reynolds number and at zero angle of attack, the flat plate was also tested with a boundary-layer trip attached 1.5 in. downstream of the leading edge. This trip consisted of 1/16-in.-diam stainless steel spheres with 1/4-in. spacing. All the heat-transfer-rate studies with the phase-change paint, along with all the 3-D model tests, were conducted at the maximum freestream Reynolds number. A summary of the test program is presented as follows:

TEST SUMMARY a. 2-D (Flat Plate) Test Summary

Cavity Interference Study			Cavity Bleed Chamber							Type of Data			Photographs			
Reg $\times 10^{-6}$	α , deg	Cavity Insert	Pressure, psia				Temperature			Pressure	Heat Transfer	Paint	Sch	Sha	Hol	
			0	7	14	26	Maximum	Minimum	Vary							
Trip	0	2-in. -diam Cavity	x	x		x			x		x			x		
5.0	↓	↓	x	x		x			x		x					
			x	x		x			x		x		x*	x		
			x	x		x			x		x					
1.0	↓	↓	x								x					
					50	150			x		x		x		x	
			x	25		x			x		x					
5.0	↓	↓	x								x					
											x		x		x	
											x		x		x	
5.0	↓	1-in. -diam Cavity	x								x					
			x								x		x			
			x								x		x			
5.0	↓	0.5-in. -diam Cavity	x									x				
			x									x				
			x									x				

*Paint data was obtained without cavity bleed, $p_{o,j} = 0$.

Note: Sch = Schlieren, Sha = Shadowgraph, and Hol = Hologram

a. Concluded

Jet Interference Study				Nozzle Chamber							Type of Data			Photographs		
$Re_d \times 10^{-8}$	α , deg	Supersonic Conical Nozzle Insert	Jet Gas	Pressure, psia				Temperature			Pressure	Heat Transfer	Paint	Sch	Sha	Hol
				0	40	115	230	Maximum	Minimum	Vary						
5.0	0	0.5-in. -diam	Air	x	x	x	x	x			x	x		x		x
	11						x	x	x		x	x		x		x
	20						x	x	x		x	x		x		x
	30						x	x	x		x	x		x		x
1.0	0		Air	x	x	x	x	x			x			x		
	11						x	x			x			x		
	30						x	x			x			x		
	0				x	x	x		x							x
5.0	0		He				x									
	11						x									
	30						x									
	0						x									
5.0	0	Cluster	Air				x				x	x		x		x
	11						x				x	x		x		x
	30						x				x	x		x		x
	0						x				x	x		x		x
1.0	0		Air				x				x			x		
	11						x				x			x		
	30						x				x			x		
	0						x				x			x		

*Paint data was obtained with cavity bleed, $P_{0j} = 0$

Note: Sch = Schlieren, Sha = Shadowgraph, and Hol = Hologram

b. 3-D Model Test Summary

$Re_d \times 10^{-8}$	α , deg	Supersonic Conical Nozzle Insert	Jet Gas	Chamber Pressure, psia		Type of Data	
				0	230	Pressure	Paint
1.0	0	0.24-in. -diam	Air	x	x	x	x
	15				x		x
	27			x	x	x	x
	0				x	x	x
1.0	0	Cluster	Air		x	x	x
	27				x	x	x

SECTION IV
RESULTS

In the absence of a lateral jet from an auxiliary control system (ACS), the variations in the external flow over the nozzle cavity affects the pressure and thermal loading not only around the cavity lip but also within the cavity. The first section of these results will be concerned with the effects of an external stream on the flow in the vicinity of a cavity or a flush-mounted nozzle in a flat plate surface. Included in this first section is an evaluation of the nature of the boundary layer on the flat plate at the nozzle location.

The second section will summarize some of the lateral jet augmentation effects and thermal loading produced by the interference between the ACS nozzle jet stream and the external free-stream flow over the flat plate. A more complete set of the test results is included in the appendixes to this report.

The final section will contain results obtained on the 2-percent-scale version of the B-9U booster nose section with an ACS nozzle jet located in the yaw plane of this axisymmetric nose section.

4.1 FLAT PLATE CHARACTERISTICS

The nature of the boundary layer on the flat plate is summarized in Fig. 5 in terms of the heat-transfer-rate distribution on the flat plate. At zero angle of attack (Fig. 5a),

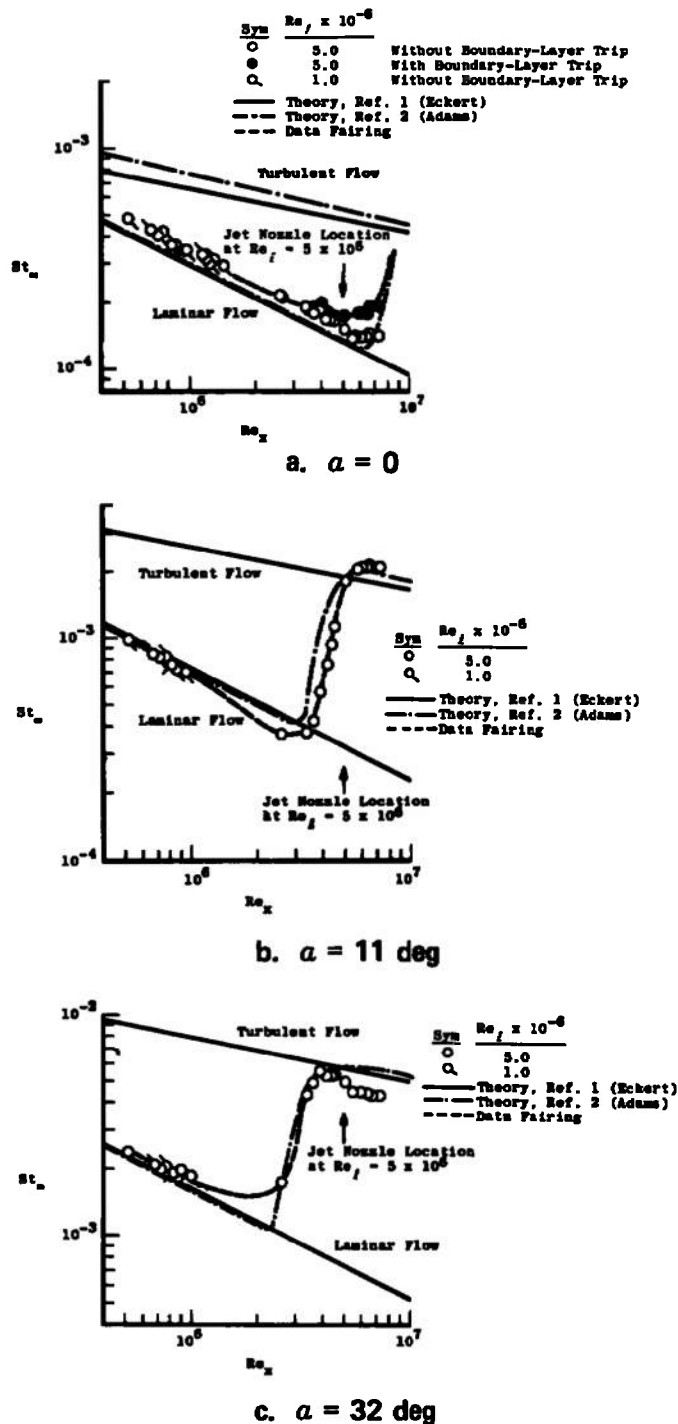


Fig. 5 Undisturbed Flat Plate Heat-Transfer-Rate Distributions

the flow remained laminar over nearly the entire length of the plate and the addition of the boundary-layer trip 1.5 in. downstream of the flat plate leading edge moved the beginning of transition up on the flat plate surface. With or without the boundary-layer trip, the flow was not fully turbulent anywhere on the flat plate.

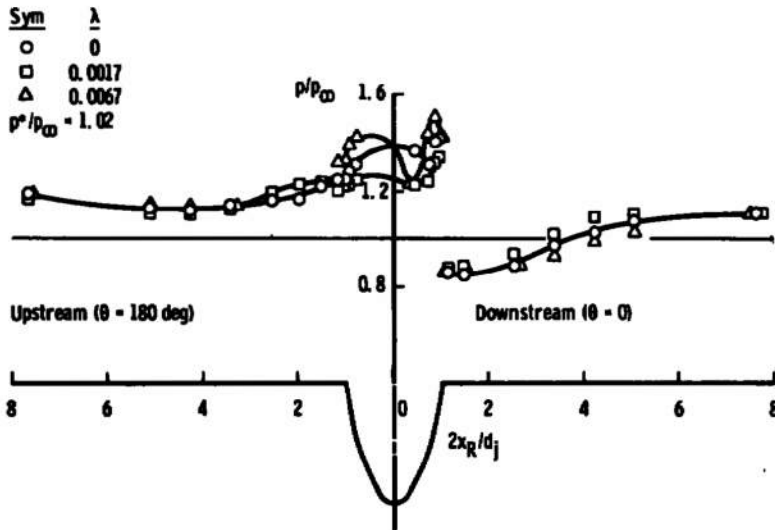
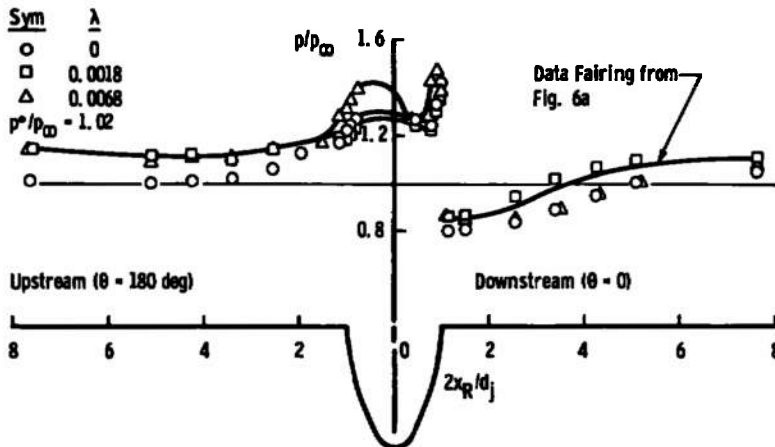
Also included in Fig. 5 are theoretical estimates of the heat-transfer-rate distributions on a two-dimensional surface where the boundary layer remains either laminar or turbulent over the entire length of the flat plate. The estimates used to define a reference heat-transfer-rate value were based on the analytical results discussed in Chapter 10 of Ref. 1. Also, Adams' analytical technique, Ref. 2, was used to estimate the variation in the heat-transfer rates through the boundary-layer transition region.

At 11-deg angle of attack and at the maximum free-stream Reynolds number of 5×10^6 (Fig. 5b), the boundary layer becomes fully turbulent on the plate near the cavity and nozzle inserts (i.e., near $x = 16.0$ in.). The beginning of the boundary-layer transition occurs at a Reynolds number of 3×10^6 , that is, at $x = 10$ in. At 32-deg angle of attack and at the maximum free-stream Reynolds number (Fig. 5c), boundary-layer transition begins at a Reynolds number of 2.3×10^6 (i.e., at $x = 7.5$ in.). A boundary-layer trip was not used when the model was pitched and therefore these results in Figs. 5b and 5c represent natural boundary-layer transition locations. At the minimum free-stream Reynolds number of 1×10^6 , the boundary layer remained laminar over the entire length of the flat plate even at angles of attack of 11 and 32 deg.

4.2 FLAT PLATE CAVITY RESULTS

Theoretically (see Ref. 3), in an open cavity flow field, bleeding a little gas into a two-dimensional cavity should reduce the pressure and thermal loading in the cavity region. The open cavity flow field case is obtained when the ratio of the width (or diameter) to depth of the cavity is small enough so that the external flow crosses the cavity without impinging or attaching itself to the bottom or side of the cavity. The results presented in Figs. 6a and 6b were obtained for two bleed rates with an axisymmetric cavity flush mounted in the flat plate at zero angle of attack. The smaller bleed rate reduced the pressure level slightly within the cavity while the higher bleed rate produced peak pressure loadings which exceeded the no-bleed values. The ratio of the bleed rate (lbm/sec) to the free-stream mass flow, passing through an area equal to the nozzle exit area was defined as λ . High-pressure air was bled into the nozzle cavity through a small hole in the bottom of the cavity (see Fig. 1b).

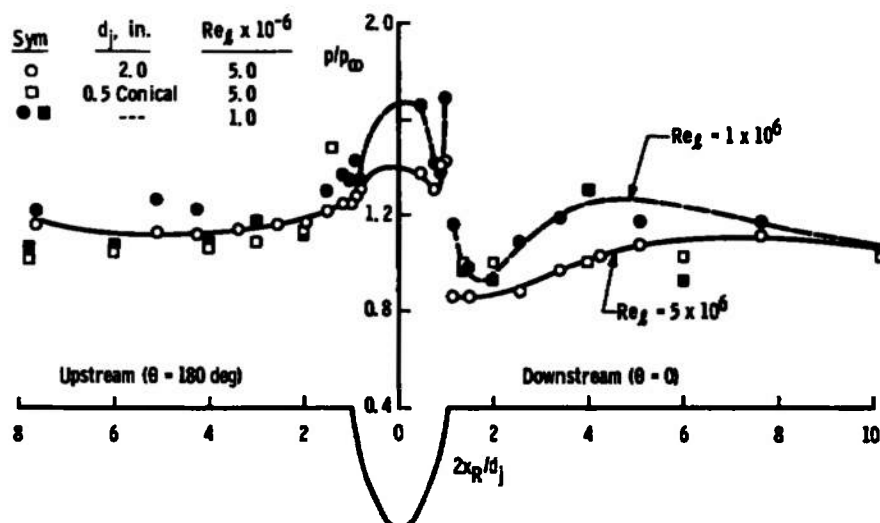
Just upstream of the cavity, for all cases, the laminar boundary layer separated causing a slight increase in surface pressure, while downstream of the cavity, the pressure fell below the undisturbed flat plate value, that is, below p^* or $p/p^* < 1.0$ as shown in Fig. 6a. In general, the cavity influence on the flat plate surface pressure remained within 3 or 4 nozzle exit radii of the cavity. The slight gradient in the pressure distribution upstream of $2x_R/d_j$ values of 4 (along $\theta = 180$ deg) was due to the laminar boundary-layer growth along the flat plate.

a. 2-in.-diam Cavity, $Re_\delta = 5 \times 10^6$, $\alpha = 0$ b. 2-in.-diam Cavity, $Re_\delta = 5 \times 10^6$ with Boundary Layer Trip, $\alpha = 0$ Fig. 6 Influence of Cavity Bleed on the Pressure Distribution at $Re_\delta = 5 \times 10^6$

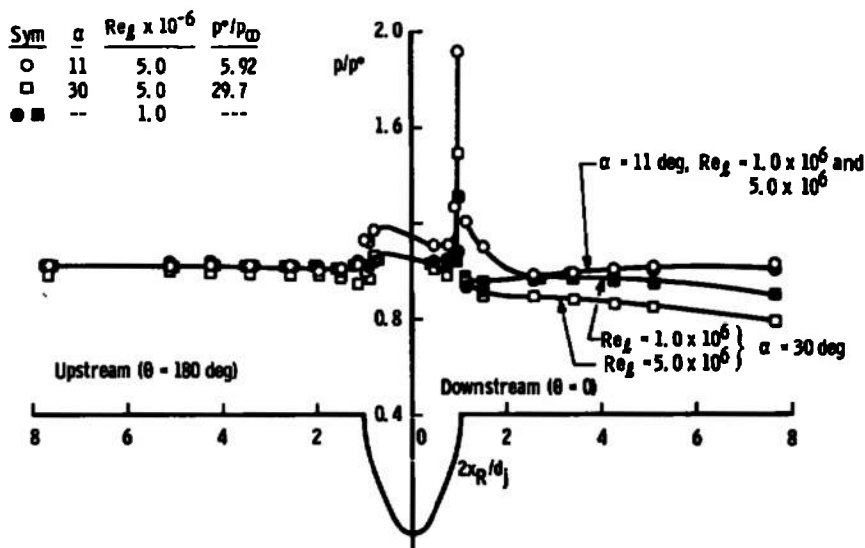
The addition of the boundary-layer trip had little effect on these cavity results since the flat plate boundary layer in the cavity region remained laminar and unaffected by the trip (compare Figs. 6a with 6b). Most of the shifts in the overall pressure levels, particularly the $\lambda = 0$ data, on the flat plate can be attributed to either the uncertainty in the pressure measurements or to slight deviations in the zero angle-of-attack position and not to the addition of the boundary-layer trip.

Cavity size, free-stream Reynolds number, angle of attack and boundary-layer effects on the pressure distribution occur within the cavity and in the immediate vicinity (within two or three cavity diameters) of the cavity as shown in Fig. 7. In Fig. 7a, a large

amount of scatter exists in the low Reynolds number data obtained at zero angle of attack because the measured pressures approached the repeatability of the pressure instrumentation (see Section 2.2). At angles of attack of 11 and 30 deg (Fig. 7b), the pressures were higher and this scatter was not present.



a. Cavity Size and Reynolds Number Effects at $\alpha = 0$



b. Boundary Layer and Angle-of-Attack Effects at $\alpha = 11$ and 30 deg with the 2.0-in.-diam Cavity

Fig. 7 Cavity Size, Reynolds Number, Boundary Layer, and Angle-of-Attack Effects on the Pressure Distribution Around a Cavity

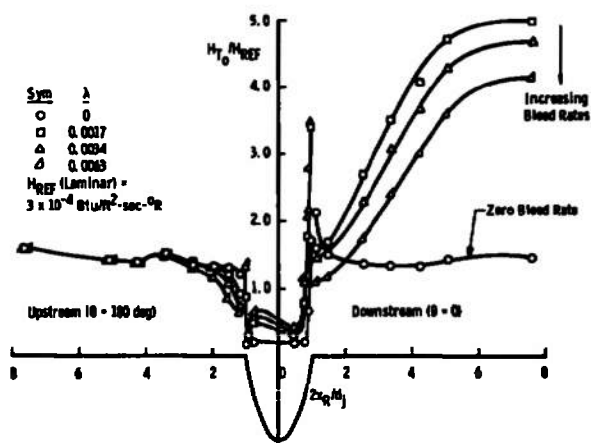
An attempt was made to correlate the pressure loading in terms of the cavity radius, that is, p/p_∞ as a function of $2x_R/d_j$, but the limited results in Fig. 7a indicate that the pressure distribution was not always a simple function of the cavity size. Close to the smaller cavity (1/2-in.-diam) on the flat plate surface at $Re_\infty = 5 \times 10^6$, the local pressures were higher. At the lower free-stream Reynolds number, neglecting the scatter in the data, there seemed to be a better correlation between the smaller (1/2-in.-diam) and larger (2-in.-diam) cavity pressure distributions in the immediate vicinity of the cavity (i.e., $2x_R/d_j \leq 4$). There were no pressure taps within the 1/2-in.-diam nozzle so no comparisons were available for the internal 2-in.-diam cavity data.

A comparison of the two data line fairings (the solid and dashed lines) in Fig. 7a, illustrates one effect the variation in the free-stream Reynolds number has on the pressure loading within and downstream of the cavity. At both Reynolds numbers, the boundary layer was laminar. Apparently, thickening the boundary layer, that is, reducing the free-stream Reynolds number, increased the level of the pressure ratio distribution within and downstream of the cavity.

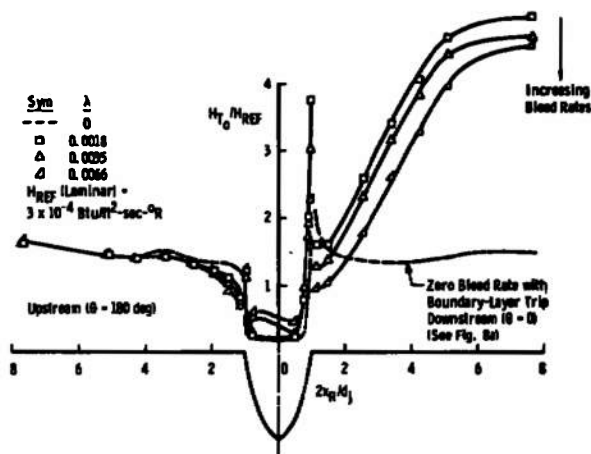
At angles of attack of 11 and 30 deg (Fig. 7b), the pressure distributions were normalized by the theoretical inviscid flat plate pressure (i.e., based on the oblique shock relationships). At 11-deg angle of attack, increasing the free-stream Reynolds number from 1×10^6 to 5×10^6 thinned the boundary layer but caused transition to begin in the vicinity of the cavity (see Fig. 5b). The level of the pressure ratios increased within the cavity and immediately downstream of the cavity ($2x_R/d_j \leq 2.5$) as the boundary layer changed from a laminar to a transitional condition.

At 30-deg angle of attack, increasing the free-stream Reynolds number causes the boundary layer in the vicinity of the cavity to go from a fully laminar (at $Re_\infty = 1 \times 10^6$) to a fully turbulent (at $Re_\infty = 5 \times 10^6$) condition. In this case, only the distribution downstream of the cavity seems to change with the laminar boundary-layer condition producing higher pressure ratios aft of the cavity. The three-dimensional flow field effects about the outer edges of the flat plate at high angles of attack were responsible for the continuing decay in the pressure ratio near the flat plate trailing edge (see Ref. 4 for further explanation).

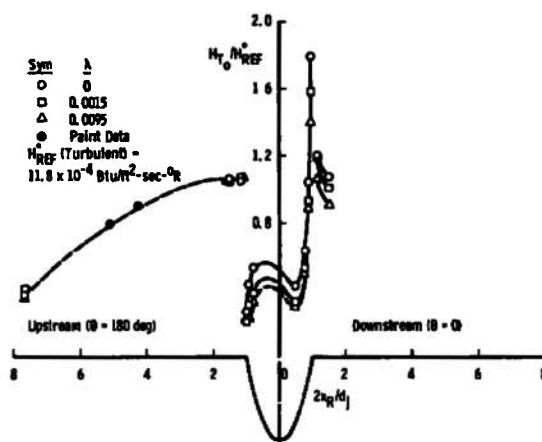
The influence of cavity bleed on the thermal loading is summarized in Fig. 8. The H_{REF} value used to normalize the heat-transfer-rate measurements is the theoretical film heat-transfer coefficient existing on the flat plate at the cavity insert location (i.e., at $x = 16.0$ -in.). In Figs. 8a and 8b, the flow over the flat plate at zero angle of attack was assumed to be laminar in computing the appropriate H_{REF} value. The presence or absence of a boundary-layer trip had little effect on the nature of the boundary layer or on the measured heat-transfer rates in the vicinity of the cavity. The ratio H_{T_o}/H_{REF} is equivalent to the ratio of measured heat-transfer rate to the theoretical heat-transfer rate, \dot{q}/\dot{q}_{REF} .



a. 2-in.-diam Cavity, $Re_l = 5 \times 10^6$ with a Boundary-Layer Trip, $\alpha = 0$



b. 2-in.-diam Cavity, $Re_l = 5 \times 10^6$, $\alpha = 0$



c. 2-in.-diam Cavity, $Re_l = 5 \times 10^6$, $\alpha = 30 \text{ deg}$

Fig. 8 Influence of Cavity Bleed on the Heat-Transfer-Rate Distribution at $Re_l = 5 \times 10^6$

At zero angle of attack in the presence of a laminar boundary layer (Figs. 8a and 8b), increasing the cavity bleed decreased the heat-transfer rate upstream of the cavity and immediately aft of the cavity ($2x_R/d_j < 1.5$) and increased the heat-transfer rate within the cavity. Further downstream of the cavity, the minimum bleed rate produced the maximum increase in the heat-transfer rate which leveled off at a value 3.3 times higher than the thermal loading existing on the plate without cavity bleed. Additional increases in the bleed rate simply reduced this maximum heat-transfer rate aft of the cavity, and in all cases these maximum rates exceeded the no-bleed heat-transfer rate. In general, the trend in the heat-transfer rates obtained with and without cavity bleed were not in agreement with trends predicted theoretically for a two-dimensional cavity in Ref. 3.

Better agreement between the theoretical trends with cavity bleed was obtained when the flat plate was inclined 30 deg to the flow (Fig. 8c). The local boundary layer approaching the cavity was fully turbulent and the local Mach number was about 2.6. In this case, as predicted theoretically, the increase in bleed rate reduced the thermal loading in the vicinity of the cavity (downstream) on the flat plate surface and also in the cavity. Included in this figure are data points (solid symbols) obtained from the temperature sensitive paint test which will be discussed later. In this figure, the heat-transfer rate ratio upstream falls below unity because the turbulent film heat-transfer rate based on the theoretical local conditions existing at $x = 16$ in. on the flat plate were used to define H_{REF} . As shown previously in Fig. 5c, the local heat-transfer rate increases from a laminar value to a turbulent value as the flow approaches the cavity when the flat plate was inclined 30 deg toward the free-stream flow.

In the regions on the flat plate which were directly influenced by the cavity disturbance, the cavity radius ($d_j/2$) becomes a useful normalizing parameter for correlating the heat-transfer-rate distributions as shown in Fig. 9. Upstream of the cavity, ahead of the cavity disturbance, the heat-transfer rates are dependent on the flat plate surface length and not the cavity size. For example, in Fig. 9a, upstream of $2x_R/d_j$ of 3 or 4, the correlated results separate because of the variation in cavity size. Along the reattachment surface of the cavity ($0.6 \leq 2x_R/d_j \leq 1.0$ and $\theta = 0$), the results obtained with different size cavities and at two different Reynolds numbers correlate reasonably well as shown in Figs. 9a, b, and c. In some cases, the data downstream of the cavity correlate reasonably well as a function of the normalized surface coordinate. Possibly the failure to correlate the results obtained with the 2.0-in.-diam cavity at the maximum Reynolds number at $\alpha = 0$ (Fig. 9a) can be attributed to a slight misalignment of the flat plate with the free-stream flow direction at zero angle of attack. A slight variation in the angle of attack has a significant effect on the measured heat transfer rate and on the H_{REF} value used to normalize the heat-transfer distribution. This problem does not exist with the results obtained at $\alpha = 10$ deg in Fig. 9b. At the maximum angle of attack (Fig 9c), the correlation fails downstream of the cavity because of the variation of the flat plate flow field edge effects as the boundary layer varied from fully laminar at $Re_j = 1 \times 10^6$ to fully turbulent at $Re_j = 5 \times 10^6$.

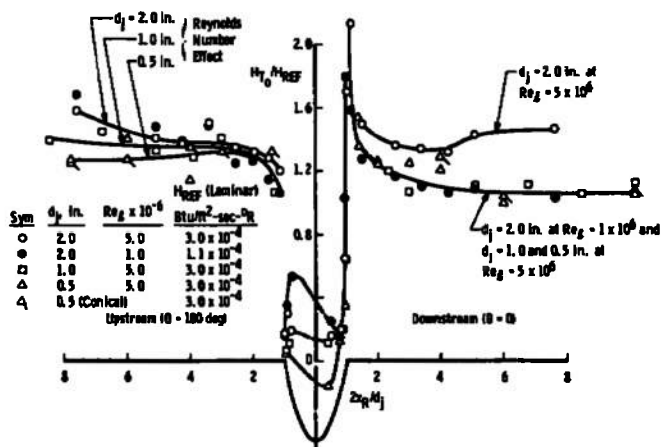
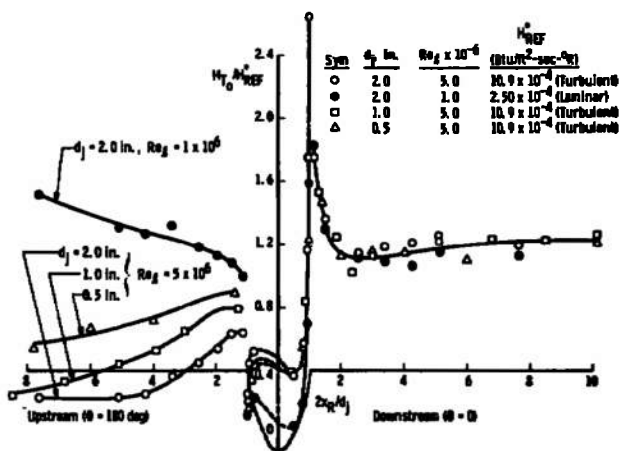
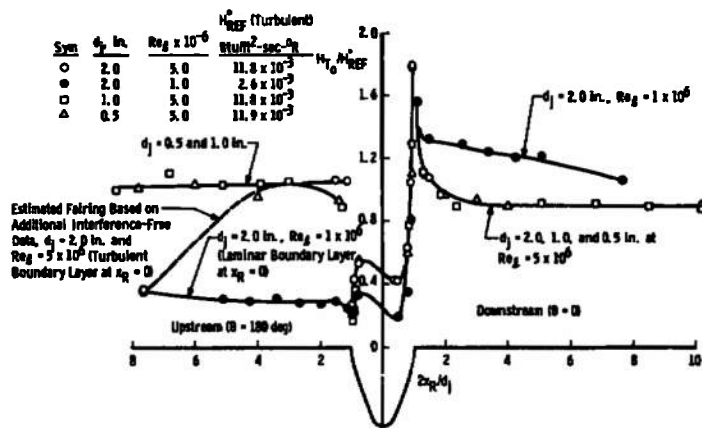
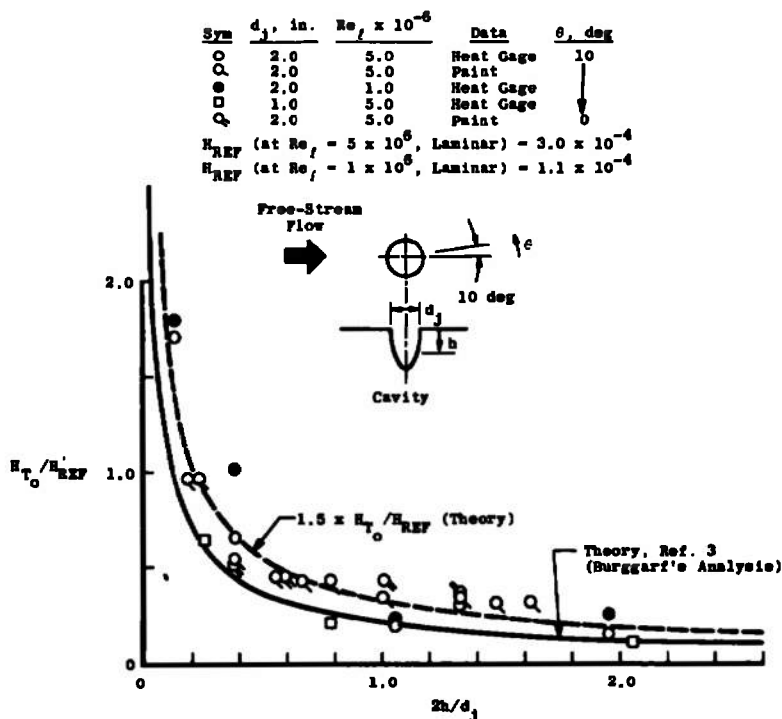
a. $\alpha = 0$ b. $\alpha = 10$ degc. $\alpha = 28$ deg

Fig. 9 Cavity Size, Reynolds Number, Boundary Layer, and Angle-of-Attack Effects on the Thermal Loading Within and Around the Cavity in a Flat Plate

Along the rearward facing surfaces of the cavity ($2x_R/d_j \leq 1.0$ at $\theta = 180$ deg), the normalized coordinate $2x_R/d_j$ does not correlate the heat-transfer-rate distributions obtained at $\alpha = 0$. At angle of attack, this correlation of the heat-transfer rates improves.

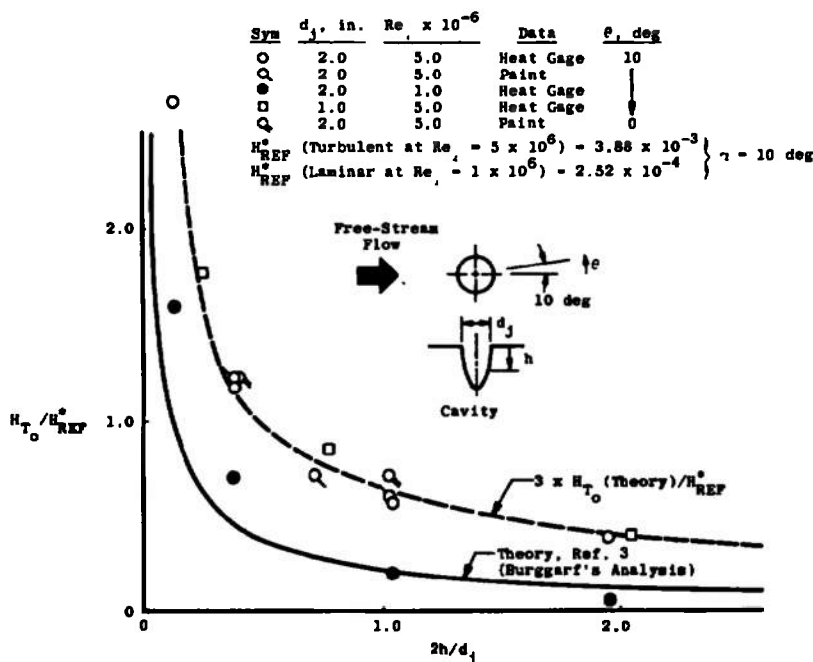
Within the cavity along the surfaces where the flow reattaches to the cavity wall, the film heat-transfer coefficient ratio (H_{T_o}/H_{REF}) is primarily a function of the cavity geometry as shown in Fig. 10. The value H_{REF} , the zero angle of attack value, or H^*_{REF} , the angle of attack value, is the local film heat-transfer coefficient that would theoretically exist on the flat plate at the point occupied by the cavity. Obviously, changes in the nature of the boundary layer at the cavity location and the variations in the local inviscid flow field resulting from a change in the model angle of attack will alter these reference film heat-transfer coefficients, H_{REF} and H^*_{REF} .

Most of the experimental data are based on heat-transfer-rate measurements made along an angular ray of 10 deg, but data based on the phase-change paint tests in Figs. 10a and b indicate that the variation in heat rates from $\theta = 0$ to $\theta = 10$ deg was very small.



a. $\alpha = 0$

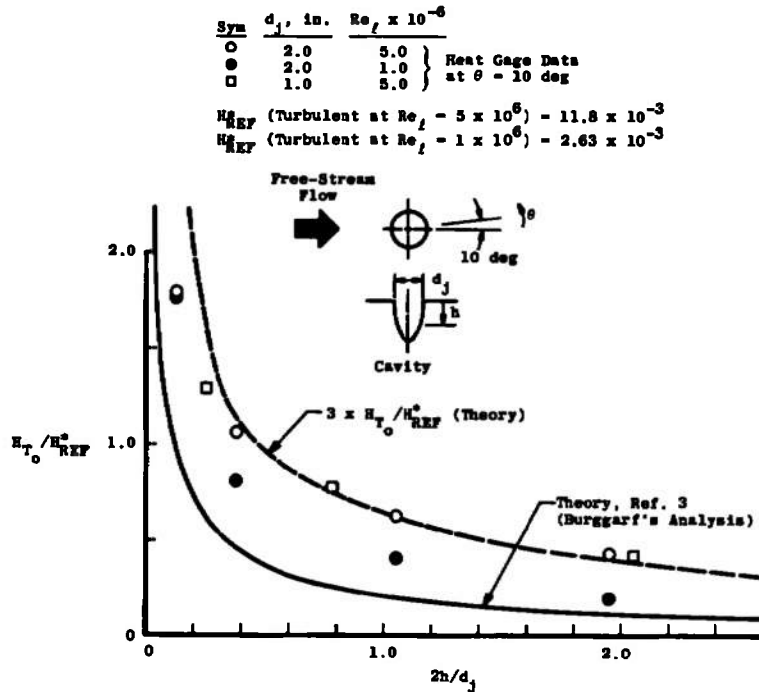
Fig. 10 Correlation of the Heat-Transfer-Rate Distributions Along the Reattachment Surface of a Cavity ($\theta = 0$) in a Flat Plate



b. $\alpha = 10$ deg
 Fig. 10 Continued

As noted in Ref. 3, the two-dimensional cavity analysis of J. W. Hodgson indicates that this normalized heat-transfer coefficient ratio is dependent on the cavity size and is not a unique function of this normalized cavity coordinate $2h/d_j$; however, the analysis of O. R. Burggraf, also in Ref. 3, produced a result which is in better agreement with the trends in the present data (i.e., H_{T0}/H_{REF}^* is a function of $2h/d_j$). For example, the results in Fig. 10a show that the data obtained with two cavity sizes at two different free-stream Reynolds numbers (two different H_{REF}^* values) correlated very well in terms of the nondimensionalized cavity coordinate, $2h/d_j$. In general, the experimentally defined curve obtained with the flat plate at $\alpha = 0$ indicated that the measured film heat-transfer coefficients were 1.5 times greater than those predicted by Burggraf. At the higher angles of attack where the local Mach number over the flat plate surface was lower, the reference film heat-transfer coefficient, H_{REF}^* , was greater than the corresponding value (H_{REF}) at zero angle of attack, and the data correlate along a curve which indicate the experimentally defined film heat-transfer coefficients obtained at $Re_q = 5 \times 10^6$ are three times greater than theoretical estimates of Burggraf. This difference between the data and the theory may be simply based on the fact that Burggraf's analysis was for a two-dimensional cavity and the present experimental results were obtained with an

axisymmetric three-dimensional contoured cavity. The low Reynolds number data were closer to the theory, but this difference between the two groups of Reynolds number data (i.e., data at $Re_\infty = 1 \times 10^6$ and data at $Re_\infty = 5 \times 10^6$) was attributed to uncertainties in the method used to estimate the undisturbed film heat-transfer ratio (H_{REF} or H^*_{REF}) existing at the cavity location on the flat plate.



c. $\alpha = 28$ deg
 Fig. 10 Concluded

This correlation does not appear to work as well for the heat-transfer-rate distributions along the separation surfaces of the cavity, that is along the surfaces for ray angles (θ) between 180 to 160 deg as shown in Fig. 11. Fortunately, these heating rates were considerably lower than those on the reattachment surface and therefore may not represent a serious design problem for the auxiliary control system for the space shuttle.

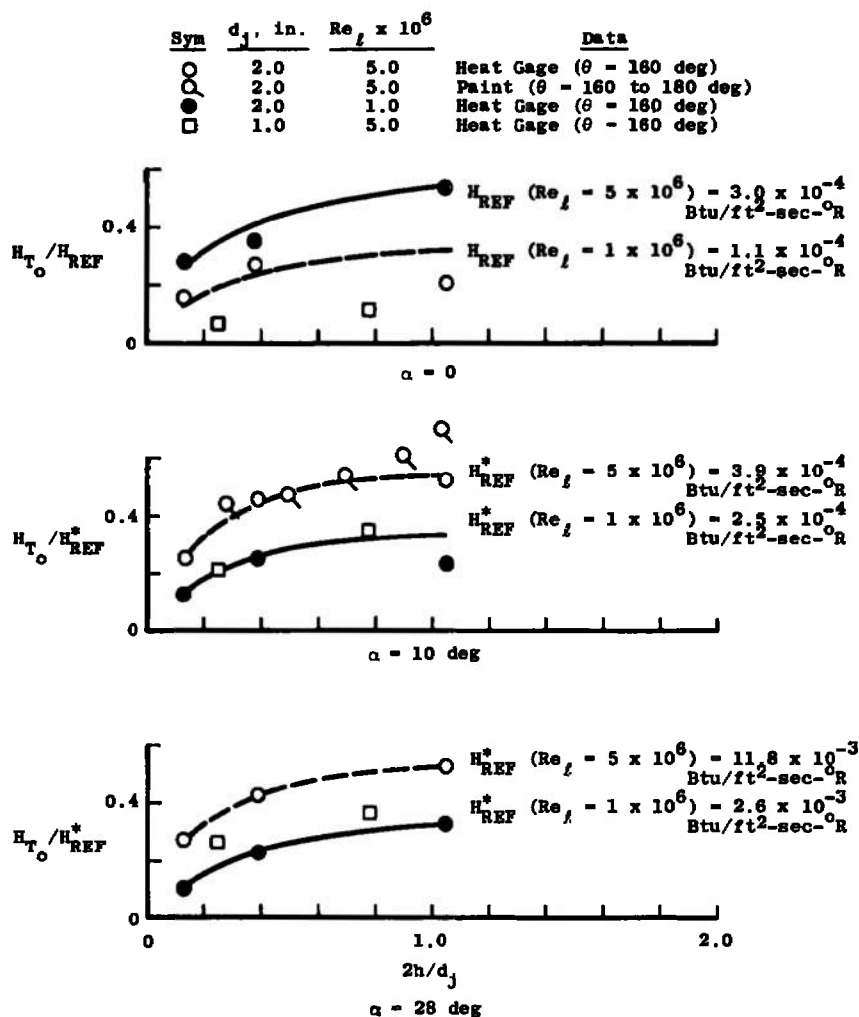


Fig. 11 Heat-Transfer-Rate Distribution Along the Separation Surface of the Cavity ($\theta = 160$ to 180 deg) in a Flat Plate

4.3 FLAT PLATE JET INTERFERENCE RESULTS

A typical pressure distribution on a flat plate around a flush-mounted supersonic conical nozzle produced by the interference of an expanding supersonic air jet plume with an enveloping hypersonic stream ($M_\infty = 8$) is shown in Fig. 12. This distribution represents the incremental change in the flat plate pressure along a normalized radial surface element on the flat plate emanating from the nozzle. The center of the nozzle is located 16.0 in. downstream from the flat plate leading edge and is the characteristic length (ℓ) of the flat plate. The normalizing radial coordinate parameter \bar{x}_R was based on an analysis described in Ref. 5, namely

$$\bar{x}_R = (2x_R/d_j) \bar{x}_{R_0}$$

where

$$\bar{x}_{R_0} = \sqrt{p_\infty / (\gamma p_j M_j^2)}$$

In Ref. 5, this coordinate \bar{x}_R was defined somewhat differently and applied only to sonic jets, but to make the parameter more general and applicable to supersonic jets, the term \bar{x}_{R0} was defined in terms of the jet exit stream properties instead of the nozzle chamber properties. At angle of attack, the free-stream ambient pressure (p_∞) was replaced by the theoretical undisturbed inviscid static pressure (p^*) that would exist on the flat plate, i.e., the value predicted by the oblique shock relationships.

In general, the pressure distribution up to and including the pressure spike (for example up to $\bar{x}_R = 0.3$ at $\theta = 180$ deg) is strongly dependent on the jet pressure (i.e., a function of \bar{x}_R). As noted in Fig. 12, a change in the jet pressure by a factor of 6 and the jet stagnation temperature by a factor of 2 did not significantly influence this normalized distribution. Outboard of the pressure spike, the local stream Reynolds number and state of the boundary layer influences the pressure distribution as indicated by the additional distributions presented in Appendix I.

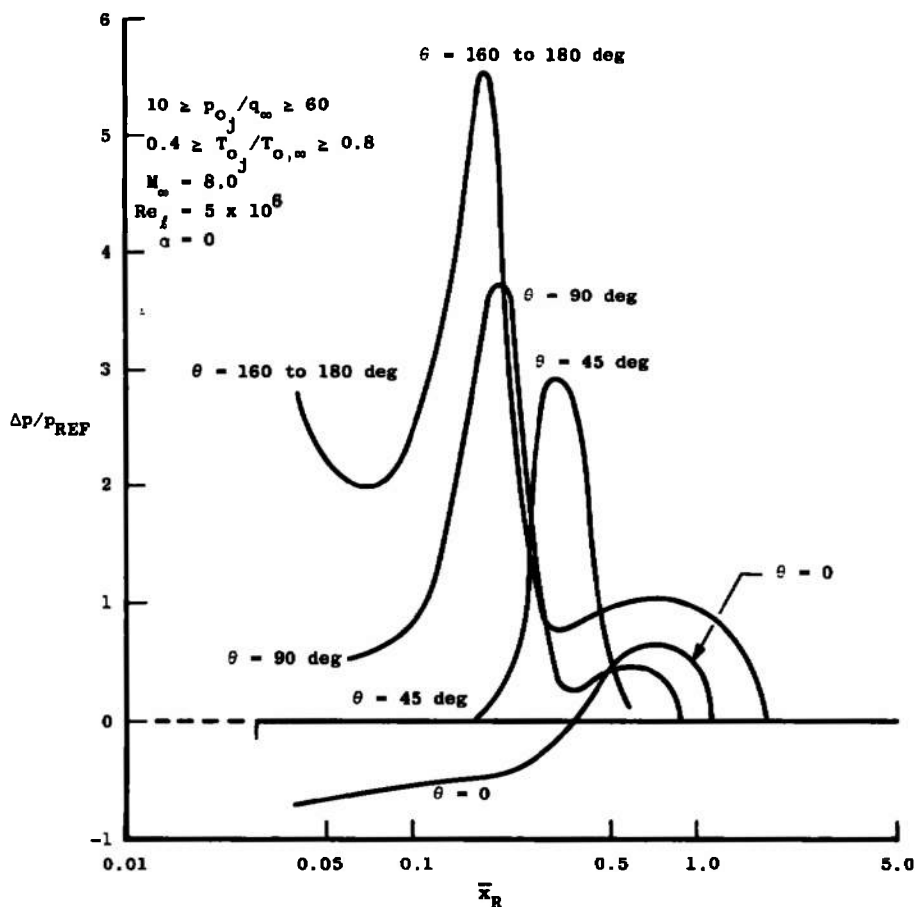


Fig. 12 Typical Pressure Distributions Around a Single Supersonic Air Jet Flush Mounted in a Flat Plate, $\alpha = 0$

The position of the pressure spike in these distributions moves outward as the jet disturbance propagates around the nozzle (i.e., as θ decreases from 180 deg to about 15 deg). Also, the magnitude of the pressure spike decreases roughly as a function of $(1 + \cos \theta)$. The actual magnitude of the pressure spike, which is important in terms of correlating the data, depends on the magnitude of the jet disturbance. For example, the width of the pressure spike varies as the square root of the jet pressure ($x_R = \bar{x}_R \cdot d_j / 2\sqrt{p_j M_j^2 / R_\infty}$) and as the jet pressure decreases, the physical size of the pressure tap used in the vicinity of this spike to measure the surface pressure yields an average value (a lower value) rather than the peak value. At the lower free-stream Reynolds numbers where the jet interference was significantly larger and the pressure spikes spanned a greater region of the flat plate surface (see Fig. I-3, Appendix I), the peak pressures reached a value of 7.8 or 40 percent higher than those shown in Fig. 12.

Interferograms of the flow field produced by a supersonic jet from a conical nozzle operating at the conditions corresponding to the pressure data of Fig. 12 are shown in Fig. 13. The variation in the fringe line spacing corresponds to a variation in the local gas density. In a high density region such as the model bow wave, the separated boundary-

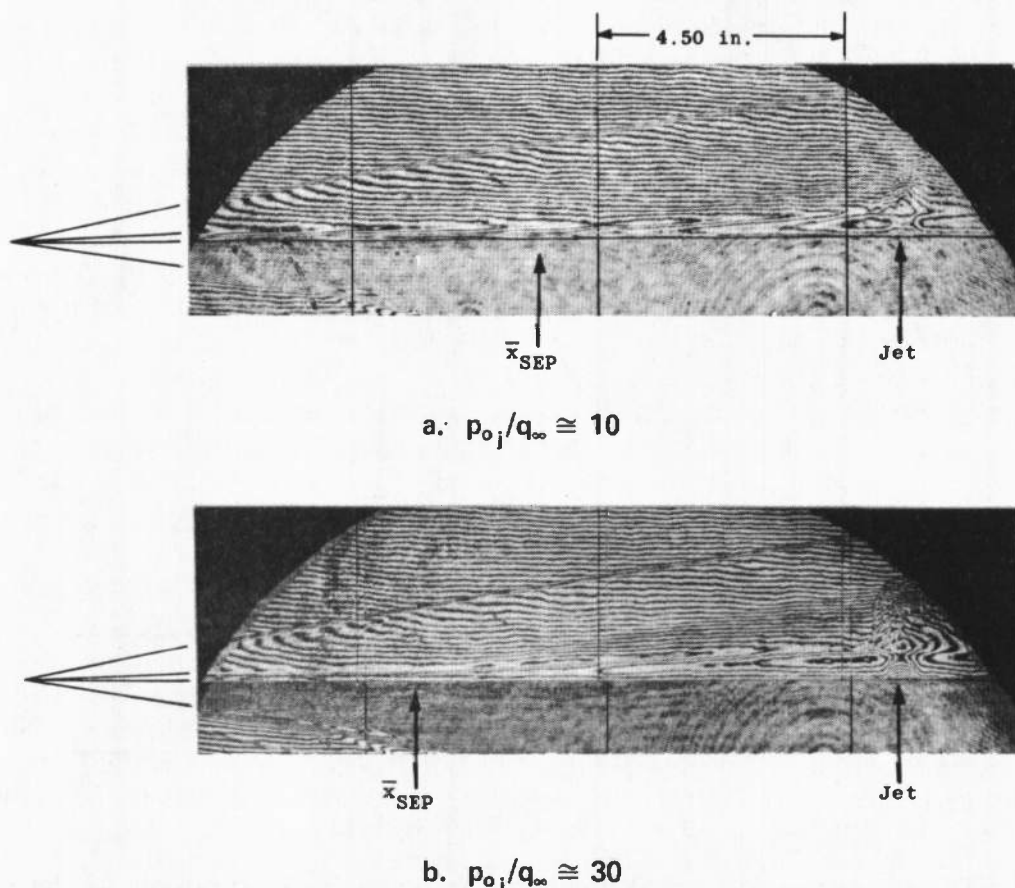
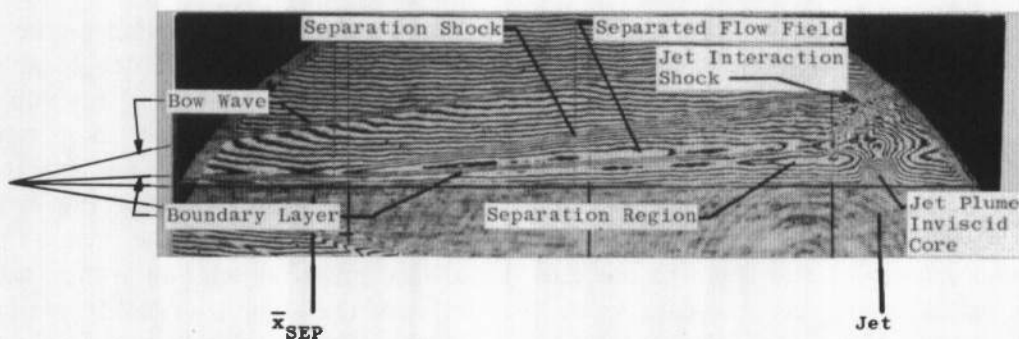


Fig. 13 Supersonic Lateral Air Jet Interaction Effects on a Flat Plate at $\alpha = 0$, $M_\infty = 8.0$ and $Re_\ell = 5 \times 10^6$ (Single Nozzle, $M_j = 2.84$, $d_j = 0.50$ in.)



c. $p_{o_j}/q_\infty \cong 60$
 Fig. 13 Concluded

layer shock, the boundary layer or the jet plume, the line density increases. For example, as the jet pressure increases, the jet plume, an expanding high density flow field, emerges from the nozzle exit and becomes clearly evident in Fig. 13c. The jet plume acts as a protuberance on the flat plate causing the approaching laminar boundary layer to separate ahead of the jet. The previously correlated results in Fig. 12 indicate that the size of this protuberance which determines the length of separated flow varies approximately as the nozzle exit diameter and as the square root of the jet exit pressure.

Varying the flat plate angle of attack changes the local Mach number, Reynolds number, and boundary layer on the flat plate in the vicinity of the jet nozzle. The angle-of-attack effects on the jet interference is summarized in Fig. 14 and shows that the pressure spike location upstream of the jet remains at \bar{x}_R value of 0.18. Downstream of the jet, the increase in angle of attack causes the peak pressure to decrease but remain in a fixed position relative to the jet (i.e., \bar{x}_R varies but the $2x_R/d_j$ locations of the peak is about 20.4). These results indicate that in the presence of transitional or turbulent boundary-layer flow, the peak pressure aft of the circular jet increases with the local stream Mach number. In the presence of a laminar boundary layer, that is, at the lower free-stream Reynolds number of 1×10^6 , there were no significant peaks in the pressure distribution aft of the jet at zero nor at 30-deg angle of attack (see Fig. I-5).

In Ref. 5, the correlated pressure distributions obtained at Mach number 18.5 on a flat plate with a sonic jet indicated that the pressure spike occurred at an \bar{x}_R value of 0.22 which is only 22 percent greater than the present value obtained for a supersonic jet. Also, the results of Ref. 5 obtained in the presence of a laminar boundary layer on the flat plate indicated that as the ratio of the jet stagnation to free-stream stagnation temperature increased, the peak pressure aft of the jet diminished. As shown in Fig. I-1g, varying the jet gas temperature when the boundary layer is transitional did not influence the pressure distribution aft of the jet, but when the boundary layer was fully laminar in the jet interference region and the jet gas temperature was high, the pressure peak aft of the jet was not present as is shown in Fig. I-3d. Thus the results in Ref. 5 and the present data suggest that the pressure loading aft of the jet along the $\theta = 0$ ray

is negligible if the jet interference occurs in the presence of a laminar boundary layer and the ratio T_{o_j}/T_{o_∞} is high, approaching unity.

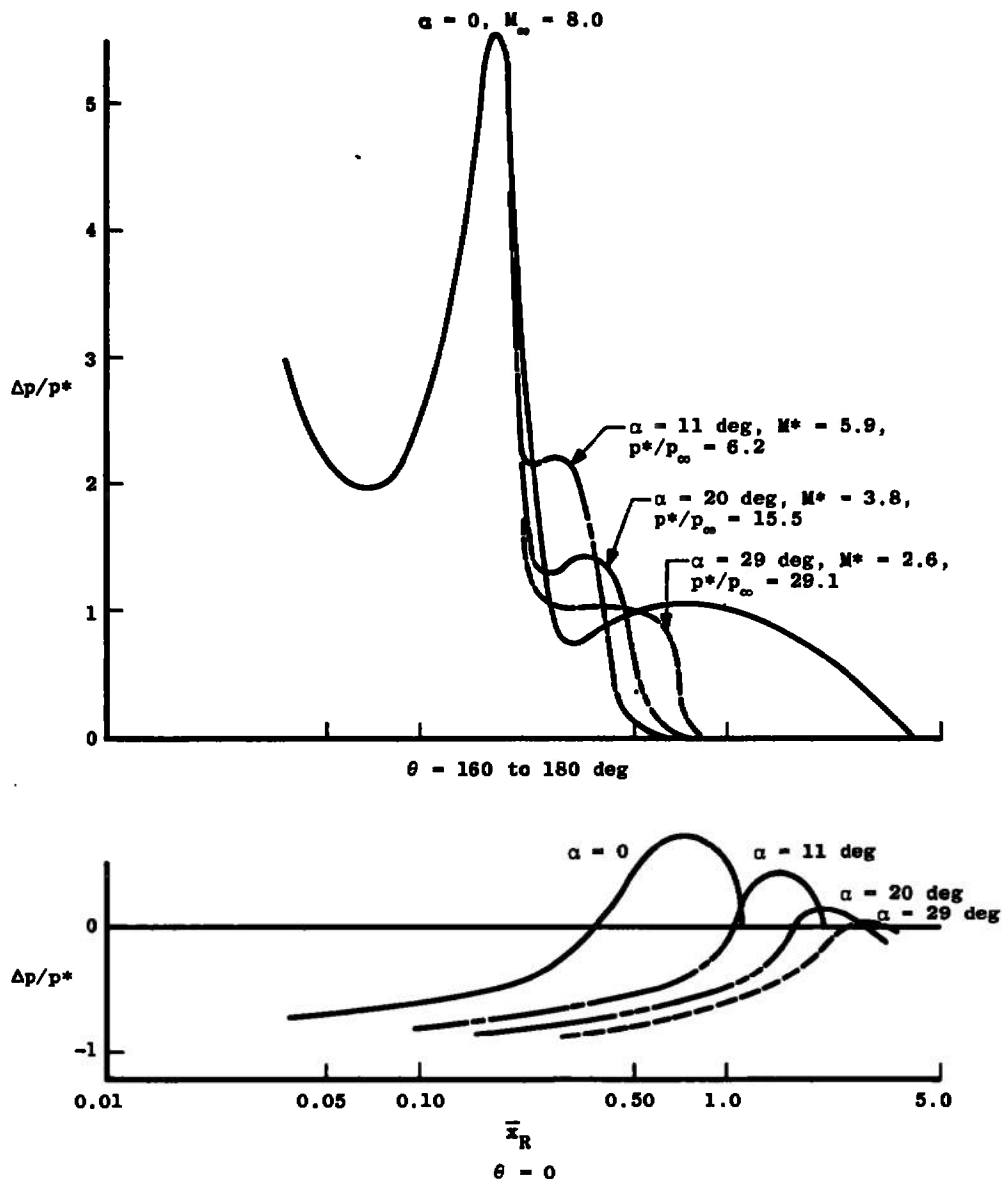


Fig. 14 Angle-of-Attack Effect on the Pressure Distribution Around a Single Supersonic Air Jet, $p_{o_j}/q_\infty \cong 60$, $T_{o_j}/T_{o_\infty} = 0.4$, $M_\infty = 8.0$, and $Re_\eta = 5 \times 10^6$

A comparison of the pressure distributions generated by a helium jet to those generated by an air jet are summarized in Fig. 15. The pressure spike location ahead of the jet ($\theta = 180 \text{ deg}$) in the helium jet interaction would not correlate as a simple function of the normalized coordinate \bar{x}_R . The \bar{x}_R values defining the location of the pressure spike for the helium jet pressure distribution were smaller than the one locating

the spike in the jet pressure distribution. Also, the magnitude of the peak pressure upstream of the helium jet was at least twice the value produced by the air jets. Upstream of these pressure spikes, the incremental change in pressure level existing in the separated boundary-layer region ahead of the helium jet disturbance was less than one-half the pressure value existing in the separation region ahead of the air jets. Downstream of the jet ($\theta = 0$), the variation in the jet gas did not significantly influence the pressure distribution.

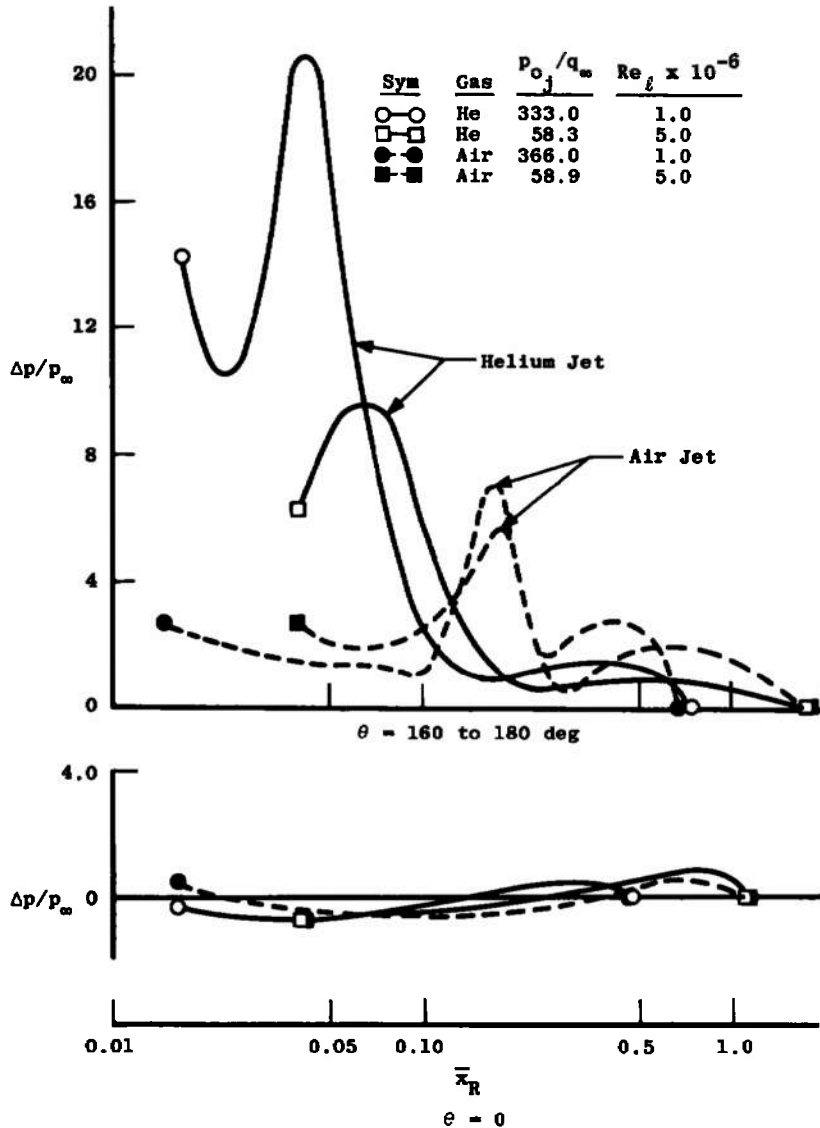


Fig. 15 Helium and Air Gas Jet Effects on the Pressure Distributions Around a Single Supersonic Nozzle, $\alpha = 0$

The flow field produced by a helium jet from a flat plate is shown in Fig. 16 and is compared to an air jet operating at a slightly higher nozzle pressure. These interferograms were taken with the flat plate at 11-deg angle of attack (the zero-degree angle of attack interferograms were of a poorer quality and therefore omitted). The beginning and end of boundary-layer transition on the flat plate with the jets off are indicated in the figure. The most significant feature in this comparison of the air and helium jets is the complete absence, no visual indication, of the helium jet inviscid plume core. Only the density gradients associated with changes in the external stream produced by the lateral jets are visible in Fig. 16b, while in Fig. 16a the combined changes in density produced by the jet gas and the external stream are present. In fact, the jet density variations are so strong that the plume core is visible in Fig. 16a.

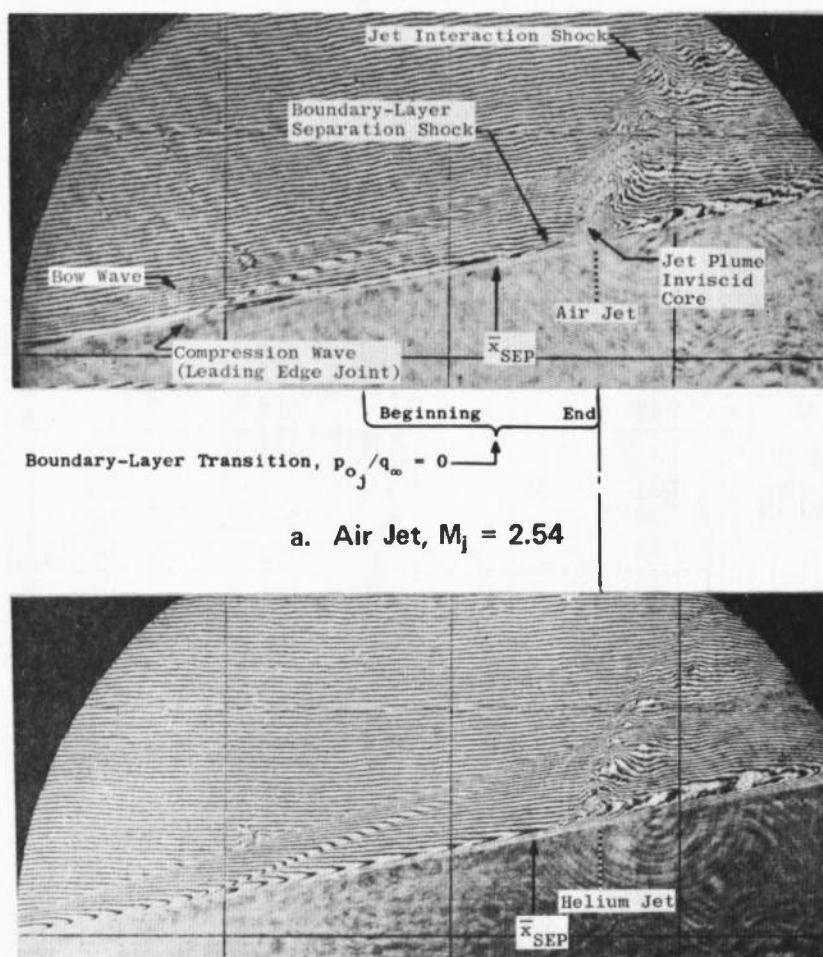


Fig. 16 Comparison of Helium and Air Jet Plume Interference Effects on a Flat Plate at $\alpha = 11$ deg, Supersonic Nozzle (Area Ratio of 2.73), $d_j = 0.50$ in., $p_{0j}/q_\infty \cong 58$, $M_\infty = 8.0$, and $Re_\ell = 5 \times 10^6$

Another feature clearly shown in Fig. 16a which was present in nearly all the interferograms is the irregularity of the jet interaction shock. These bubbles or nonuniformities in the curvature of the jet interaction shock indicate that the interference of the jet with the external stream was an unsteady flow field phenomenon. The exposure time for the holograms used in reconstructing the interferograms is 20×10^{-9} seconds and thus freezes any motions slower than about 50×10^6 cycles per second. Even the turbulent structure in the boundary layer aft of the jet appears as an irregular fringe line, whereas the fringes in the boundary layer upstream of the jet are quite smooth or of a laminar nature.

A cluster of four supersonic conical nozzles was tested in place of the single supersonic conical nozzle on the flat plate. The net exit area of the cluster of nozzles was about 92 percent of the exit area of the single nozzle. Assuming the effective diameter of the cluster of nozzles was equal to twice the diameter of one of the four nozzles, the pressure distribution obtained in terms of the normalized coordinate \bar{x}_R is given in Fig. 17 and compared directly to the single nozzle results. In general, the distributions were quite similar and the pressure spike locations were essentially the same, but the magnitude of the peak pressure of the nozzle cluster was significantly smaller.

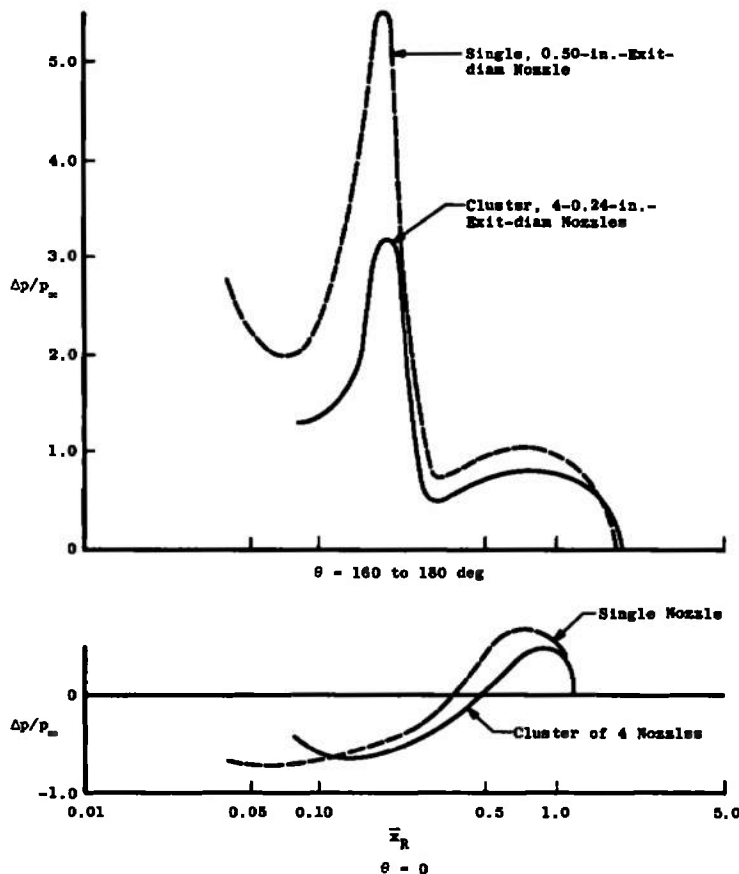
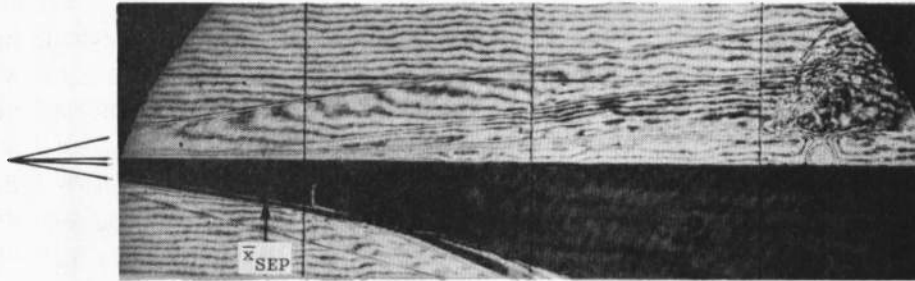
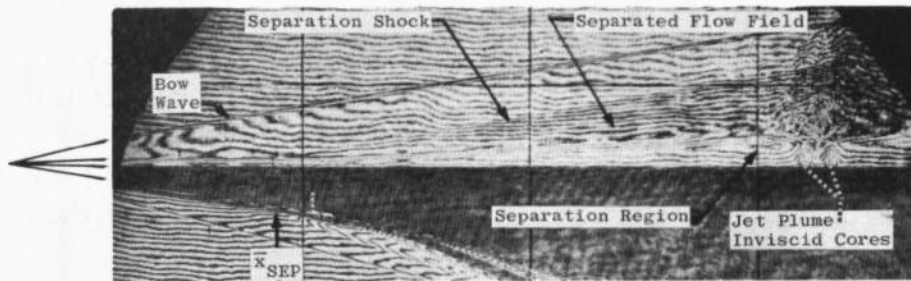


Fig. 17 Comparison of Cluster Nozzle with Single Nozzle Flat Plate Pressure Distributions, Air Jet, $p_{o1}/q_{\infty} \cong 60$, $T_{o1}/T_{o,\infty} = 0.4$, $\alpha = 0$, and $Re_l = 5 \times 10^6$

The similarity of the flow field characteristics produced by a single supersonic nozzle and a cluster of four supersonic nozzles operating at the same mass flow rate is shown in Fig. 18. The primary difference between the two flow fields is the fact that the cluster of four nozzles shows two well defined inviscid jet plume cores instead of one as in the case of the single jet. The four nozzles in the cluster are aligned optically in pairs so that only two jet plumes would appear in the interferogram. The other features of the flow field such as the length of separated flow and the location of the jet interaction shock for the single and cluster nozzle configurations were almost identical.



a. Single Supersonic Nozzle, Air Jet $d_j = 0.50$ in., $M_j = 2.54$, $(p_j/q_\infty)A_j = 0.65$, and $T_{o,j}/T_{o,\infty} = 0.65$

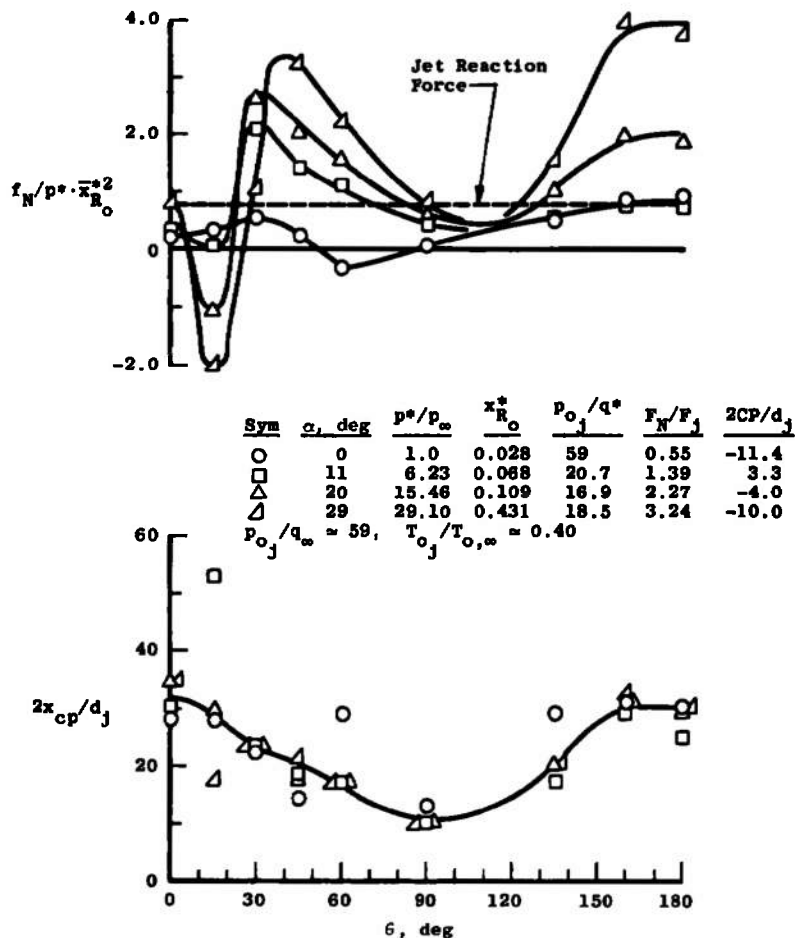


b. Cluster of Four Supersonic Nozzles, Air Jet $d_j = 0.24$ in., $M_j = 2.54$, $(p_j/q_\infty)A_j(\text{net}) = 0.59$, and $T_{o,j}/T_{o,\infty} = 0.59$

Fig. 18 Comparison of the Single Supersonic Nozzle and a Cluster of Four Supersonic Nozzles Flow Field Disturbances on a Flat Plate at $\alpha = 0$, $M_\infty = 8.0$, and $Re_\ell = 5 \times 10^6$

The loading on a flat plate around the single supersonic jet at various angles of attack is illustrated in Fig. 19. These results represent the local loading on the flat plate along the radial elements emanating from the nozzle, normalized by the local undisturbed theoretical inviscid static pressure on the plate, and multiplied by the jet correlation term $\sqrt{p^*/(\gamma p_j M_j^2)}$. The dashed line represents the corresponding normalized theoretical distribution of the jet thrust distributed radially over the face of the nozzle exit. Included in these figures are tabulated estimates of the net loading generated on the flat plate

by the jet disturbance (F_N) normalized by the reaction force of the jet (F_j) exhausting into the local pressure field (p^*). Additional loading distributions around the single nozzle and the cluster nozzle configurations are included in Appendix I (Figs. I-8 to I-11).

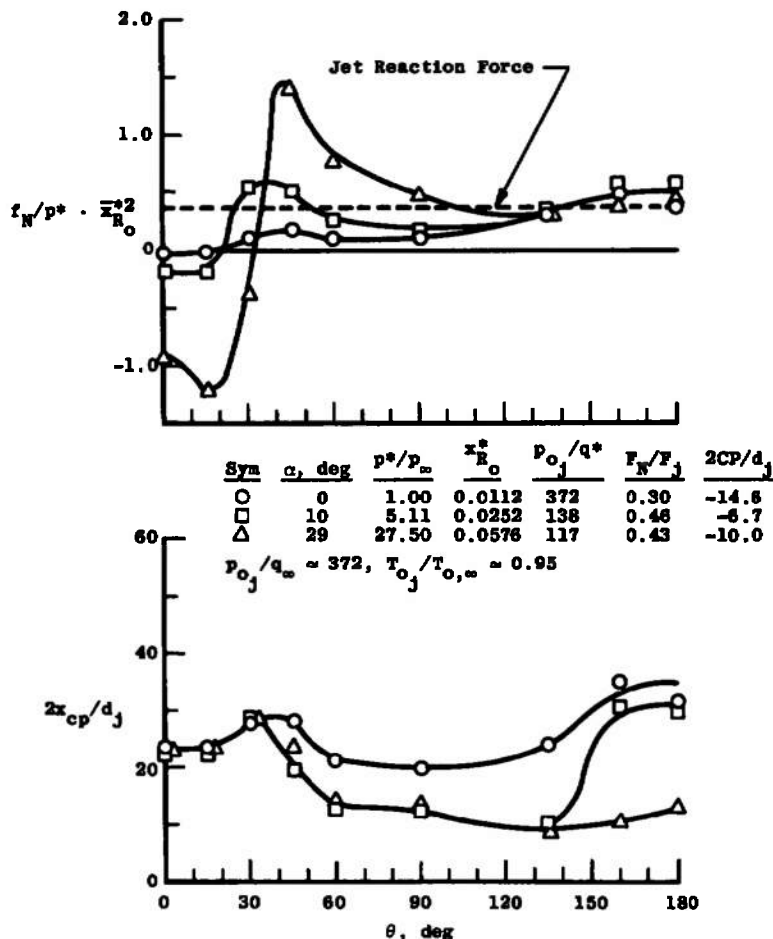


a. $Re_\theta = 5 \times 10^6$

Fig. 19 Angle-of-Attack Effects on the Circumferential Loading Around a Single Conical Nozzle Air Jet Disturbance

The loading data presented in Fig. 19 shows that increasing the local stream Mach number (by decreasing α) and the corresponding change in the local boundary layer from turbulent (Fig. 19a at $\alpha = 11$ deg) to laminar (Fig. 19b at $\alpha = 10$ deg) produces a decrease in the loading along radial elements aft of the jet between $\theta = 30$ and 90 deg. Although not shown in these figures, varying the jet gas temperature had no effect on the surface loadings (see Fig. I-9). Similarly these results (Fig. 19) and the additional data in Appendix I show that as the local ratio of jet exit pressure to local stream dynamic pressure increases, the ratio of the net change in surface loading to jet reaction force decreases.

In the lower half of Fig. 19, the effective center of pressure of the radial loading element normalized by the nozzle exit radius is presented as a function of the radial angle, θ . In general, at $Re_j = 5 \times 10^6$, this center of pressure distribution (x_{cp}) did not seem to vary significantly with the local stream properties (i.e., it was fairly independent of the flat plate angle of attack).

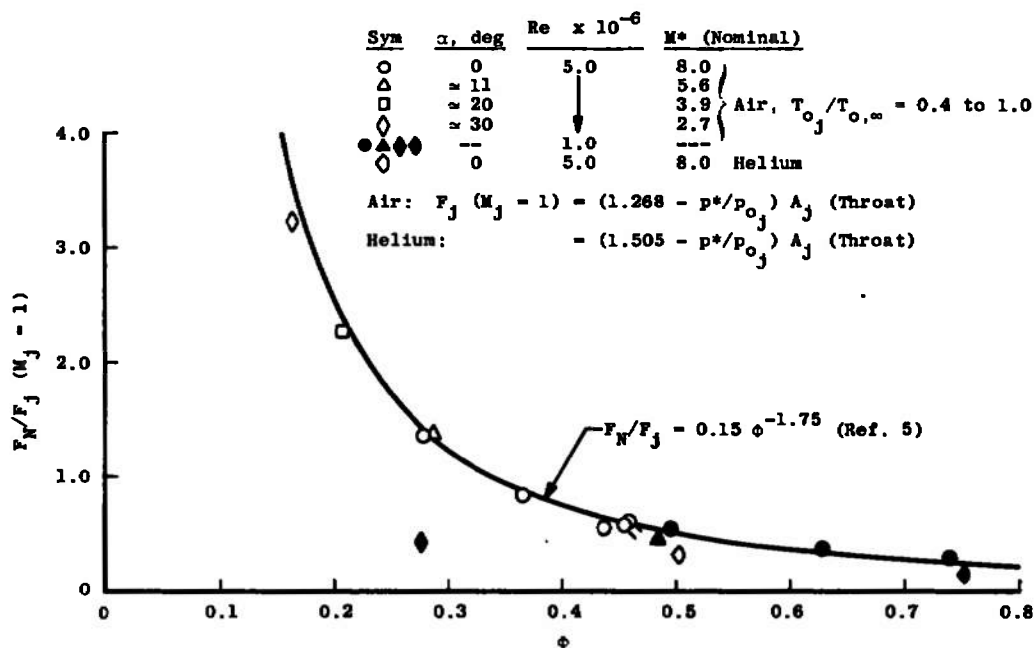


b. $Re_j = 1 \times 10^6$

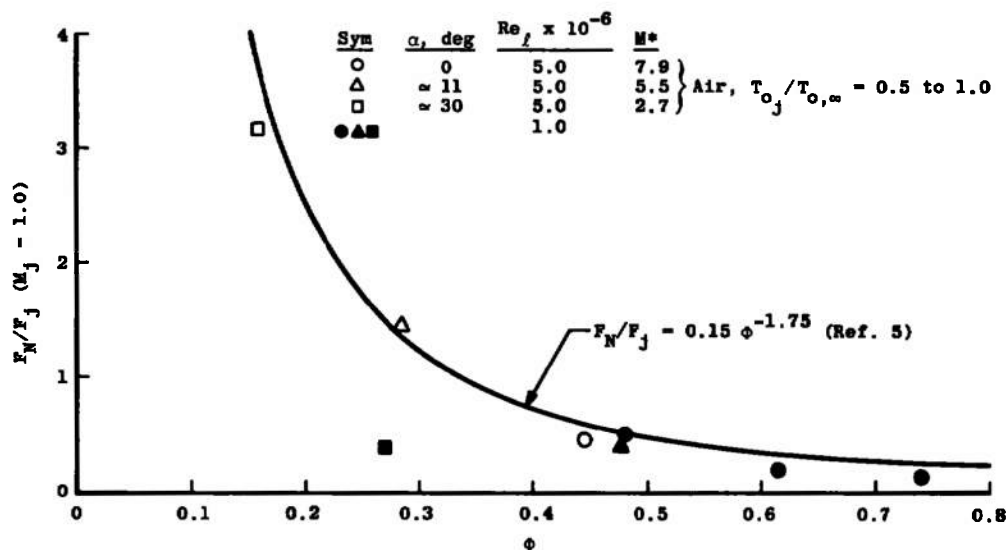
Fig. 19 Concluded

There was some scatter in the high Reynolds number x_{cp} locations and more scatter in the lower Reynolds number center-of-pressure locations. Of course, any scatter in the pressure measurement results in a poorly defined pressure distribution which would influence the numerical evaluations of the pressure integrals used in computing the loading and center-of-pressure locations around the jet. The worst repeatability in these pressure measurements as noted in Section 2.2 was obtained at zero angle of attack and the lower Reynolds number of 1×10^6 .

The ratio of the net change in surface loading normalized by the thrust of a sonic jet with an exit diameter equal to the supersonic nozzle throat diameter correlates reasonably well as a function of the jet parameter Φ as shown in Fig. 20. This parameter,



a. Single Supersonic Nozzle, Air Jet



b. Cluster of Four Supersonic Nozzles, Air Jet

Fig. 20 Correlation of the Supersonic Lateral Air Jet Augmentation Factors

Φ_j was formulated in Ref. 5 from an application of the blast wave analogy to the jet interaction phenomenon and has the following form.

$$\Phi = \left\{ \left(\frac{p_{o,j}}{p_{\infty} M_{\infty}^2} \right) (\kappa \lambda_t)^{-3/4} \right\} \sqrt{\frac{d_{jt}}{\ell/\beta}} \quad (29)$$

where

$$\lambda_t = \rho_{jt} u_{jt} / (\rho_{\infty} u_{\infty})$$

$$\kappa = 1 + \left(1 + \frac{2}{\gamma-1} M_{\infty}^2 \right) \left(\frac{C_{p,j} T_{o,j}}{C_{p,\infty} T_{o,\infty}} \right) + \left(\frac{2}{\gamma-1} \right) \frac{1}{\gamma M_{\infty}^2}$$

and

$$\beta = \sqrt{M_{\infty}^2 - 1}$$

In this correlation parameter, all the jet properties are referenced to the conditions existing at the nozzle throat instead of the conditions existing at the nozzle exit.

The empirical curve fit applied to the sonic jet results of Ref. 5, namely

$$F_N/F_j = 0.15\phi^{-1.75} \quad (30)$$

is included in Fig. 20 and provided a good curve fit for the present supersonic lateral jet results. The angle-of-attack effects, except for the data point obtained at 30 deg at the minimum Reynolds number (1×10^6) agreed with the empirical function. At angle of attack, the correlation parameter Φ was evaluated in terms of the local stream properties (p^* , M^* , ρ^* , u^*) on the flat plate instead of the free-stream properties.

In general, the data obtained with the cluster of four nozzles and presented as a function of ϕ was also found to agree with the empirical curve as shown in Fig. 20b. Again, the result obtained at the maximum angle of attack and at the minimum free-stream Reynolds number (1×10^6) did not correlate with the rest of the data.

Also, an attempt was made to correlate the length of the disturbance generated on the flat plate upstream of the jet nozzle and these results are given in Fig. 21. The length of the disturbance produced by the jet interaction upstream of the jet was defined as \bar{x}_{SEP} which was normalized by the nozzle exit radius and multiplied by the jet parameter $\sqrt{p^*/(\gamma_j p_j M_j^2)}$ to form a correlation length, \bar{x}_{SEP} . The data obtained at Mach number 18.5 with a sonic jet in the presence of a laminar boundary layer (Ref. 5) are included in this figure and agreed quite well with the present supersonic lateral jet data obtained in the presence of a laminar boundary layer. The high Reynolds number data obtained at angle of attack in the presence of a turbulent boundary layer formed a correlation which indicated the separation length parameter \bar{x}_{SEP} varies more rapidly with the

parameter $(p_j/q^*)A_j$ (i.e., \bar{x}_{SEP} proportional to $[(p_j^*/q^*)A_j]^{2.7}$). in the presence of a laminar boundary, the separation length parameter \bar{x}_{SEP} was proportional to $[(p_j/q^*)A_j]^{0.16}$ and a weaker function of the jet pressure.

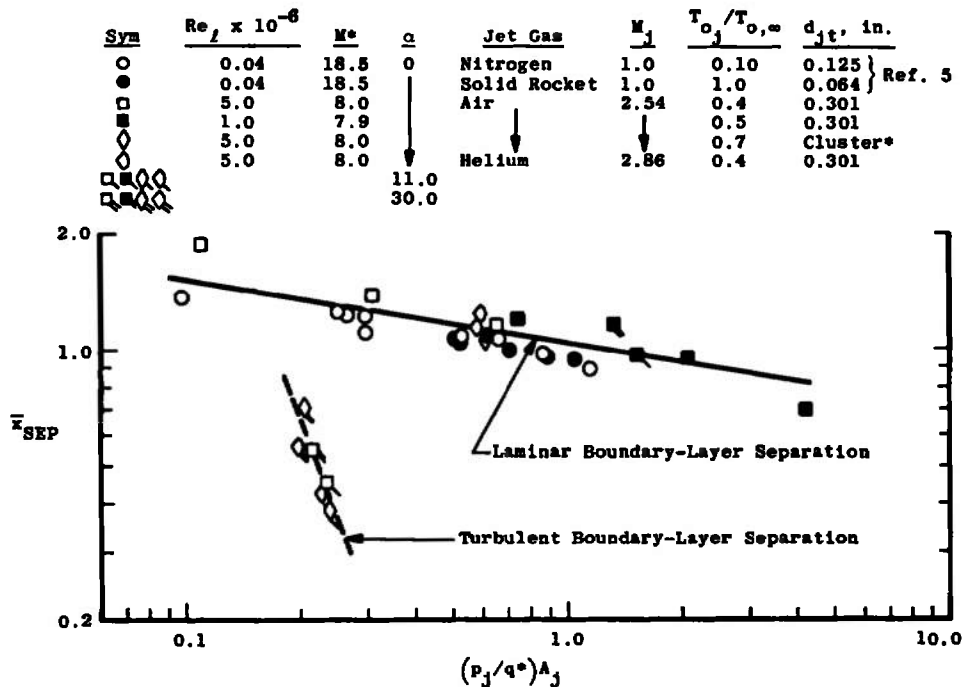
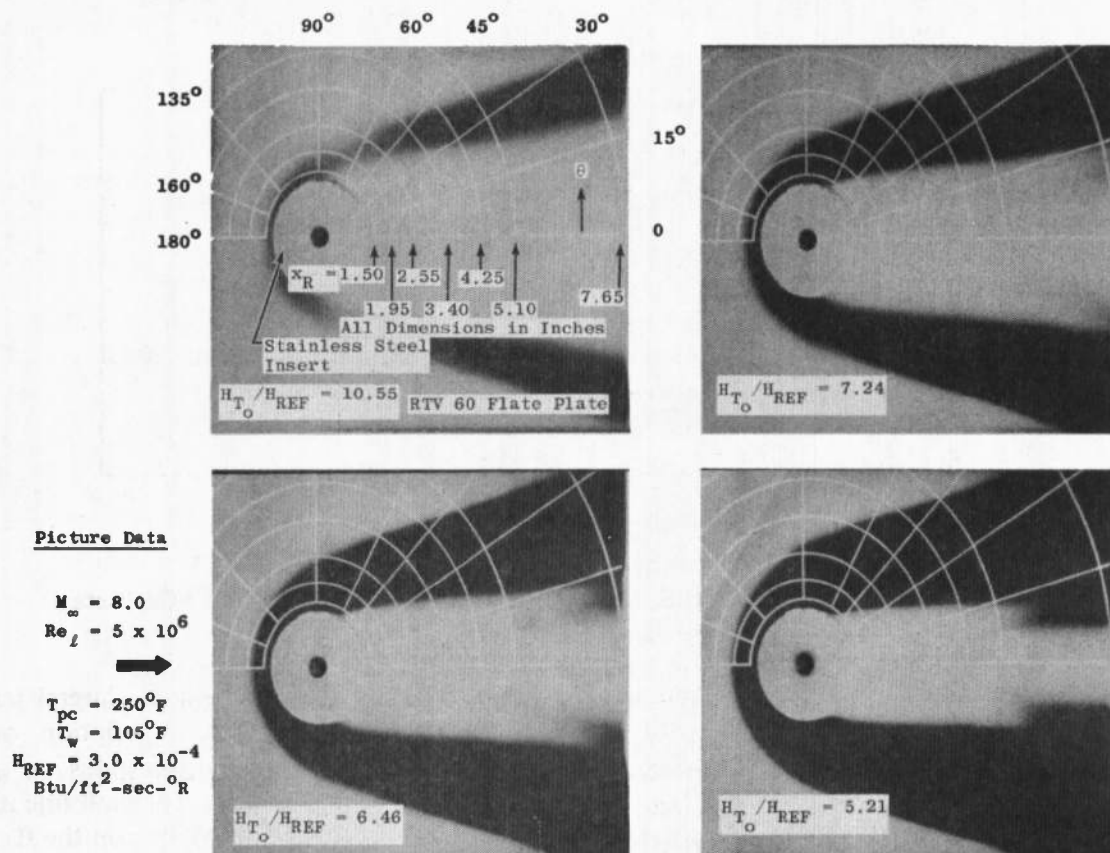


Fig. 21 Location of the Initial Lateral Air Jet Disturbance on the Flat Plate

The heat-gage data obtained on the flat plate with the single supersonic lateral jet disturbance was complemented with phase-changing paint results. A description of this phase-change paint technique for determining quantitative heat-transfer rates on a surface similar to those shown in Figs. 22 and 23 can be found in Ref. 6. The melt line in these photographs is the locus of a constant film heat-transfer coefficient existing on the flat plate produced by the supersonic lateral jet disturbance. The value of the film heat-transfer coefficient for the melt line is listed below each individual photograph.

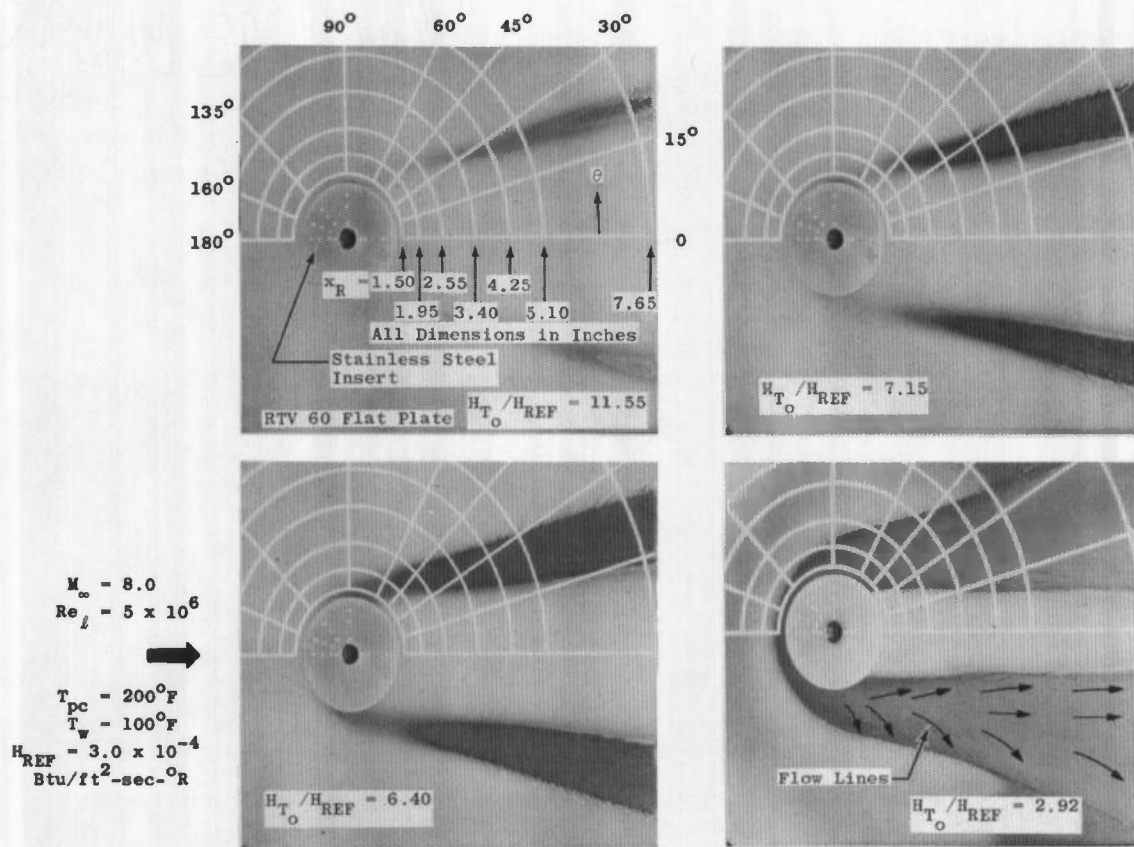
In the presence of a laminar boundary layer, the maximum heat rate (the beginning or onset of the melt line) begins just upstream of the jet on the stainless steel nozzle insert as indicated by the heat-gage data and downstream of the nozzle insert as shown by the paint data. The melt line was not present on the stainless steel because the thermodynamic properties of the steel delays the paint melting relative to the visible melt line existing on the silicone rubber surface. As time progressed and the associated heat ratio decreased, these two melt regions (the one upstream and the two downstream of the jet) joined together forming a horseshoe type of melt pattern. This melt pattern was formed, as noted in Ref. 5, by two counter rotating horseshoe vortices formed by the

lateral jet disturbance. Reducing the strength of the jet (decreasing $p_{o,j}$) reduced the region encompassed by the melt line (compare the $H_{T_o}/H_{REF} = 7.2$ melt lines in Figs. 22a and b). Superimposed on the melt lines in Fig. 22b are the flow patterns produced by the melted paint as influenced by the jet disturbance. These flow patterns were very similar to those obtained at lower free-stream Mach numbers in the presence of laminar boundary layers and shown in Ref. 7.



a. Supersonic Air Jet: $d_j = 0.50$ in., $M_j = 2.54$, and $p_{o,j}/q_{\infty} \cong 58$

Fig. 22 Typical Phase-Changing Paint Photograph of Heat-Transfer-Rate Distribution on a Flat Plate in the Presence of a Laminar Boundary Layer at $\alpha = 0$ with a Supersonic Air Jet ($T_{o,j}/T_{o,\infty} = 0.47$)



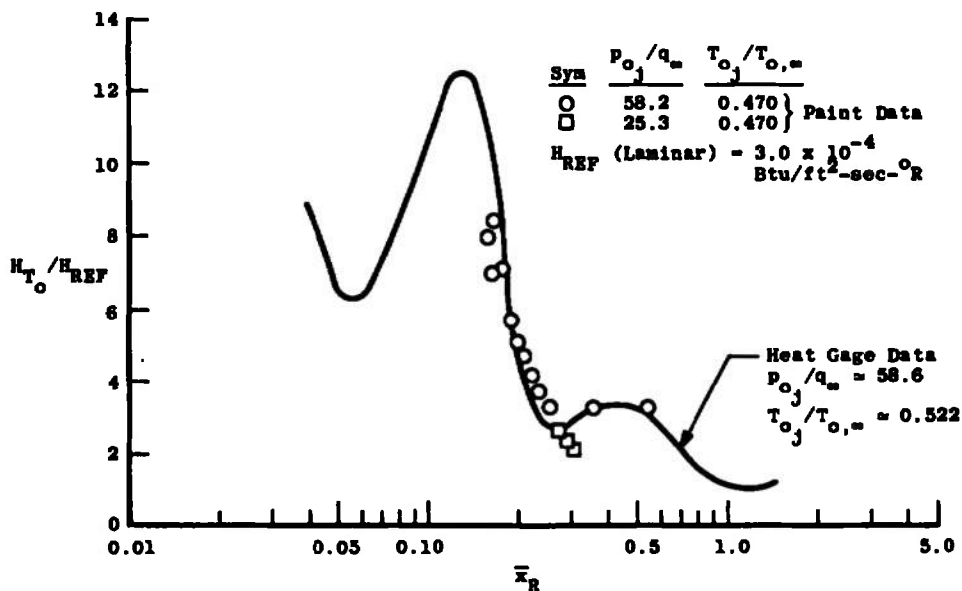
b. Supersonic Air Jet: $d_j = 0.50$ in., $M_j = 2.54$, and $p_{o_j}/q_\infty \cong 25$

Fig. 22 Concluded

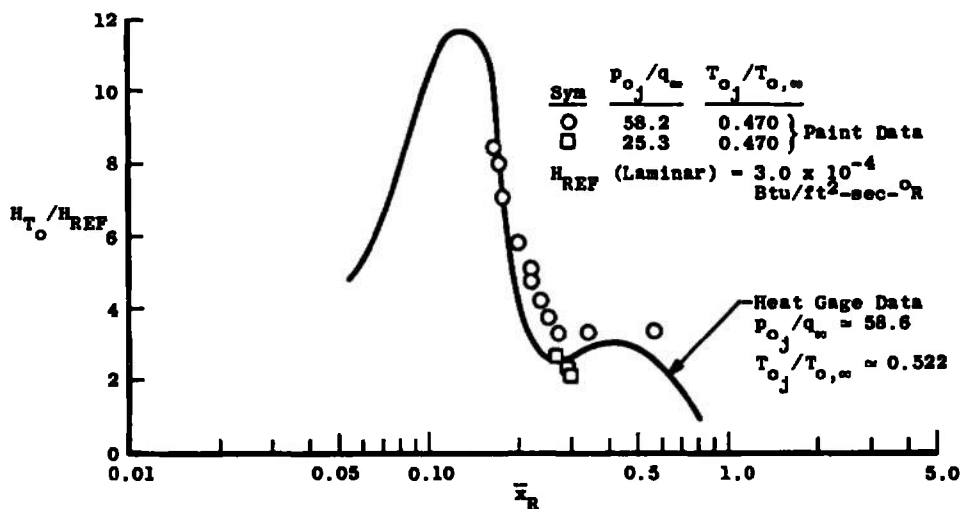
A comparison of the paint data results with the heat-gage data is given in Fig. 23. Although the paint data did not define the heat-transfer-rate distribution near the nozzle, that is on the stainless steel insert, the agreement was very good considering that a slight difference in jet gas temperature had an effect on the heat-transfer rate. This jet gas temperature effect on the heat-transfer rates will be discussed later.

As the jet disturbance propagated around the nozzle on the flat plate, the peak heat-transfer value which corresponded to the peak pressure point location diminished from a maximum value upstream of the jet ($\theta = 180$ deg) to a smaller value at $\theta = 60$ deg. Although the peak pressure value continued to decrease as radial angular element decreased below $\theta = 60$ deg, the peak heat-transfer rate increased as θ approached 30 deg, as shown in Fig. 23d and possibly, further aft of the jet, higher values existed close to $\theta = 15$ deg as suggested by the paint data of Fig. 22. Immediately aft of the jet the heat-transfer rates were very low as indicated by the fact that the paint did not melt in this region.

At angle of attack and at the high free-stream Reynolds number of 5×10^6 , the boundary layer was turbulent and the heat transfer melt lines take on a different pattern in the presence of a lateral jet disturbance as shown in Fig. 24. High heat-transfer rates not only exist immediately upstream of the jet but also aft of the jet. This heat-transfer rate paint pattern corresponds quite closely to the patterns generated on the 3-D model which will be presented in the next section.



a. $\theta = 180 \text{ deg}$



b. $\theta = 135 \text{ deg}$

Fig. 23 Comparison of Phase-Changing Paint Data with the Heat Gage Data Obtained on a Flat Plate at $\alpha = 0$, $M_\infty = 8.0$, and $Re_\infty = 5 \times 10^6$

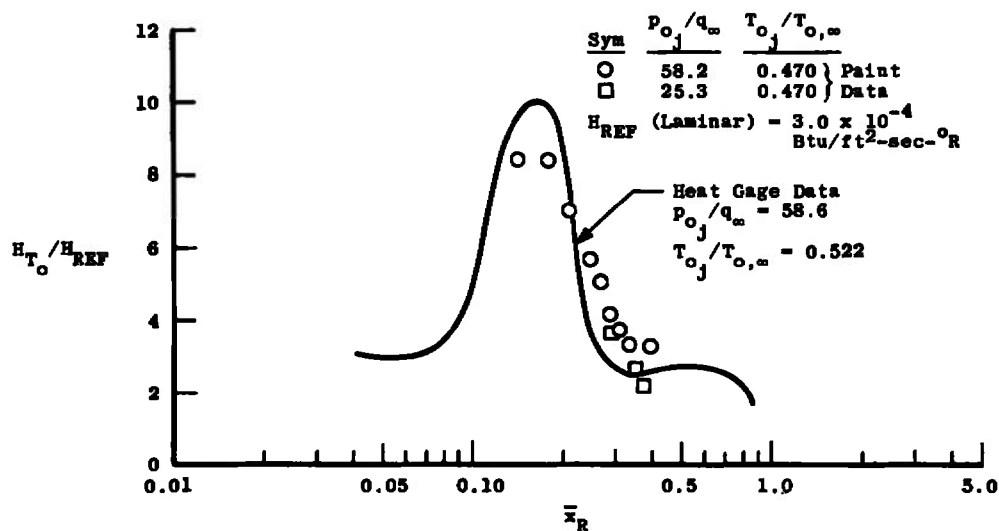
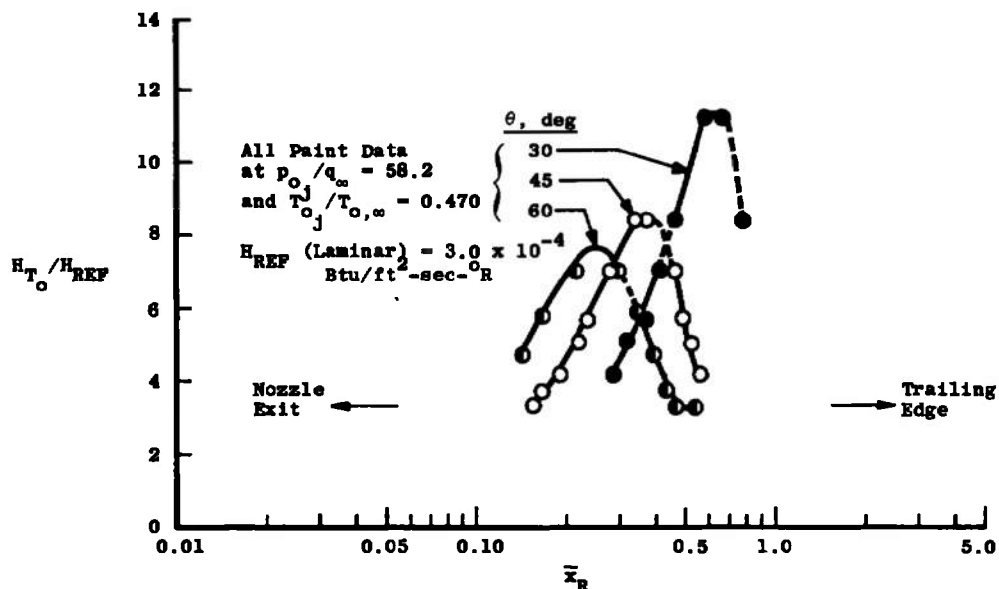
c. $\theta = 90$ degd. $\theta = 30, 45, \text{ and } 60$ deg

Fig. 23 Concluded

Some of the other significant results obtained from heat-gage measurements presented in Appendix I, Figs. I-12 to I-17 are summarized in Figs. 25 and 26. The results in Fig. 25 show that increasing the lateral jet strength (that is, increasing p_{o_j}) while holding the jet gas temperature constant or decreasing the jet temperature at a constant jet strength will decrease the magnitude of the peak heat-transfer rate on the flat plate. The location of this peak value occurs at \bar{x}_R value of nominal 0.14 when the gas temperature ratio ($T_{o_j}/T_{o,\infty}$) was about 0.4, but as the gas temperature increased, the peak appeared to

move away from the jet toward the location of the peak in the pressure distribution, that is, toward $\bar{x}_R = 0.18$. Thus, as the specific total enthalpy of the jet stream approached that of the external stream gas in the mixing region of the separated flow ahead of the jet, the peak heat-transfer-rate location apparently approached the location of the pressure spike in the pressure distribution. Another feature shown in Fig. 25b is that the heat-transfer-rate distribution upstream of this peak, in the region of the separated boundary layer, varies as the jet gas stagnation temperature. This demonstrates that the jet gas enters the separated boundary-layer region upstream of the jet disturbance and alters the aerothermodynamic properties in this separation region.

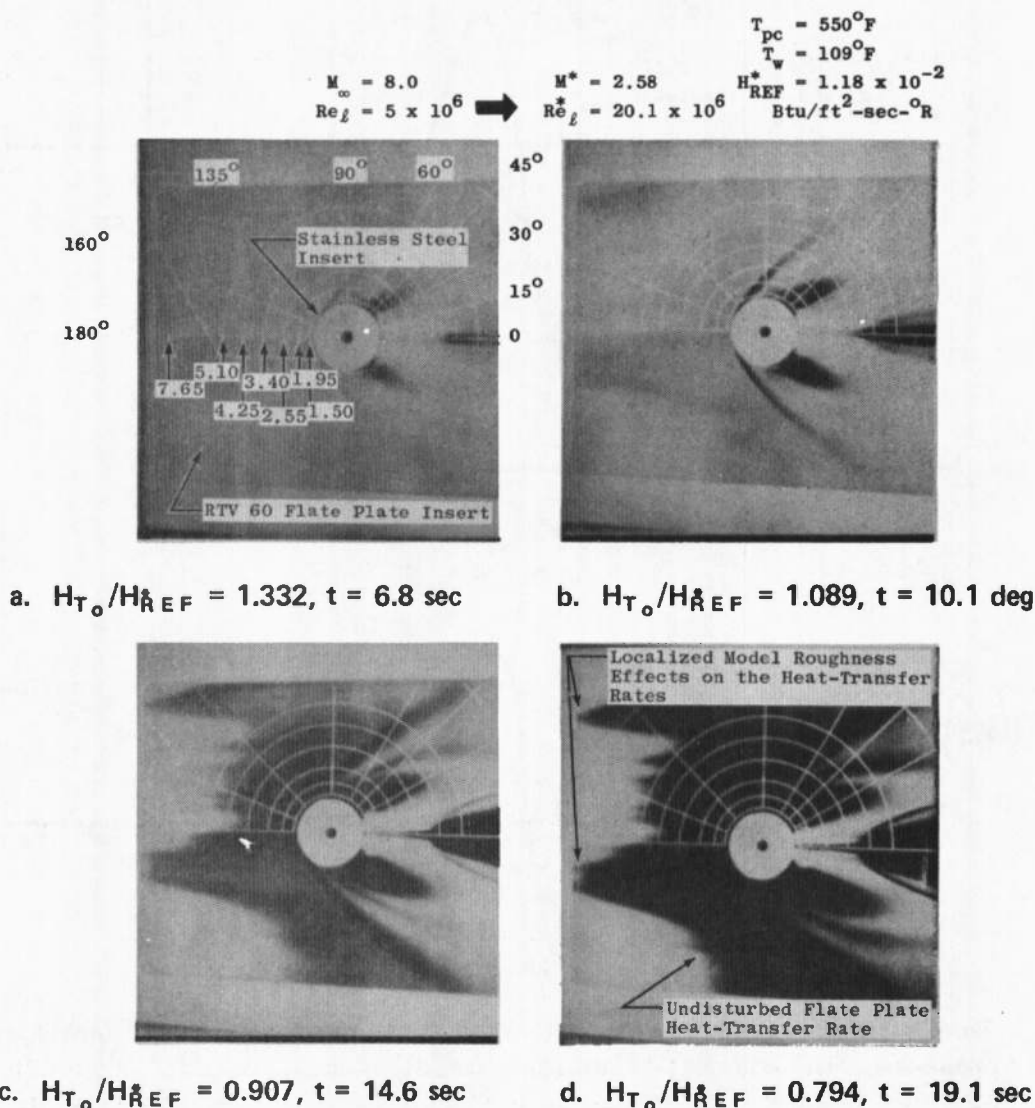


Fig. 24 Phase-Changing Paint Heat-Transfer-Rate Results Obtained on a Flat Plate at $\alpha = 30$ deg in the Presence of a Turbulent Boundary Layer with a Supersonic Air Jet, $M_j = 2.54$, $d_j = 0.50$ in., $p_{o_j}/q_\infty \cong 60.0$, and $T_{o_j}/T_{o,\infty} = 0.44$

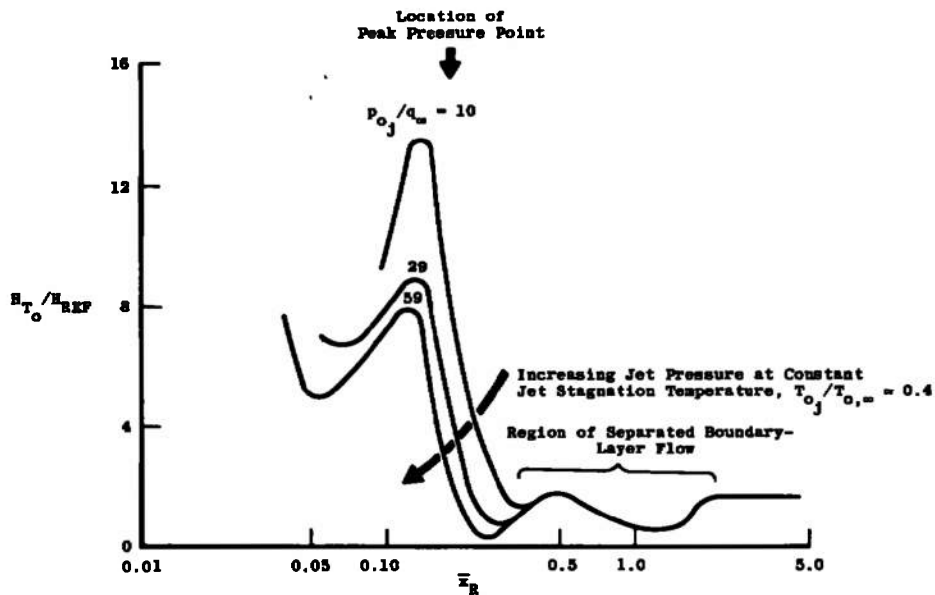
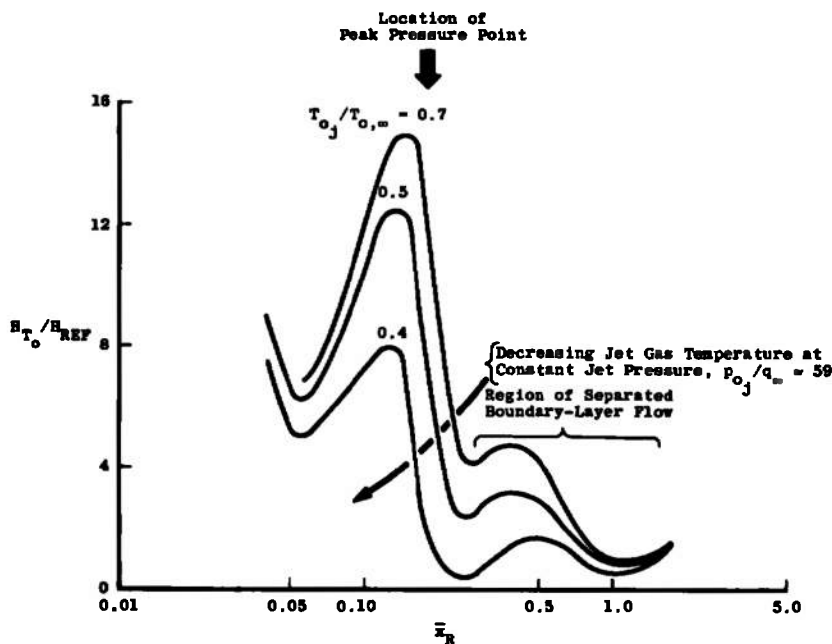
a. Variable Jet Pressure, $\theta = 160$ to 180 degb. Variable Jet Gas Stagnation Temperature, $\theta = 160$ to 180 deg

Fig. 25 Air Jet Stagnation Pressure and Temperature Effects on the Heat-Transfer-Rate Distribution on a Flat Plate ($\alpha = 0$) Around a Supersonic Nozzle, $M_j = 2.54$, $d_j = 0.50$ in., $M_\infty = 8.0$, and $Re_\ell = 5 \times 10^6$

Increasing the angle of attack of the flat plate caused the peak heat-transfer rates to increase, but as in the case of the pressure distribution the location of this peak heat-transfer rate remained at the same \bar{x}_R value as shown in Fig. 26. Also, downstream of the jet the nominal heat-transfer rate increased with angle of attack and moved toward the jet. The results in Fig. 26 are presented in terms of the theoretical undisturbed turbulent heat-transfer rate existing on the flat plate at the location occupied by the supersonic nozzle.

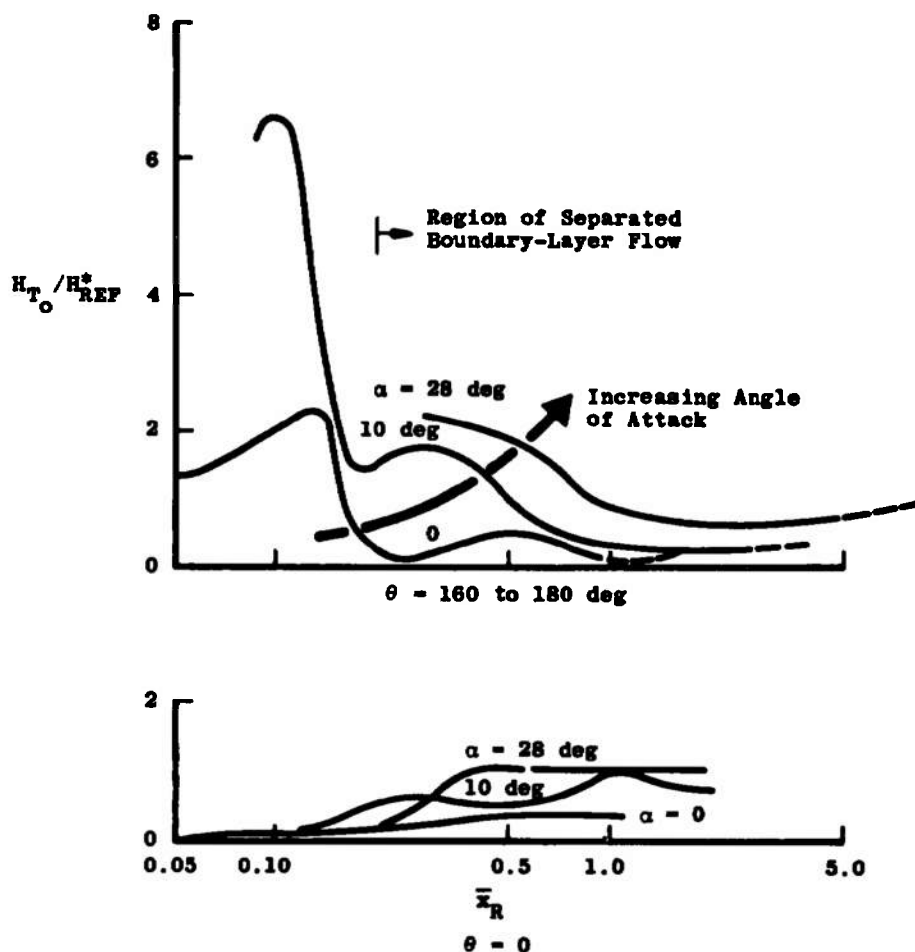


Fig. 26 Angle-of-Attack Effects on the Heat-Transfer Rates on a Flat Plate Around an Air Jet from a Supersonic Nozzle, $M_j = 2.54$, $p_{o,j}/q_\infty \cong 60$, $T_{o,j}/T_{o,\infty} = 0.41$, $M_\infty = 8.0$, and $Re_\ell = 5 \times 10^6$

A comparison of the heat-transfer rates generated by a helium jet with those produced by an air jet operating at the same jet gas temperature and pressure is summarized in Fig. 27. As in the case of the pressure distributions (Fig. 15), varying the gas pressure or the free-stream Reynolds number did not shift the correlated location (\bar{x}_R) of the peak heat-transfer rate for the air jet. In the case of the helium jet, the peak heat-transfer

rates would not correlate as a function of \bar{x}_R and the peak values were almost an order of magnitude greater than those produced by the air jet. Also, the variation of the peak heat-transfer rate with jet pressure ratio (p_{0j}/q_∞) for helium was opposite to the trend in the air jet data. As in the case of the pressure distribution, the \bar{x}_R value locating the peak heat transfer rate produced by the helium jet was less than the correlated \bar{x}_R used to locate the peak value in the distribution produced by the air jet.

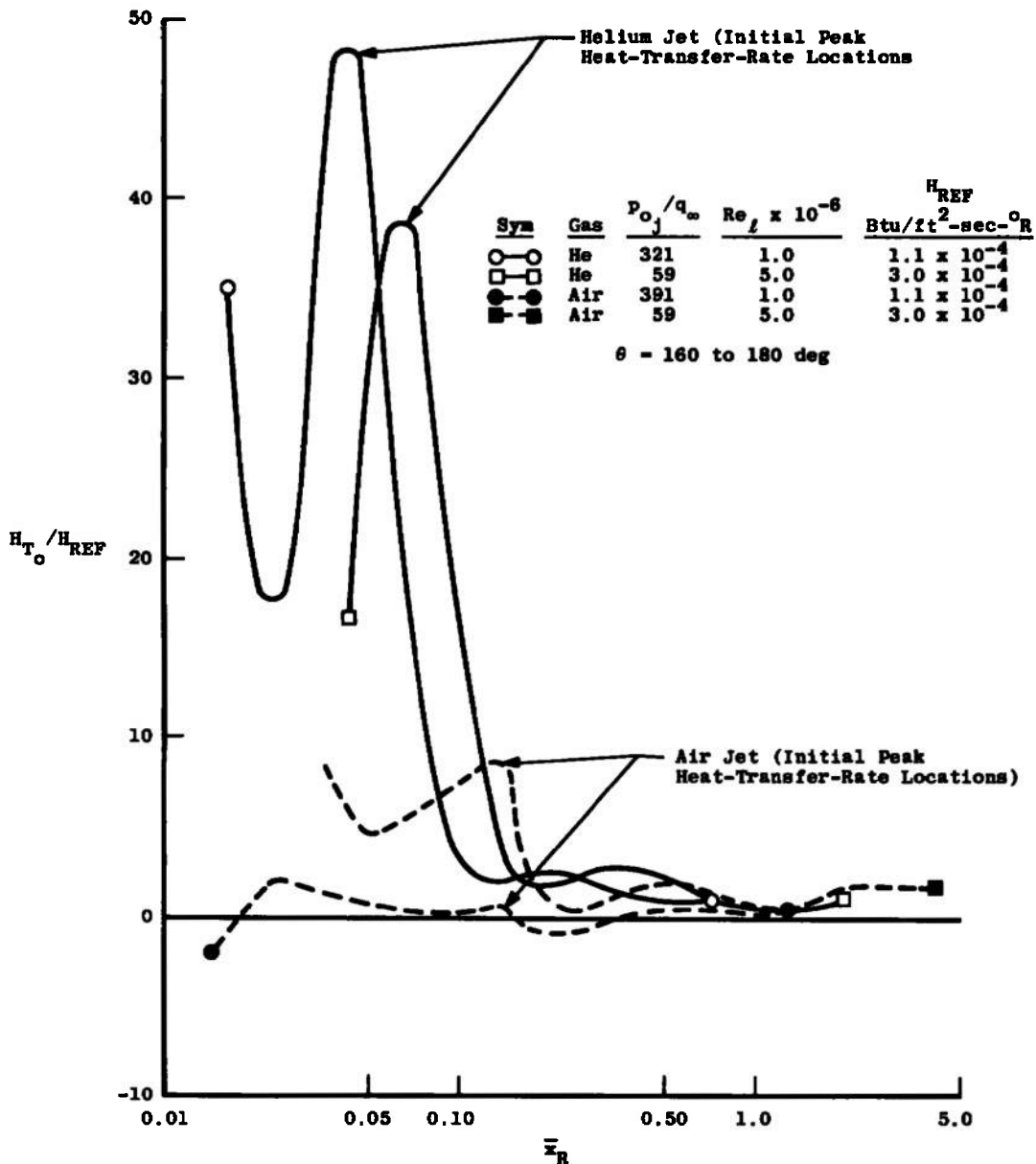
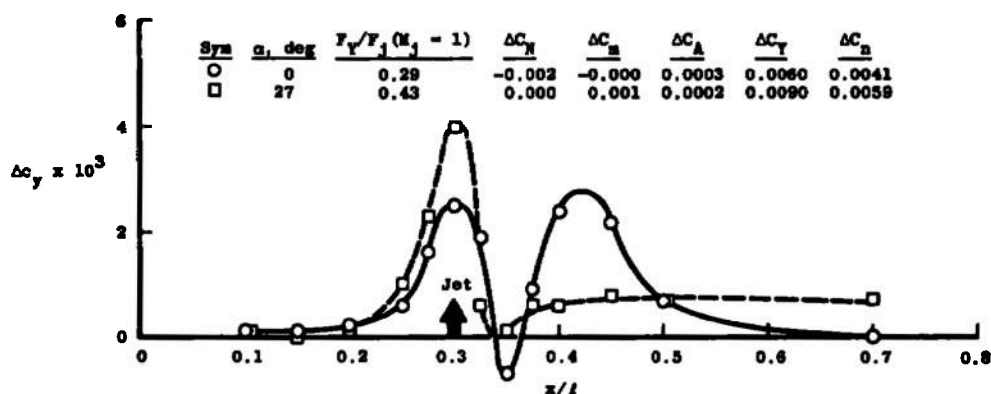


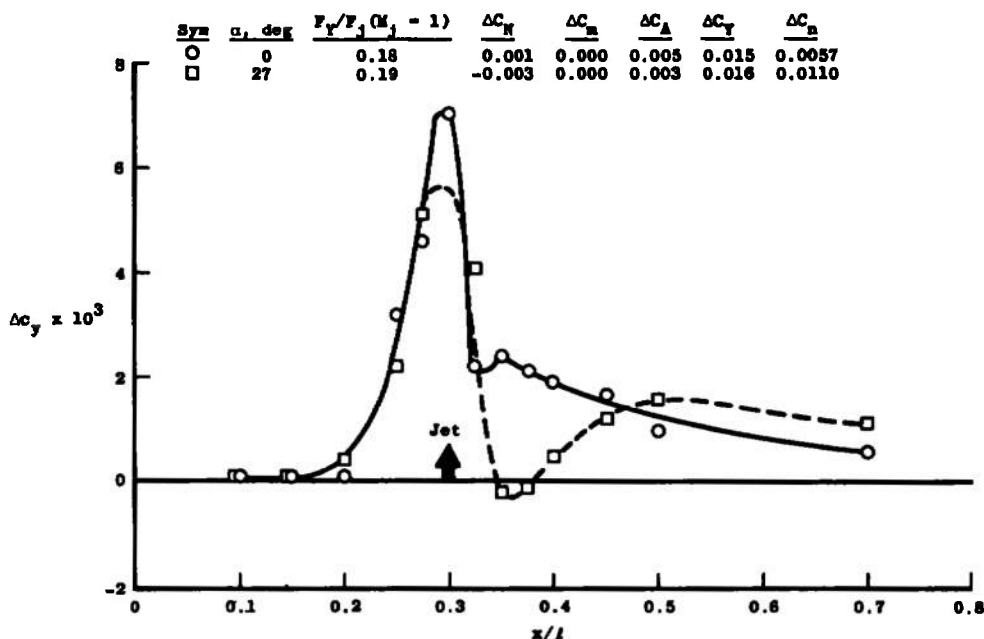
Fig. 27 Helium and Air Gas Jet Effects on the Heat-Transfer-Rate Distributions Around a Supersonic Nozzle, $\alpha = 0$

4.4 BOOSTER NOSE INTERFERENCE RESULTS

The booster nose configuration was tested with the jet control nozzles located in the yaw plane of the booster as the booster was pitched to an angle of 27 deg. The local change in side force coefficient per unit length is presented as a function of model length (x/l) in Fig. 28 for both the single jet nozzle and cluster jet nozzle configurations. Most of the pressure distributions used in evaluating the changes in surface loading produced by the jet controls are given in Figs. II-1 to II-3 (Appendix II).



a. Single Nozzle Air Jet, $p_j A_j / q_\infty = 0.0532$



b. Cluster of Four Nozzle Air Jet, $p_j A_j / q_\infty = 0.211$

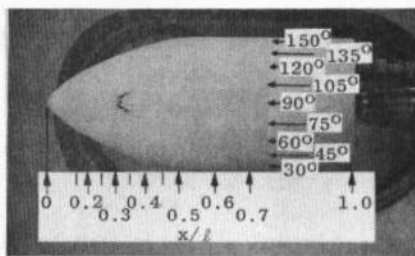
Fig. 28 Loading Produced by a Yaw Control Jet with an Exit Mach Number of 2.54 on the Convair Aerospace B-9U Booster Nose Section, $M_\infty = 8.0$ and $Re_x = 1.9 \times 10^6$

In the case of the single supersonic nozzle shown in Fig. 28a, the loading aft of the jet was slightly greater than the loading upstream of the jet when the body was at zero angle of attack, but this trend reversed as the model angle of attack increased to 27 deg. At the higher angles of attack, the change in side force and yawing moment produced by the jet control increased as indicated by the tabulated results in the figure. The incremental increase in the axial-force coefficient produced by the jet control was negligible. Also, the yaw jet control did not significantly alter the normal force and pitching moment of the 3-D model. The changes in the pitching and yawing moments listed in the figure were with respect to the jet control location.

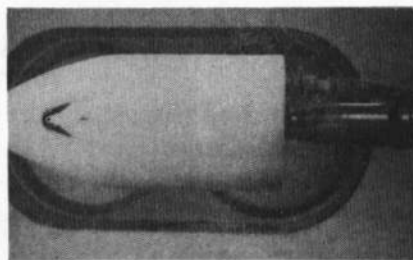
Operating the cluster nozzle configuration at the same chamber conditions as the single nozzle produced a higher jet mass flow rate, a larger jet disturbance, and a larger change in the surface loading as shown by comparing Fig. 28a to 28b. Each nozzle in the cluster of four nozzles was equal in size to the single supersonic nozzle on the 3-D body. In comparison to the single nozzle results, the angle-of-attack change from zero to 27 deg has less effect on the side force and more effect on the yawing moment about the cluster nozzle configuration. The largest change in the side force loading resulting from the increase in α occurred just downstream of the cluster nozzle location.

Included in the listing in Fig. 28 of the coefficient changes produced by the jet controls is the ratio of the change in side force (F_Y) to the reaction force of a sonic jet ($F_j(M_j = 1)$) with an exit diameter equal to the supersonic nozzle throat diameter. When compared to the \bar{F}_N/\bar{F}_j value predicted by correlation of the flat plate results presented previously in Fig. 20, the present 3-D model jet interaction augmentation factors listed in Fig. 28 are nearly five times smaller than the flat plate values. In applying the flat plate correlation results to the 3-D model results, the local stream properties on the 3-D model (estimates furnished by Dr. O. Brevig of Convair Aerospace) and the location of the jet control relative to the model nose were used to determine the correlation factor Φ . Another estimate of the 3-D model jet augmentation factor (F_N/F_j), which was in closer agreement with the experimental result, was obtained by evaluating the jet correlation parameter Φ arbitrarily in terms of the free-stream properties instead of the local 3-D model surface properties.

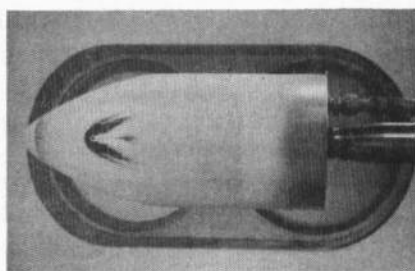
The heat-transfer-rate distribution induced on the booster nose by the lateral jet disturbance from a single supersonic nozzle is shown by the phase-change paint photographs in Fig. 29. These results show that the peak heating began just upstream of the jet. Moderate heat rates (up to H_{T_0}/H_{REF} of 0.2) existed not only upstream of the jet, but also propagated around the jet with these heat rates, also, appearing just downstream of the jet (see Fig. 29b). The reference film heat-transfer coefficient was obtained from the Fay and Riddell heat-transfer-rate equation (Ref. 8) for the stagnation point on a sphere with a nose radius of 0.02 ft which corresponded to the booster nose radius.



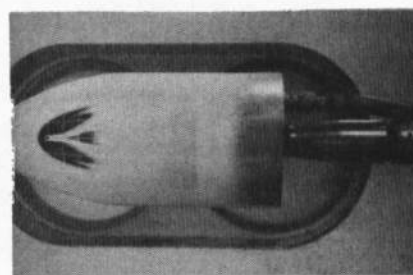
a. $H_{T_o}/H_{REF} = 0.366$ at $t = 6.8$ sec,
 $T_{p_c} = 550^\circ\text{F}$, and $T_w = 84^\circ\text{F}$



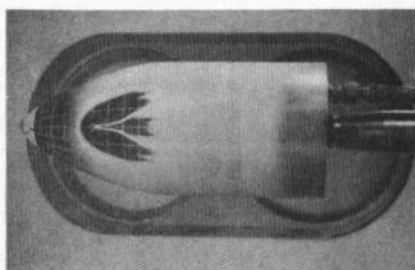
b. $H_{T_o}/H_{REF} = 0.206$ at $t = 21.6$ sec,
 $T_{p_c} = 550^\circ\text{F}$, and $T_w = 106^\circ\text{F}$



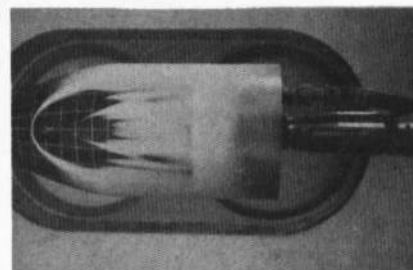
c. $H_{T_o}/H_{REF} = 0.131$ at $t = 2.4$ sec,
 $T_{p_c} = 250^\circ\text{F}$, and $T_w = 87^\circ\text{F}$



d. $H_{T_o}/H_{REF} = 0.094$ at $t = 4.6$ sec,
 $T_{p_c} = 250^\circ\text{F}$, and $T_w = 87^\circ\text{F}$



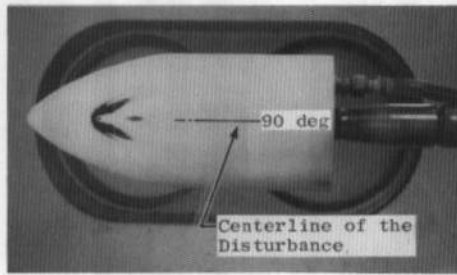
e. $H_{T_o}/H_{REF} = 0.063$ at $t = 10.2$ sec,
 $T_{p_c} = 250^\circ\text{F}$, and $T_w = 92^\circ\text{F}$



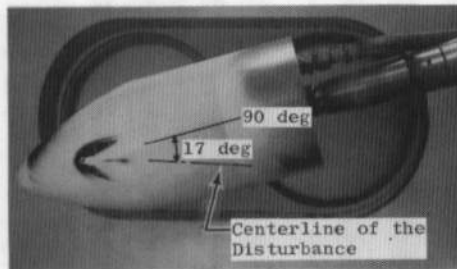
f. $H_{T_o}/H_{REF} = 0.043$ at $t = 22.5$ sec,
 $T_{p_c} = 250^\circ\text{F}$, and $T_w = 106^\circ\text{F}$

Fig. 29 Heat-Transfer-Rate Distributions on the 3-D Body with a Single Supersonic Nozzle Air Jet at $p_{o_j}/q_\infty = 58.0$, $T_{o_j}/T_{o_\infty} = 0.44$, $\alpha = 0$, $M_\infty = 8.0$, and $Re_\ell = 1.9 \times 10^6$

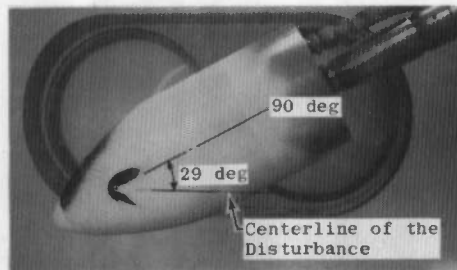
The effect of angle of attack on the heat-transfer rates around a circular jet is shown in Fig. 30. As the model angle of attack varies, the apparent axisymmetry of the heat-transfer-rate pattern about the jet rotates and remains aligned with the external free-stream flow direction. For example, the hypothetical line through the jet nozzle and the high heat-rate point aft of the nozzle remain approximately aligned with the free-stream flow as shown in Fig. 30.

a. $a = 0$

$$\begin{aligned} H_{T_O}/H_{REF} &= 0.146 \\ t &= 43 \text{ sec} \\ T_{pc} &= 550^\circ\text{F} \\ T_w &= 124^\circ\text{F} \end{aligned}$$

b. $a \cong 15 \text{ deg}$

$$\begin{aligned} H_{T_O}/H_{REF} &= 0.142 \\ t &= 18 \text{ sec} \\ T_{pc} &= 450^\circ\text{F} \\ T_w &= 104^\circ\text{F} \end{aligned}$$

c. $a \cong 27 \text{ deg}$

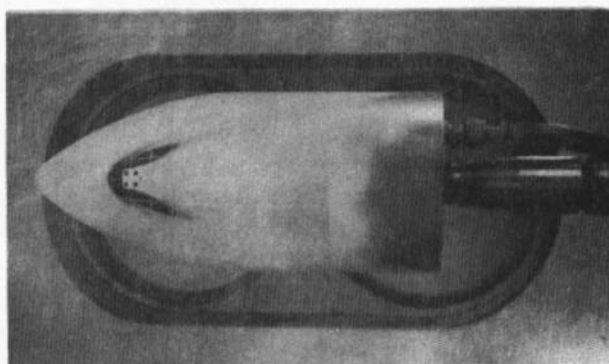
$$\begin{aligned} H_{T_O}/H_{REF} &= 0.143 \\ t &= 18 \text{ sec} \\ T_{pc} &= 450^\circ\text{F} \\ T_w &= 100^\circ\text{F} \end{aligned}$$

Fig. 30 Angle-of-Attack Effects on the Heat-Transfer-Rate Distributions Produced by a Single Supersonic Nozzle Air Jet at $p_{o_j}/q_\infty \cong 60.0$, $T_{o_j}/T_{o,\infty} = 0.44$, $M_\infty = 8.0$, and $Re_\ell = 1.9 \times 10^6$

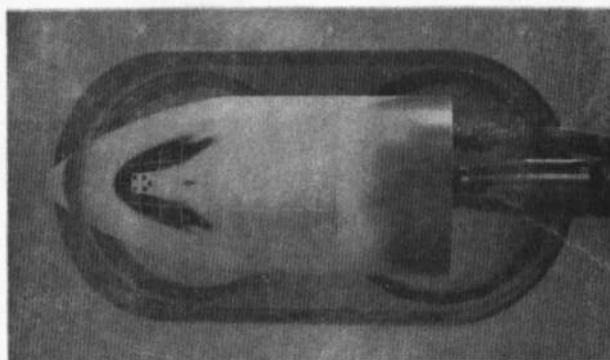
The heat-rate pattern with the cluster nozzle configuration is shown in Fig. 31. The disturbance produced by the cluster nozzle was significantly larger (compare Fig. 30a with 31a), but the general pattern around the cluster nozzle was similar to the heat-transfer-rate pattern around the single nozzle.

A comparison of the heat-transfer rates obtained from the phase-changing paint with previously measured undisturbed heat-transfer data on a booster configuration with a similar nose shape is given in Fig. 32. The experimentally defined undisturbed heat-transfer-rate data in Fig. 32 were obtained from Ref. 9. The jet disturbance on the nose section begins at about an x/ℓ of 0.25 or 4.1 nozzle exit diameters upstream of the single supersonic

jet. The maximum local heat-transfer rate was 7.6 times greater than the undisturbed value upstream of the jet and 11 times greater than the undisturbed value downstream of the jet. In this particular case, the ratio of the jet gas to free-stream total temperature was about 0.4; if this temperature ratio was increased then according to the flat plate data, the peak-heat transfer rates on the 3-D model would increase and move a little farther upstream of the jet control.



a. $H_{T_o}/H_{REF} = 0.145$ at $t = 15.8$ sec,
 $T_{p_c} = 450^\circ\text{F}$, and $T_w = 106^\circ\text{F}$



b. $H_{T_o}/H_{REF} = 0.097$ at $t = 38$ sec,
 $T_{p_c} = 450^\circ\text{F}$, and $T_w = 130^\circ\text{F}$

Fig. 31 Heat-Transfer-Rate Distribution Around a Cluster of Four Supersonic Nozzle Air Jets on the 3-D Model at $\alpha = 0$, $p_{o_j}/q_\infty \cong 64.0$, $T_{o_j}/T_{o,\infty} \cong 0.45$, $M_\infty = 8.0$, and $Re_l = 1.9 \times 10^6$

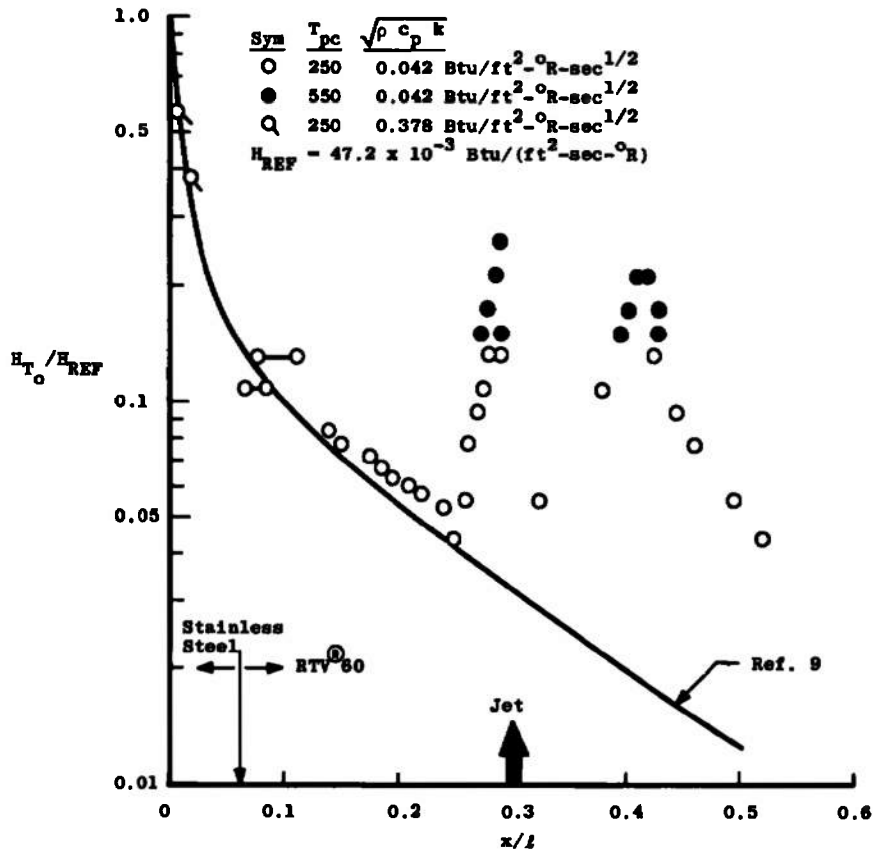


Fig. 32 Heat-Transfer-Rate Distribution Through the Lateral Air Jet Interference Region on the 3-D Model at $\alpha = 0$, Single Supersonic Nozzle Air Jet at $P_{o_j}/q_\infty \cong 58.0$, $T_{o_j}/T_{o,\infty} = 0.44$, $M_\infty = 8.0$, and $Re_l = 1.9 \times 10^6$

SECTION V

SUMMARY OF RESULTS

These results indicate that the ACS jet nozzles on a Space Shuttle orbiter can generate high heat-transfer rates within and around the flush-mounted jet nozzles in the vehicle's surface. Some of the more significant factors affecting the aerothermodynamics around the ACS nozzles are given in the following comments:

1. The nature of the boundary layer can alter the flow field effects in the vicinity of the cavity or the lateral jet. In the present tests, the boundary layer on the flat plate was laminar at all angles of attack up to 30 deg at $Re_l = 1 \times 10^6$ and also at a pitch angle of zero at $Re_l = 5 \times 10^6$. Turbulent boundary layers were present in the vicinity of the cavity when the angle of attack exceeded 10 deg and the $Re_l = 5 \times 10^6$.

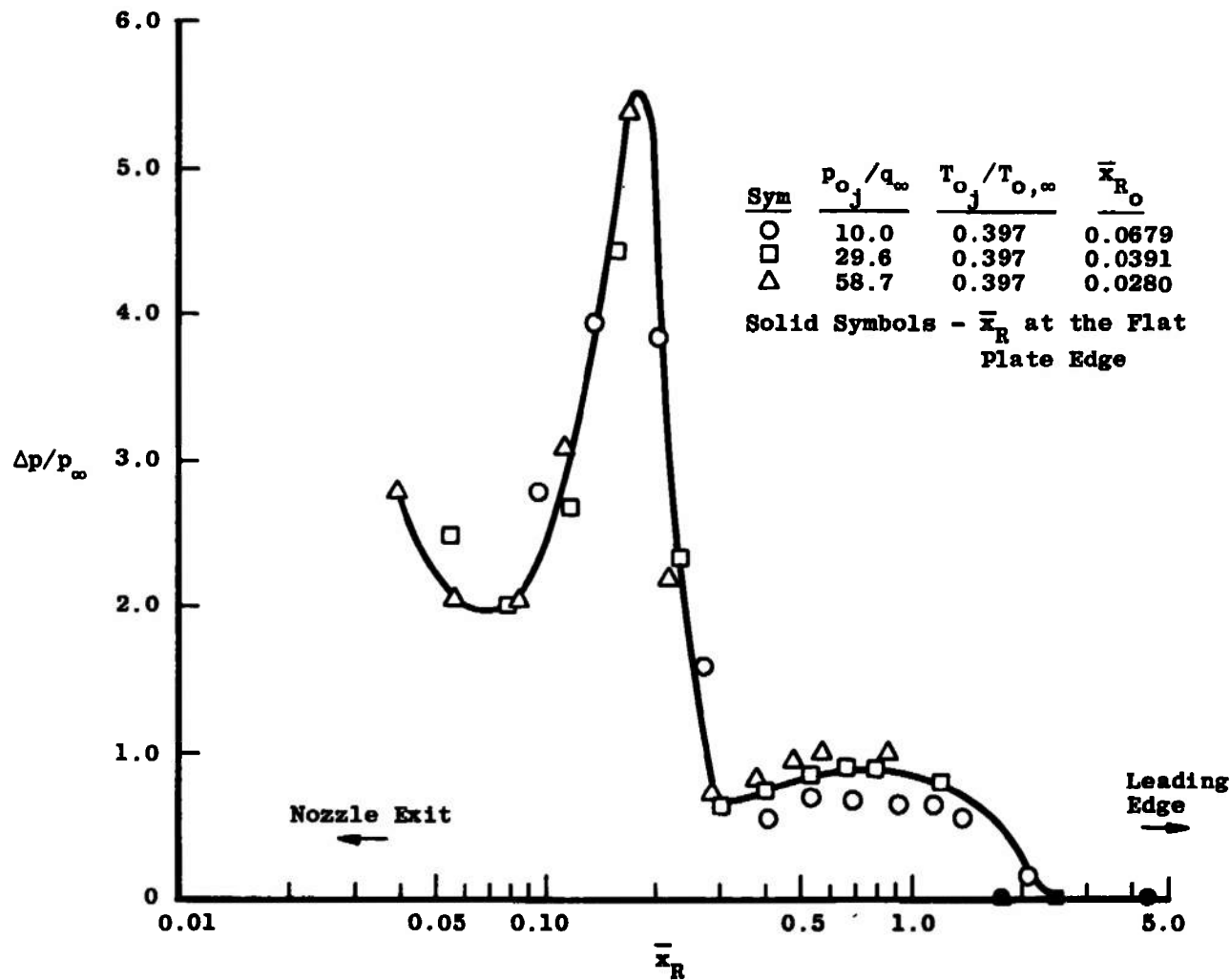
2. The heat-transfer rates along the surface where the flow over the cavity reattaches to the nozzle wall were correlated as functions of a reference film heat-transfer coefficient and the depth coordinate $2h/d_j$ as suggested by O. R. Burggraf's analysis (Ref. 3). The reference film heat-transfer coefficient is the undisturbed value that exists on the plate in the absence of the cavity. In general, this correlation accounts for variations in Reynolds number, in local stream Mach number, and in the state of the boundary layer.
3. In the presence of a laminar boundary layer at Mach number 8, the bleeding of gas into the cavity increased the heat rates within the cavity and downstream of the cavity. At angles of attack where the local boundary layer was turbulent and the local Mach number was lower, the cavity bleed reduced the heat-transfer rates within and around the cavity as qualitatively predicted by the two-dimensional cavity theory described in Ref. 3.
4. In the pressure and heat-transfer-rate distributions produced by the lateral air jet disturbance there is a maximum or peak point in these distributions. In terms of the correlated coordinate parameter \bar{x}_{R_0} , the location of these peaks remains fixed and independent of the nozzle chamber conditions, the variations in the freestream Reynolds number and the model angle of attack, that is, independent of the local stream Mach number and the nature of the boundary layer. This correlation does not apply to the helium lateral jet data where the value of \bar{x}_{R_0} varied with the jet gas pressure and temperature.
5. The heat input into the surface around a lateral jet from a supersonic nozzle varies in the same manner as the total specific enthalpy of the jet gas. Thus, increasing the jet pressure while holding the jet stagnation temperature constant causes the maximum heat rates to reduce in the immediate vicinity of the jet nozzle. This variation in the jet pressure at constant jet temperature had no measurable effect on the aerodynamic heating upstream of this peak heating rate in the separated boundary-layer region ahead of the jet disturbance, whereas an increase in the jet gas temperature while holding the jet pressure constant increased the heat rates throughout the jet interaction region.
6. The sonic lateral jet augmentation factors (F_N/F_j) obtained at Mach number 18.5 in Ref. 5 and the present flat plate supersonic lateral jet augmentation factors were correlated in terms of a parameter based on the local stream properties on the flat plate and the jet properties existing at the nozzle throat. Also, the augmentation factors formulated for the cluster nozzle configuration using an effective throat diameter was correlated with the single nozzle augmentation factors.

The jet interaction results obtained with the 3-D model were not as complete as those obtained with the flat plate, but the trends in the pressure loading and heat-transfer-rate distributions were quite similar. The parameter used to correlate the flat plate augmentation factors could not be successfully applied to the augmentation factors generated on the 3-D model. Thus, the correlation parameter of the jet interaction augmentation factor (F_N/F_j) must vary with the geometry of the surface containing the ACS.

REFERENCES

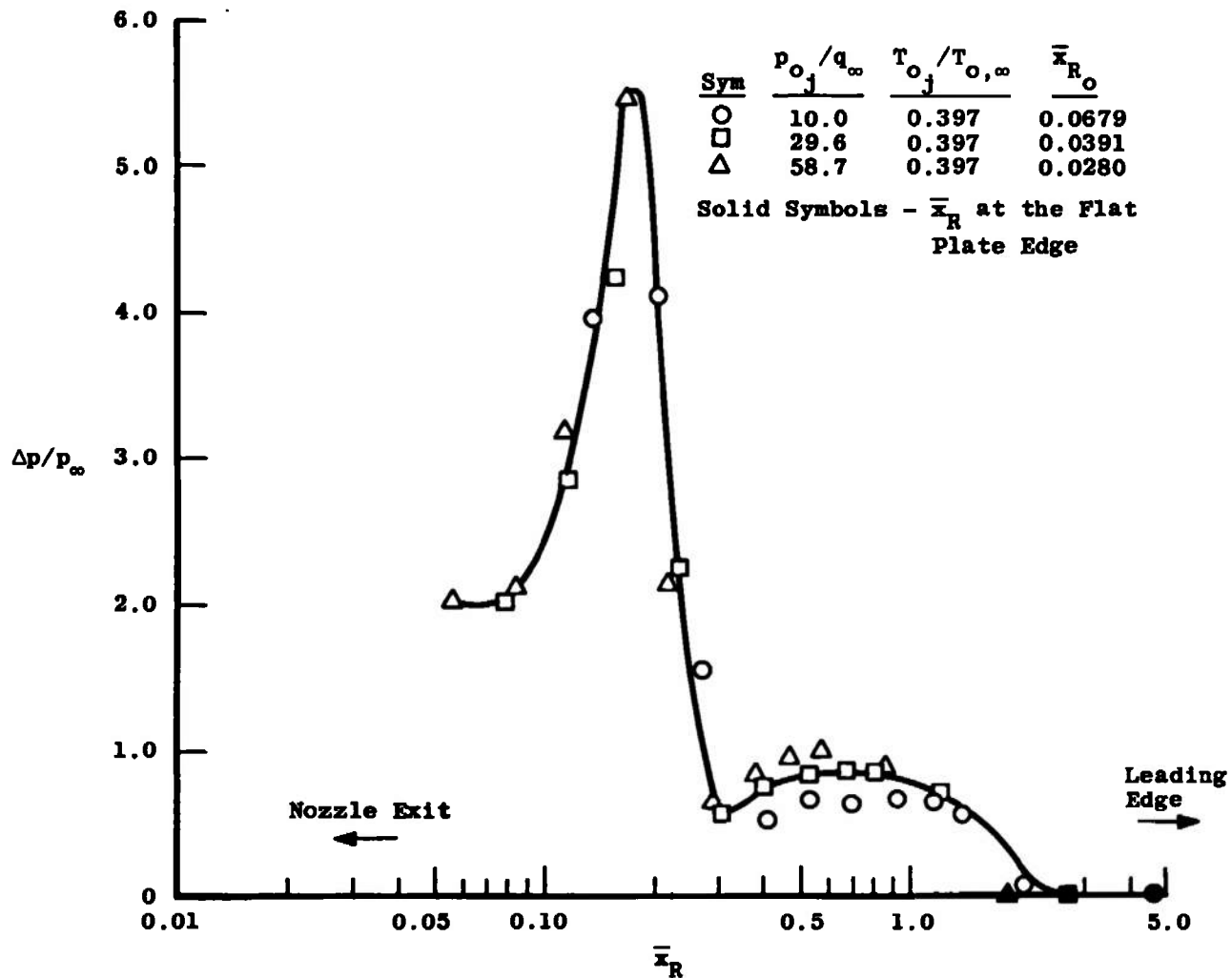
1. Eckert, E. R. G. and Drake, R. M., Jr. Heat and Mass Transfer, Chapter 10, McGraw-Hill Book Company, Inc., 1959.
2. Adams, John C., Jr. "Eddy Viscosity-Intermittency Factor Approach to Numerical Calculation of Transitional Heating on Sharp Cones in Hypersonic Flow." AEDC-TR-70-210 (AD714058), November 1970.
3. Engel, C. D. "The Propulsive Attitude Control System - An Open Cavity Heating Problem." REMTECH, Inc., RTR-008-1, April 1972.
4. Strike, W. T., Jr. "Inviscid Blunt Leading Effects on Planar Surface Pressure Distributions at Mach Number 10." AEDC-TDR-64-191 (AD450463) (see Section 4.3), October 1964.
5. Strike, W. T., Jr. and Buchanan, T. D. "Circular Sonic Lateral Jet Interaction Effects on a Flat Plate at Mach Number 18.5 Using a Small Solid Monopropellant Rocket Motor." AEDC-TR-69-205 (AD864730), January 1970.
6. Jones, R. A. and Hunt, J. L. "Use of Fusible Temperature Indicators for Obtaining Quantitative Aerodynamic Heat-Transfer Data." NASA TR R-230, February 1966.
7. Strike, W. T., Jr. "Analysis of the Aerodynamic Disturbances Generated on a Flat Plate Containing Lateral Jet Nozzles Located in a Hypersonic Stream." AEDC-TR-67-158 (AD826485), January 1968.
8. Fay, J. A. and Riddell, F. R. "Theory of Stagnation Point Transfer in Dissociated Air." Journal of Aeronautical Sciences, Vol. 25, No. 2, pp. 73-85, 1958.
9. Warmbrod, J. D. (MSFC), Martindale, W. R., and Matthews, R. K. (ARO, Inc.) "Heat Transfer Rate Measurements on Convair Booster (B-15B-2) at Nominal Mach Number 8." Chrysler Corp. (Space Division), DMS-DR-1177, Vol. 11, November, 1971.

APPENDIX I
GRAPHICAL PRESENTATION OF PRESSURE AND HEAT-TRANSFER-
RATE DISTRIBUTIONS AND PRESSURE LOADING ON A FLAT
PLATE AROUND SUPERSONIC NOZZLES

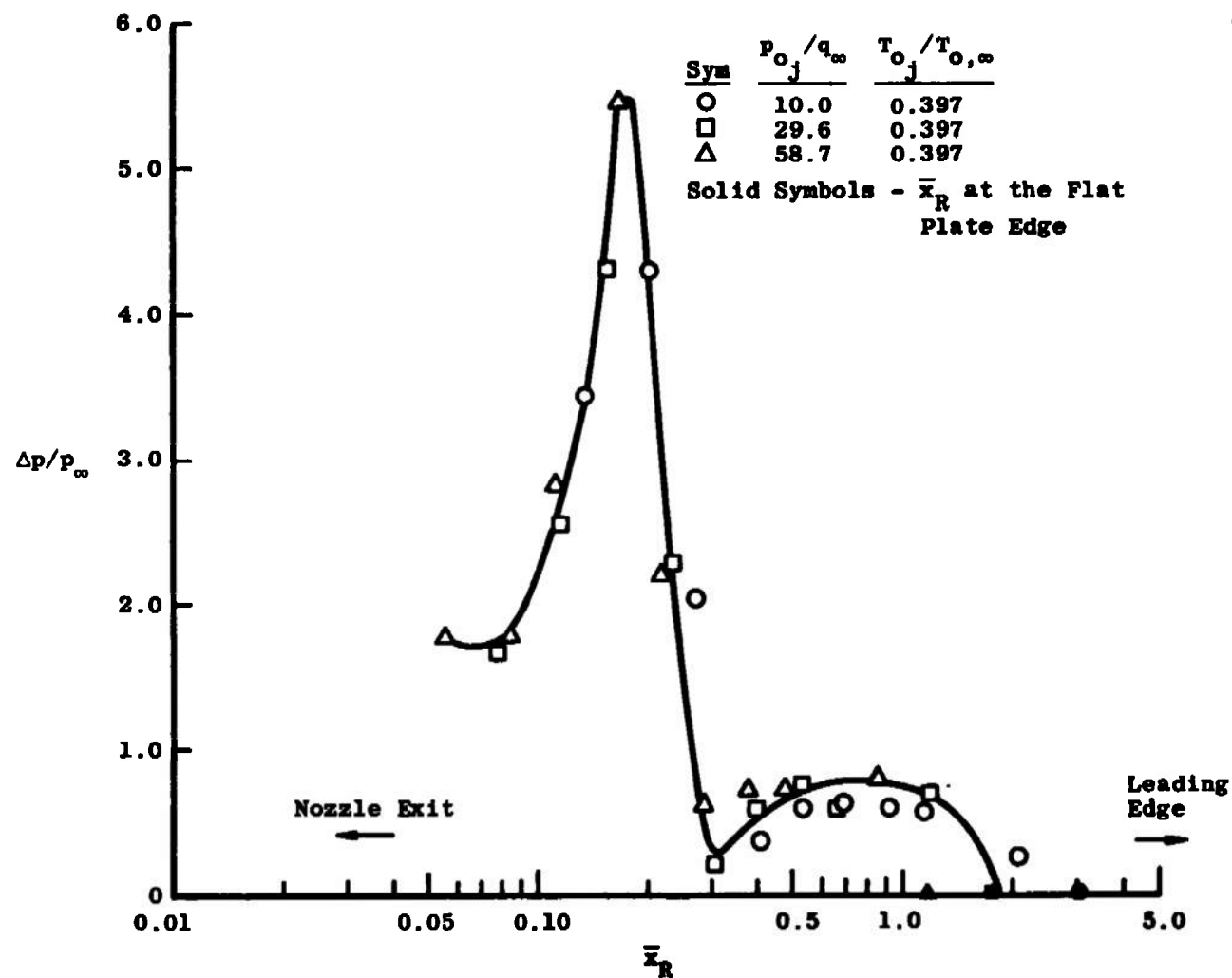


a. $\theta = 180$ deg

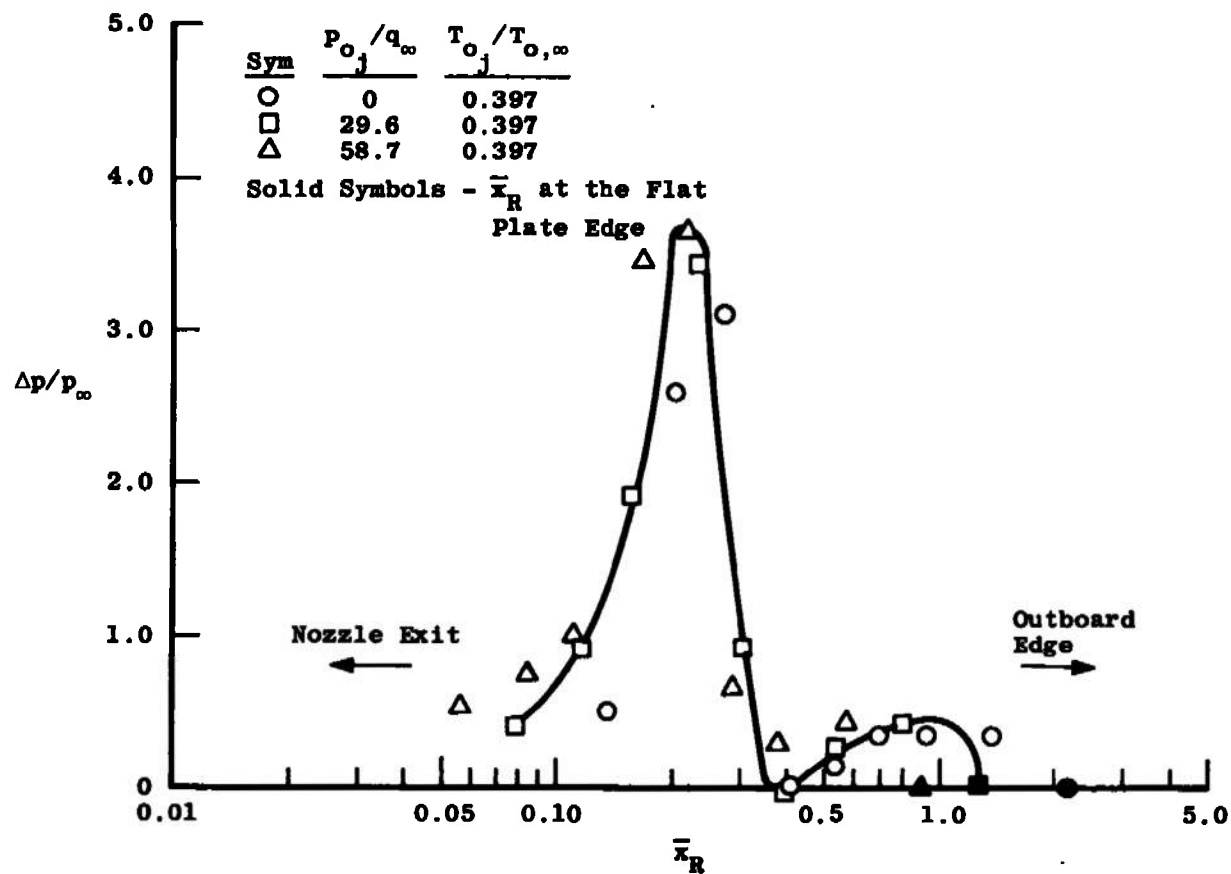
Fig. I-1 Pressure Distributions on a Flat Plate Around a Cold Air Jet from a Supersonic Nozzle, $M_j = 2.54$, $d_j = 0.50$ in., $\alpha = 0$, $M_\infty = 8.0$, and $Re_\ell = 5.0 \times 10^6$



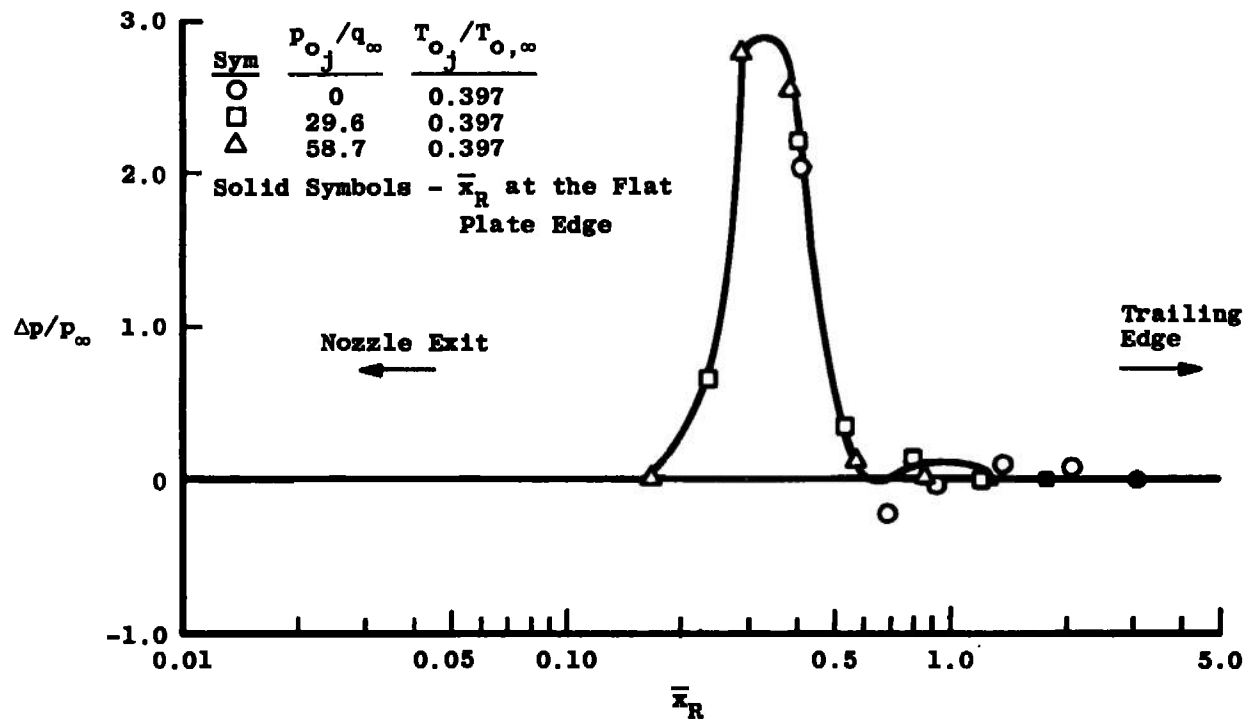
b. $\theta = 160$ deg
Fig. I-1 Continued



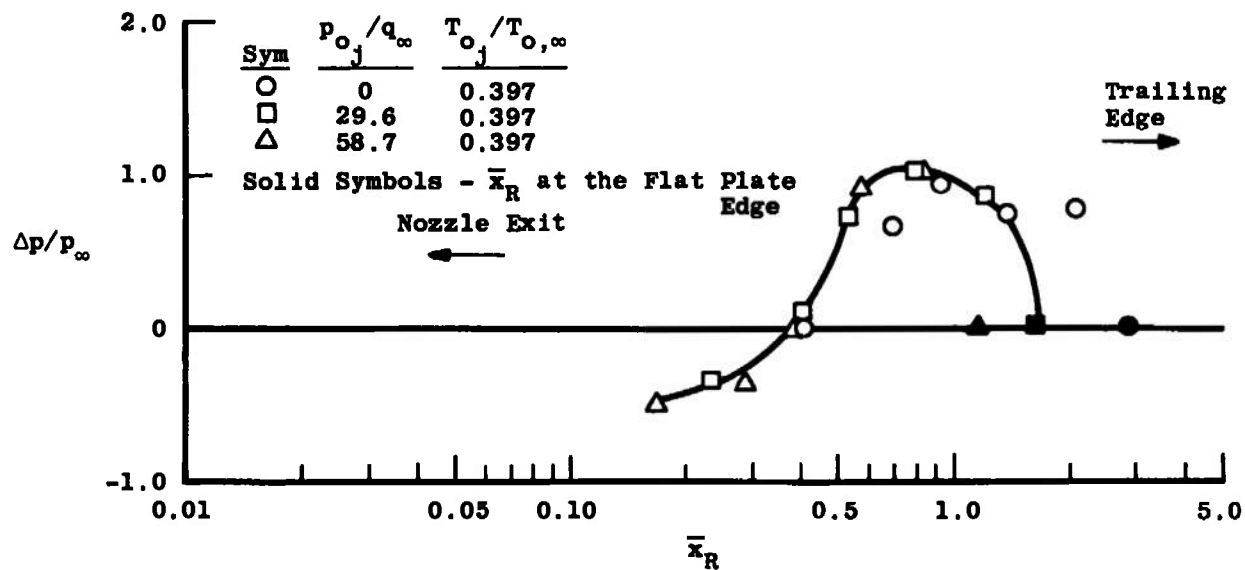
c. $\theta = 135$ deg
Fig. I-1 Continued



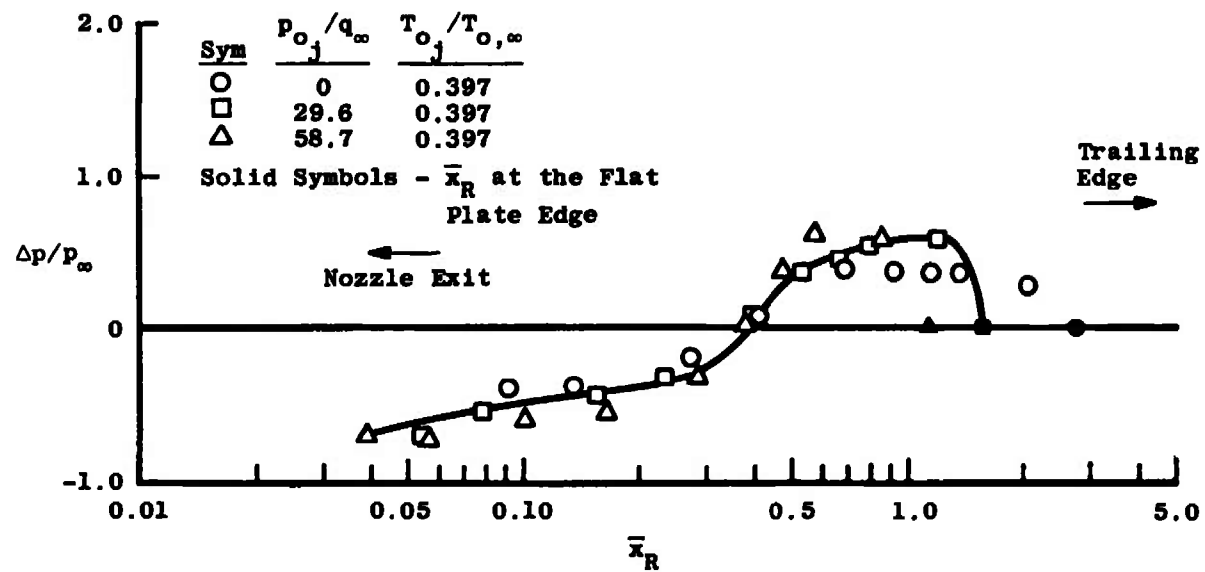
d. $\theta = 90$ deg
 Fig. I-1 Continued



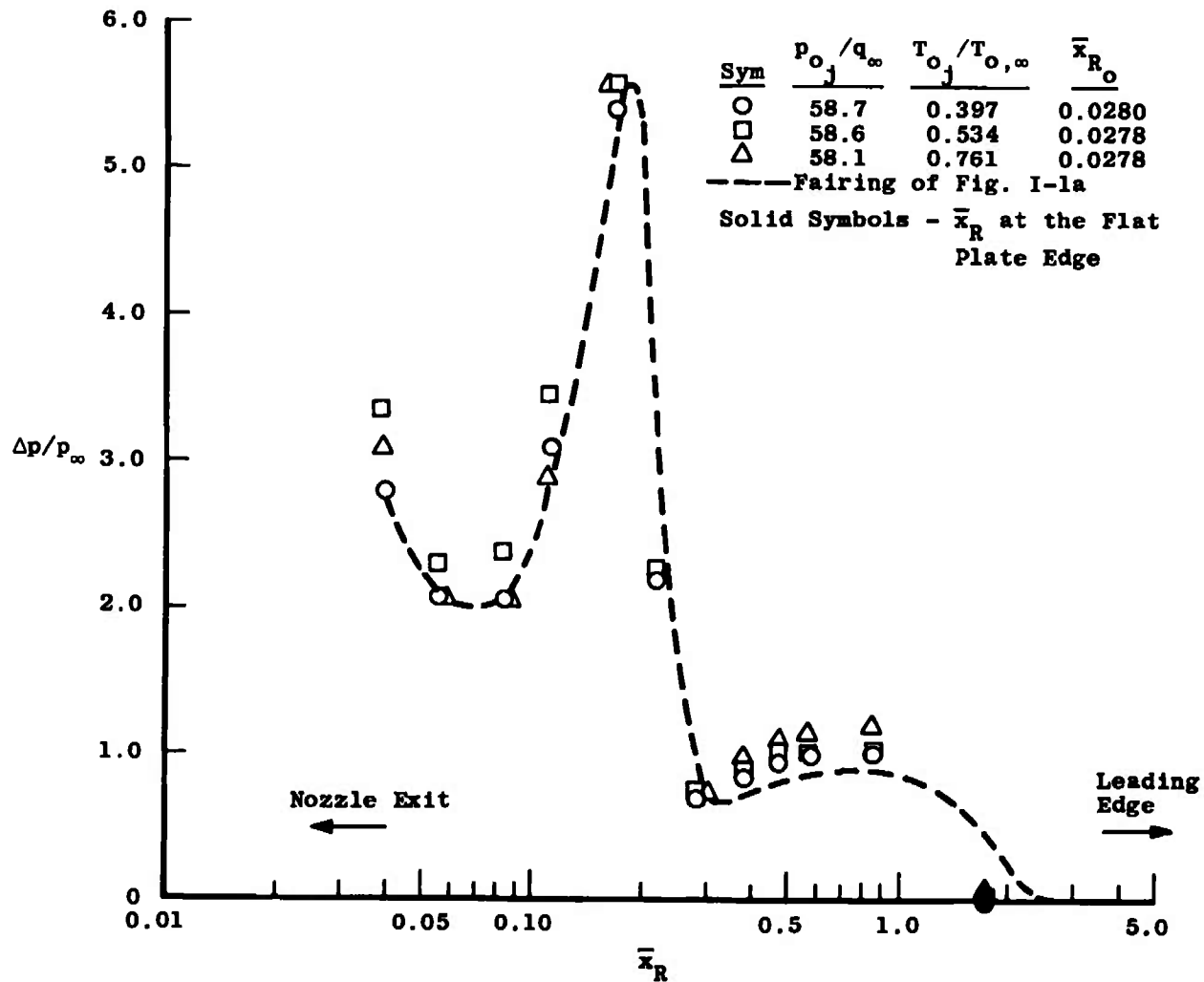
e. $\theta = 45$ deg
Fig. 1-1 Continued



f. $\theta = 15$ deg
 Fig. I-1 Continued

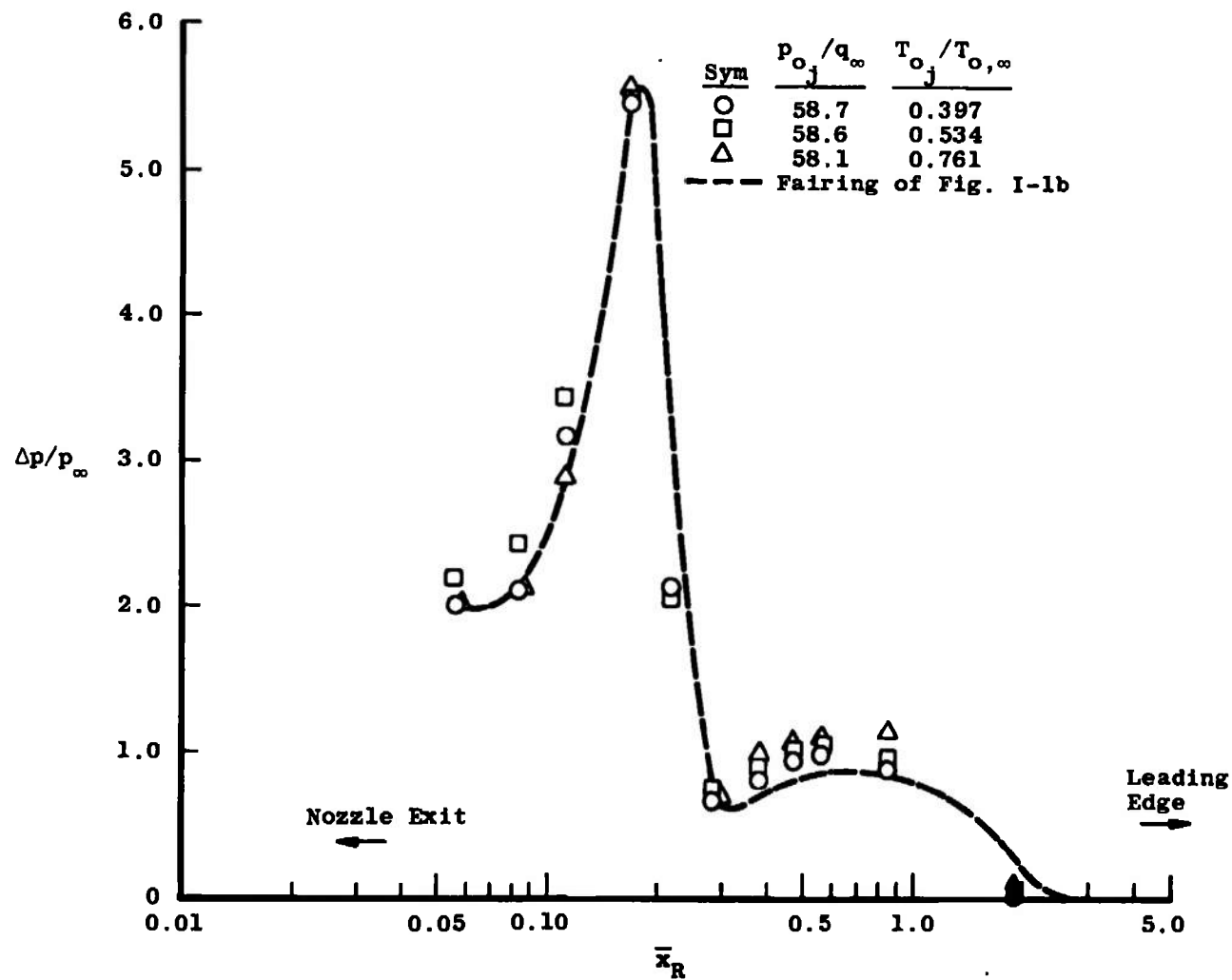


g. $\theta = 0$
Fig. 1-1 Concluded

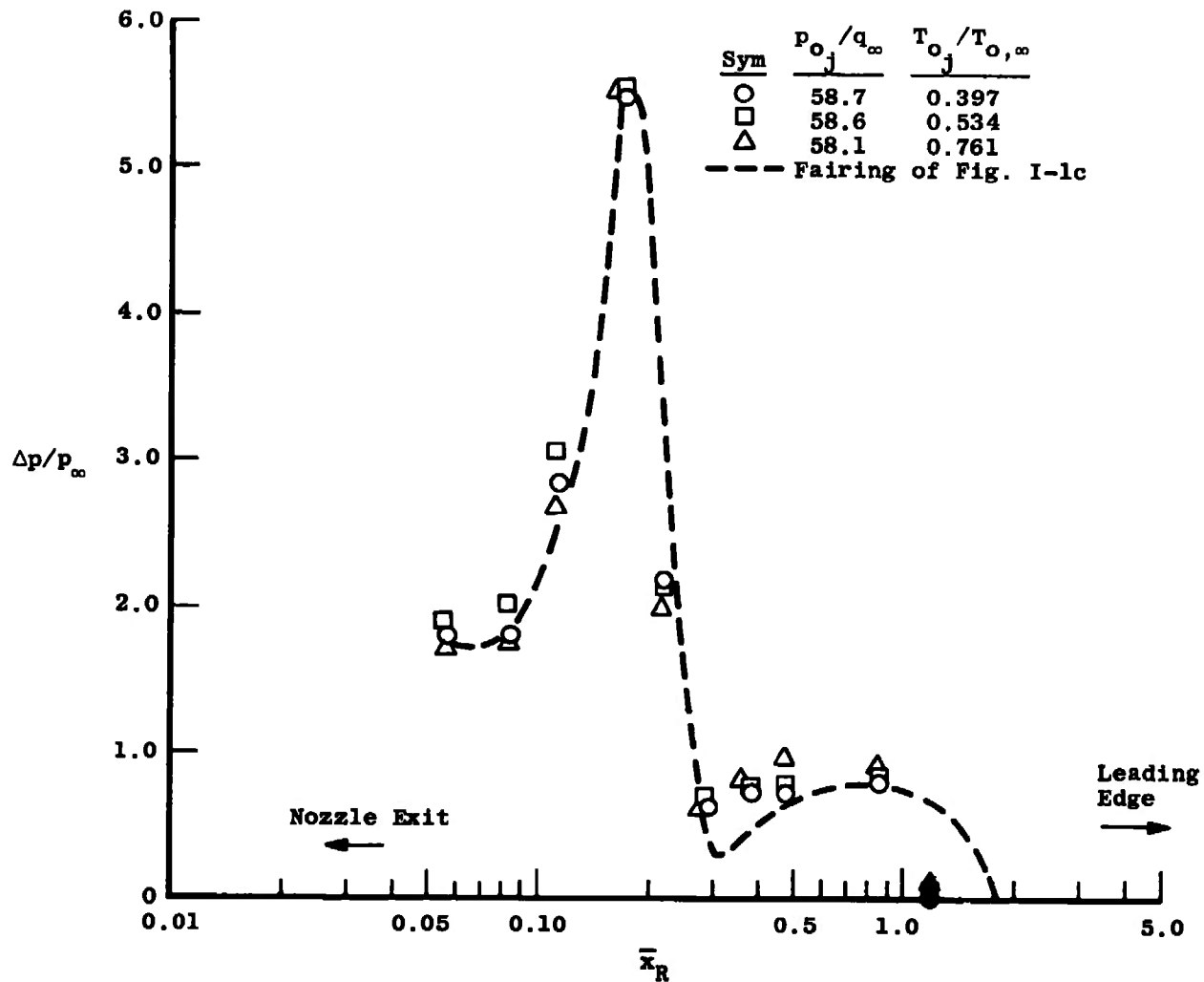


a. $\theta = 180$ deg

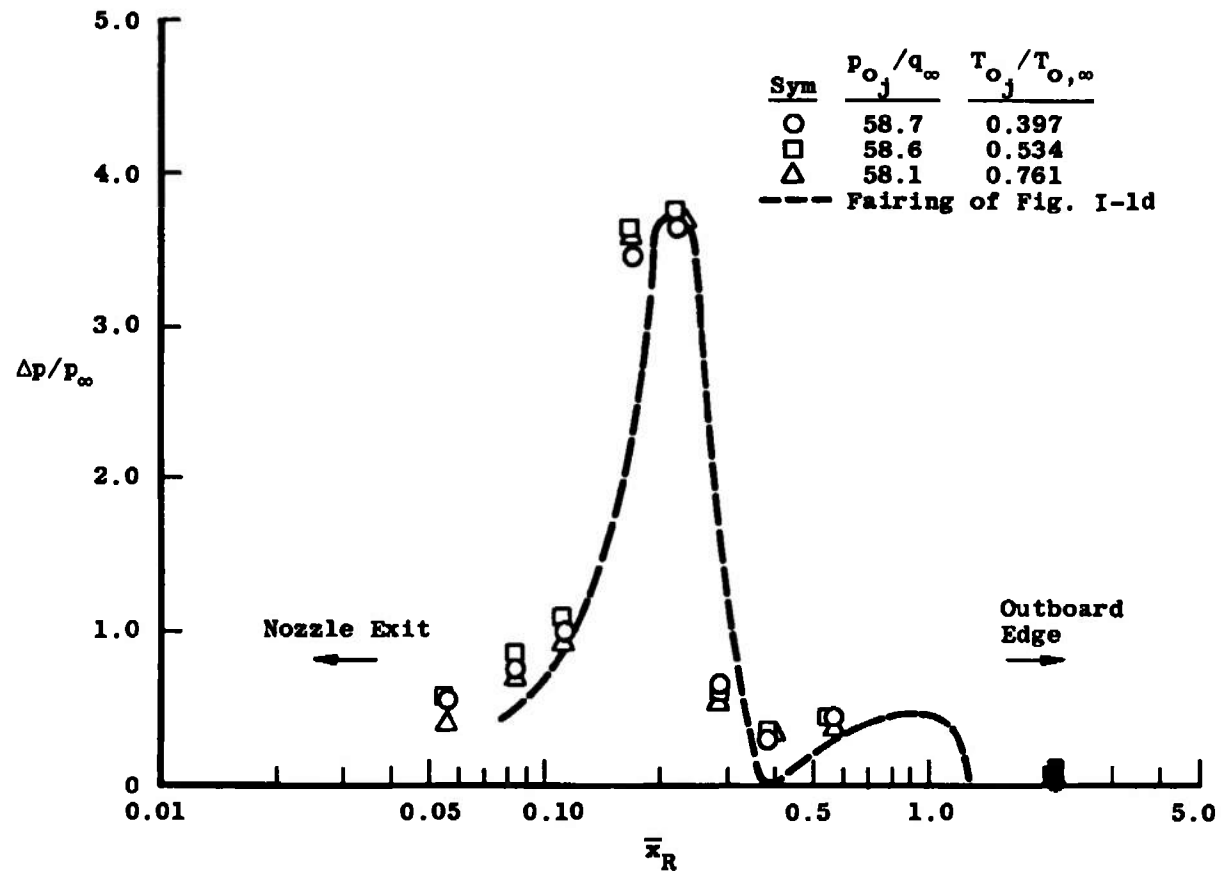
Fig. I-2 Jet Air Temperature Effects on the Pressure Distributions on a Flat Plate Around a Supersonic Nozzle, $M_j = 2.54$, $d_j = 0.50$ in., $\alpha = 0$, $M_\infty = 8.0$, and $Re_\ell = 5 \times 10^6$



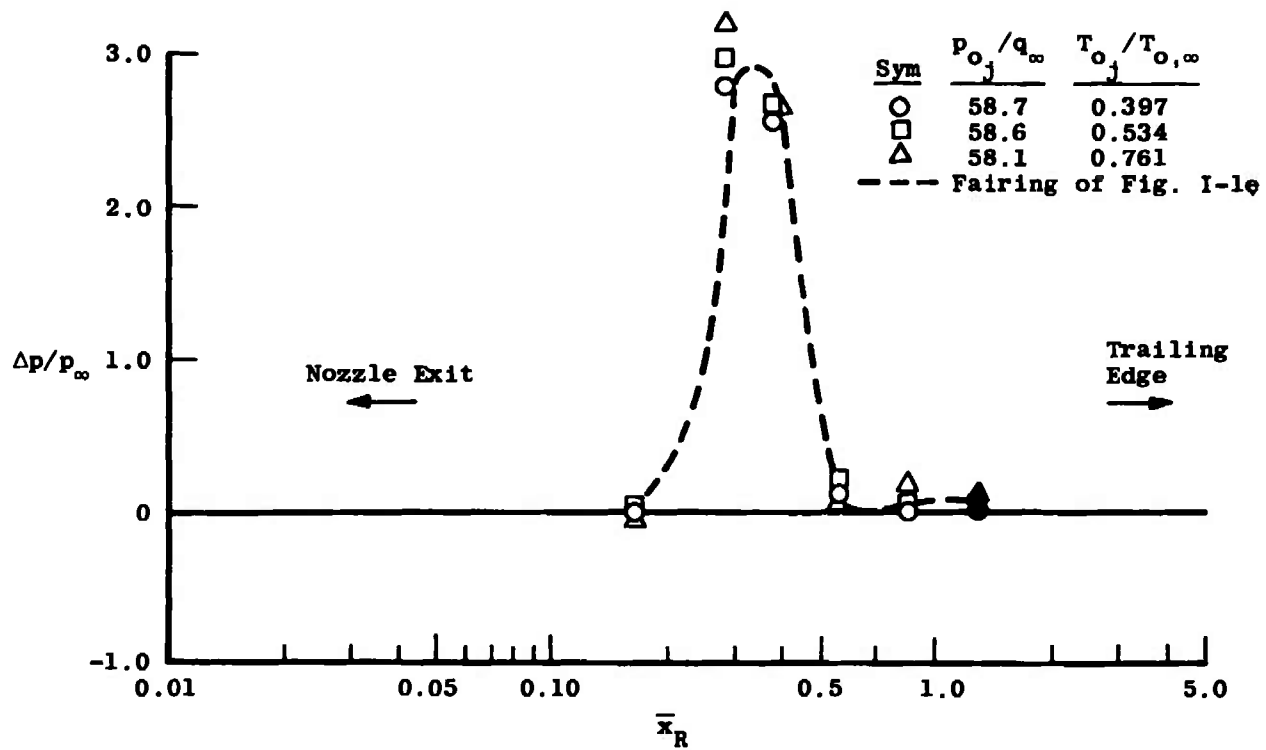
b. $\theta = 160^\circ$
Fig. I-2 Continued



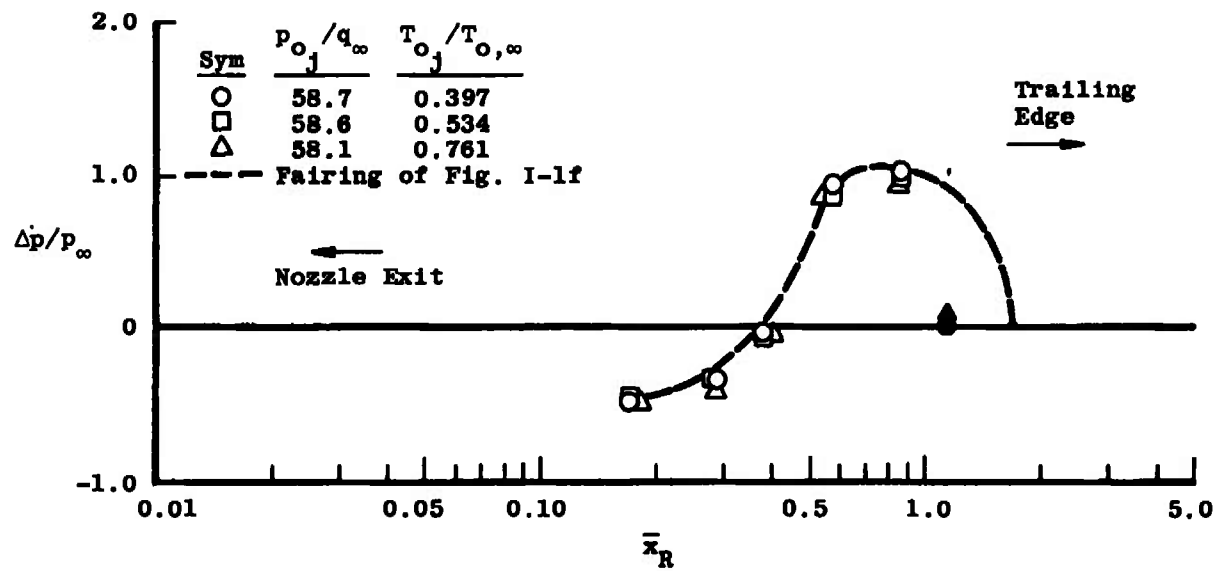
c. $\theta = 135$ deg
Fig. I-2 Continued



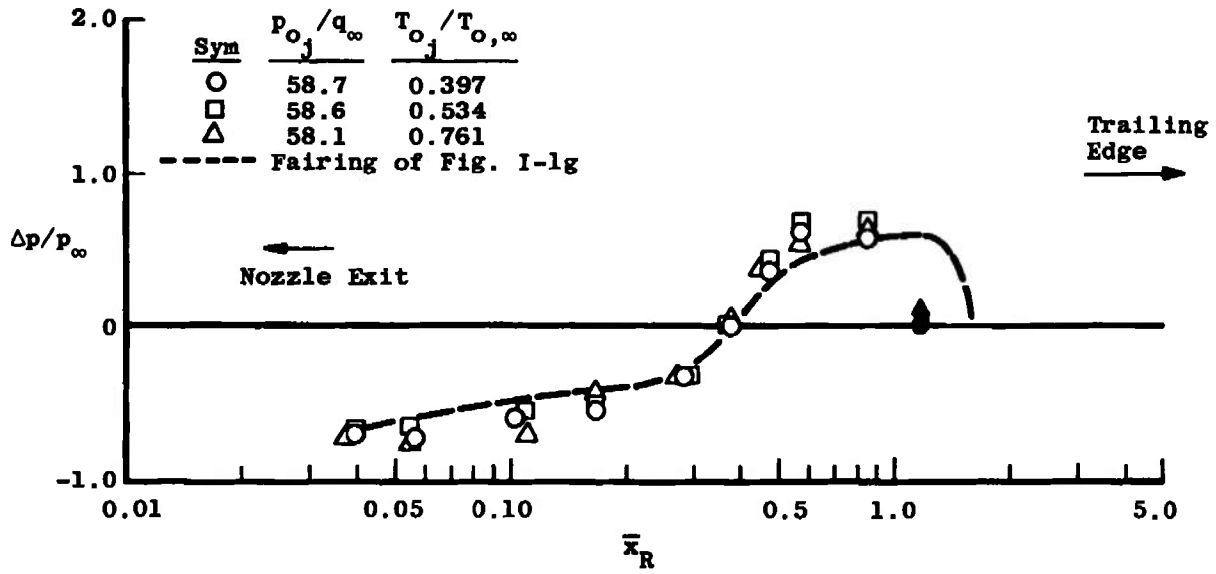
d. $\theta = 90^\circ$
Fig. I-2 Continued



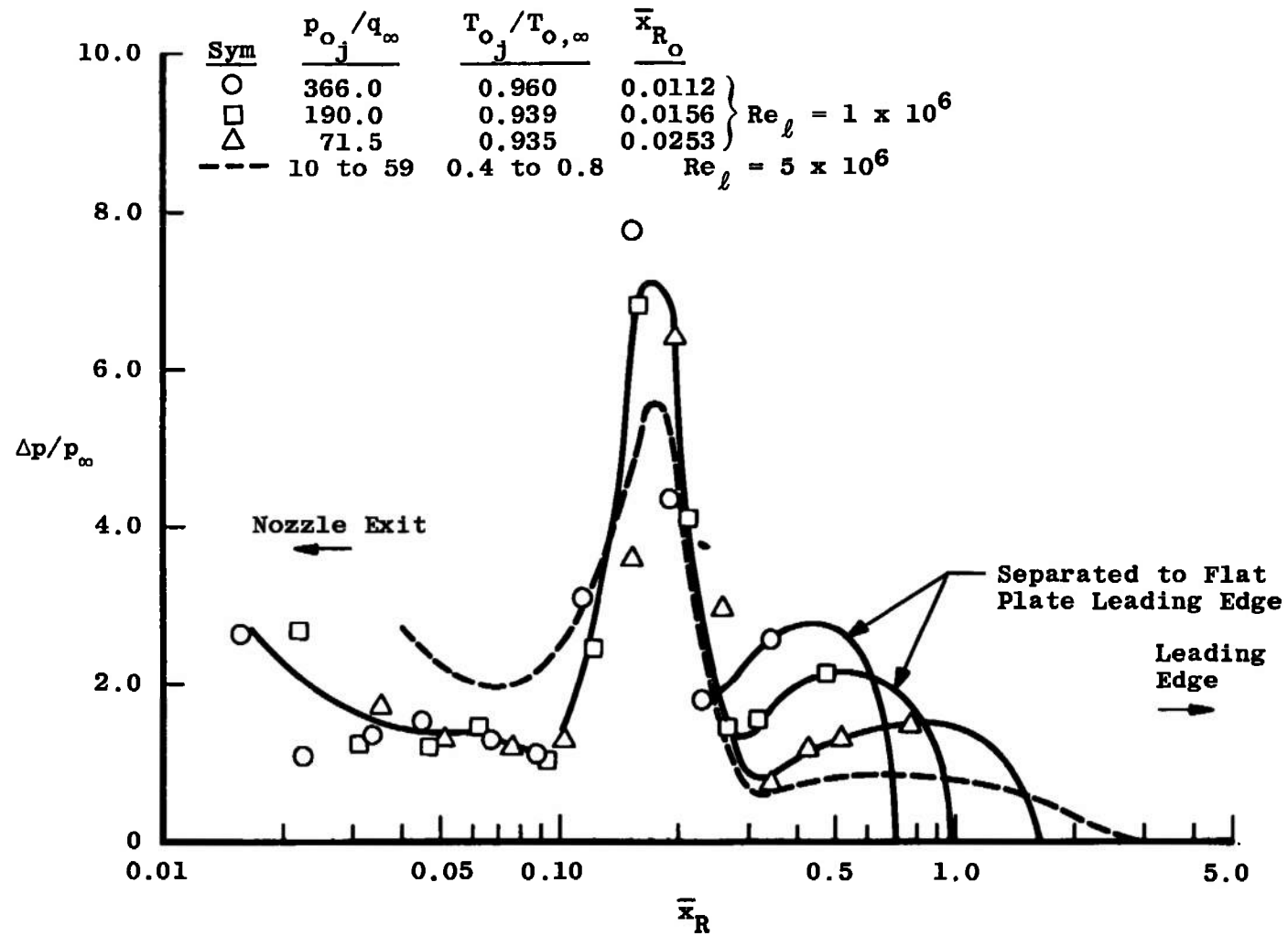
e. $\theta = 45^\circ$
Fig. 1-2 Continued



f. $\theta = 15^\circ$
Fig. I-2 Continued

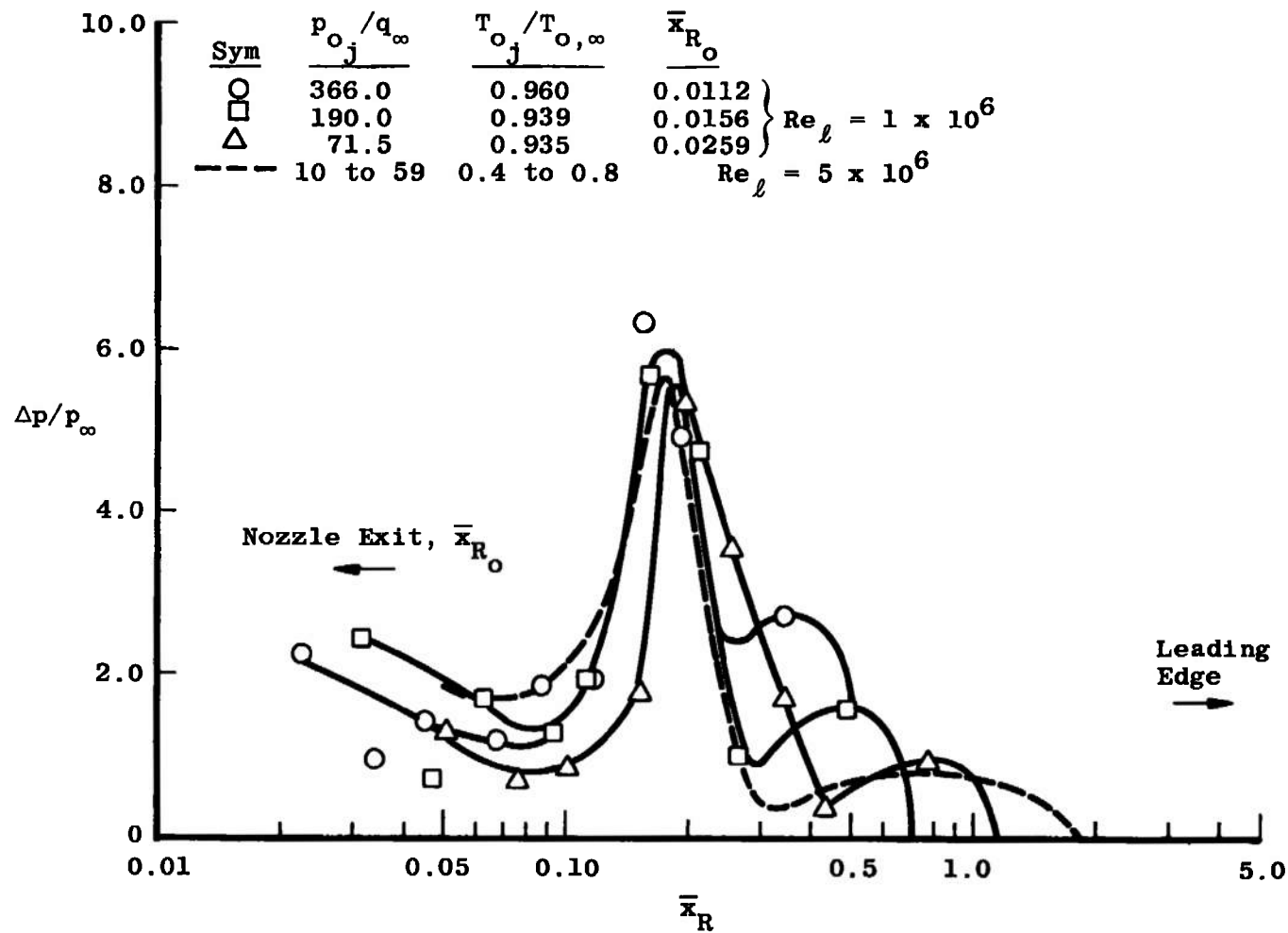


g. $\theta = 0$
Fig. 1-2 Concluded

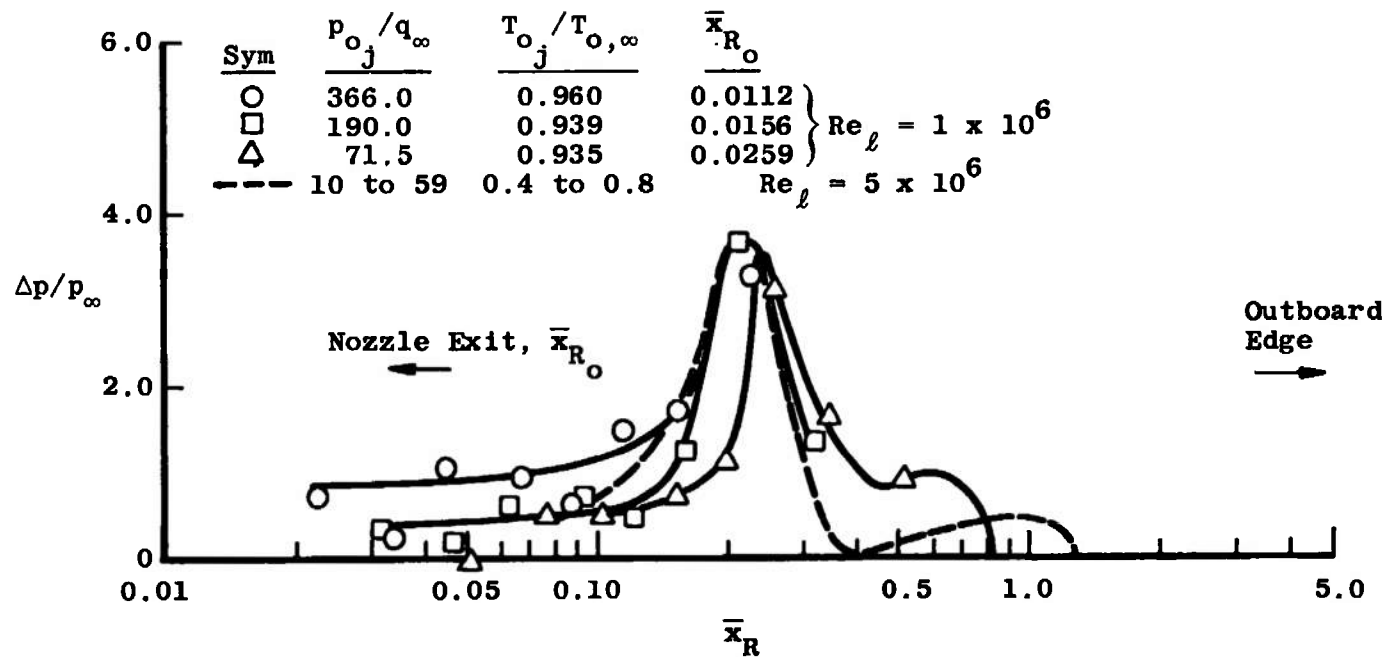


a. $\theta = 180$ deg

Fig. 1-3 Pressure Distributions on a Flat Plate Around a Hot Air Jet from a Supersonic Nozzle, $M_j = 2.54$, $d_j = 0.50$ in., $\alpha = 0$, $M_\infty = 7.9$, and $Re_\ell = 1.0 \times 10^6$



b. $\theta = 135$ deg
 Fig. 1-3 Continued



c. $\theta = 90$ deg
 Fig. I-3 Continued

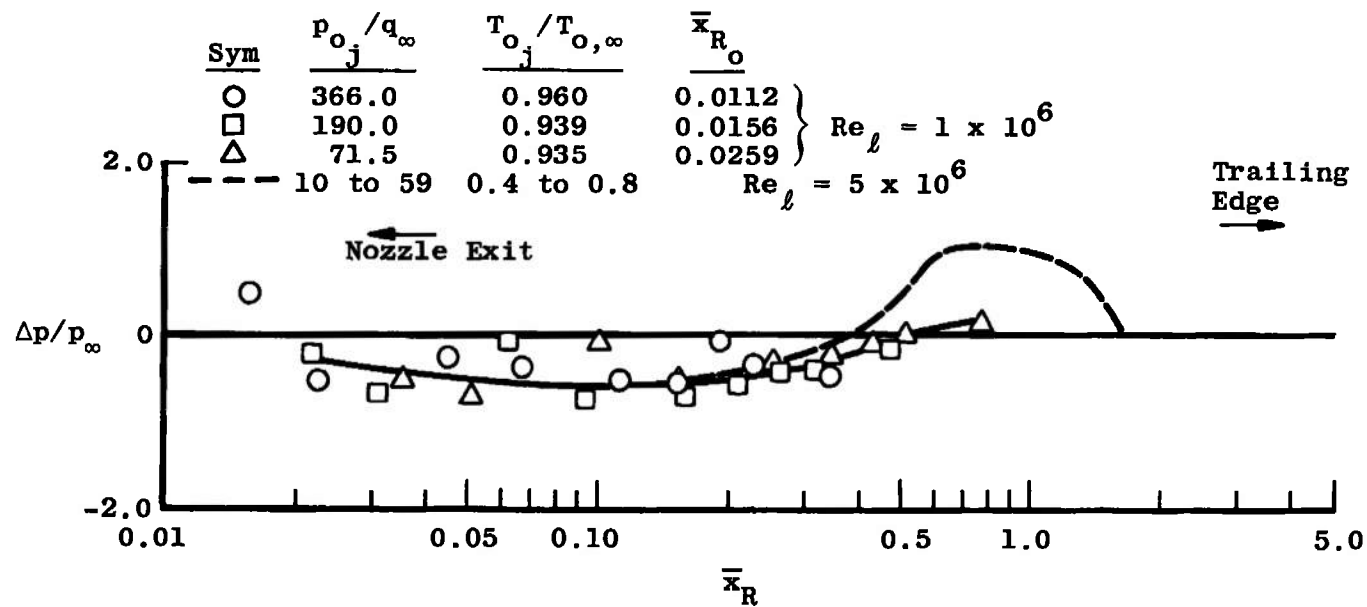
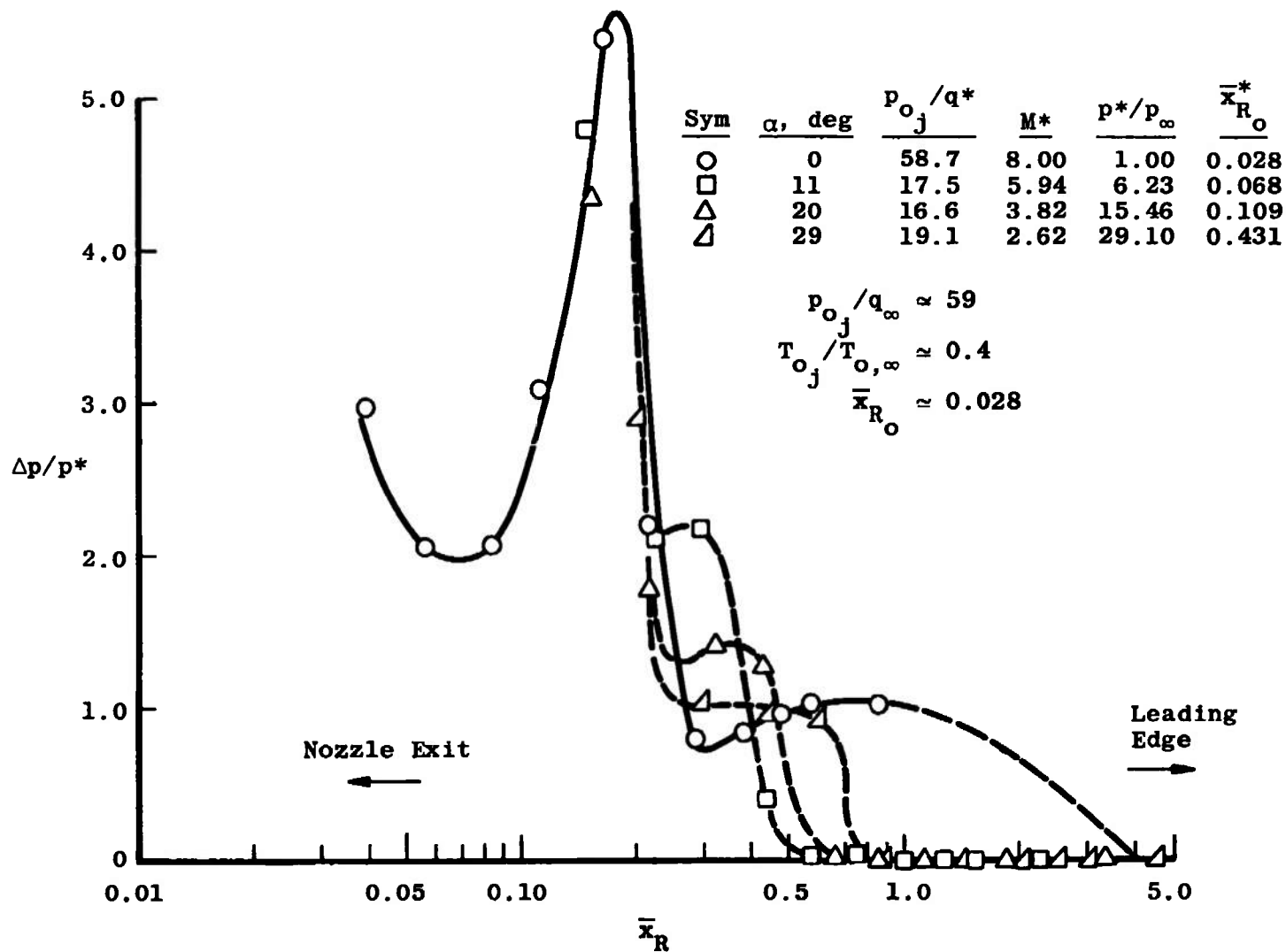
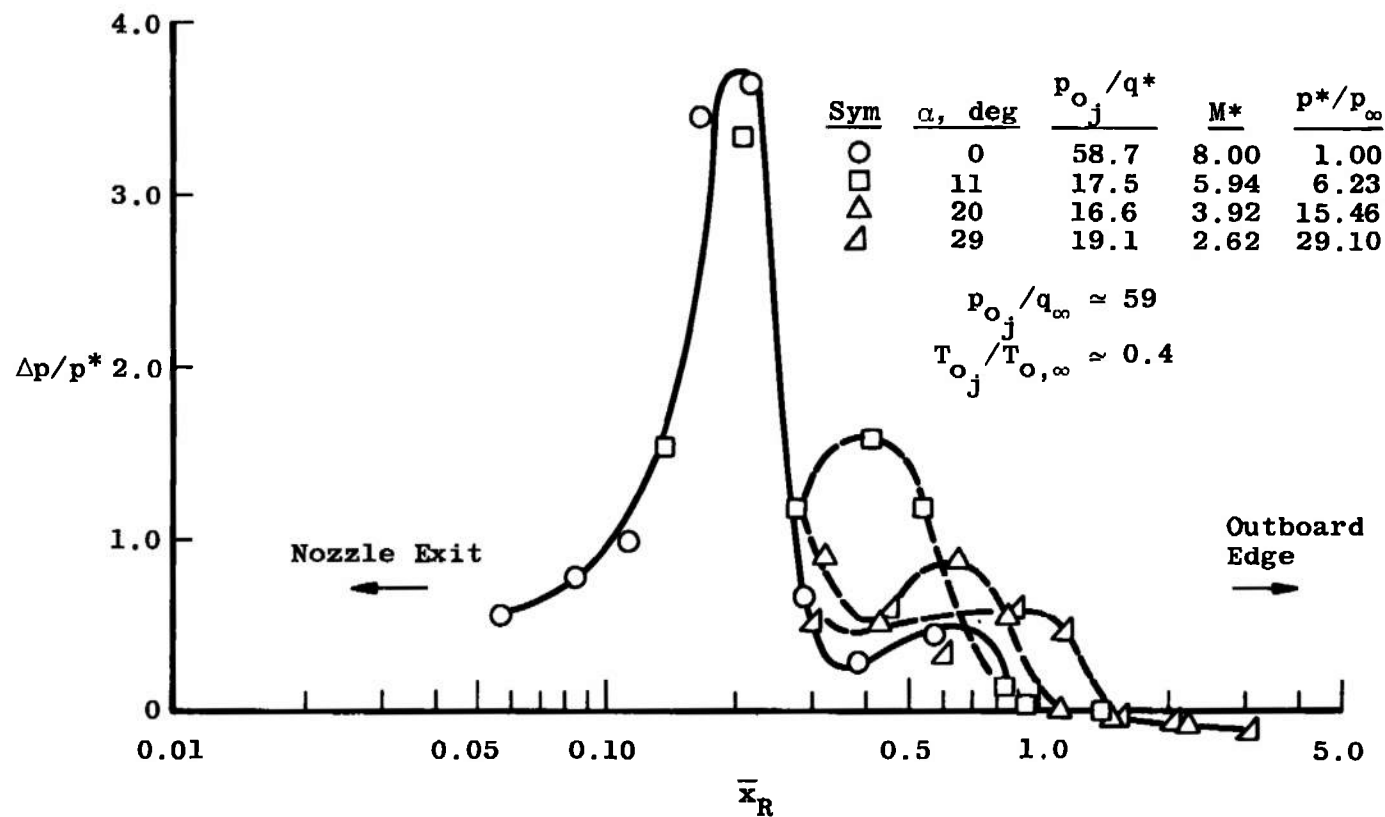
d. $\theta = 0$

Fig. 1-3 Concluded

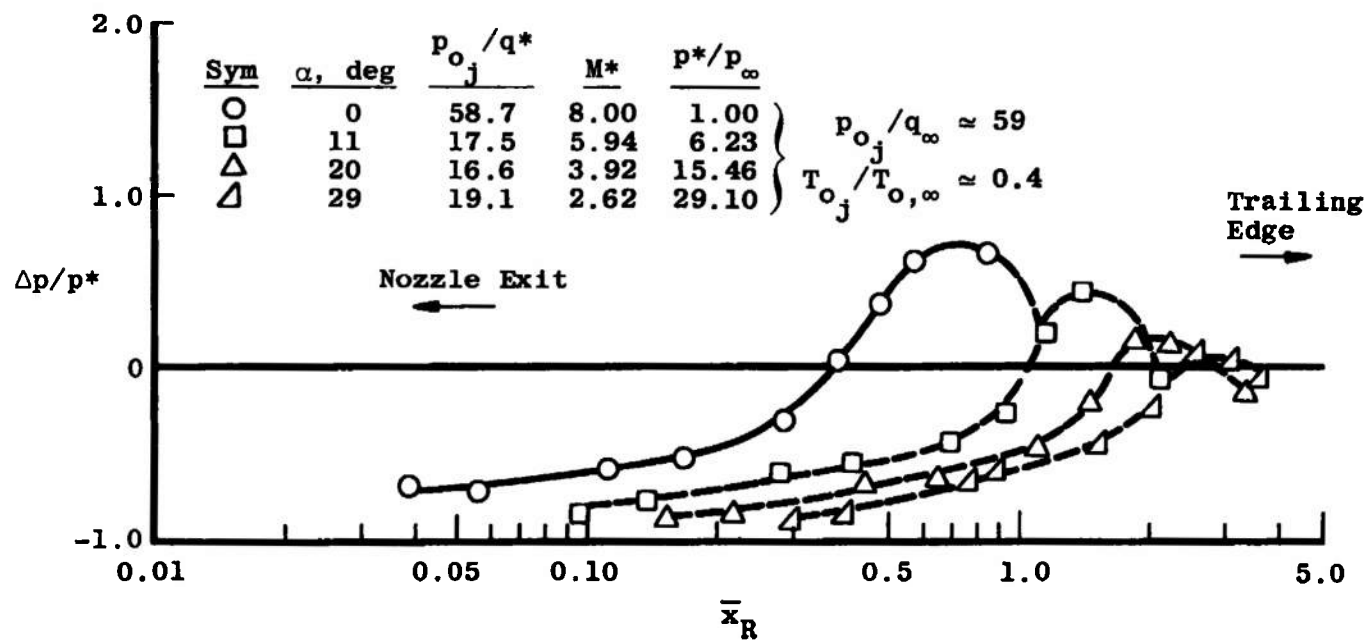


a. $\theta = 180$ deg

Fig. 1-4 Angle-of-Attack (Local Stream Property) Effects on the Pressure Distributions on a Flat Plate Around a Supersonic Nozzle, $M_j = 2.54$, $d_j = 0.50$ in., $M_\infty = 8.0$, and $Re_\ell = 5 \times 10^6$



b. $\theta = 90$ deg
 Fig. 1-4 Continued



$c, \theta = 0$
 Fig. 1-4 Concluded

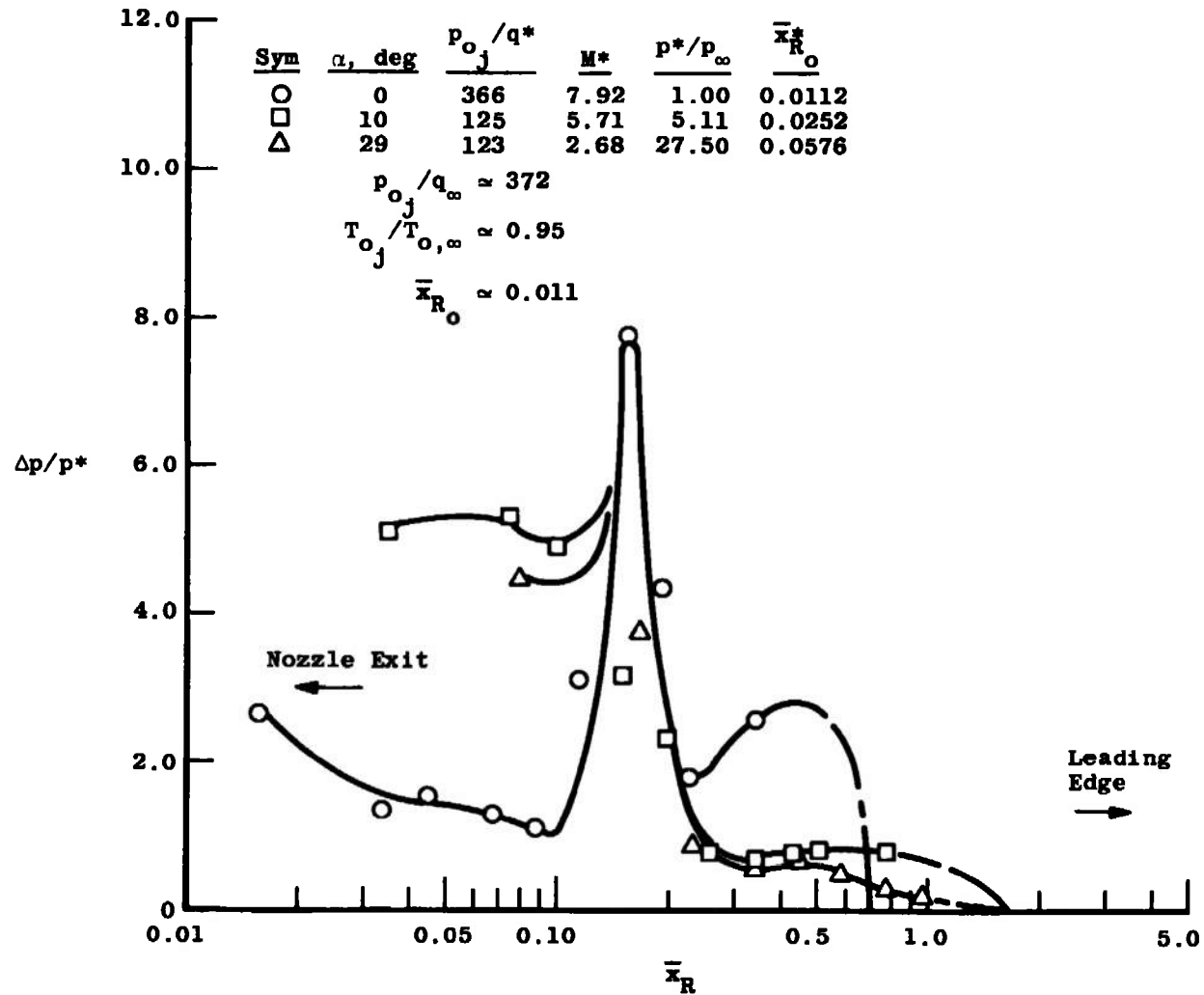
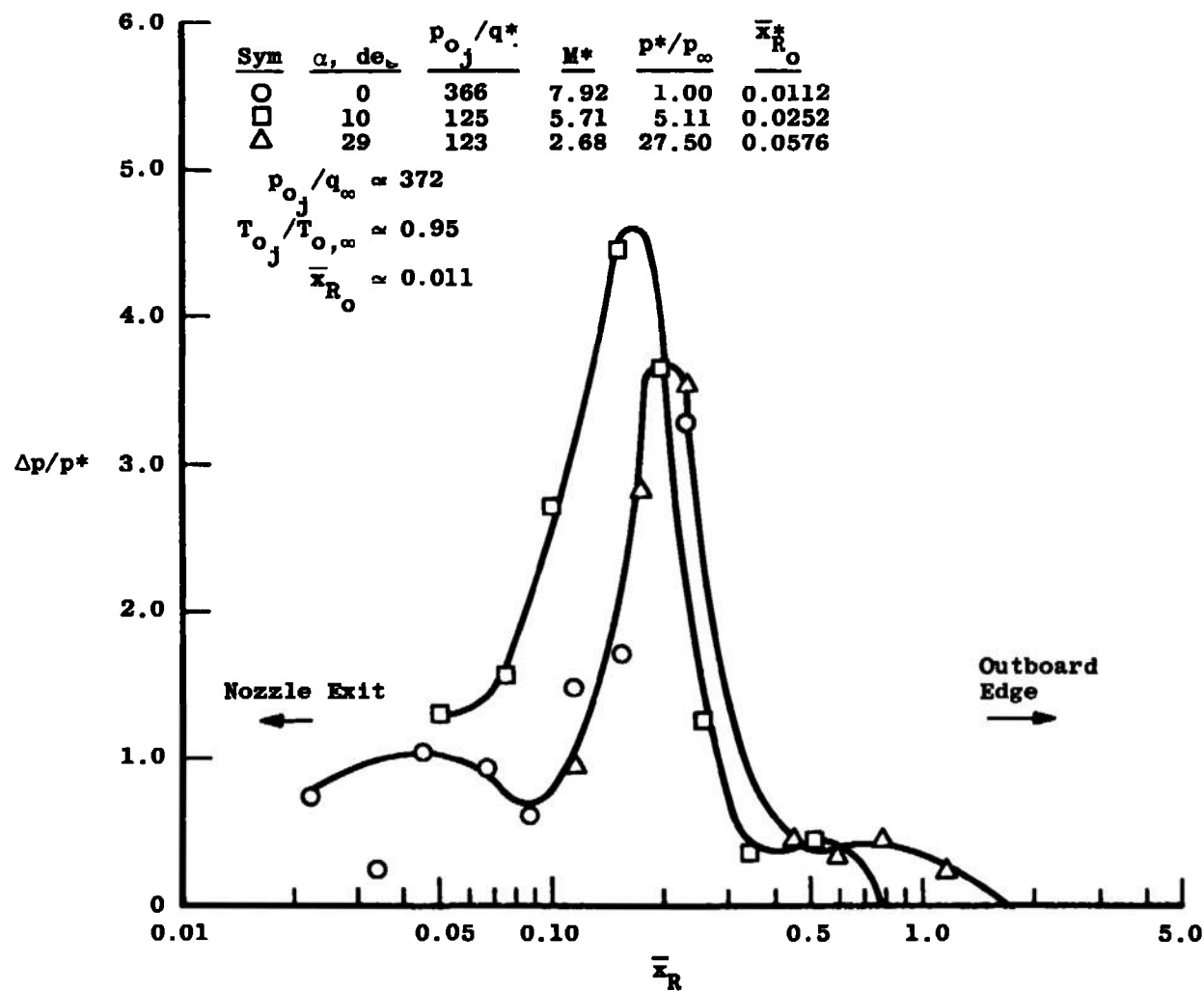
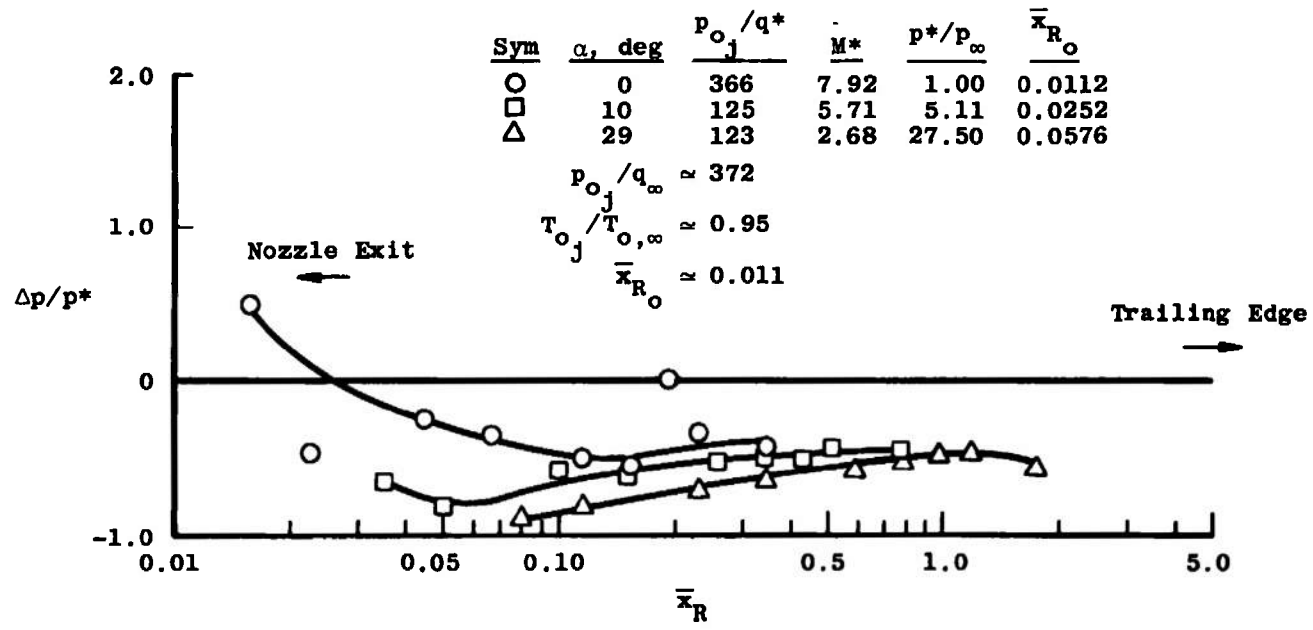
a. $\theta = 180$ deg

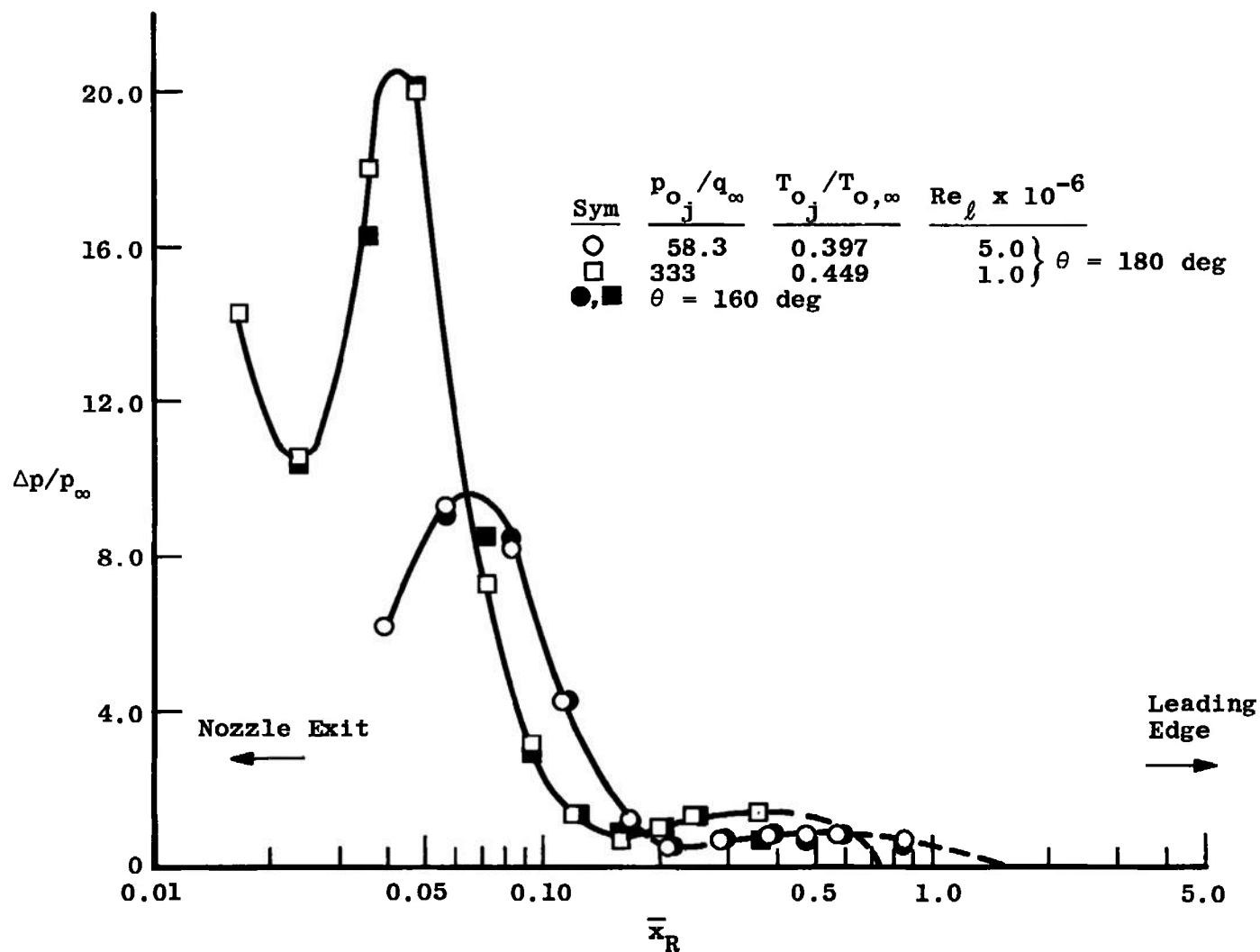
Fig. I-5 Angle-of-Attack (Local Stream Property) Effects on the Pressure Distributions on a Flat Plate Around a Supersonic Nozzle, $M_j = 2.54$, $d_j = 0.50$ in., $M_\infty = 7.9$, and $Re_\ell = 1 \times 10^6$



b. $\theta = 90$ deg
 Fig. I-5 Continued

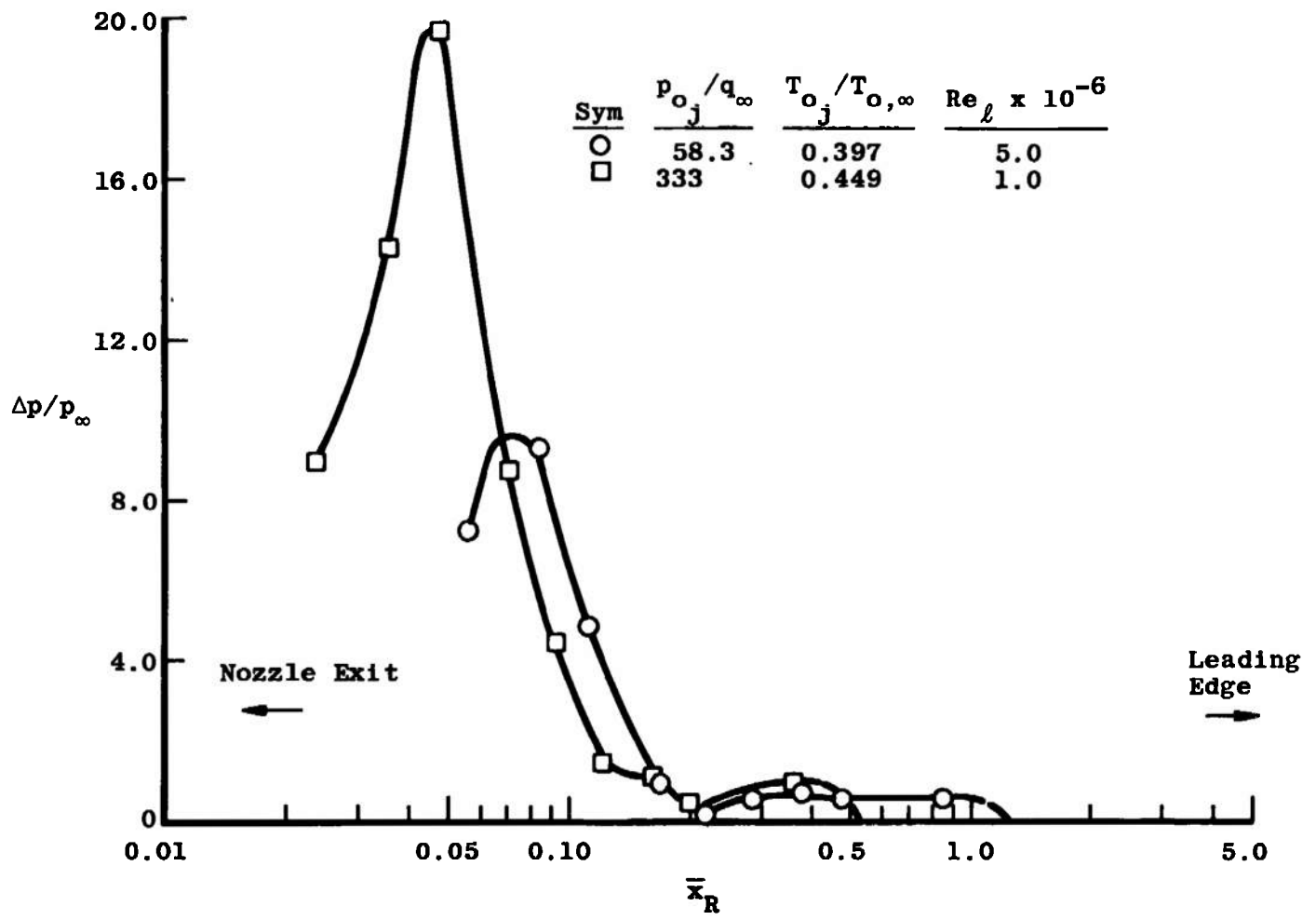


c. $\theta = 0$
 Fig. 1-5 Concluded

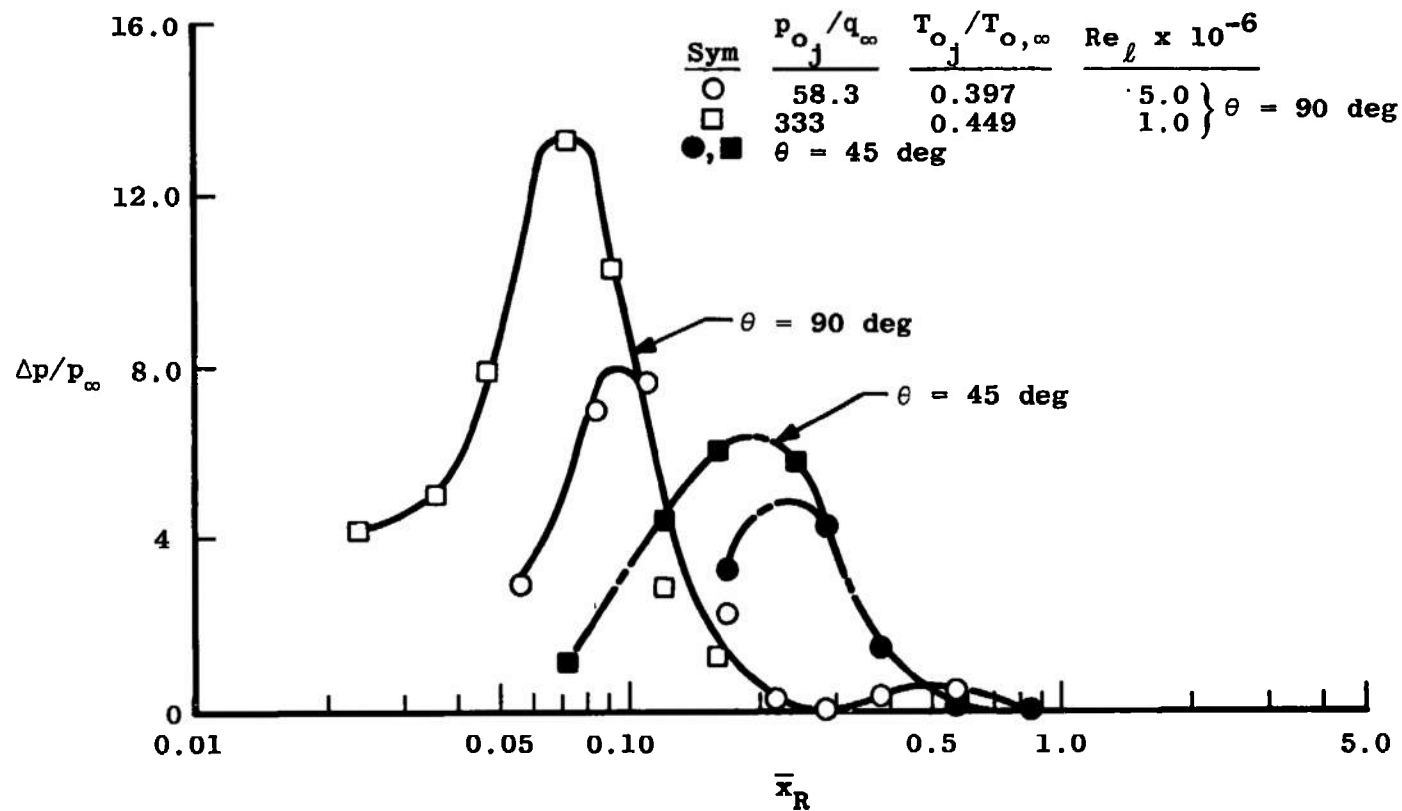


a. $\theta = 180$ and 160 deg

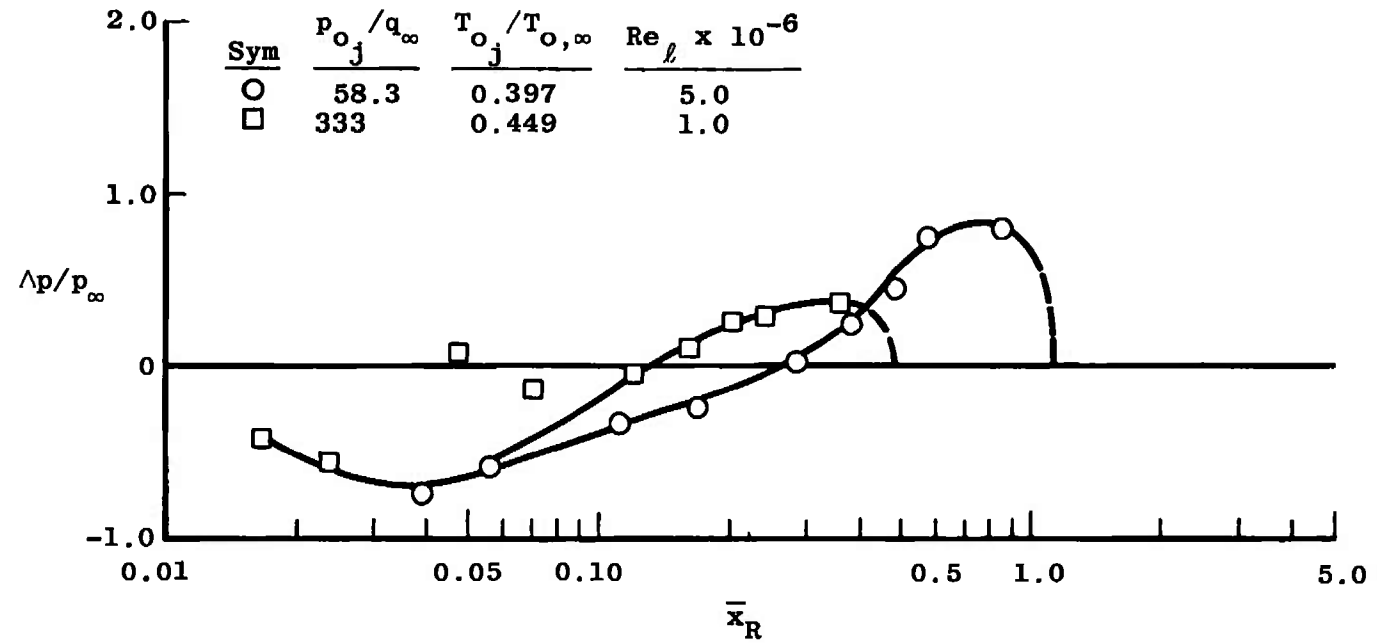
Fig. I-6 Pressure Distributions on a Flat Plate Around a Cold Helium Jet from a Supersonic Nozzle, $M_j = 2.86$, $d_j = 0.50 \text{ in.}$, $\alpha = 0$, and $M_\infty = 8$



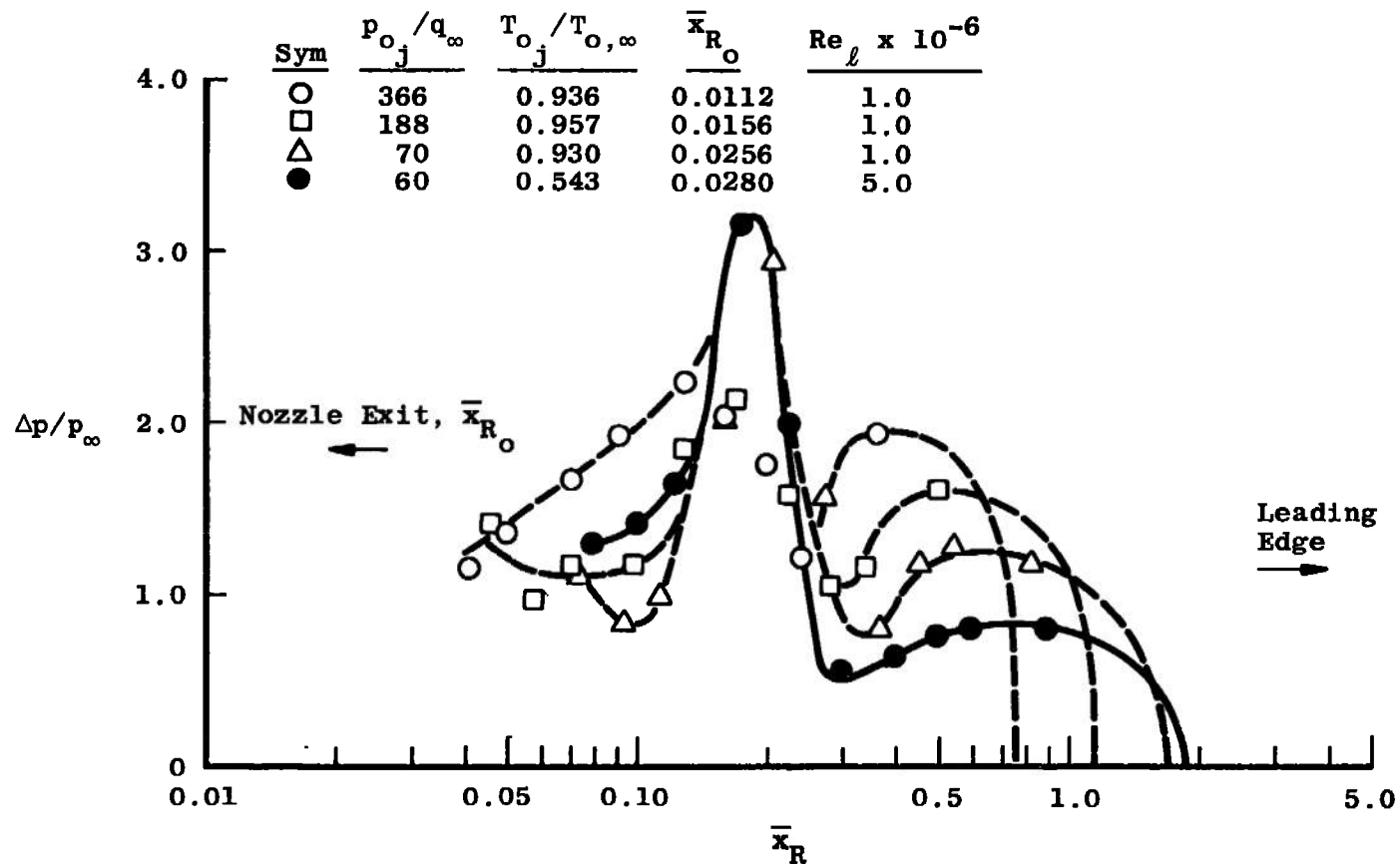
b. $\theta = 135$ deg
Fig. I-6 Continued



c. $\theta = 90$ and 45 deg
Fig. I-6 Continued

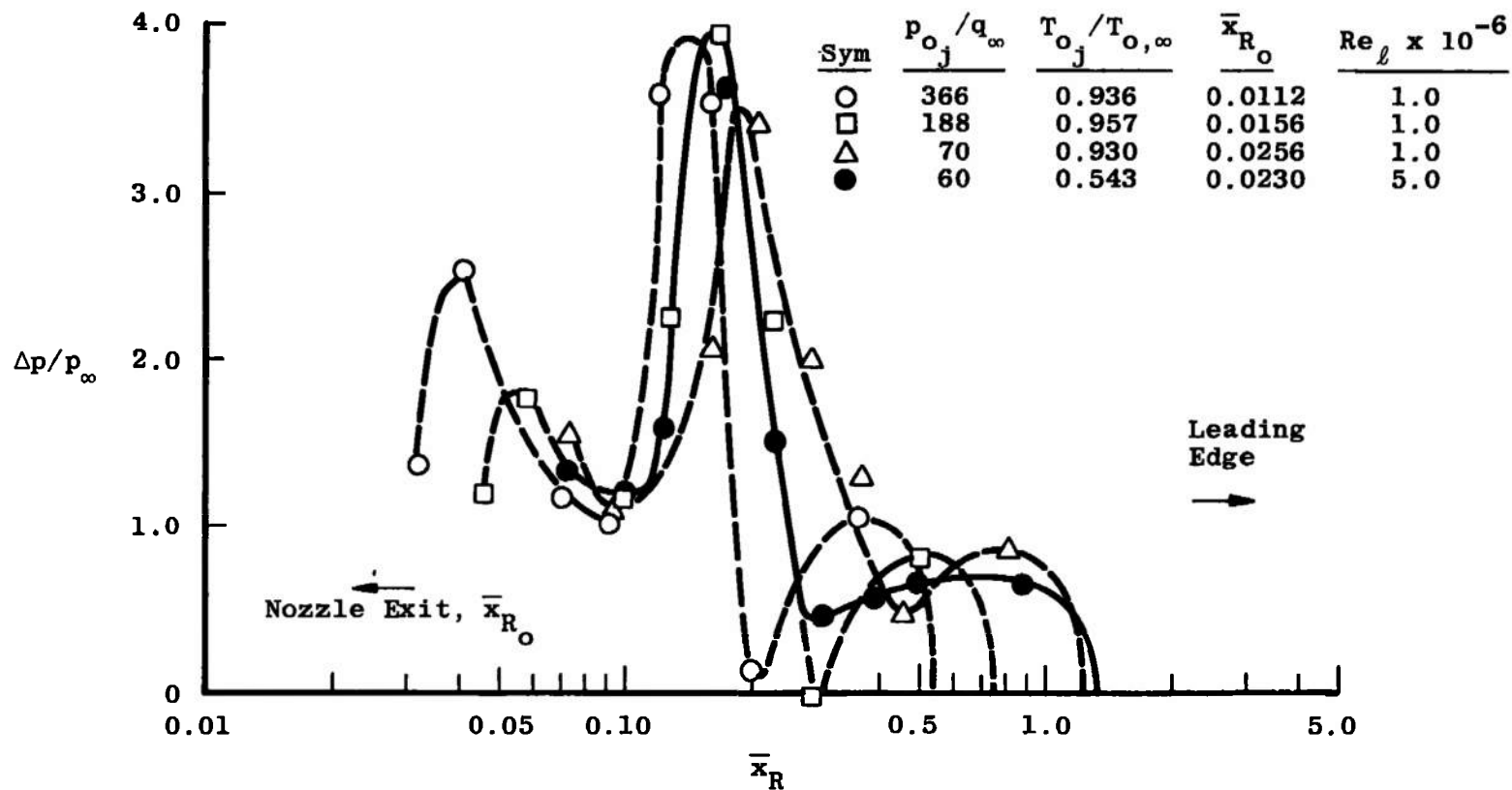


d. $\theta = 0$
Fig. 1-6 Concluded

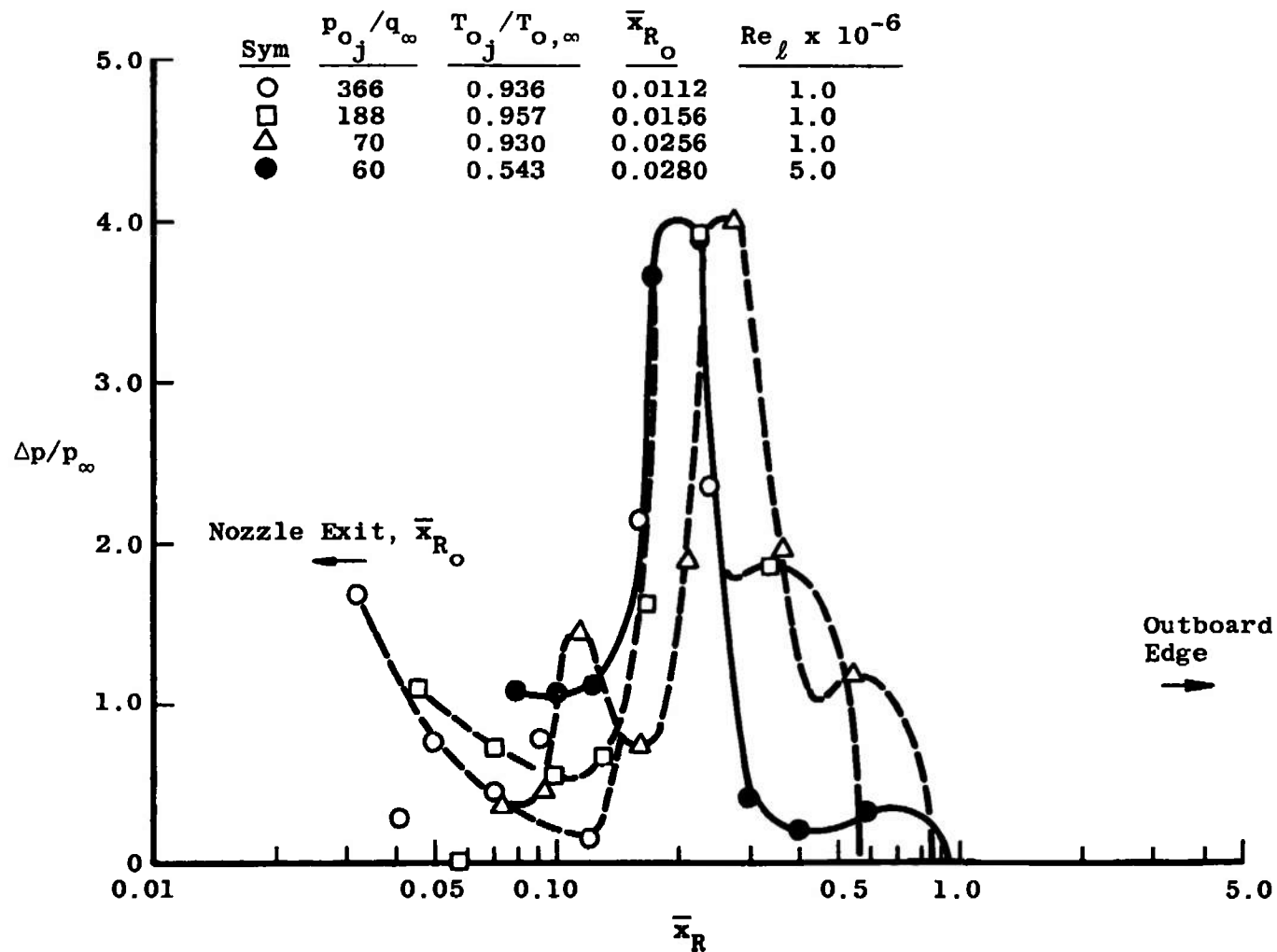


a. $\theta = 180$ deg

Fig. I-7 Pressure Distributions on a Flat Plate Around Air Jets from a Cluster of Four Supersonic Nozzles, $M_j = 2.54$, $d_j = 0.240$ in. Each, $\alpha = 0$, and $M_\infty = 8.0$



b. $\theta = 135$ deg
Fig. 1-7 Continued



c. $\theta = 90$ deg
 Fig. I-7 Continued

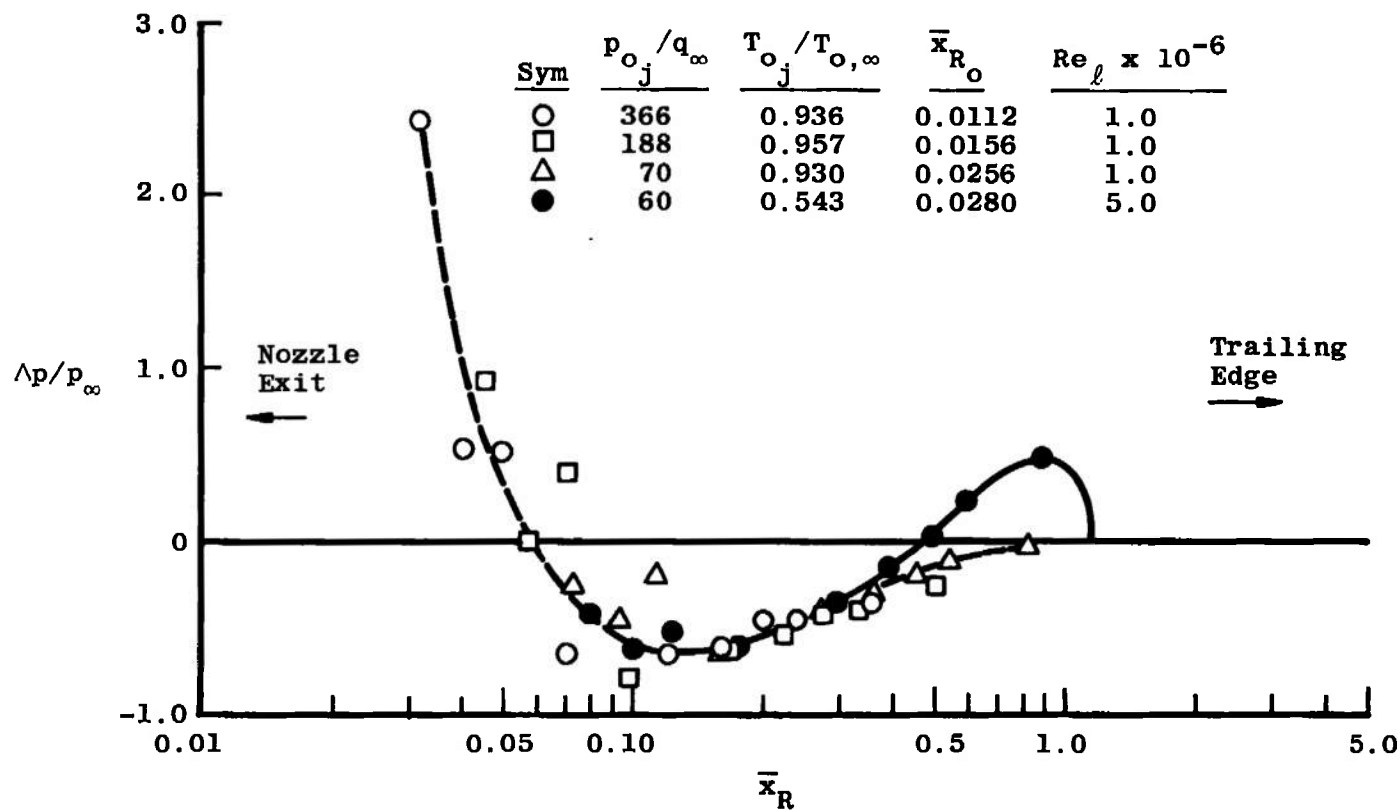
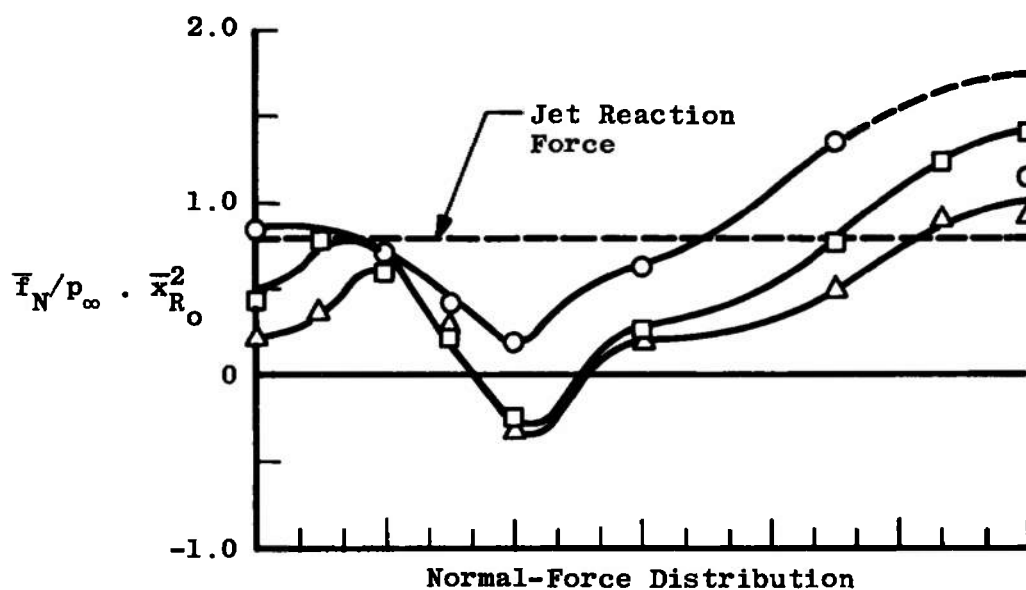
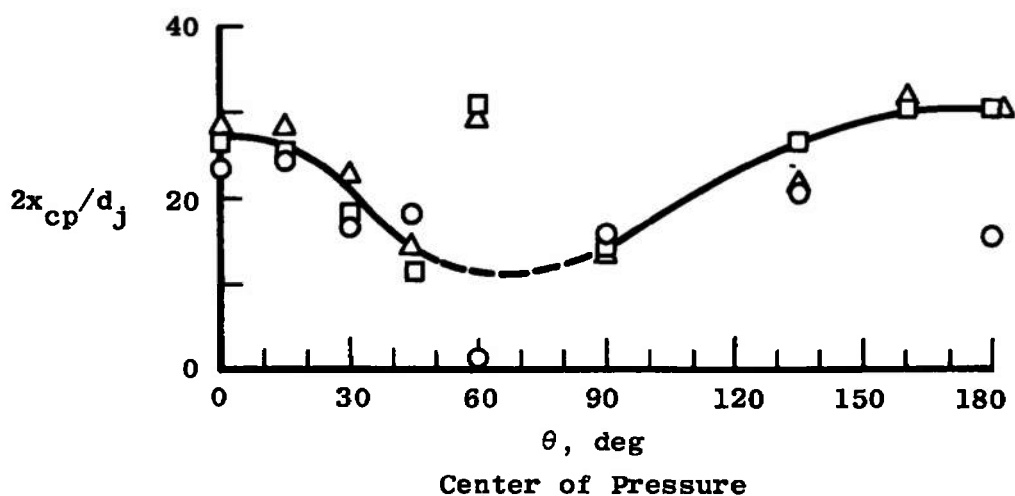
d. $\theta = 0$

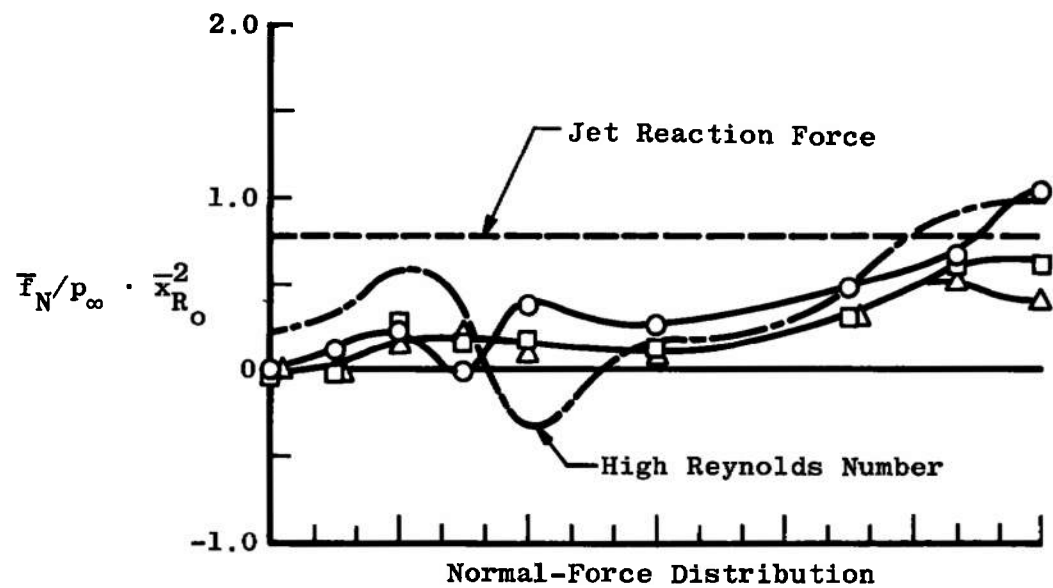
Fig. 1-7 Concluded



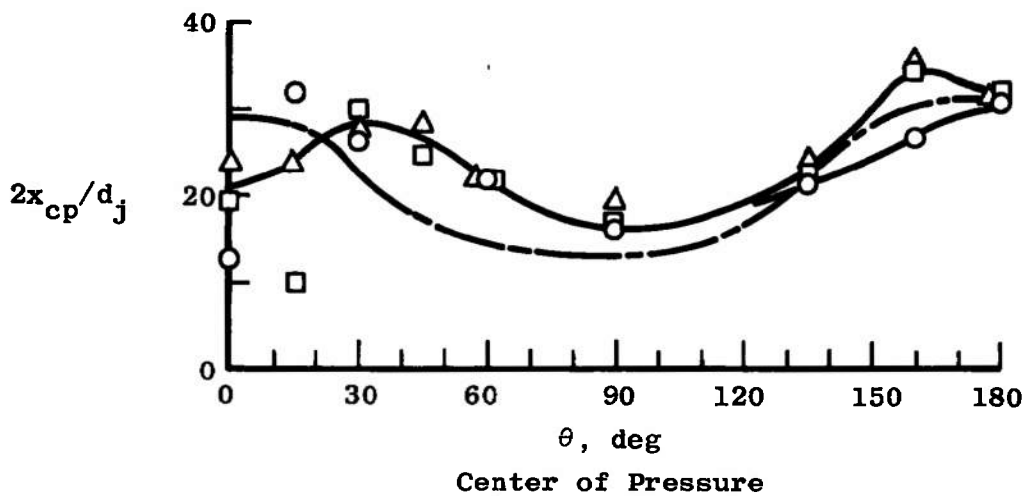
Sym	p_{o_j} / q_∞	F_N / F_j	$2CP / d_j$
○	10	1.36	----
□	29.6	0.84	-11.07
△	58.7	0.55	-11.38



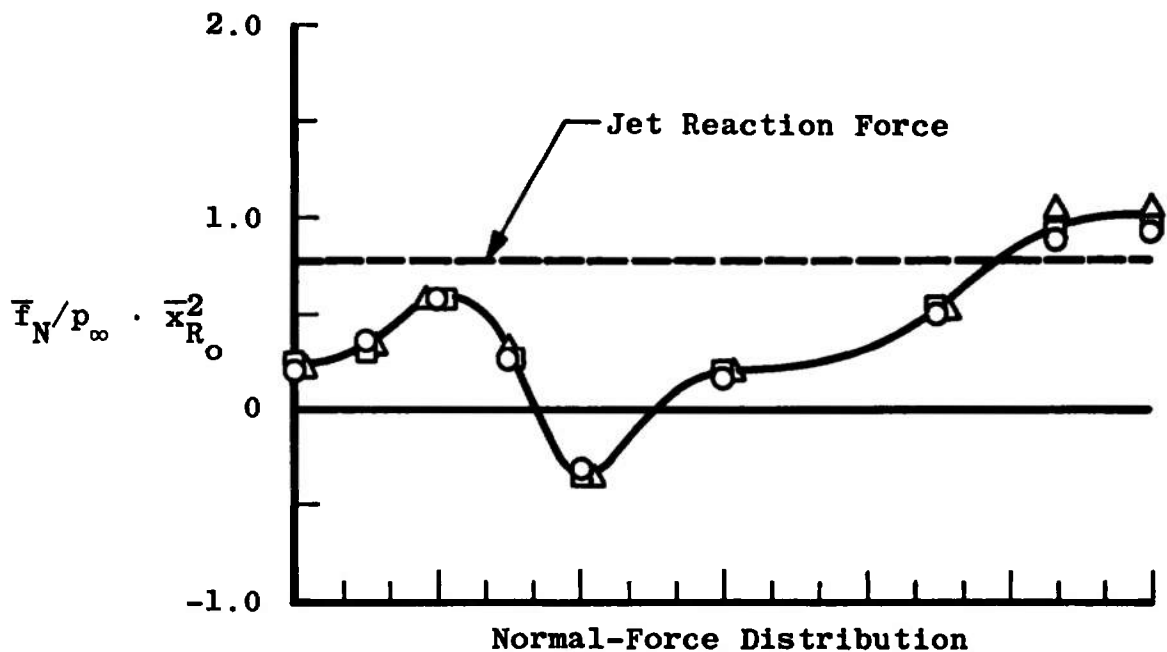
a. $Re_j = 5 \times 10^6$, $T_{o_j} / T_{o_\infty} \cong 0.4$, and $\alpha = 0$
 Fig. 1-8 Jet Chamber Pressure Effects on the Circumferential Loading
 Around a Single Conical Nozzle Jet Disturbance



Sym	p_{o_j} / q_∞	$T_{o_j} / T_{o,\infty}$	$Re_\ell \times 10^6$	F_N / F_j	$2CP / d_j$
○	72	0.935	1.0	0.55	-10.5
□	190	0.938	1.0	0.38	-13.0
△	366	0.960	1.0	0.30	-14.6
---	≈59	0.4 to 0.8	5.0	≈0.55	≈-12.0



b. $Re_\ell = 1.0 \times 10^6$, $T_{o_j} / T_{o,\infty} = 0.94$ and $\alpha = 0$
Fig. 1-8 Concluded



Sym	p_{o_j} / q_∞	$T_{o_j} / T_{o,\infty}$	F_N / F_j	$2CP/d_j$
○	58.7	0.397	0.55	-11.4
□	58.6	0.534	0.57	-11.7
△	58.1	0.761	0.60	-13.6

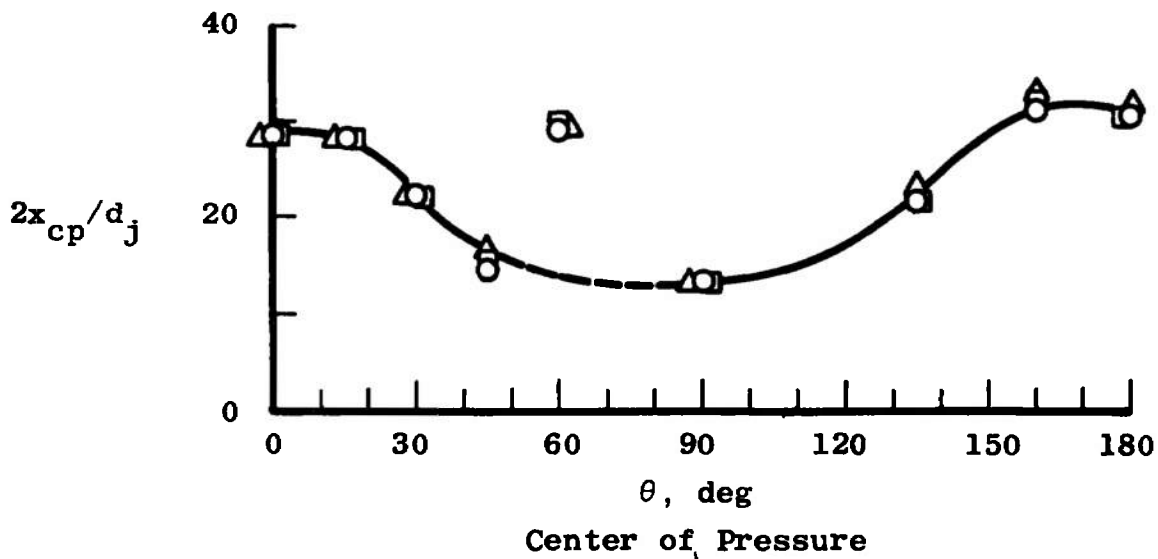
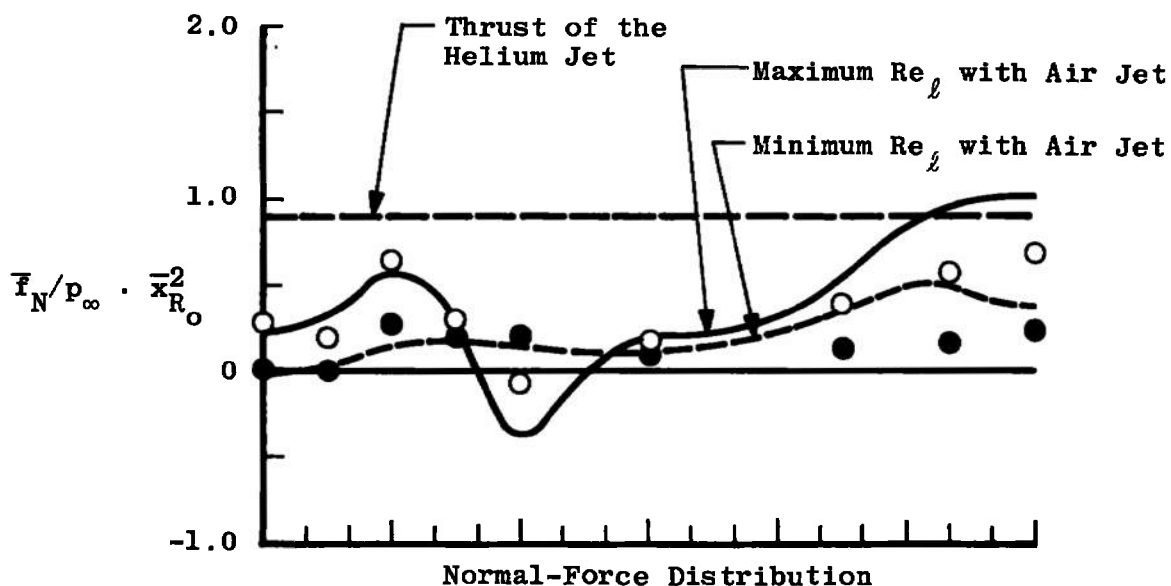


Fig. I-9 Jet Chamber Temperature Effects on the Circumferential Loading Around a Single Conical Nozzle Jet Disturbance



Sym	Gas	F_N / F_j	p_{o_j} / q_∞	$Re_\ell \times 10^{-6}$
○	Helium	0.33	58	5.0
—	Air-See Fig. I-9	0.55	59	5.0
●	Helium	0.15	333	1.0
- - -	Air-See Fig. I-8b	0.30	366	1.0

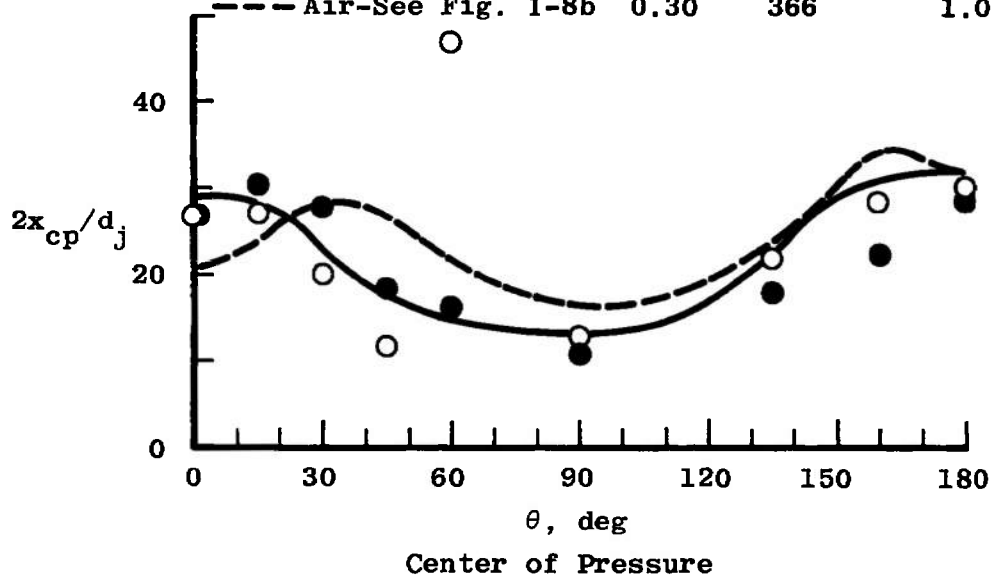
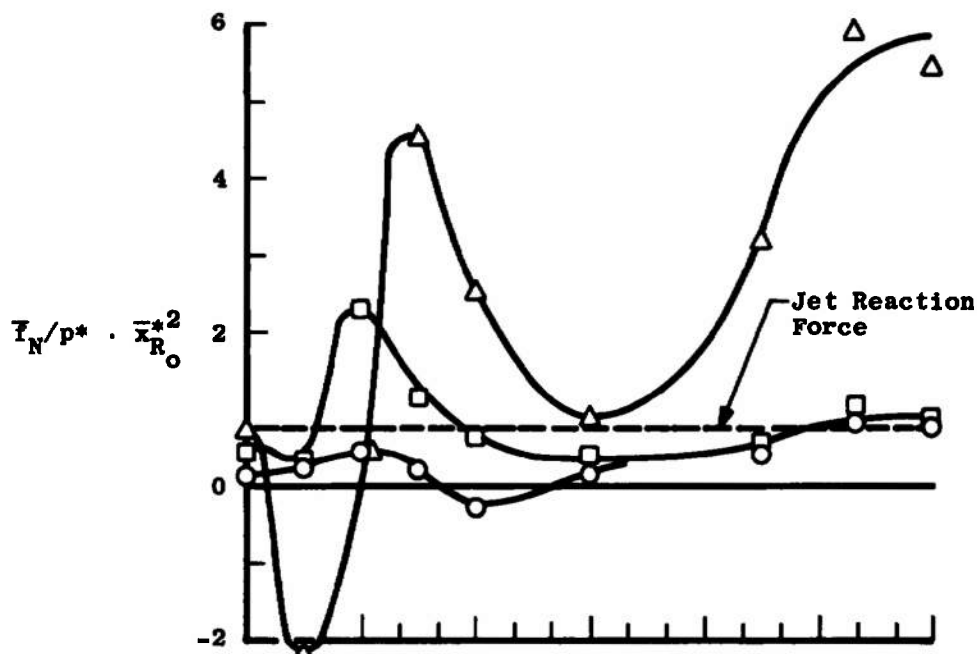
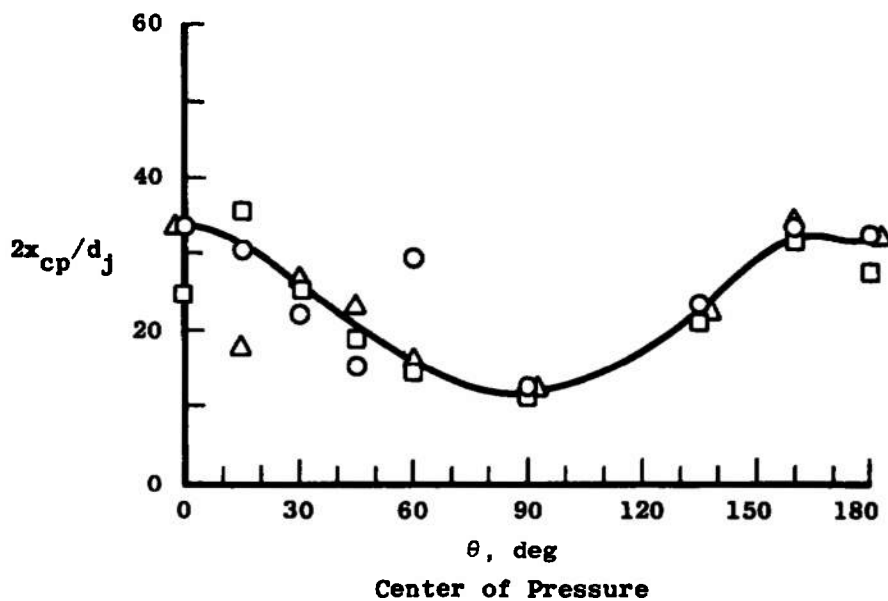


Fig. I-10 Effect of Jet Gas on the Circumferential Loading Around a Nozzle at $Re_\ell = 5 \times 10^6$ and 1×10^6 , $M_\infty \cong 8$, and $\alpha = 0$



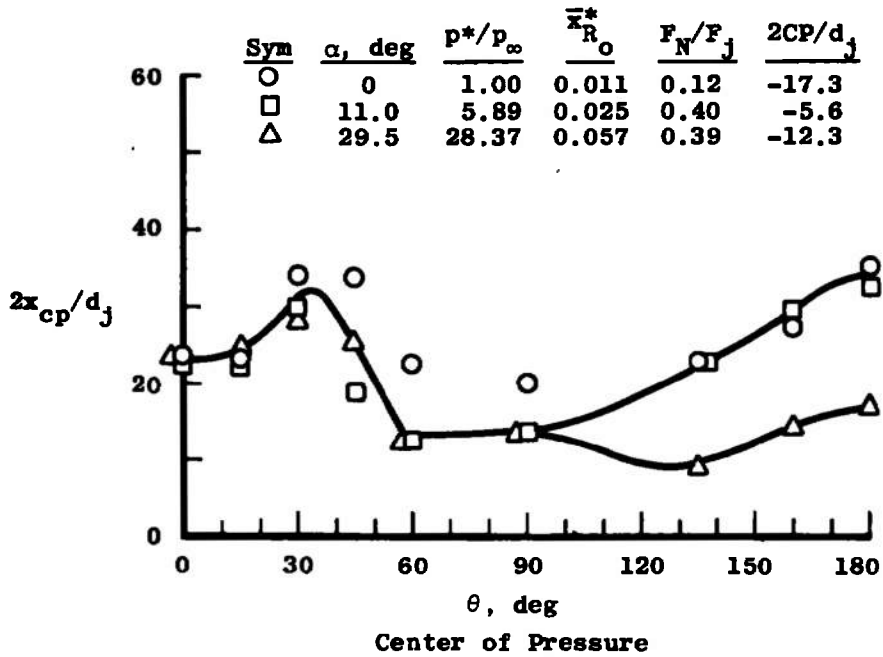
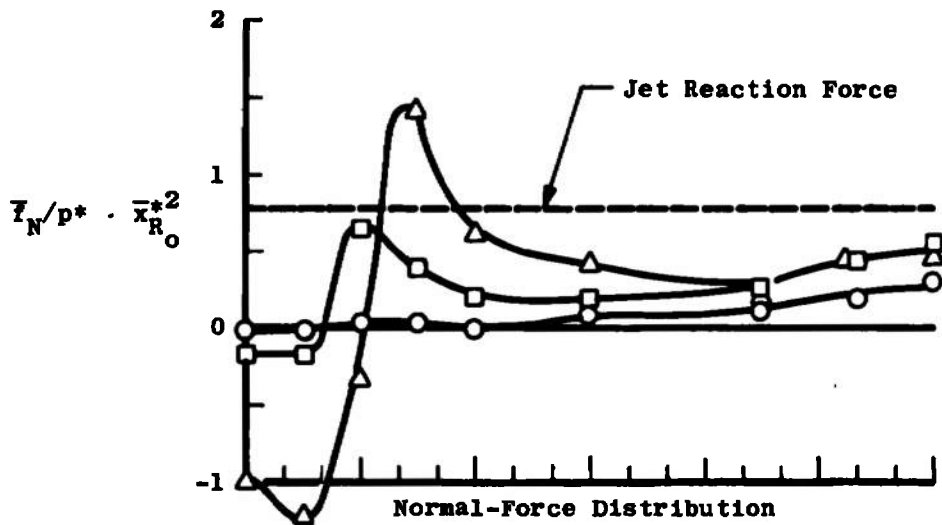
Normal-Force Distribution

Sym	α , deg	p^*/p_∞	$\bar{x}_{R_o}^*$	F_N/F_j	$2CP/d_j$
○	0	1.00	0.028	0.45	-13.9
□	11	6.23	0.064	1.44	1.62
△	31	30.99	0.144	4.06	-13.3

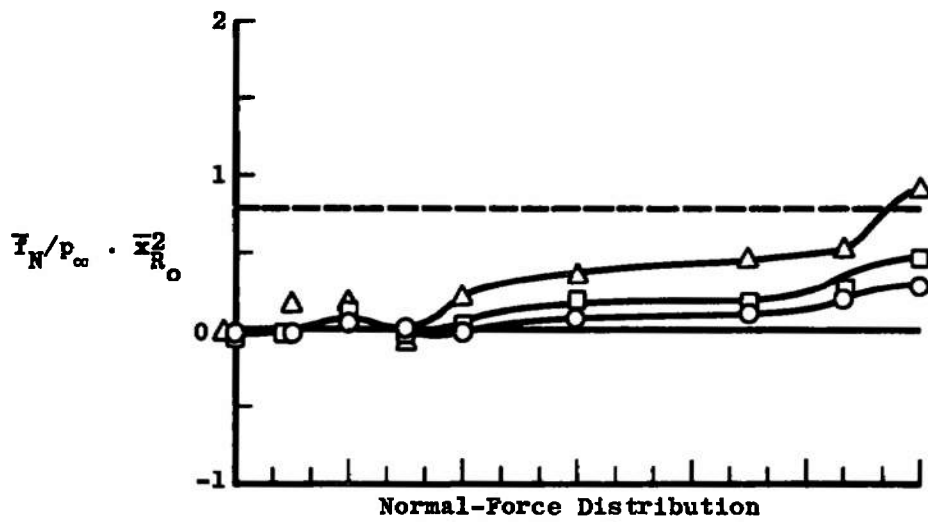


a. Angle-of-Attack Effects at $Re_\ell = 5 \times 10^6$

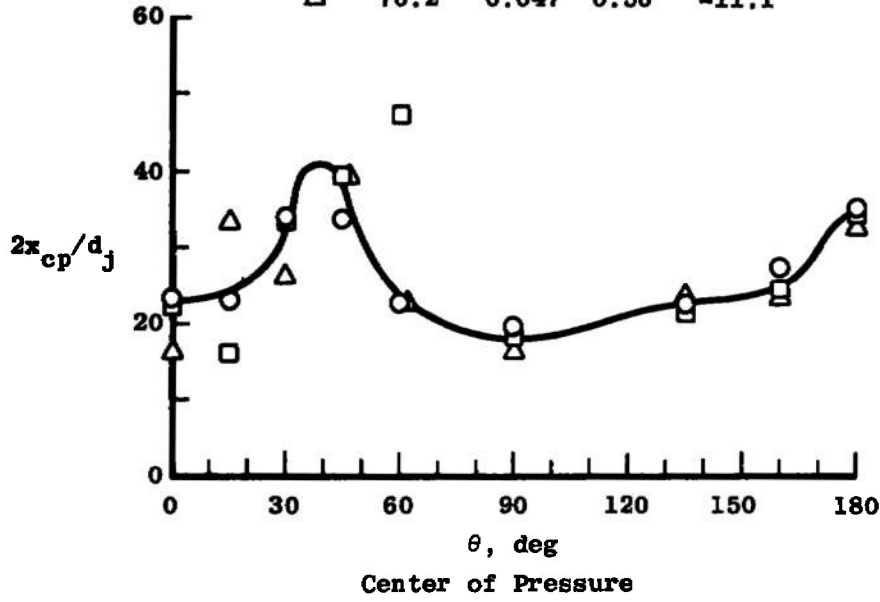
Fig. I-11 Circumferential Loading Around the Cluster Nozzle Configuration



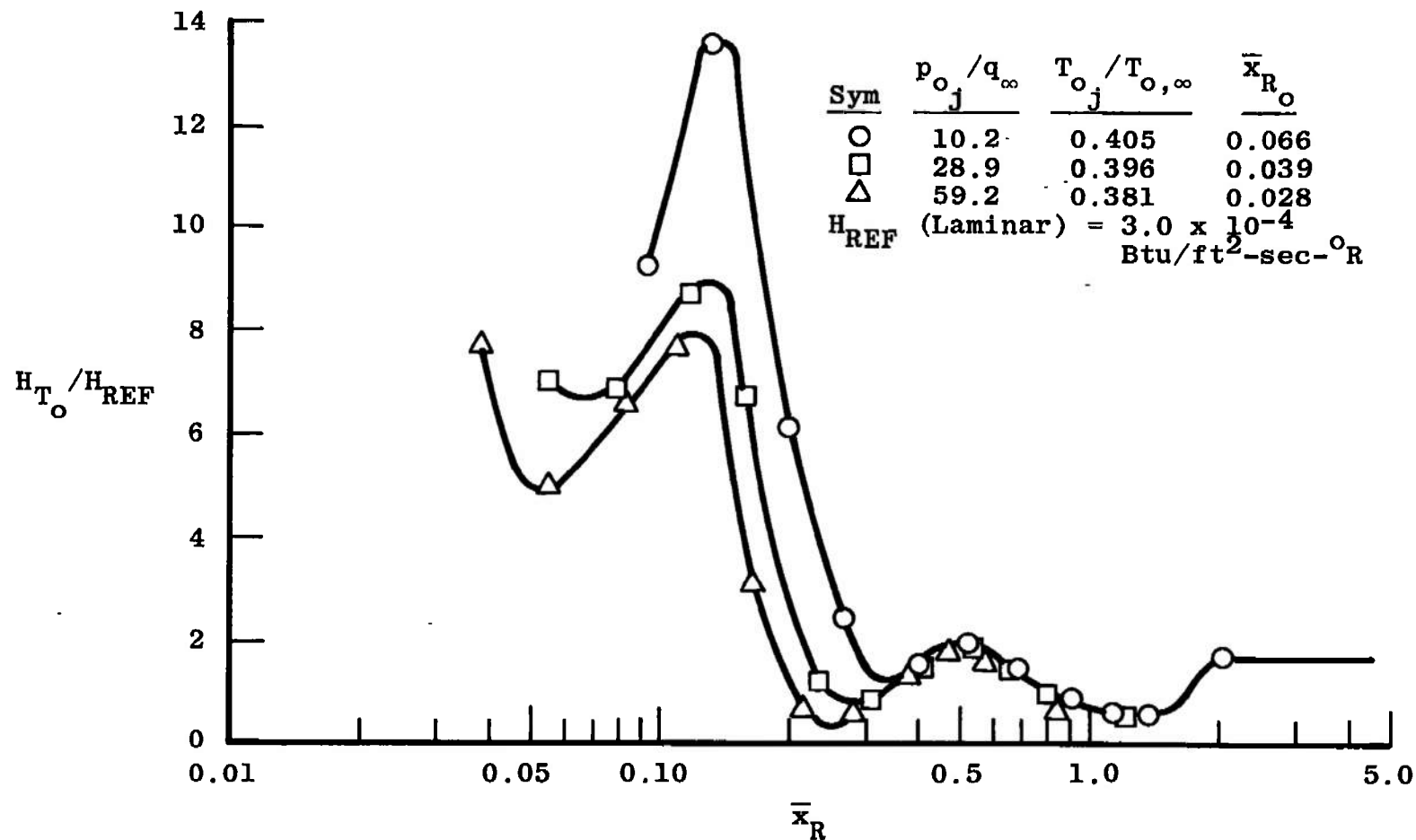
b. Angle-of-Attack Effects at $Re_\theta = 1 \times 10^6$
Fig. I-11 Continued



Sym	$p_{o,j} / q_\infty$	\bar{x}_{R_o}	F_N / F_j	$2CP / d_j$
○	366	0.011	0.12	-17.3
□	188	0.016	0.19	-13.9
△	70.2	0.047	0.50	-11.1

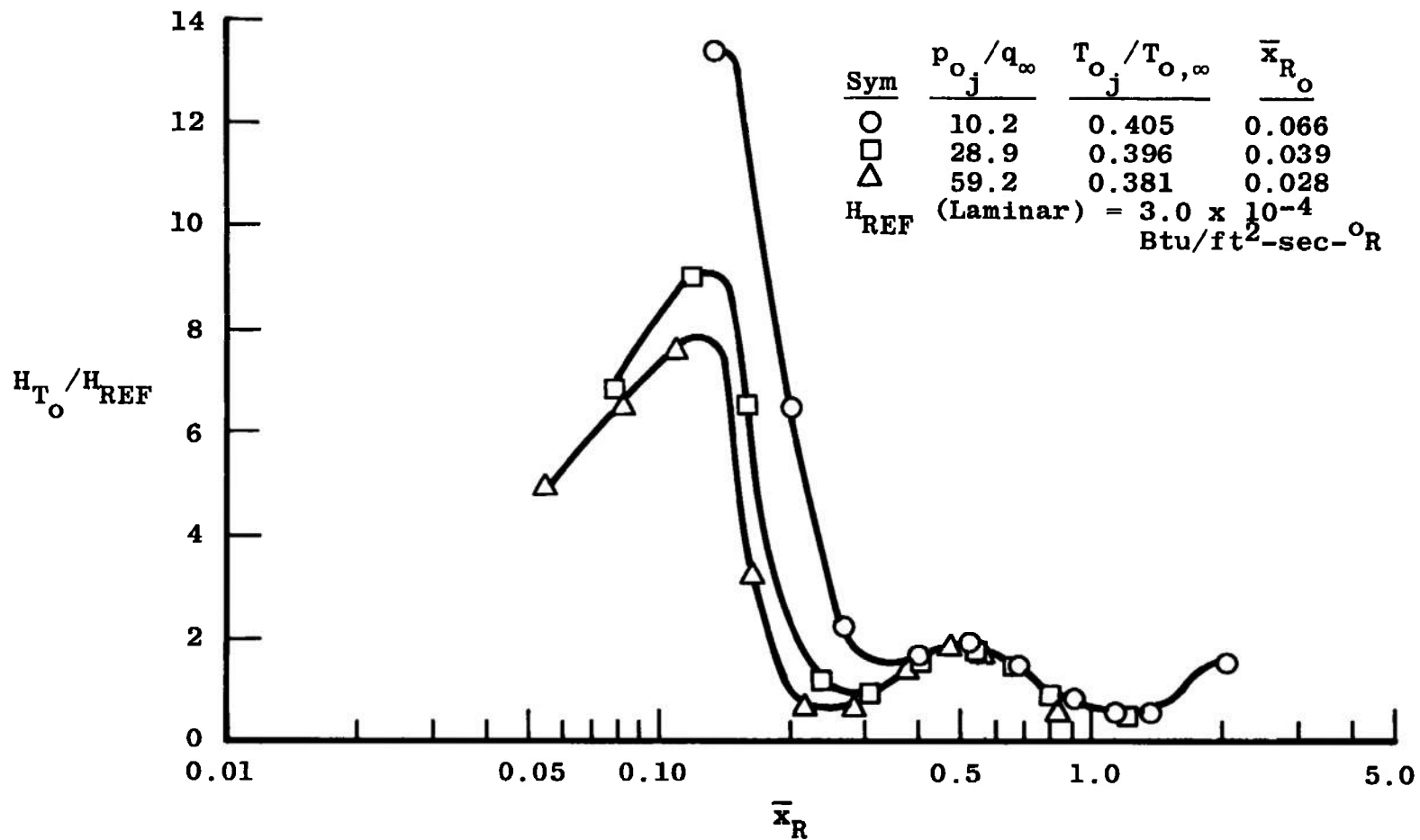


c. Jet Pressure Effects at $\alpha = 0$ and $Re_j = 1 \times 10^6$
Fig. I-11 Concluded

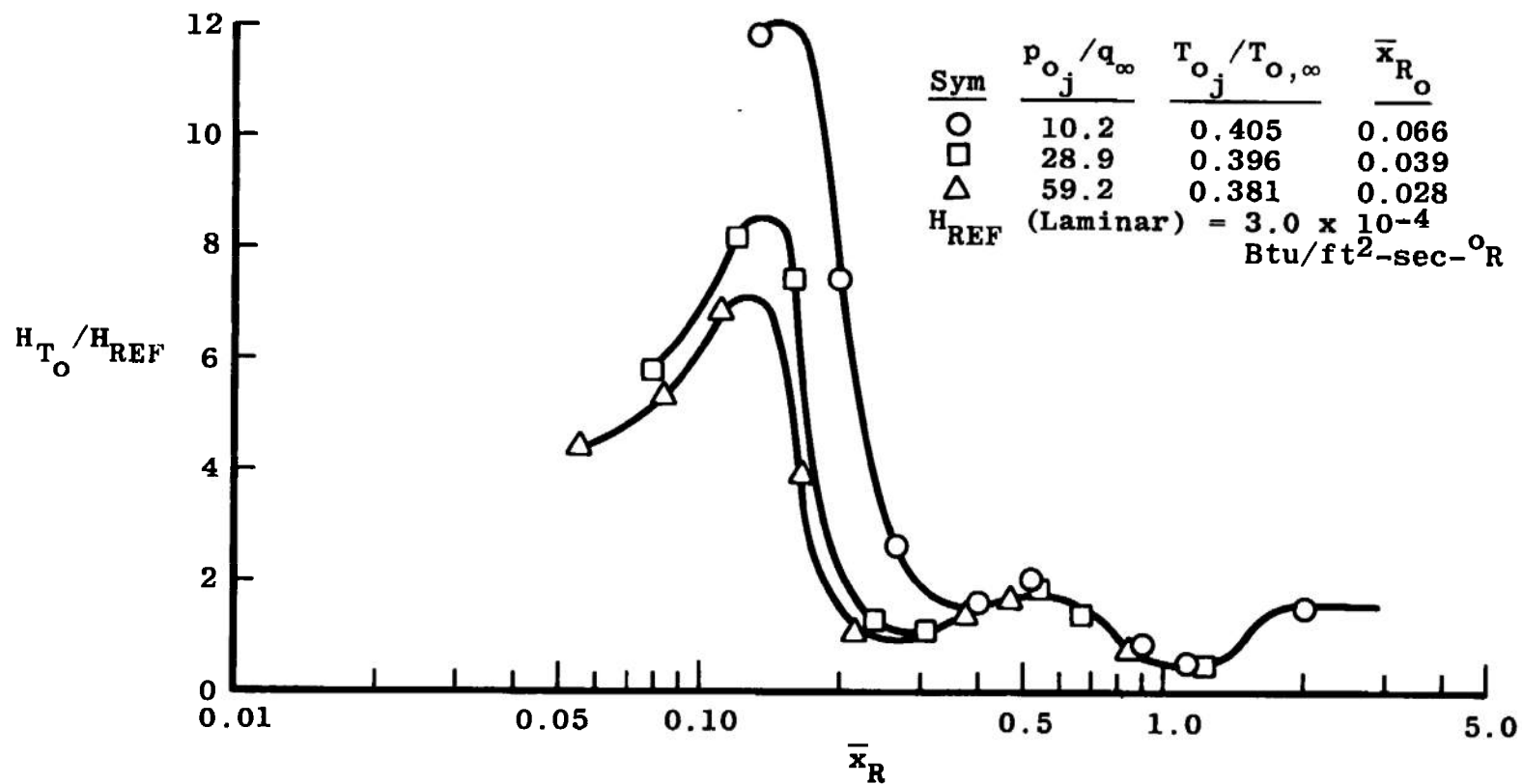


a. $\theta = 180$ deg

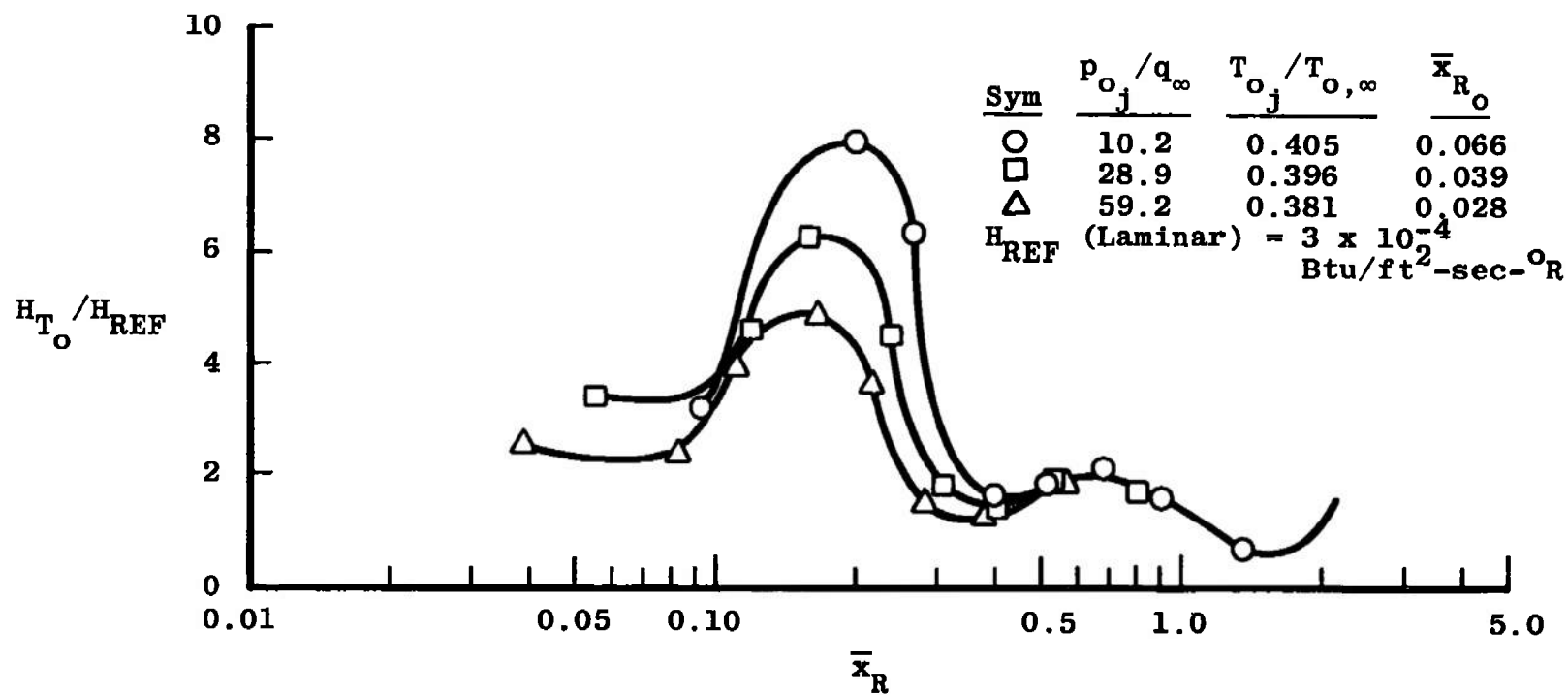
Fig. I-12 Jet Stagnation Pressure Effect on the Heat-Transfer-Rate Distributions on a Flat Plate Around a Supersonic Nozzle, $M_j = 2.54$, $d_j = 0.50$ in., $T_{o_j}/T_{o,\infty} \cong 0.4$, $\alpha = 0$, $M_\infty = 8.0$, and $Re_j = 5 \times 10^6$



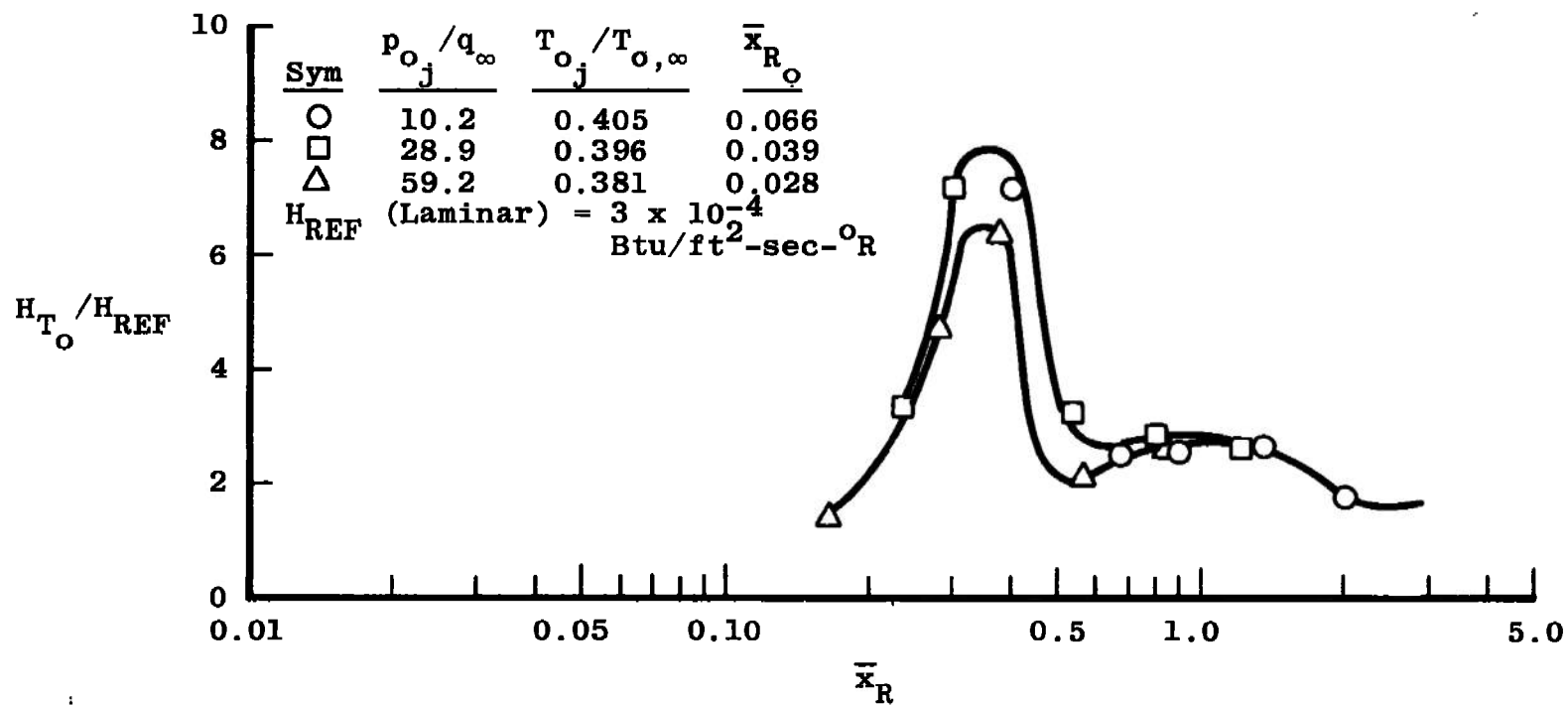
b. $\theta = 160$ deg
Fig. I-12 Continued



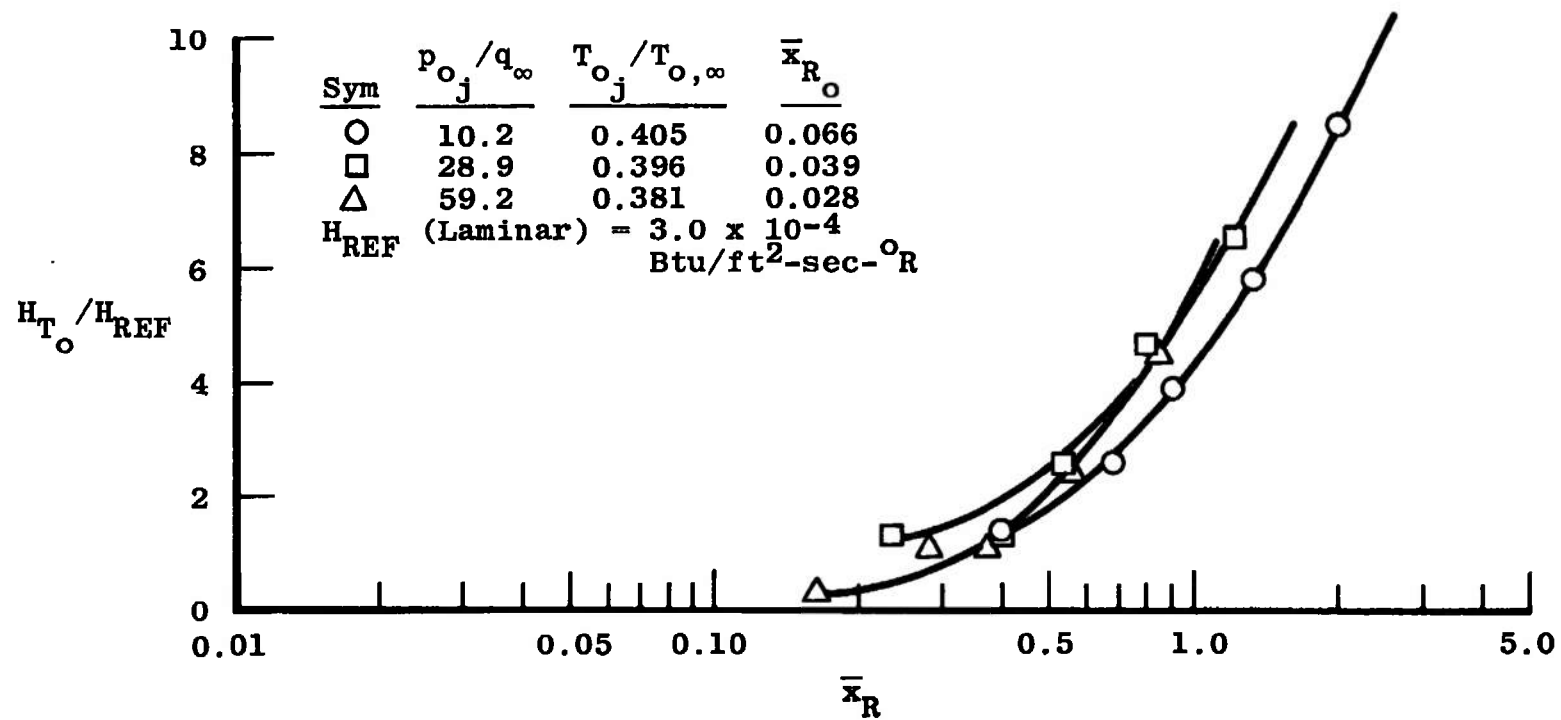
c. $\theta = 135$ deg
Fig. I-12 (Continued)



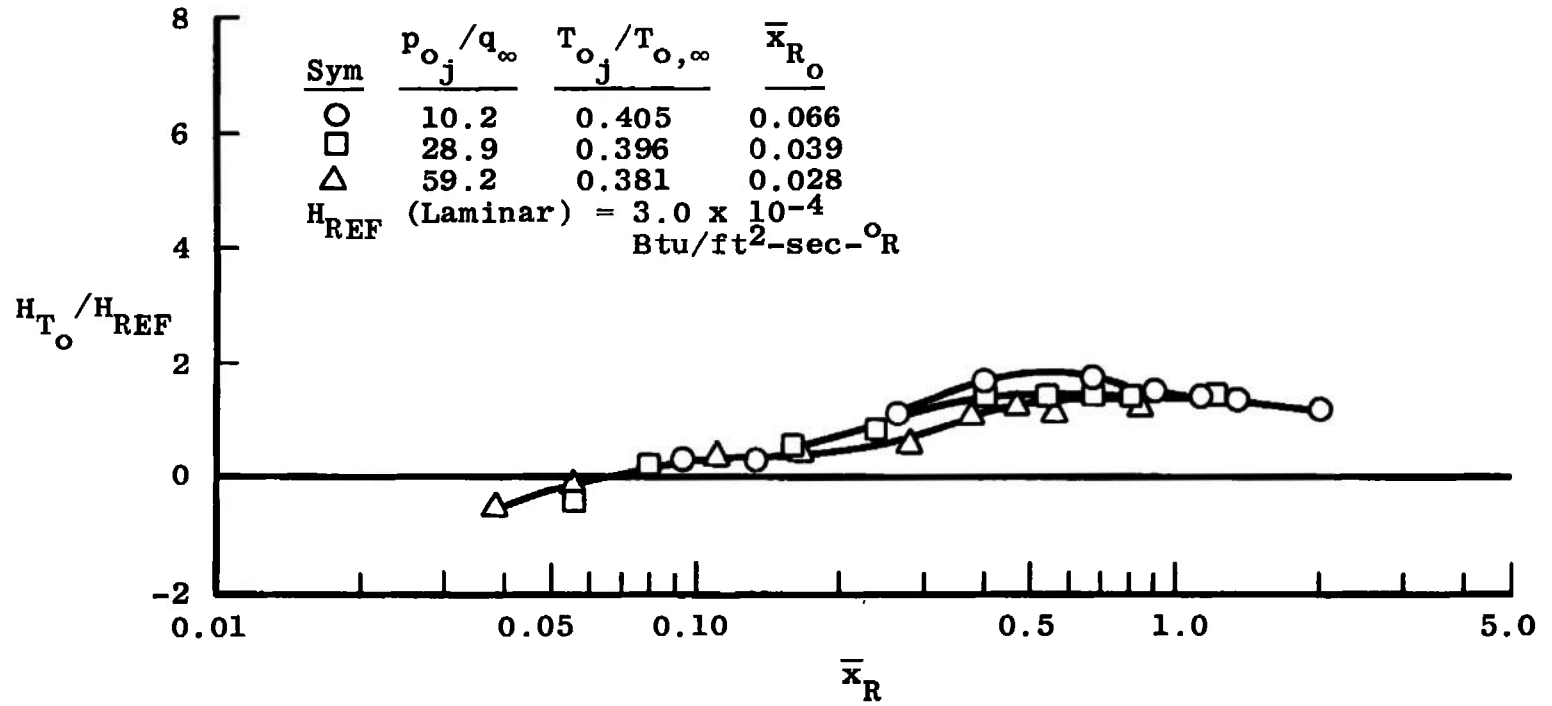
d. $\theta = 90^\circ$
Fig. I-12 Continued



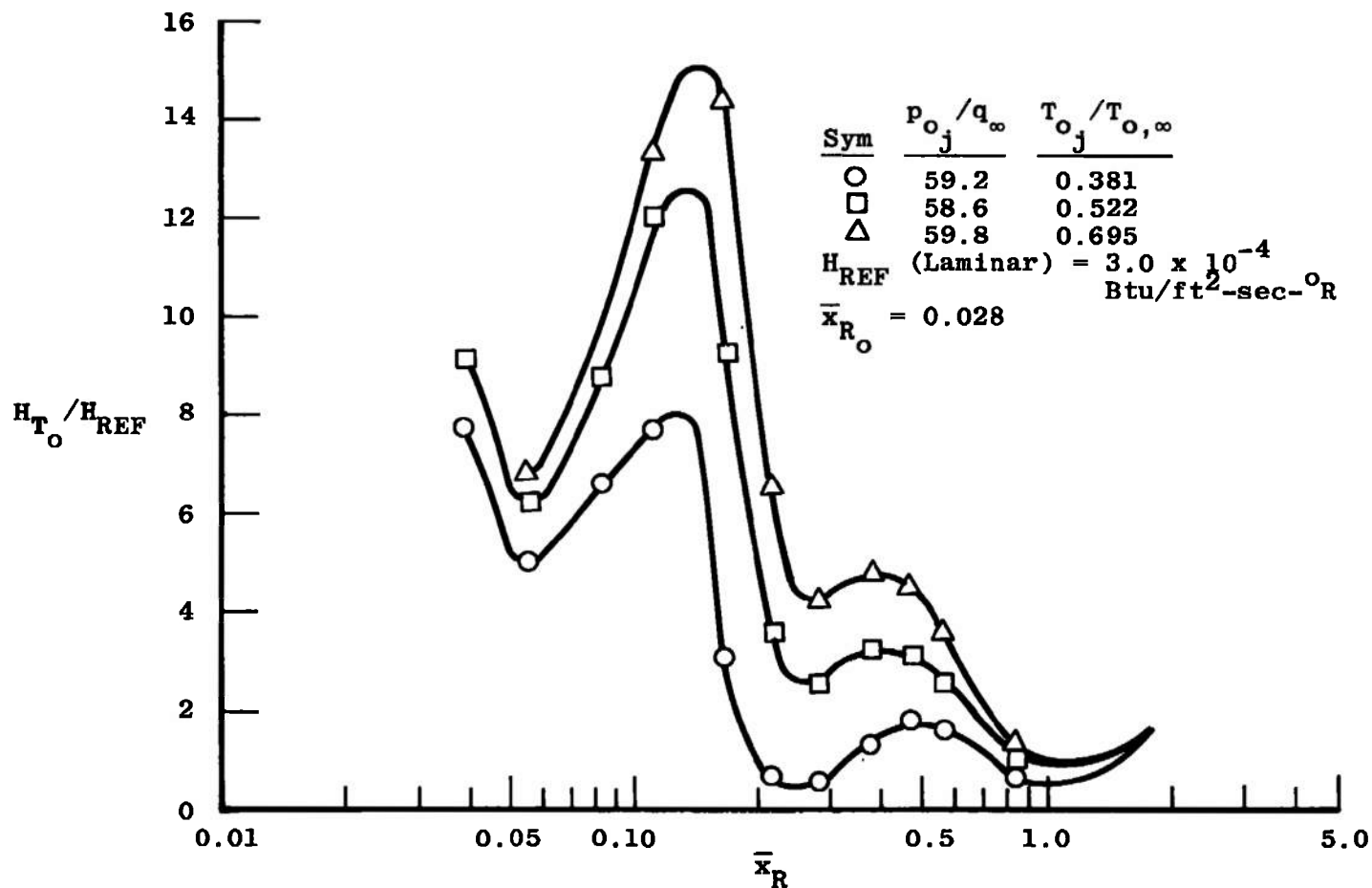
e. $\theta = 45$ deg
Fig. 1-12 Continued



f. $\theta = 15$ deg
Fig. I-12 Continued

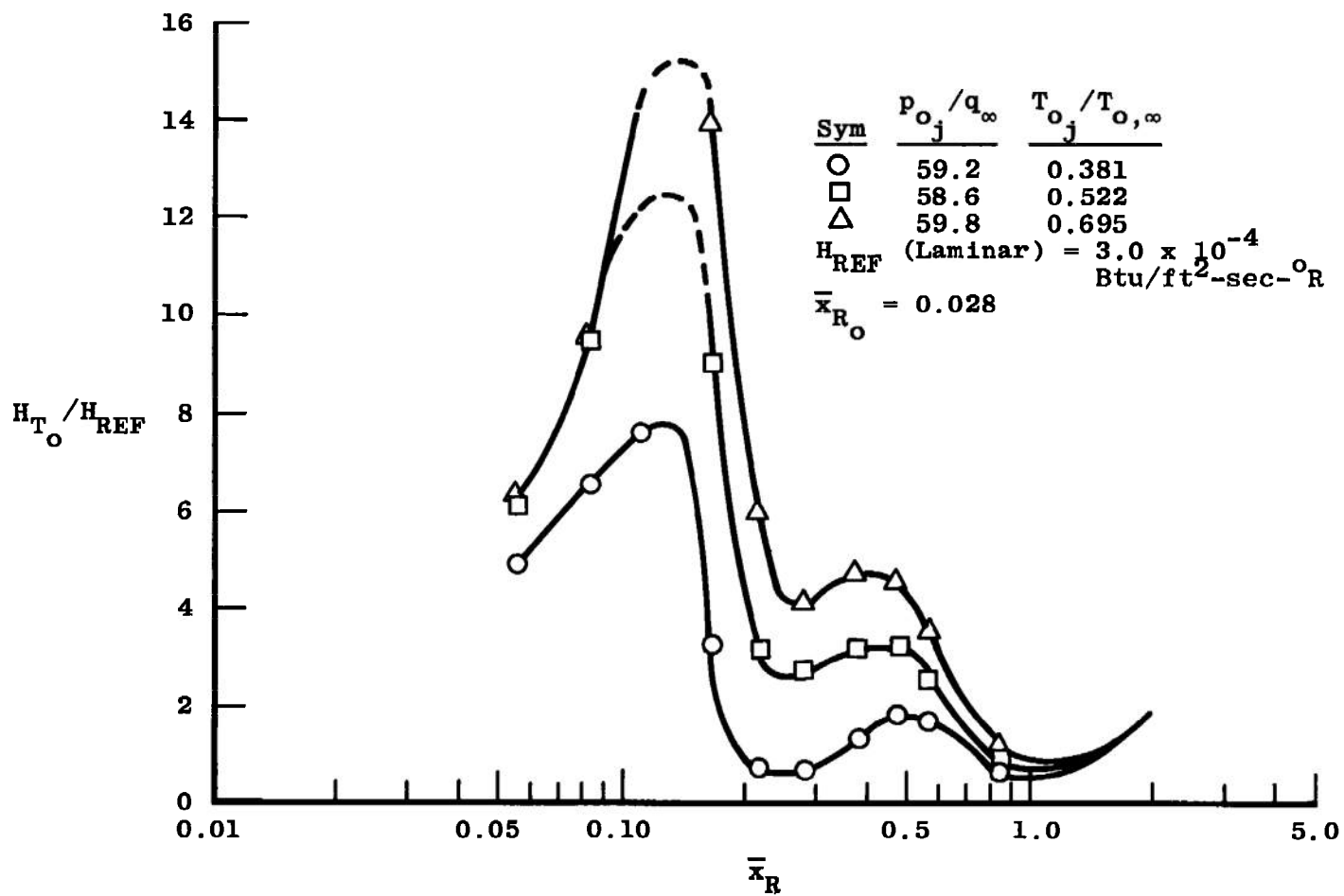


g. $\theta = 0$
Fig. I-12 Concluded

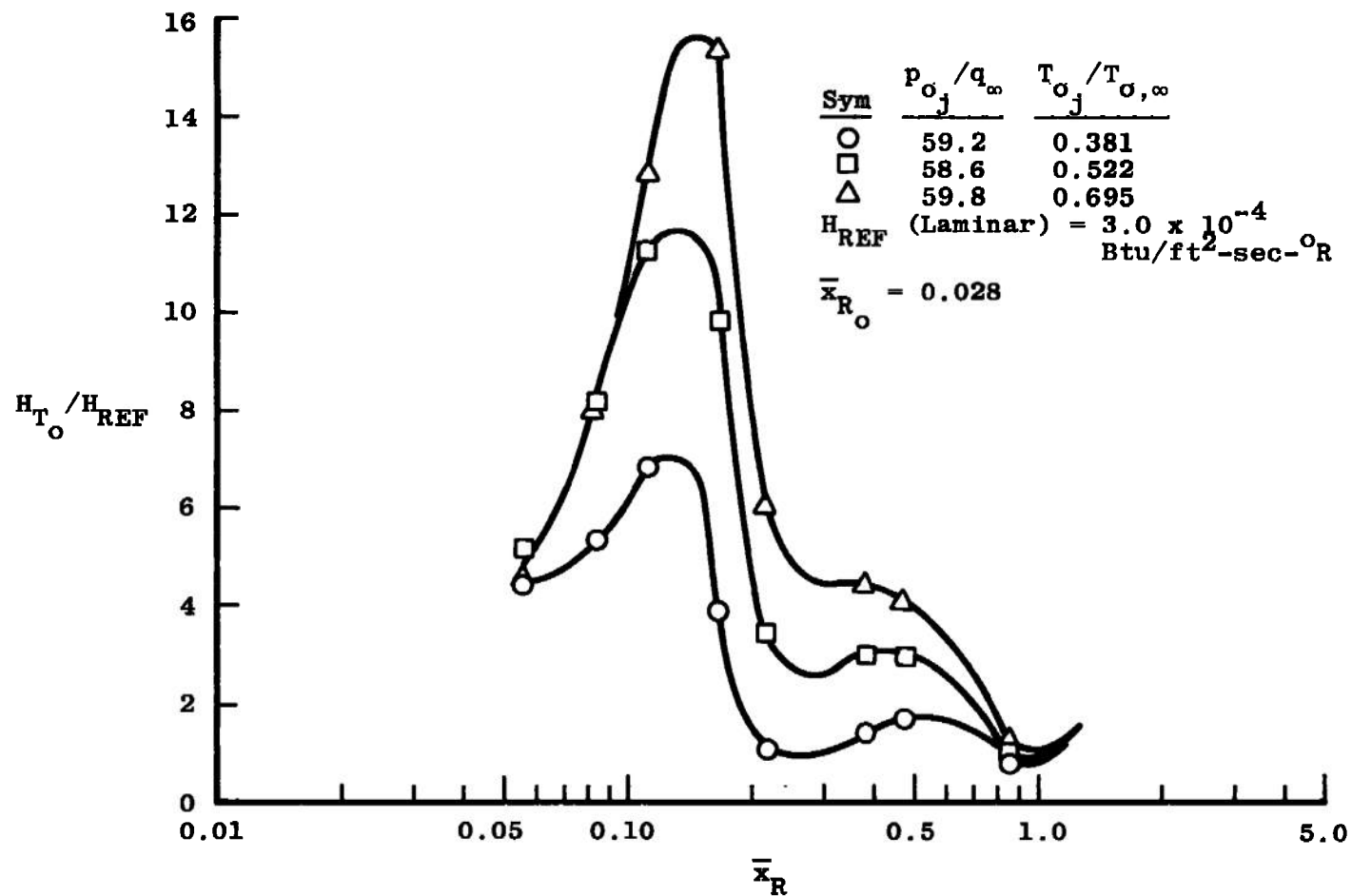


a. $\theta = 180 \text{ deg}$

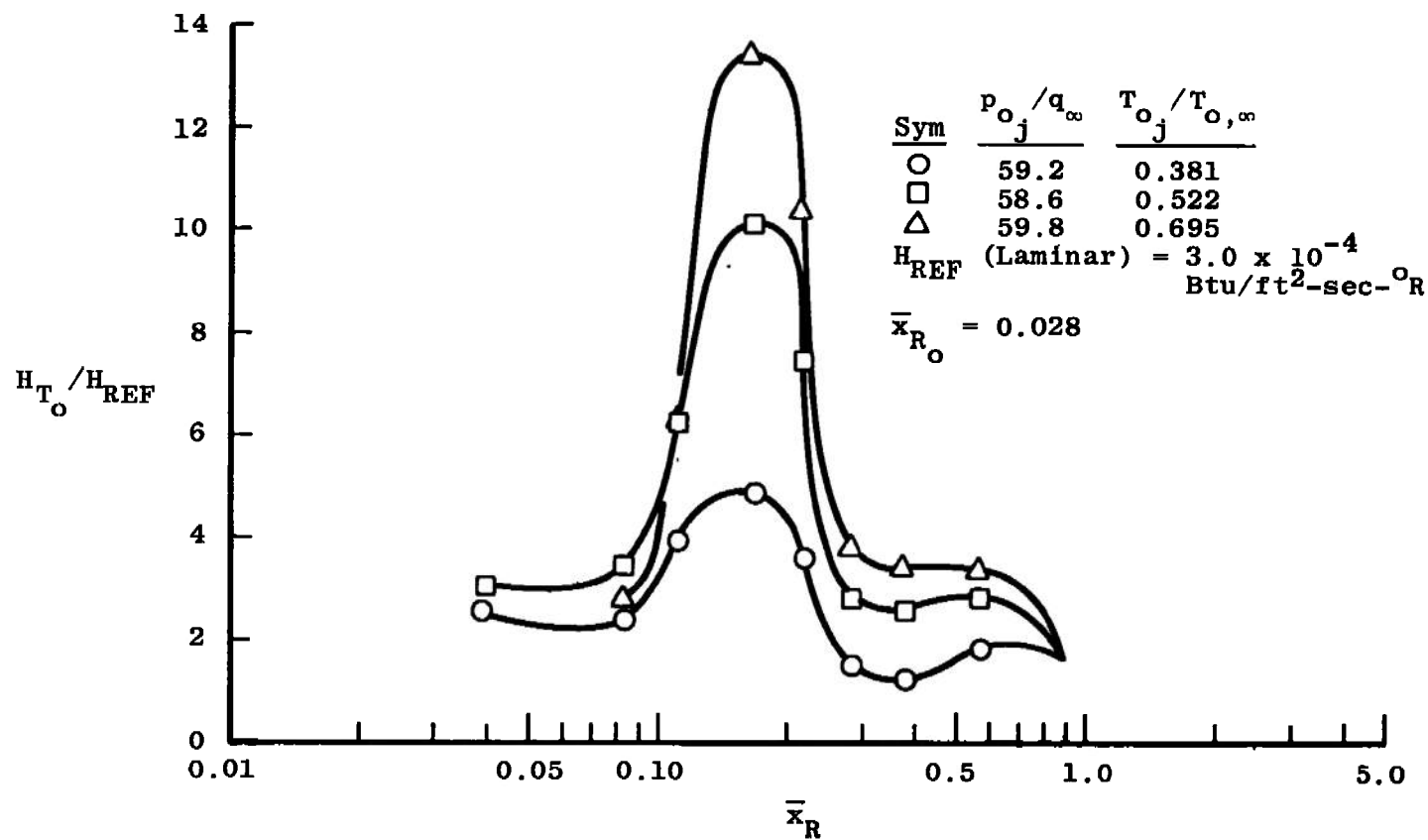
Fig. I-13 Jet Stagnation Temperature Effect on the Heat-Transfer-Rate Distributions on a Flat Plate Around a Supersonic Nozzle, $M_j = 2.54$, $d_j = 0.50 \text{ in.}$, $p_{o,j}/q_\infty \cong 59$, $\alpha = 0$, $M_\infty = 8.0$, and $Re_\ell = 5 \times 10^6$



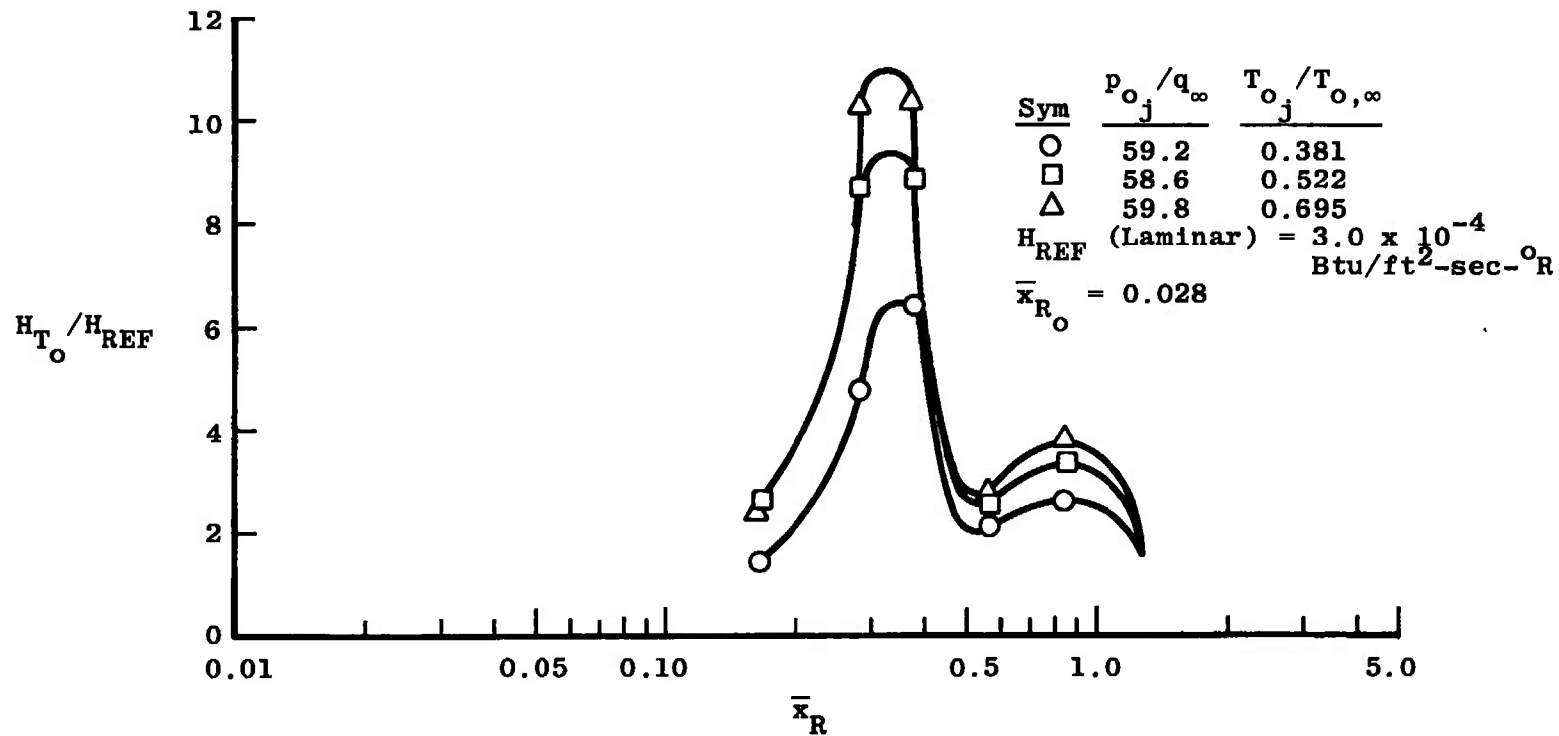
b. $\theta = 160 \text{ deg}$
 Fig. I-13 Continued



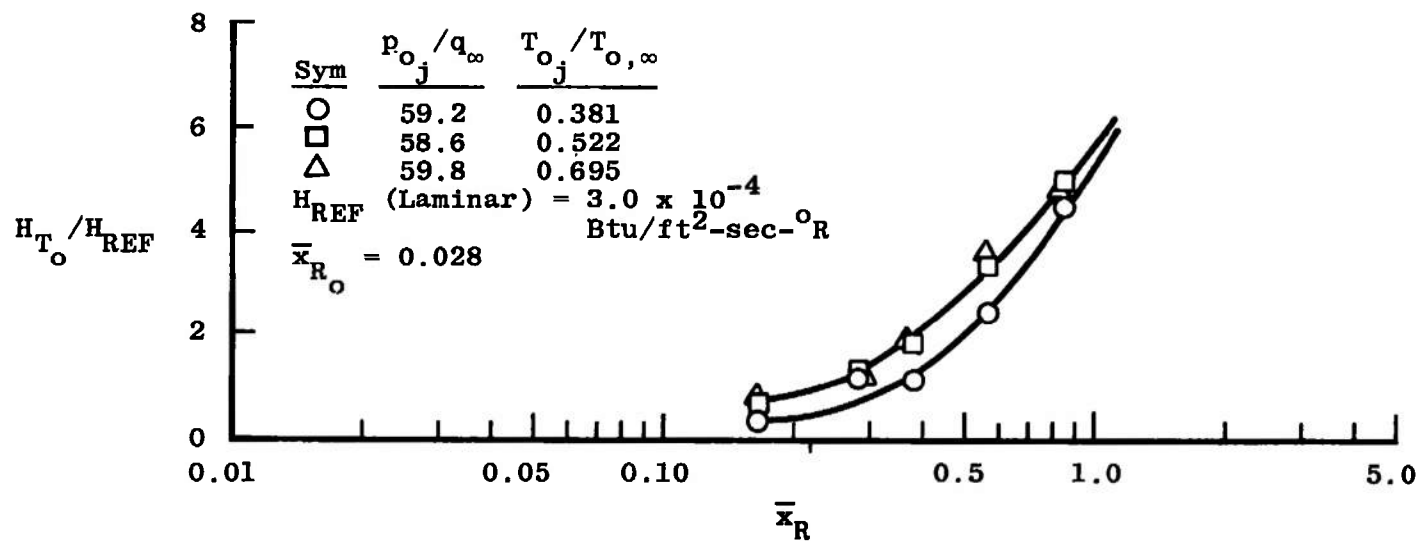
c. $\theta = 135 \text{ deg}$
 Fig. I-13 Continued



d. $\theta = 90 \text{ deg}$
 Fig. I-13 Continued



e. $\theta = 45^\circ$
Fig. 1-13 Continued



f. $\theta = 15 \text{ deg}$
 Fig. I-13 Continued

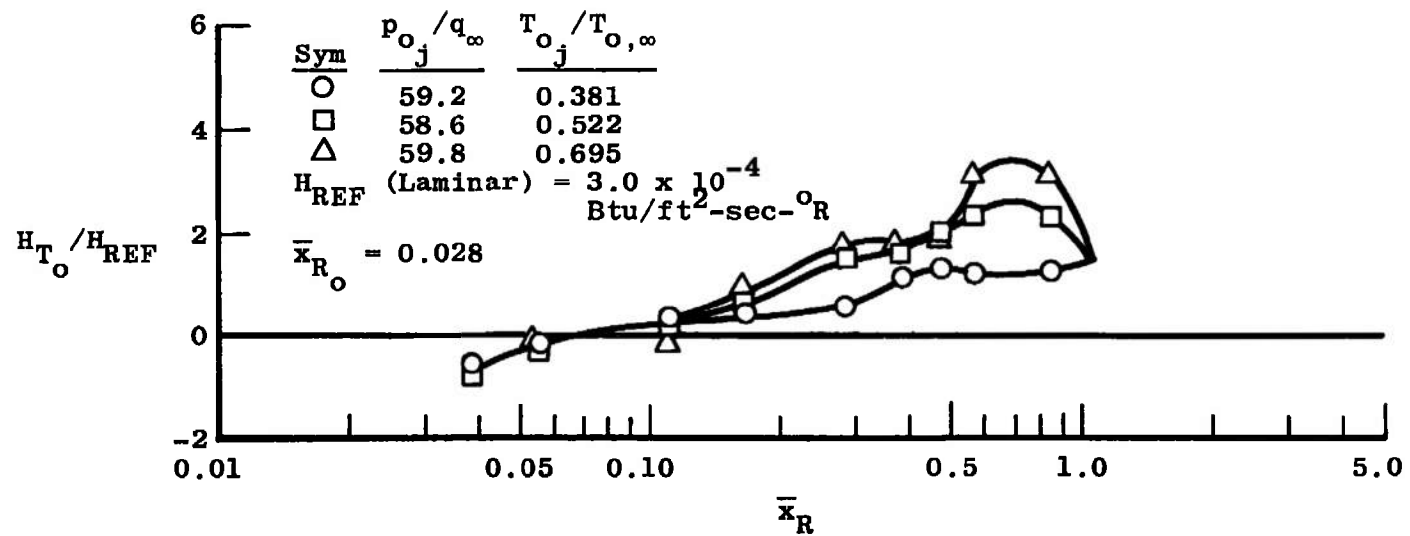
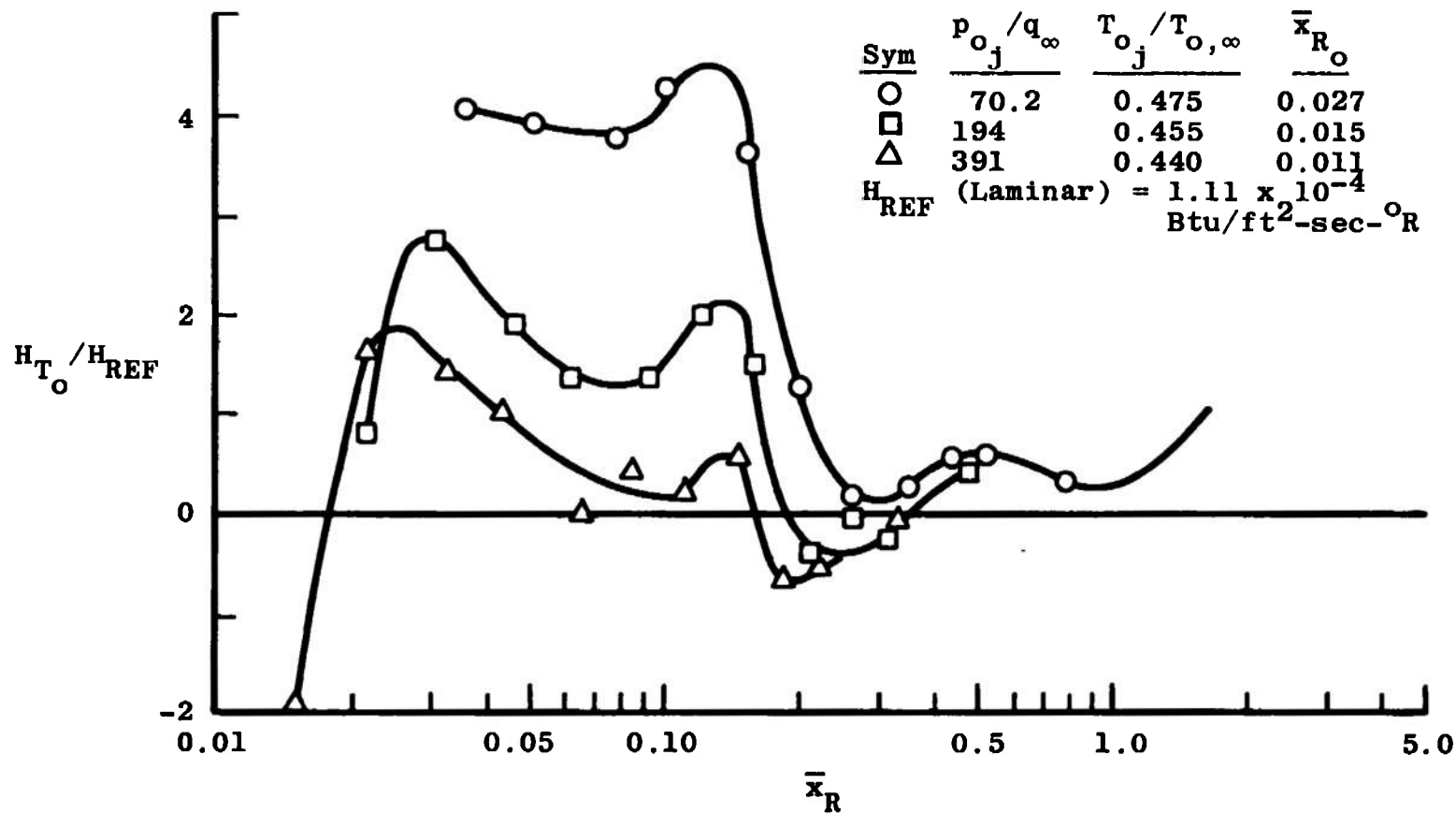
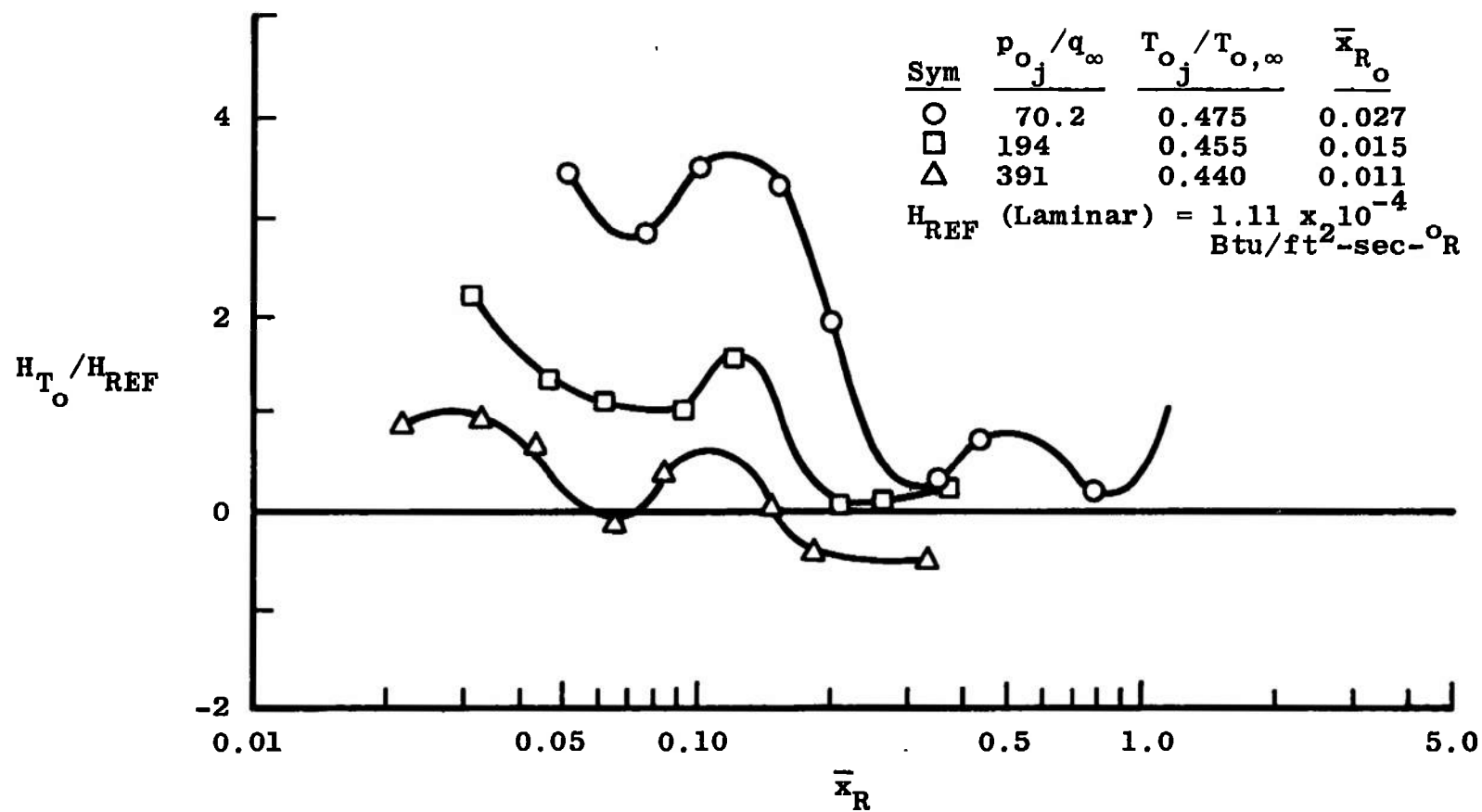
g. $\theta = 0$

Fig. I-13 Concluded

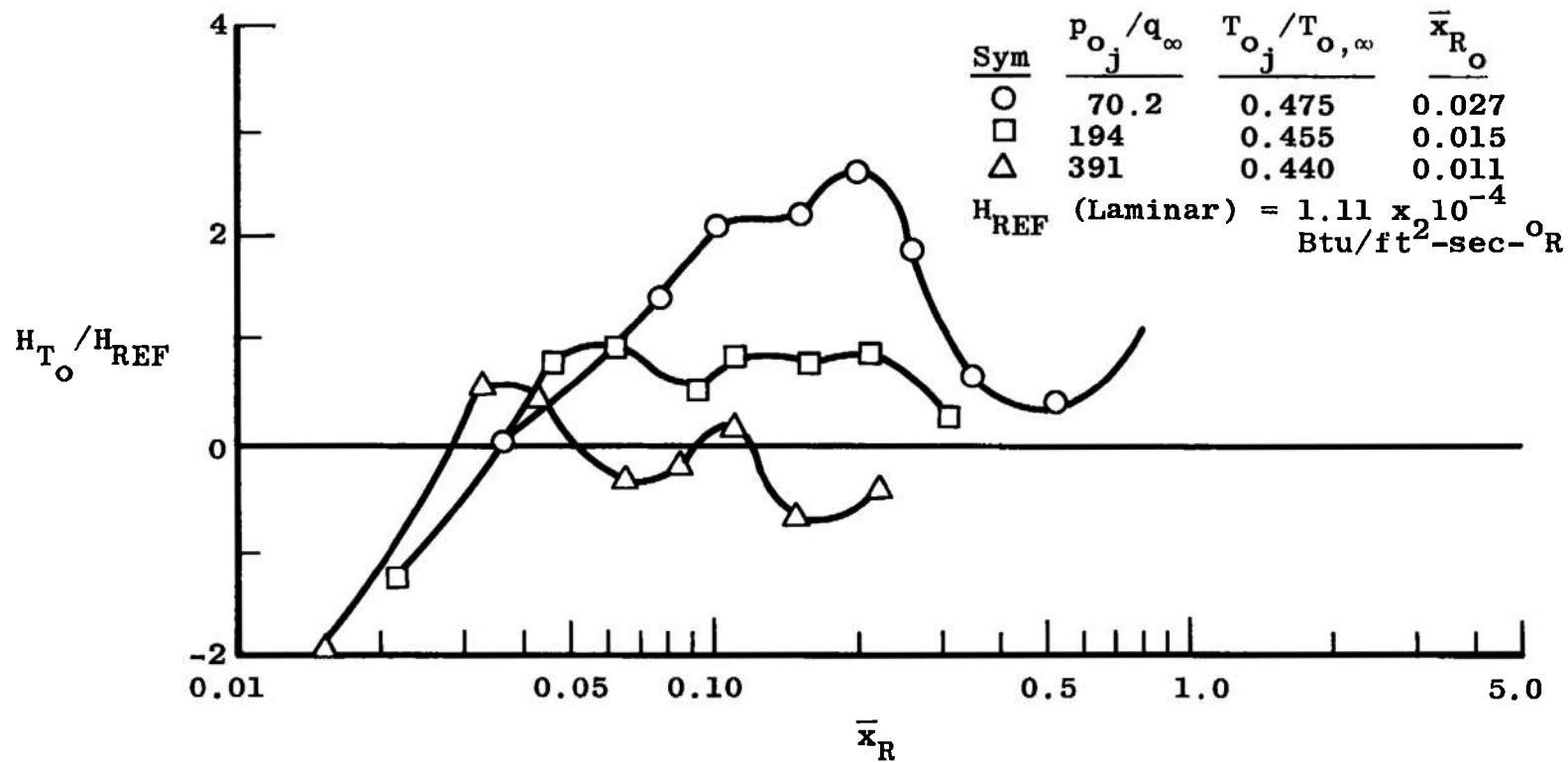


a. $\theta = 180$ deg

Fig. I-14 Heat-Transfer-Rate Distributions on a Flat Plate at $\alpha = 0$ Around a Supersonic Lateral Jet Nozzle, $M_j = 2.54$, $d_j = 0.50$ in., $T_{o,j}/T_{o,\infty} \cong 0.45$, $M_{\infty} = 7.9$, and $Re_{\theta} = 1 \times 10^6$



b. $\theta = 135 \text{ deg}$
 Fig. I-14 Continued



c. $\theta = 90 \text{ deg}$
Fig. I-14 Continued

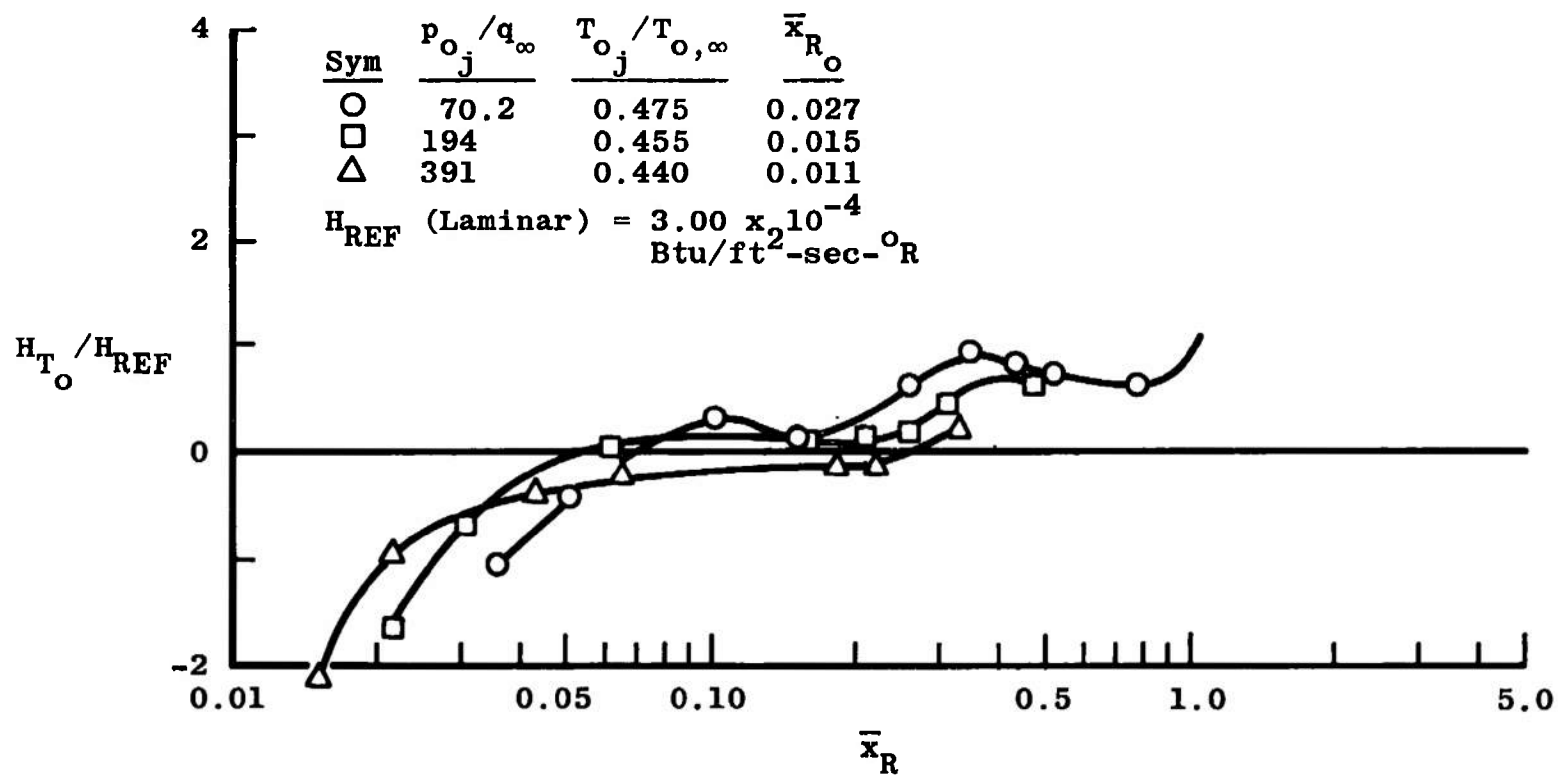
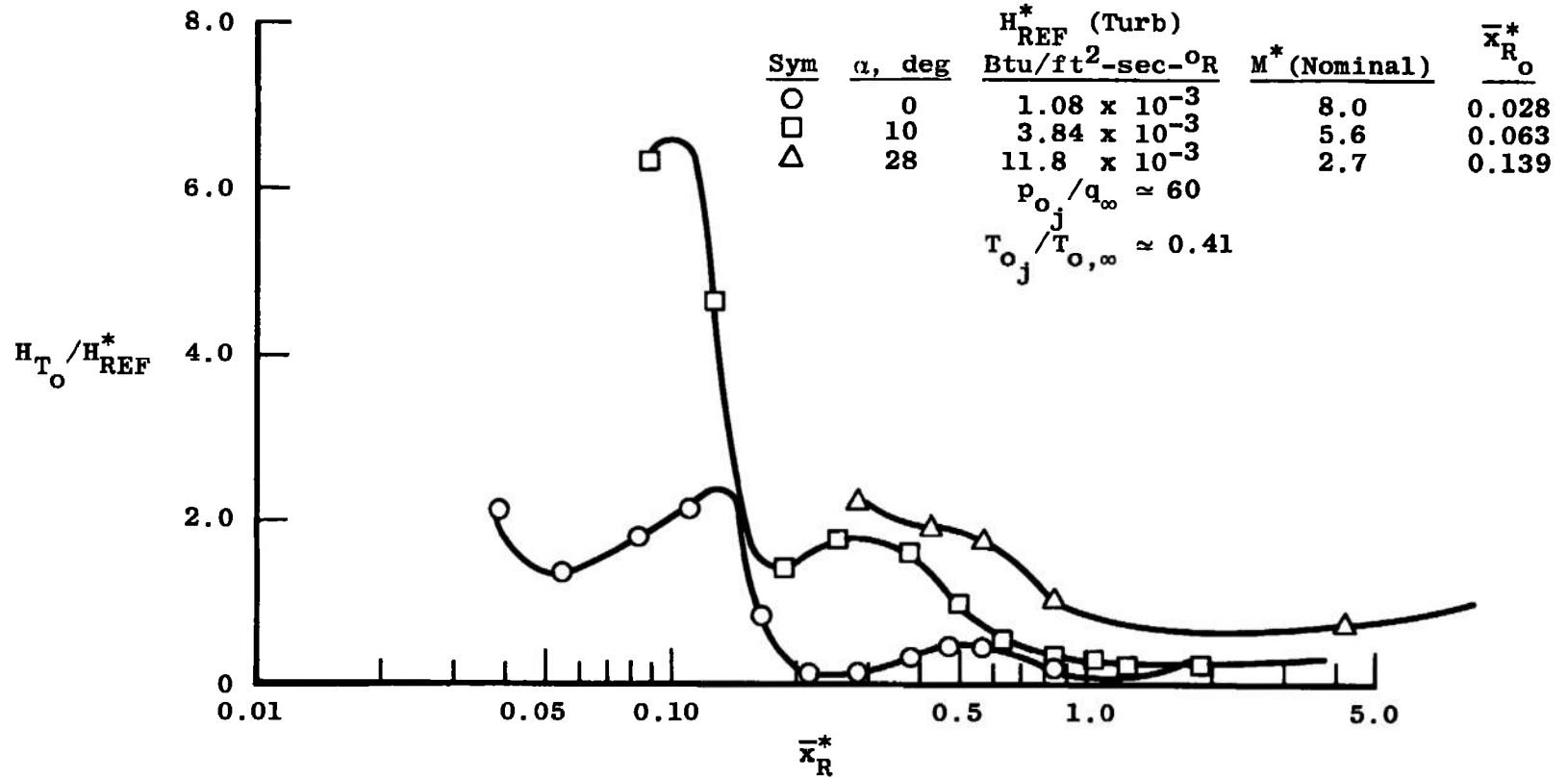
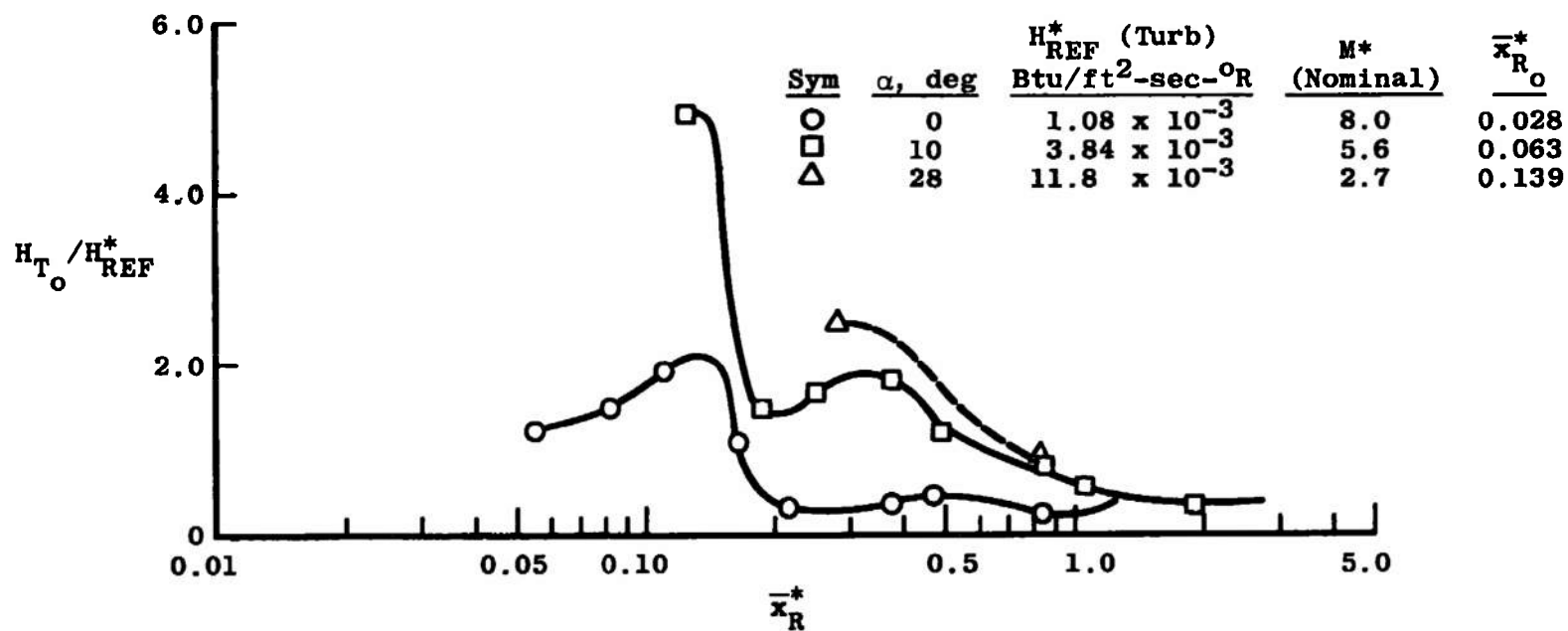
d. $\theta = 0$

Fig. I-14 Concluded

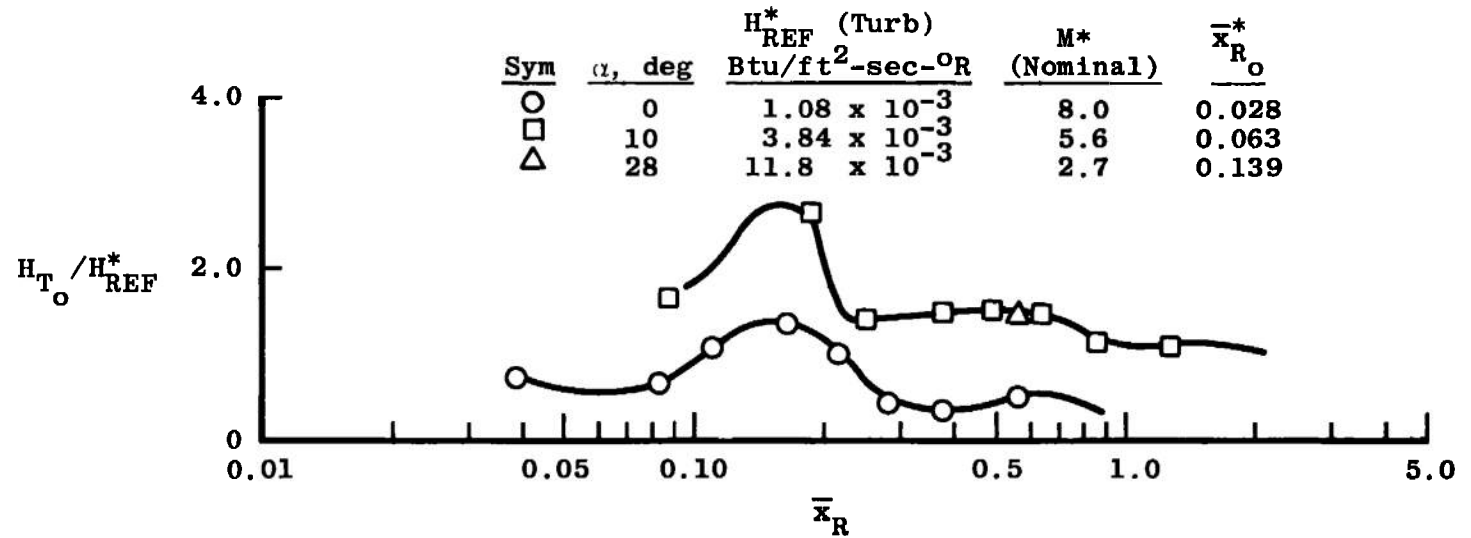


a. $\theta = 180$ deg

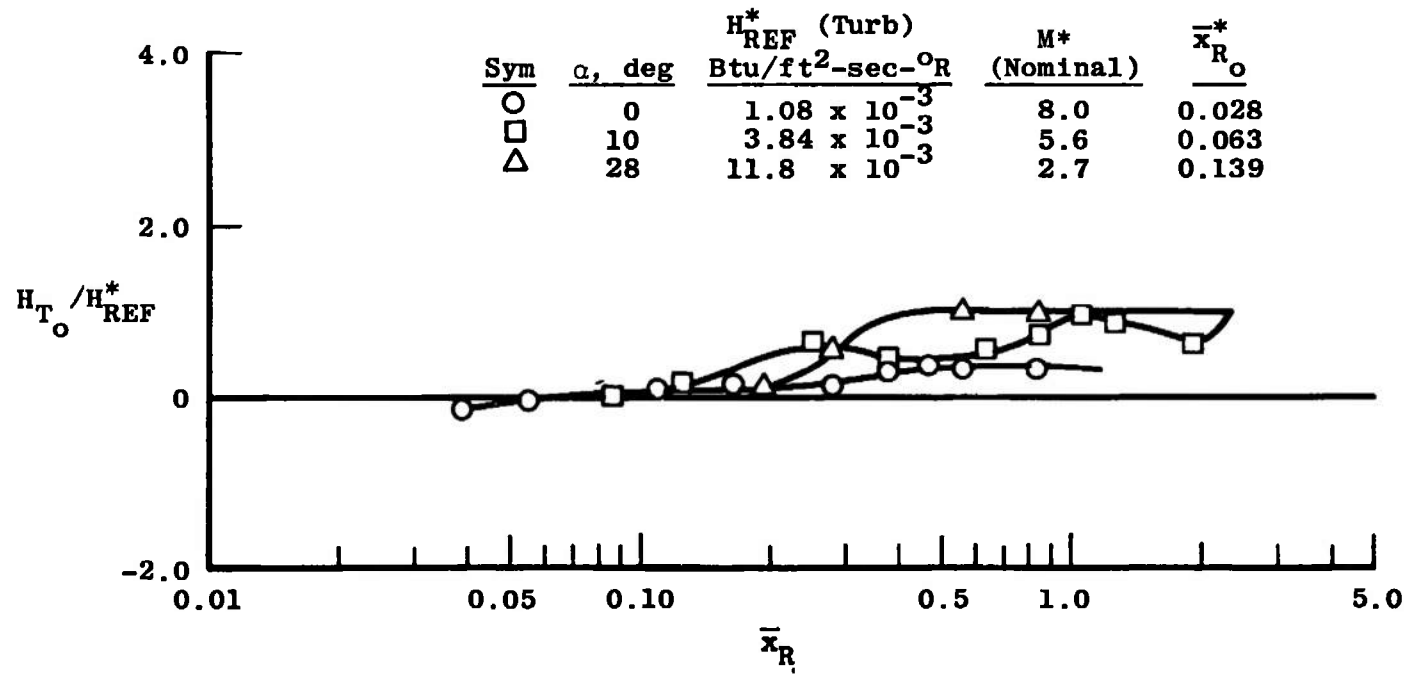
Fig. I-15 Angle-of-Attack Effects on the Flat Plate Heat-Transfer-Rate Distributions Around a Supersonic Lateral Jet Nozzle, $M_j = 2.54$, $d_j = 0.50$ in., $M_\infty = 8.0$, and $Re_l = 5 \times 10^6$



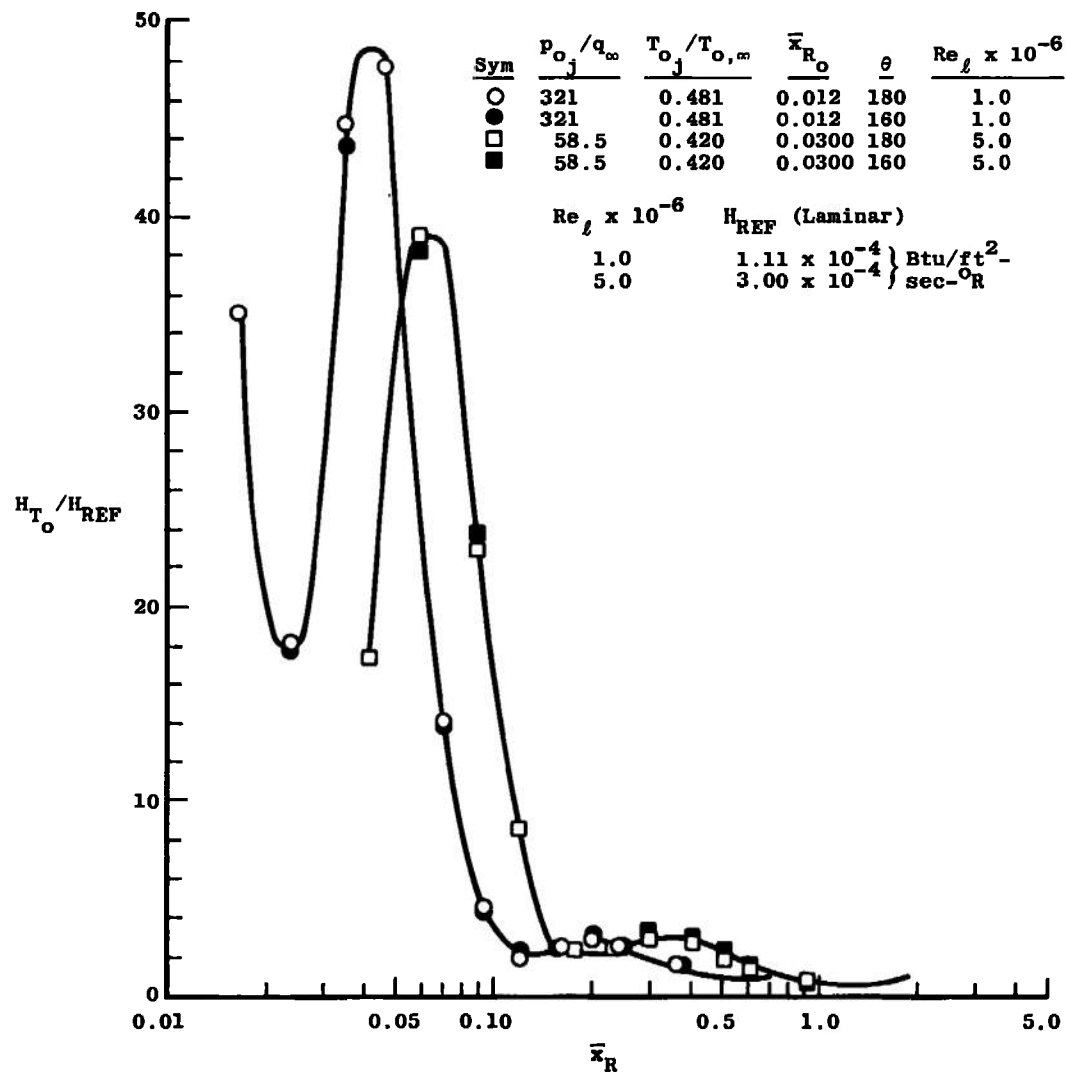
b. $\theta = 135$ deg
Fig. 1-15 Continued



c. $\theta = 90$ deg
Fig. I-15 Continued

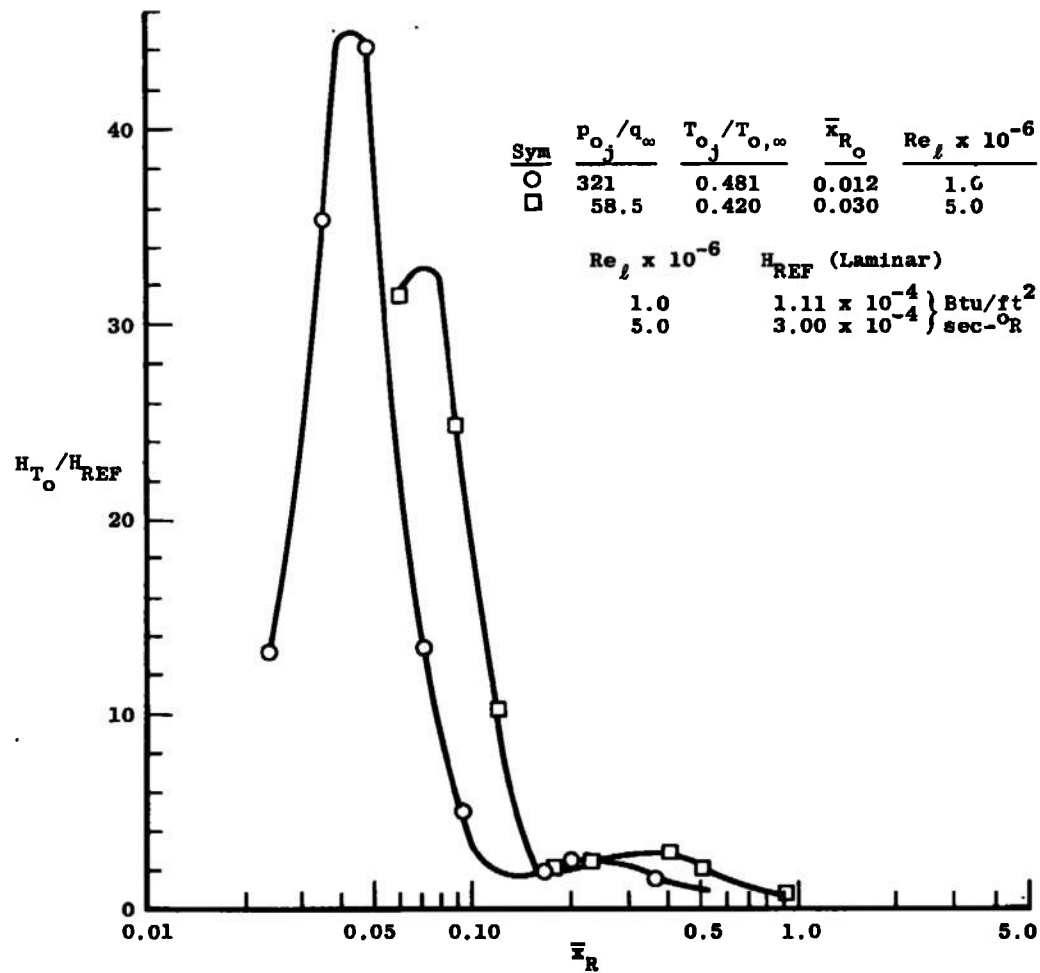


d. $\theta = 0$
Fig. I-15 Concluded

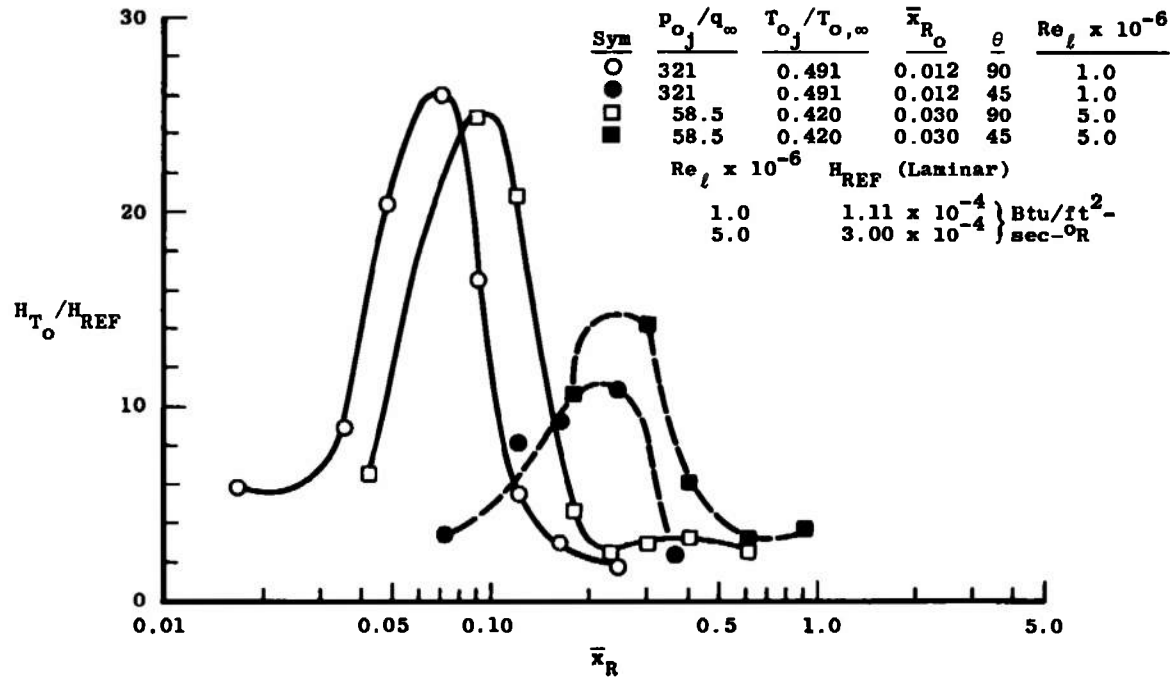


a. $\theta = 160$ and 180 deg

Fig. I-16 Heat-Transfer-Rate Distributions on a Flat Plate Around a Helium Jet from a Supersonic Nozzle, $M_j = 2.86$, $d_j = 0.50$ in., $\alpha = 0$, and M_∞ (Nominal) = 8.0



b. $\theta = 135^\circ$
Fig. I-16 Continued



c. $\theta = 45$ and 90 deg
Fig. I-16 Continued

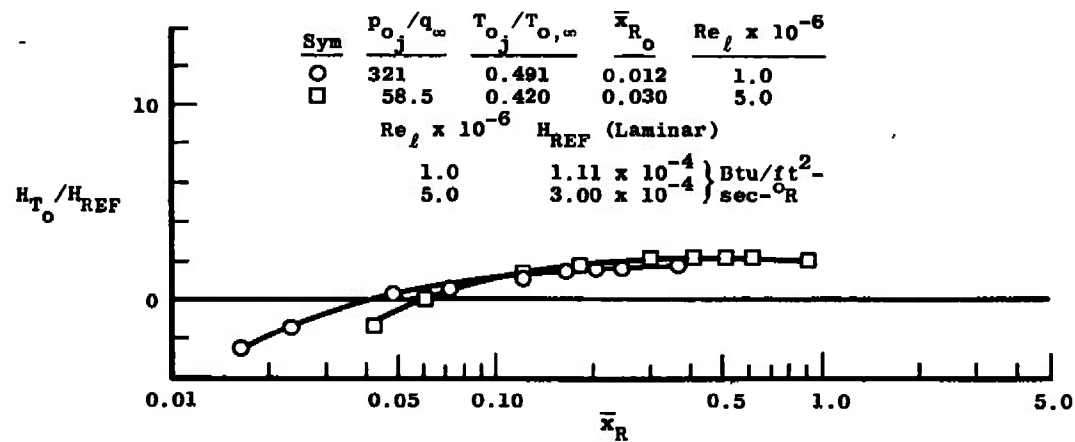
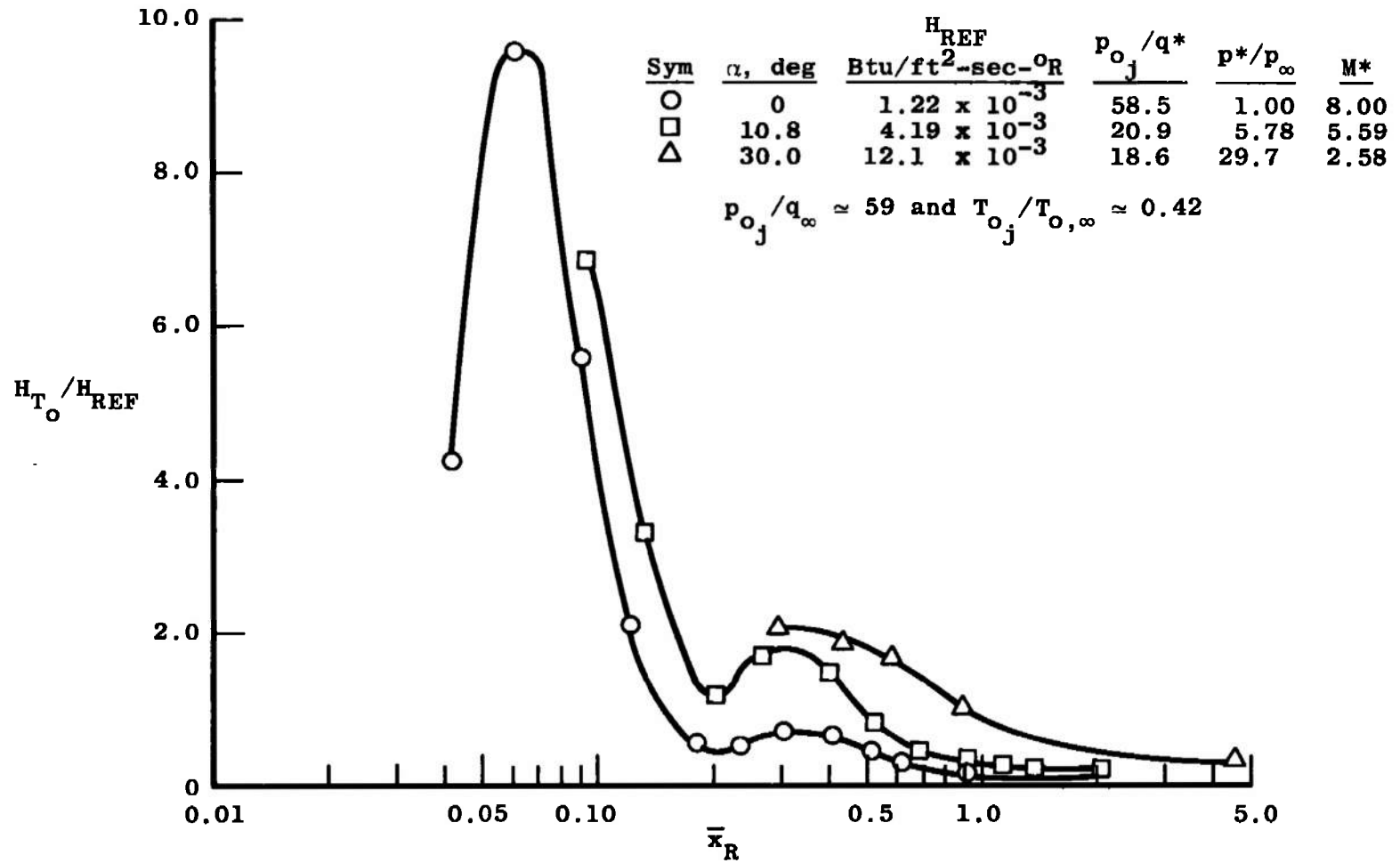
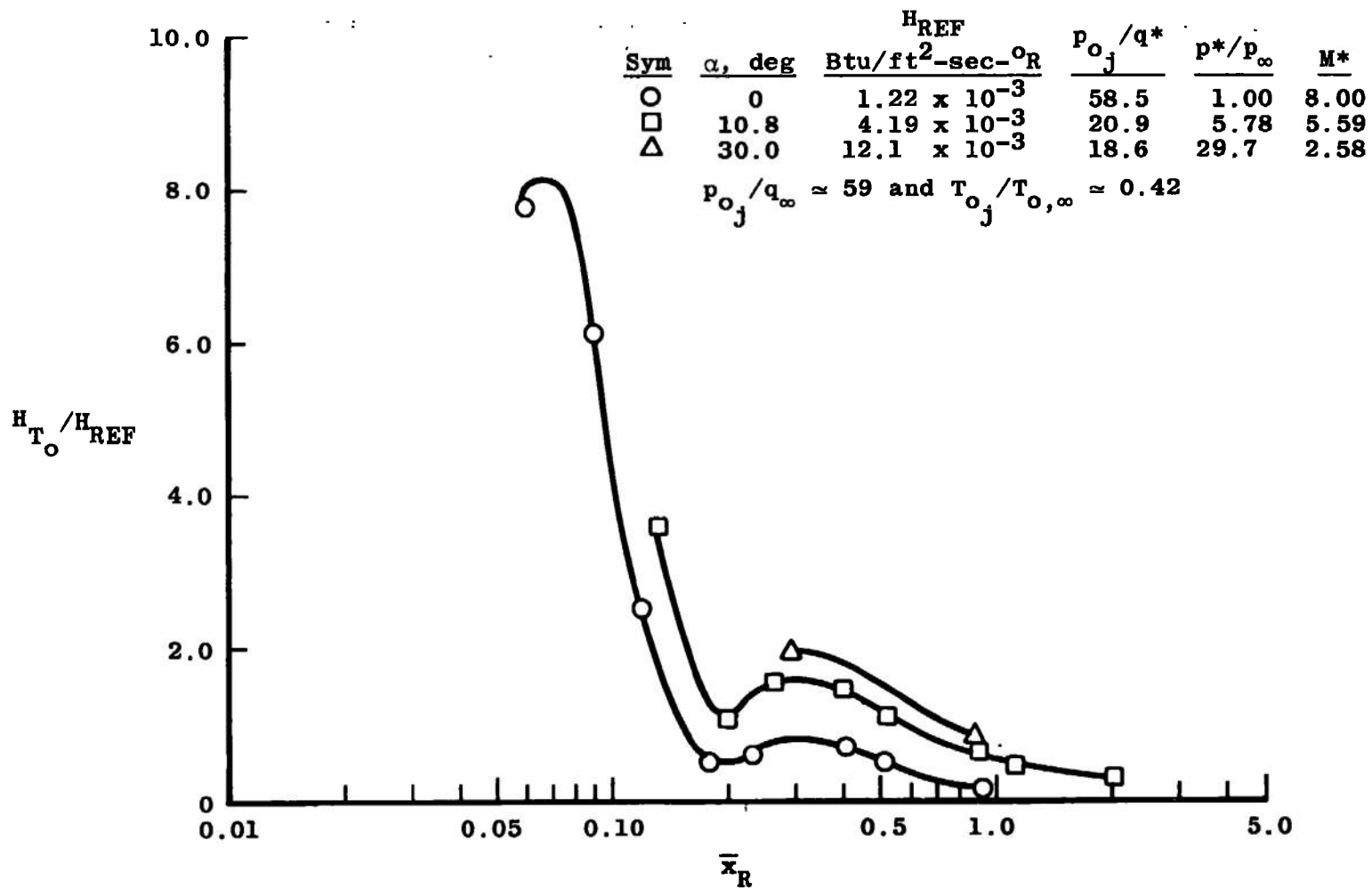
d. $\theta = 0$

Fig. I-16 Concluded

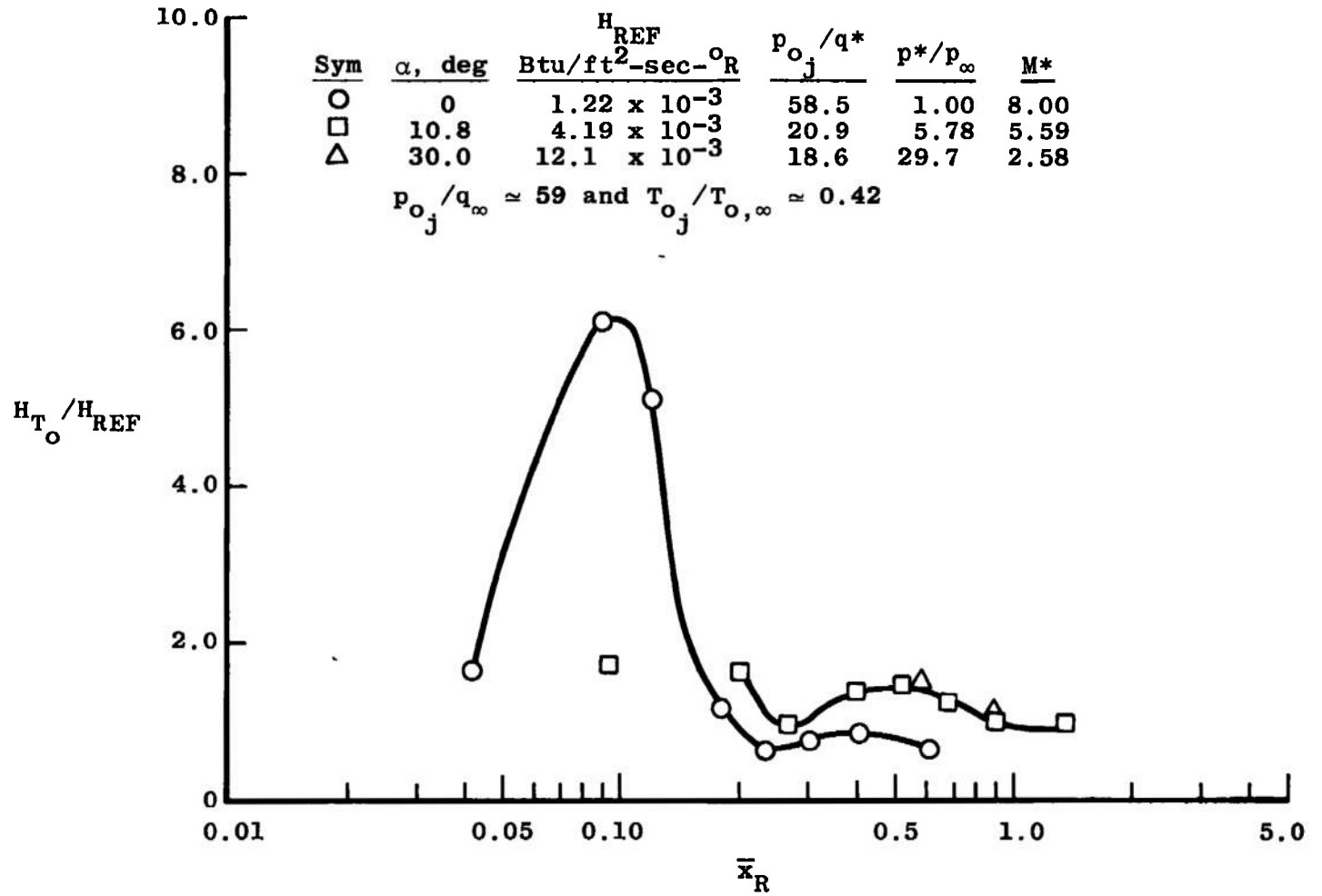


a. $\theta = 180$ deg

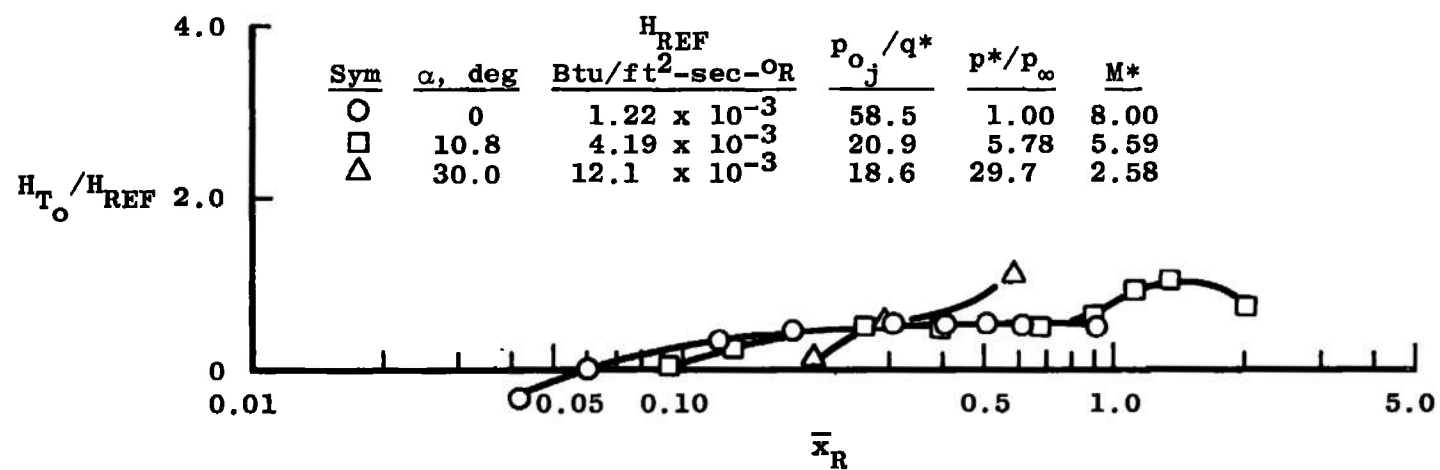
Fig. I-17 Angle-of-Attack Effects on the Heat-Transfer-Rate Distributions on a Flat Plate Around a Helium Jet from a Supersonic Nozzle, $M_j = 2.86$, $d_j = 0.50$ in., $M_\infty = 8.0$, and $Re_L = 5 \times 10^6$



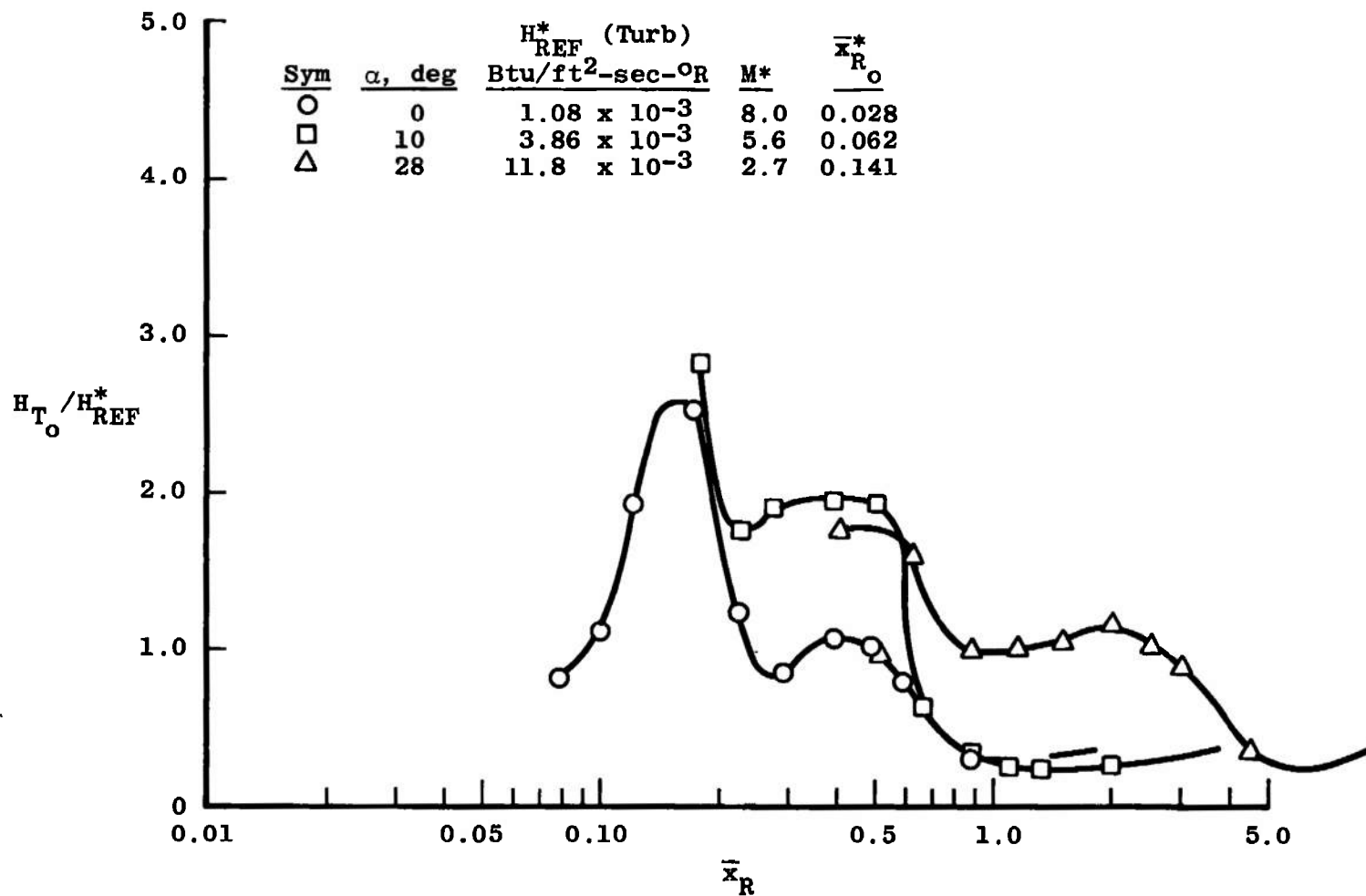
b. $\theta = 135$ deg
Fig. I-17 Continued



c. $\theta = 90$ deg
Fig. I-17 Continued

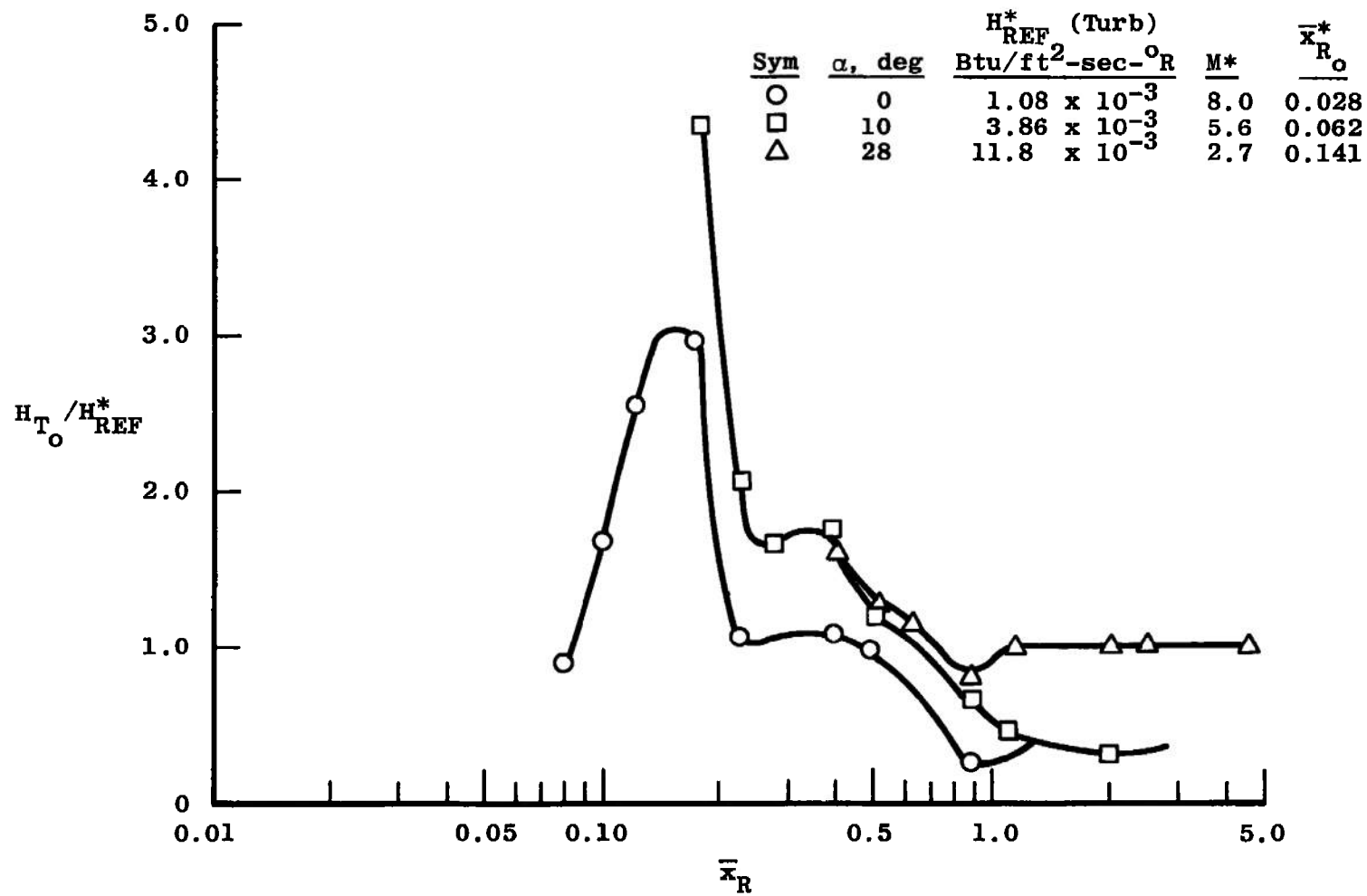


d. $\theta = 0$
Fig. I-17 Concluded

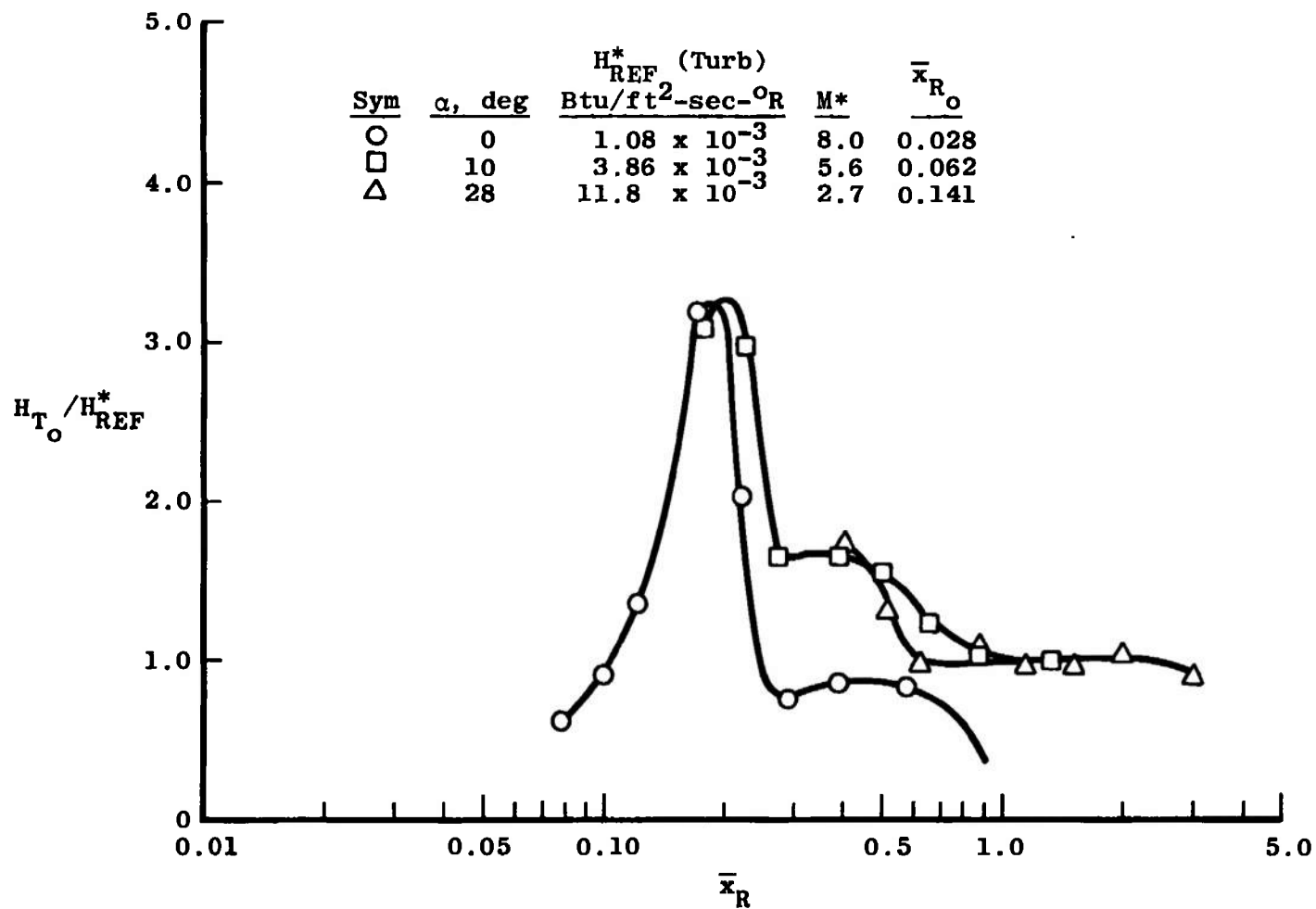


a. $\theta = 180$ deg

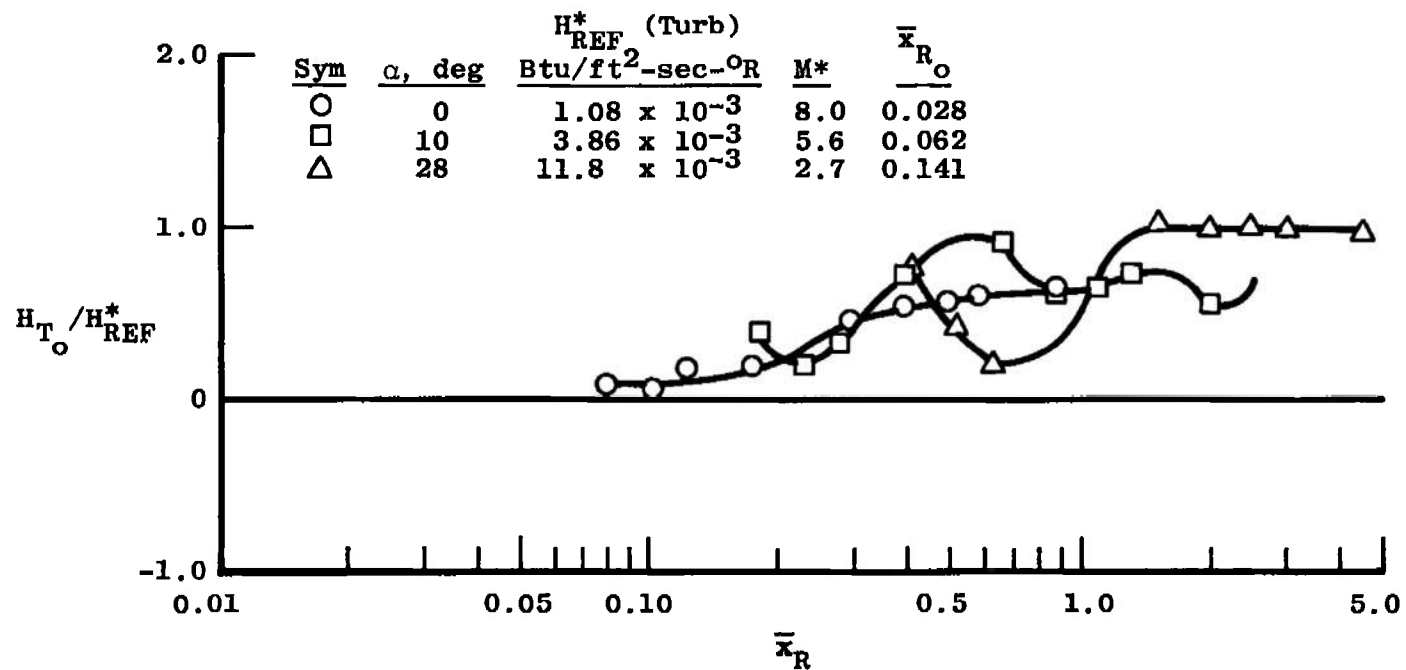
Fig. I-18 Heat-Transfer-Rate Distributions on a Flat Plate Around Air Jets from a Cluster of Four Supersonic Nozzles, $M_j = 2.54$, $d_j = 0.240$ in. Each, $M_\infty = 8.0$, and $Re_x = 5 \times 10^6$



b. $\theta = 135^\circ$
Fig. I-18 Continued

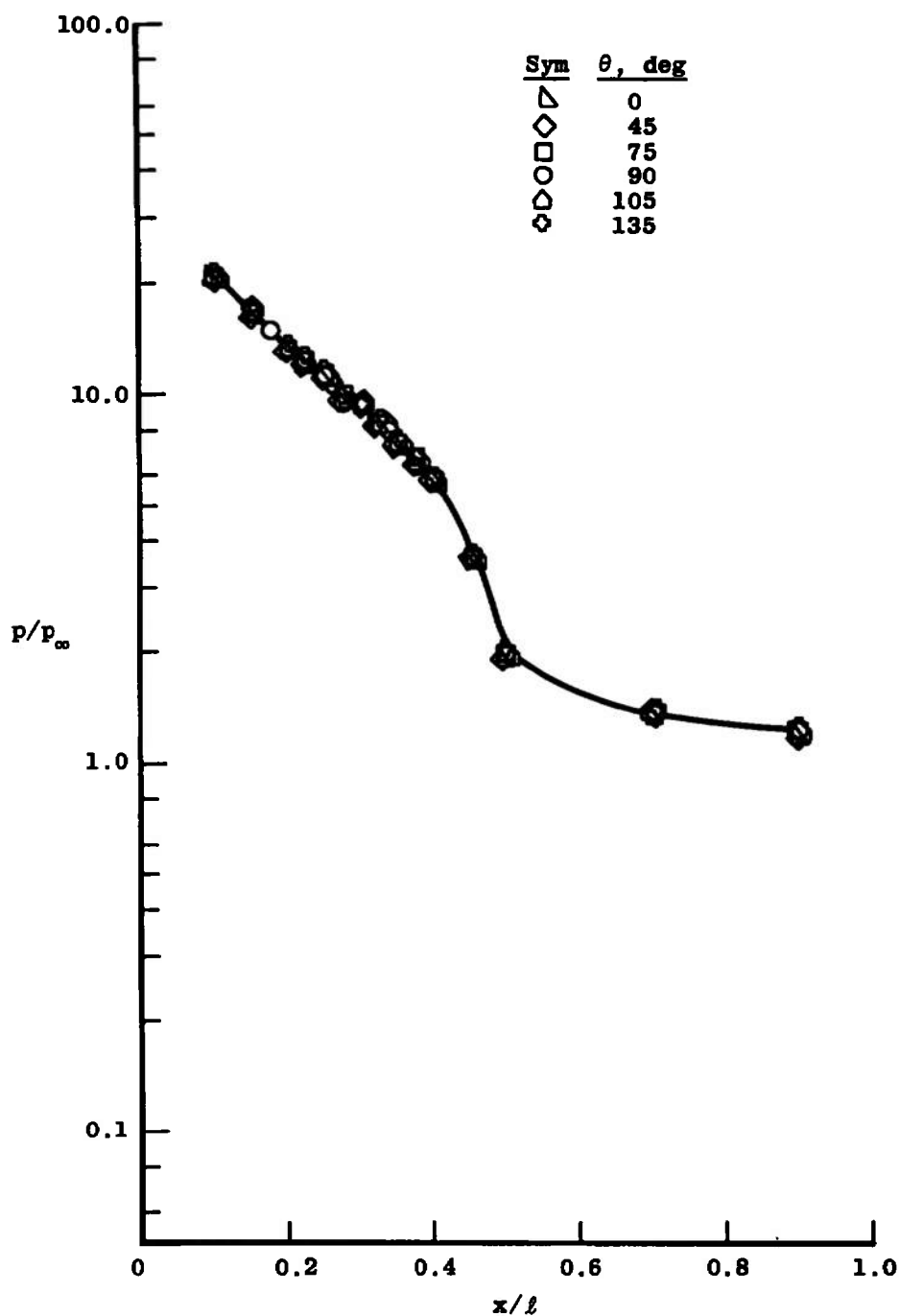


c. $\theta = 90$ deg
Fig. I-18 Continued



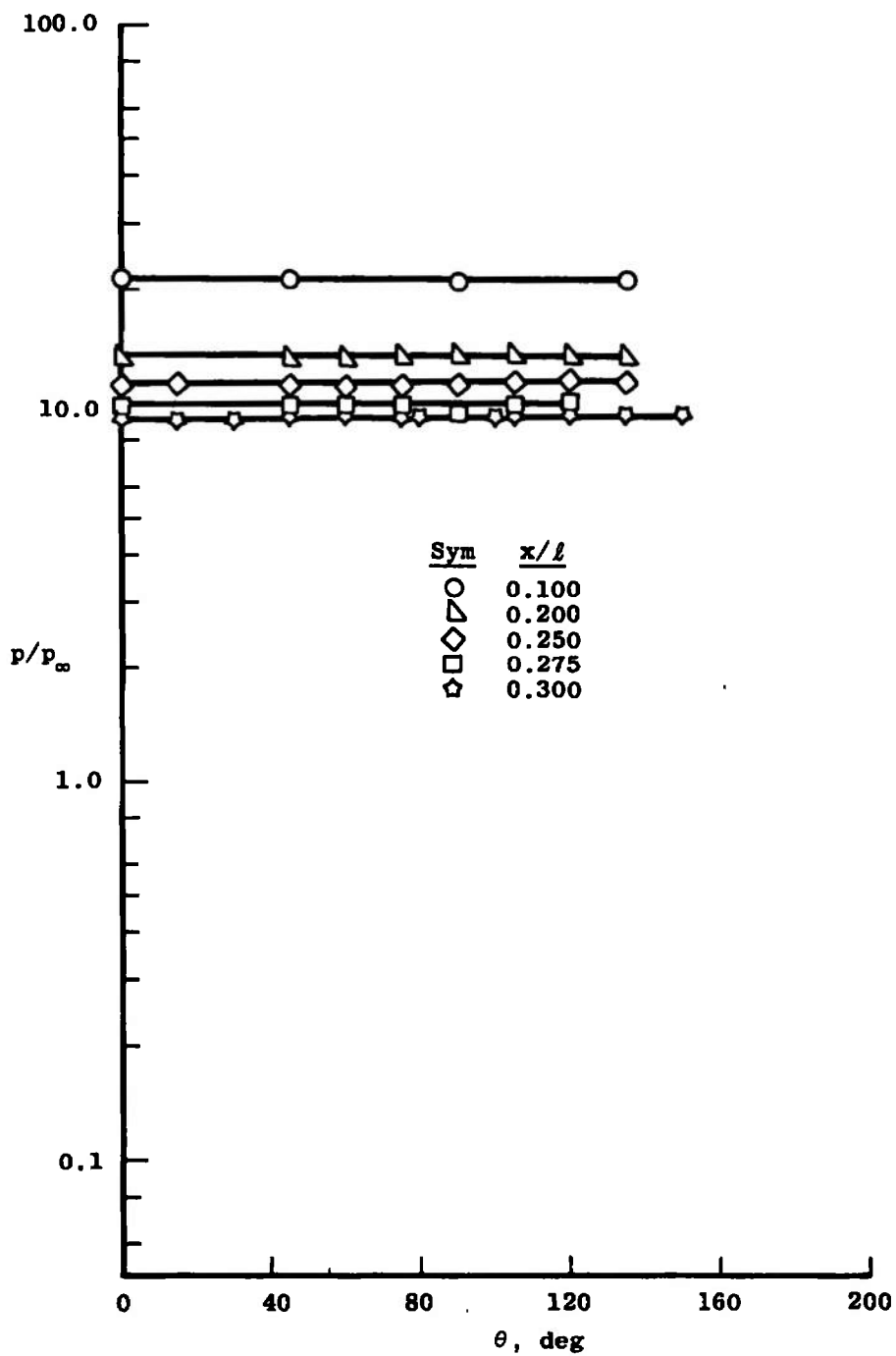
d. $\theta = 0$
Fig. 1-18 Concluded

APPENDIX II
GRAPHICAL PRESENTATION OF PRESSURE AND HEAT-TRANSFER-
RATE DISTRIBUTIONS ON THE 3-D BODY (B-9U BOOSTER NOSE
SECTION) AROUND SUPERSONIC NOZZLES

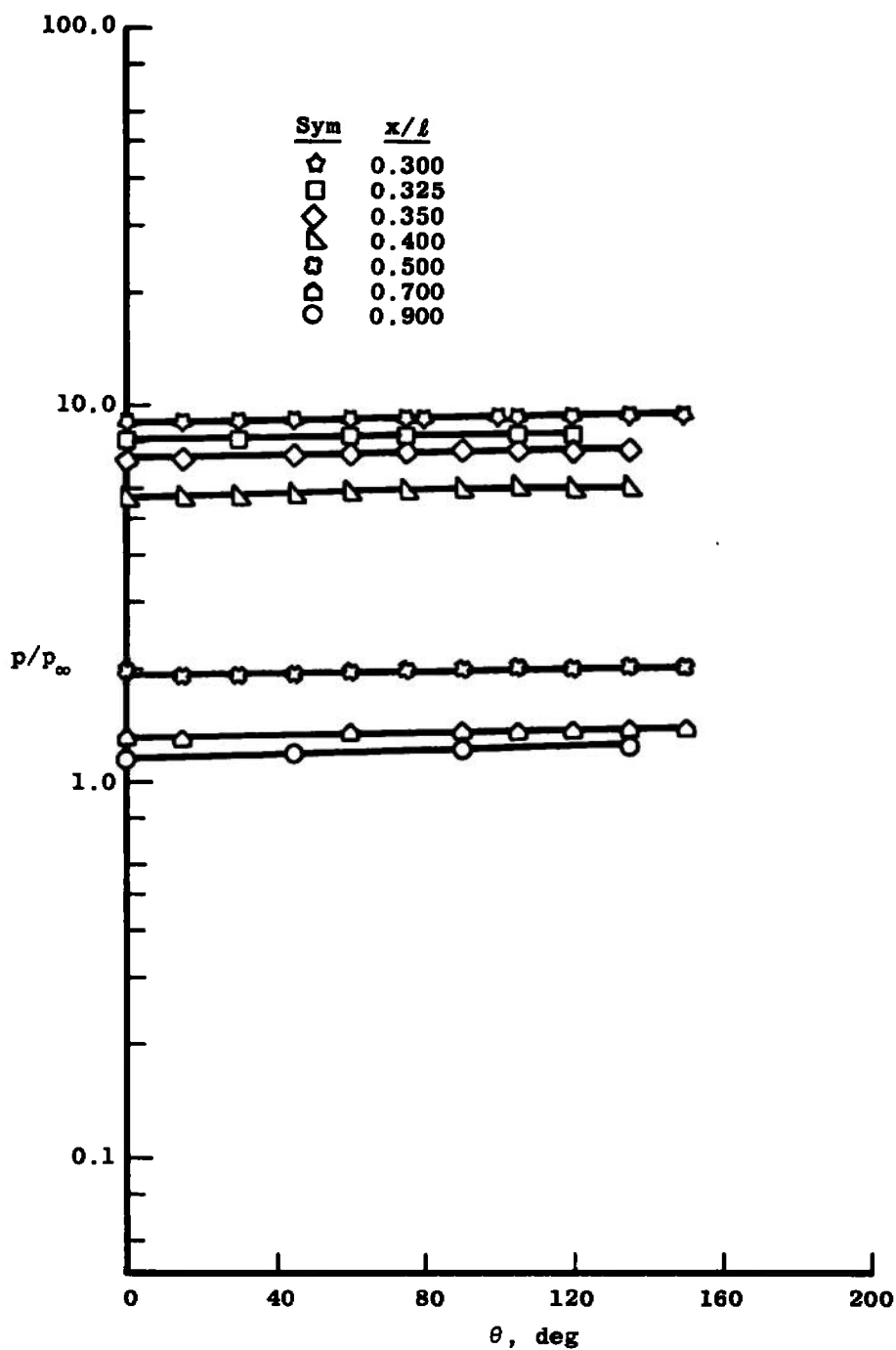


a. Axial Distributions, $\alpha = 0$

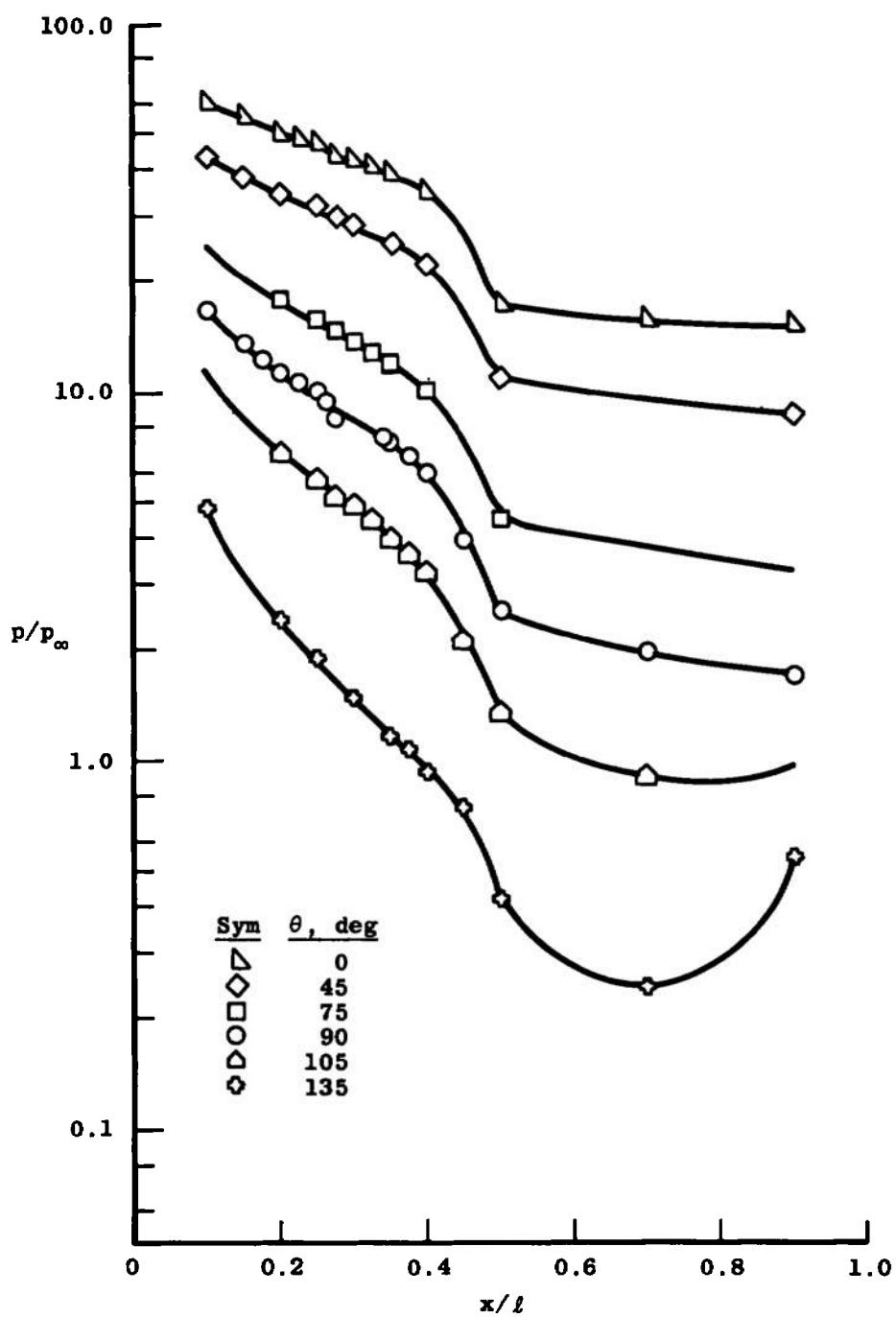
Fig. II-1 Undisturbed Pressure Distributions on the Booster Nose Section (3-D Model), $M_\infty = 8.0$, and $Re_\ell = 1.9 \times 10^6$



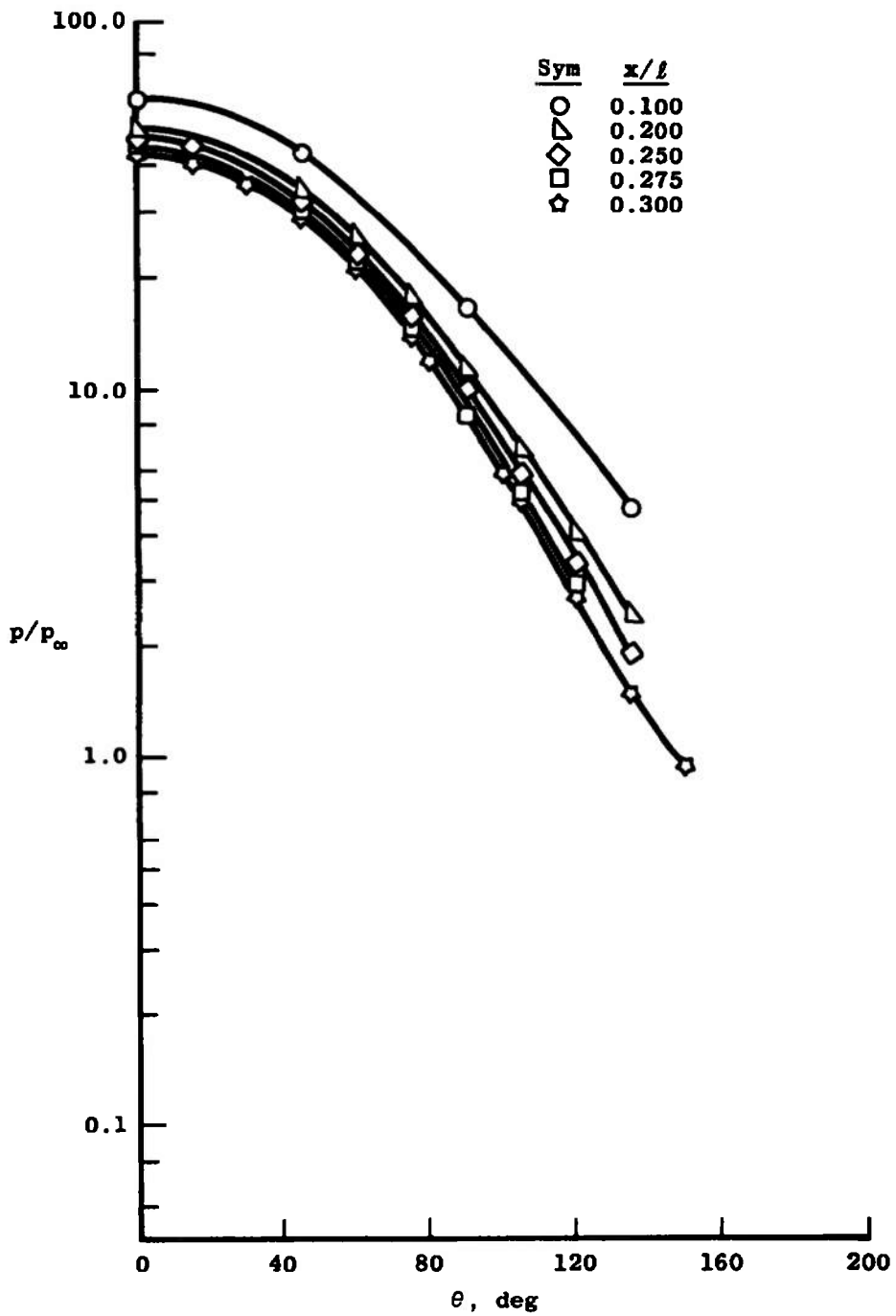
b. Radial Distributions Upstream of Jet, $\alpha = 0$
Fig. II-1 Continued



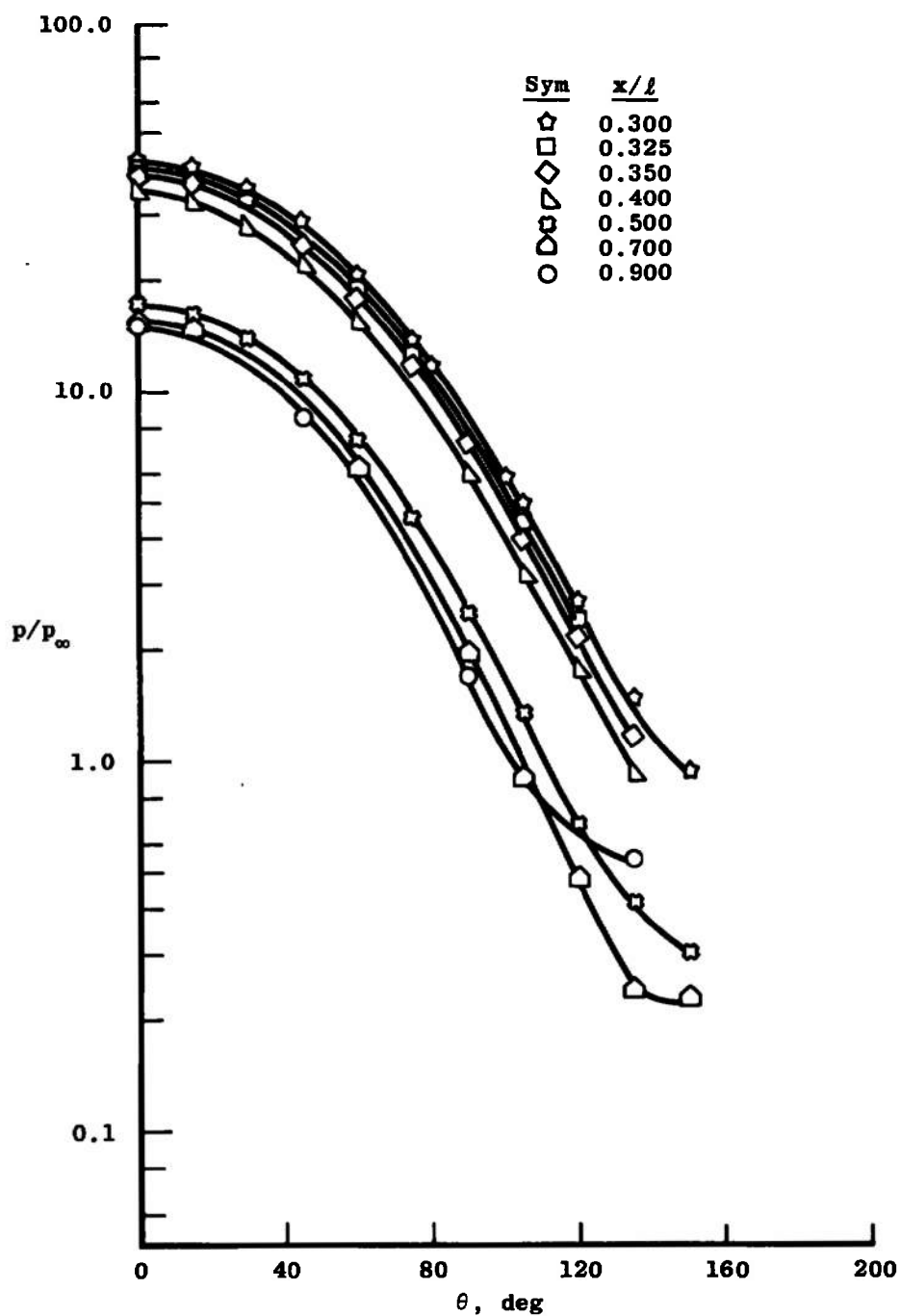
c. Radial Distributions Downstream of Jet, $\alpha = 0$
 Fig. II-1 Continued



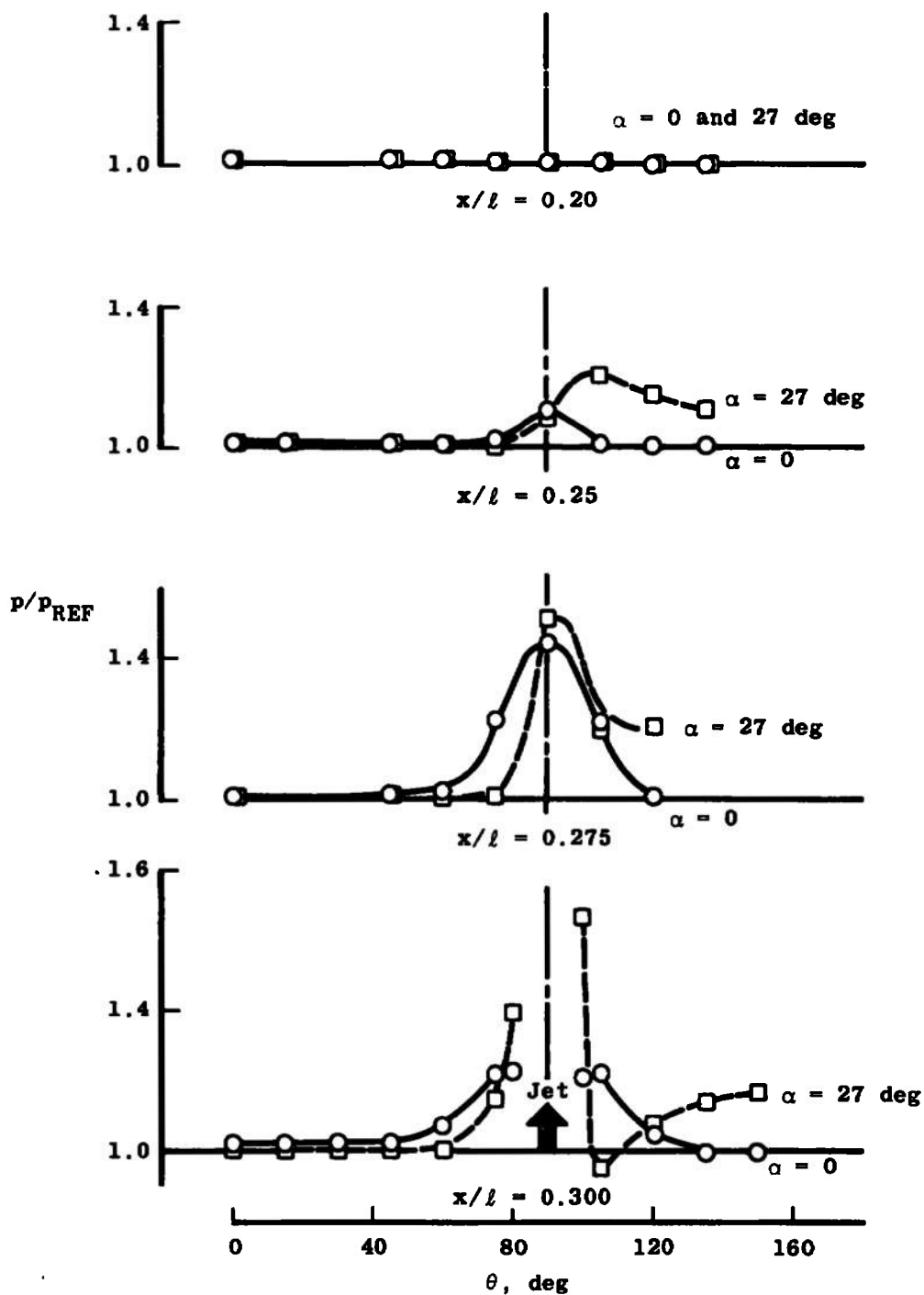
d. Axial Distributions, $\alpha = 27$ deg
Fig. II-1 Continued



e. Radial Distributions Upstream of Jet, $\alpha = 27$ deg
Fig. II-1 Continued

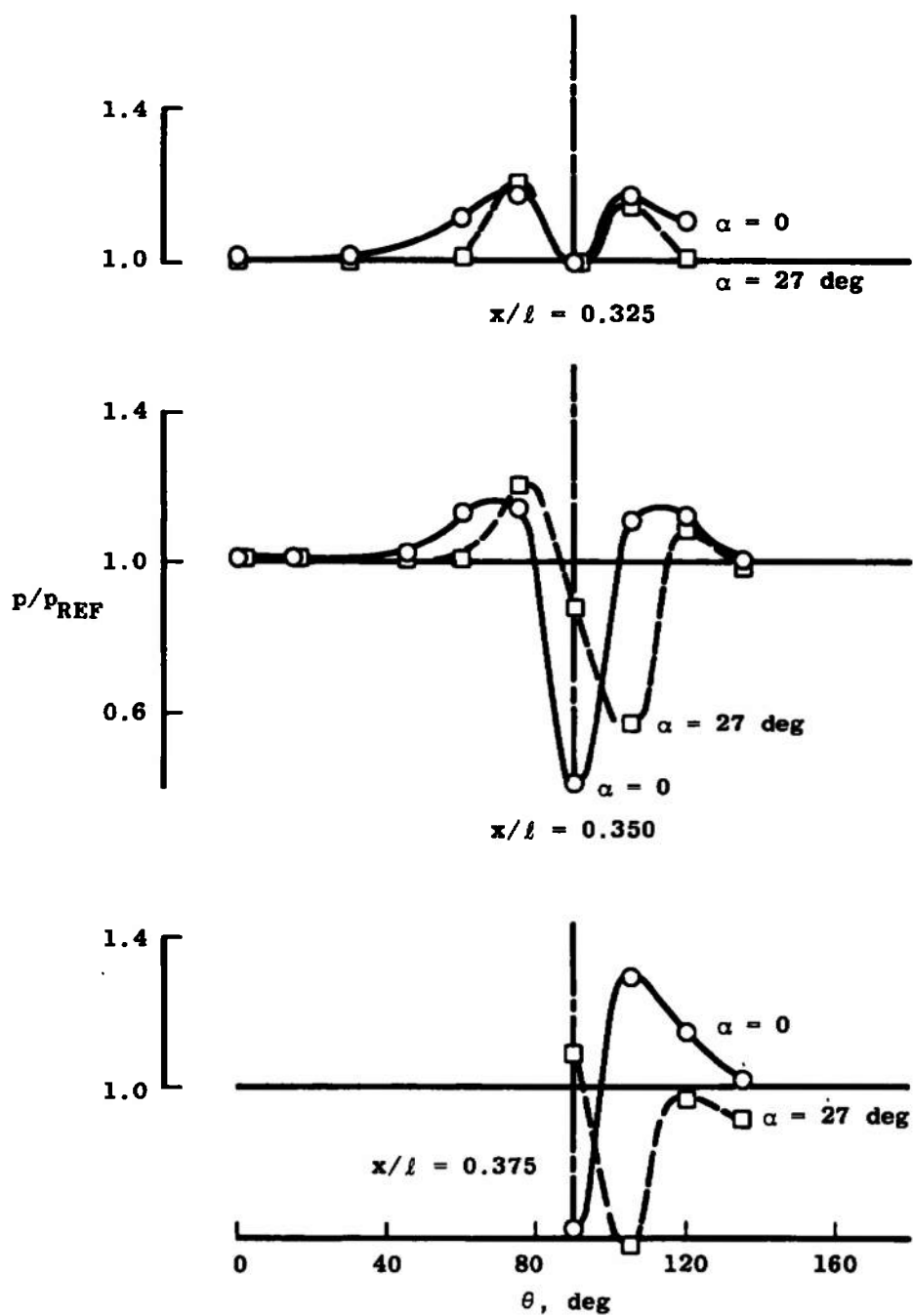


f. Radial Distributions Downstream of Jet, $\alpha = 27$ deg
Fig. II-1 Concluded

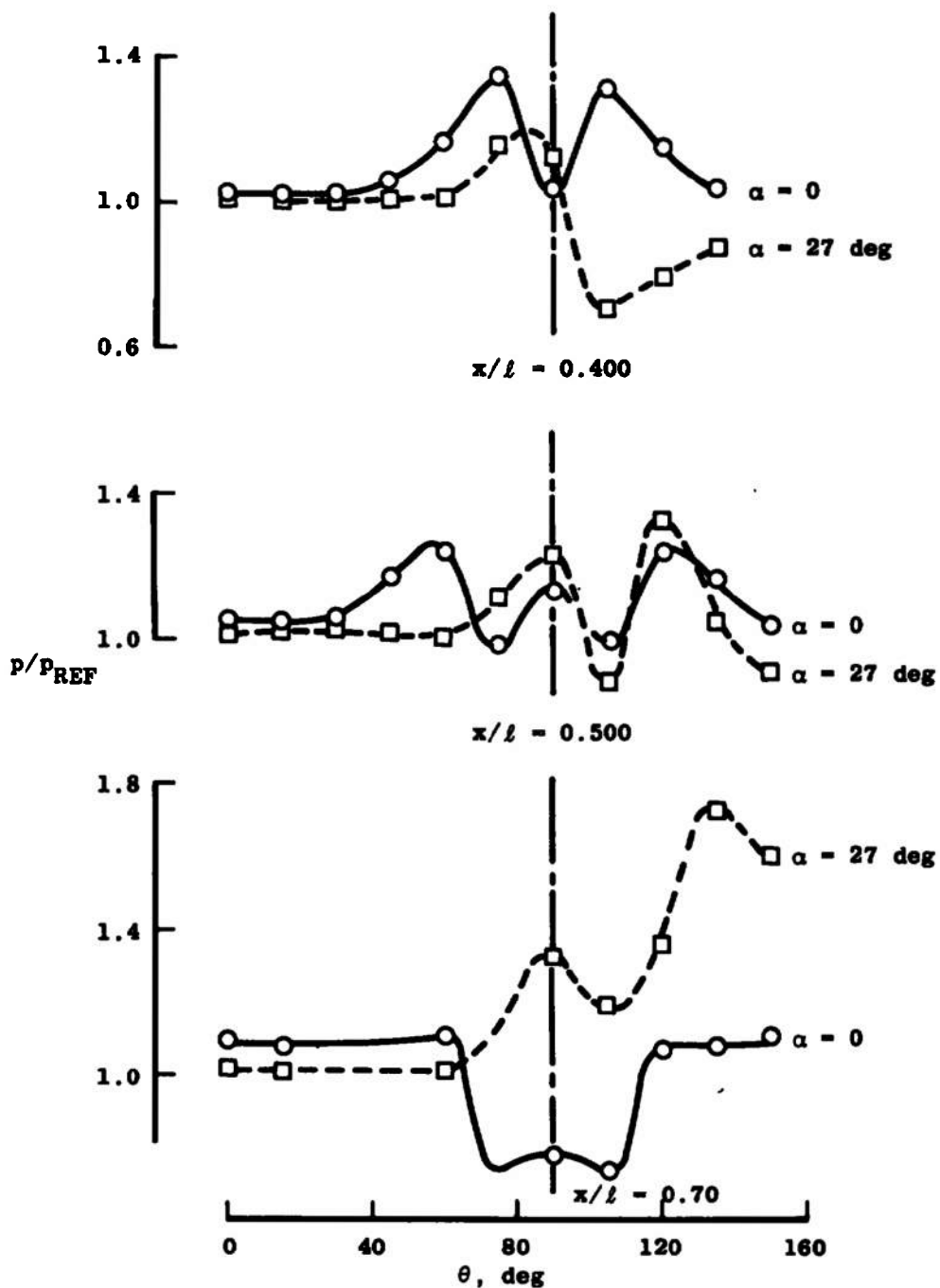


a. Upstream of Jet, $x/l = 0.20$ to 0.30

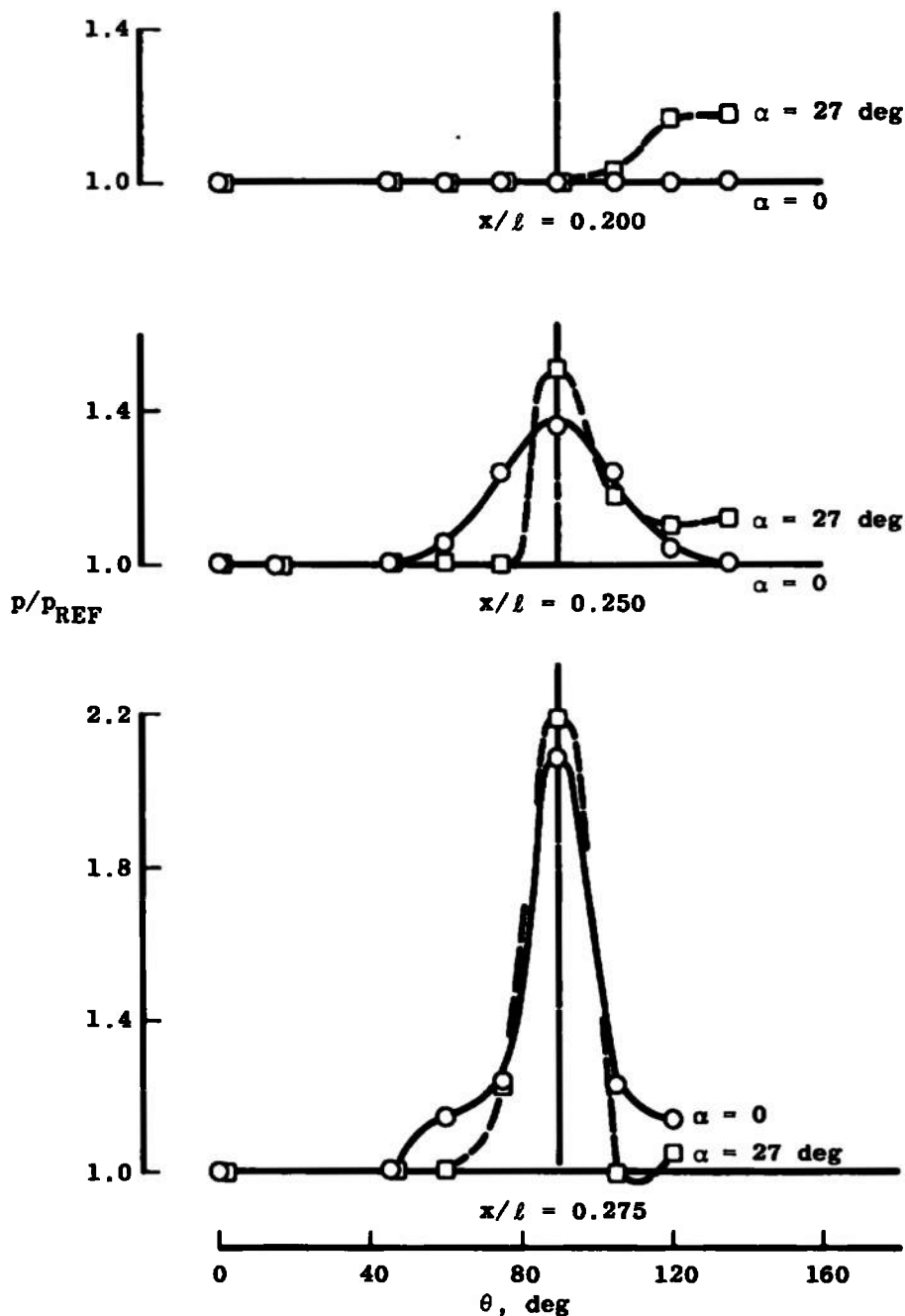
Fig. II-2 Circumferential Pressure Distributions on the 3-D Model in the Vicinity of the Air Jet from a Single Supersonic Nozzle; $M_j = 2.54$, $d_j = 0.240$, $p_{o,j}/q_\infty = 58$, $T_{o,j}/T_{o,\infty} \cong 0.4$, $M_\infty = 8.0$ and $Re_\ell = 1.9 \times 10^6$



b. Downstream of Jet, $x/l = 0.325$ to 0.375
Fig. II-2 Continued

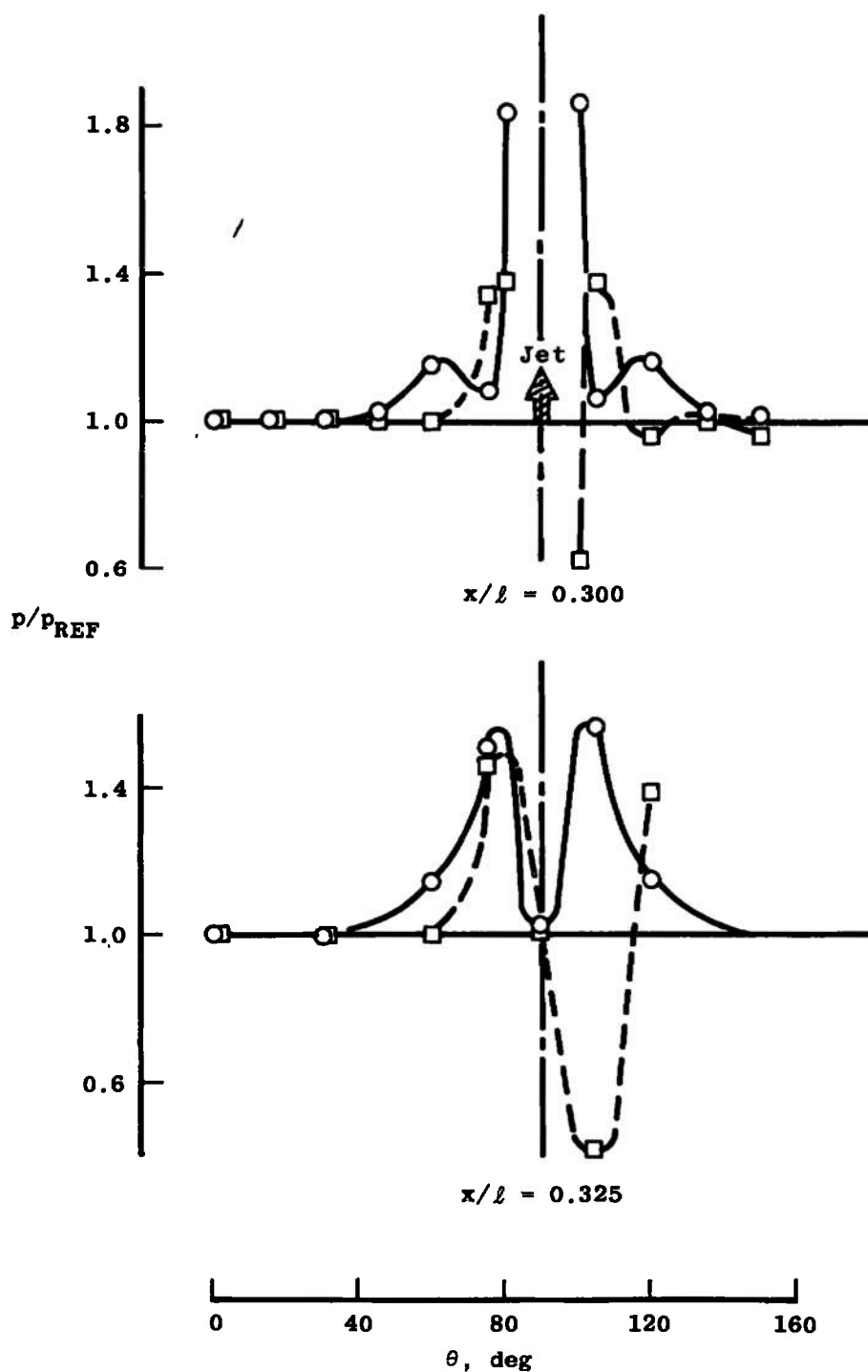


c. Downstream of Jet, $x/l = 0.40$ to 0.70
 Fig. II-2 Concluded

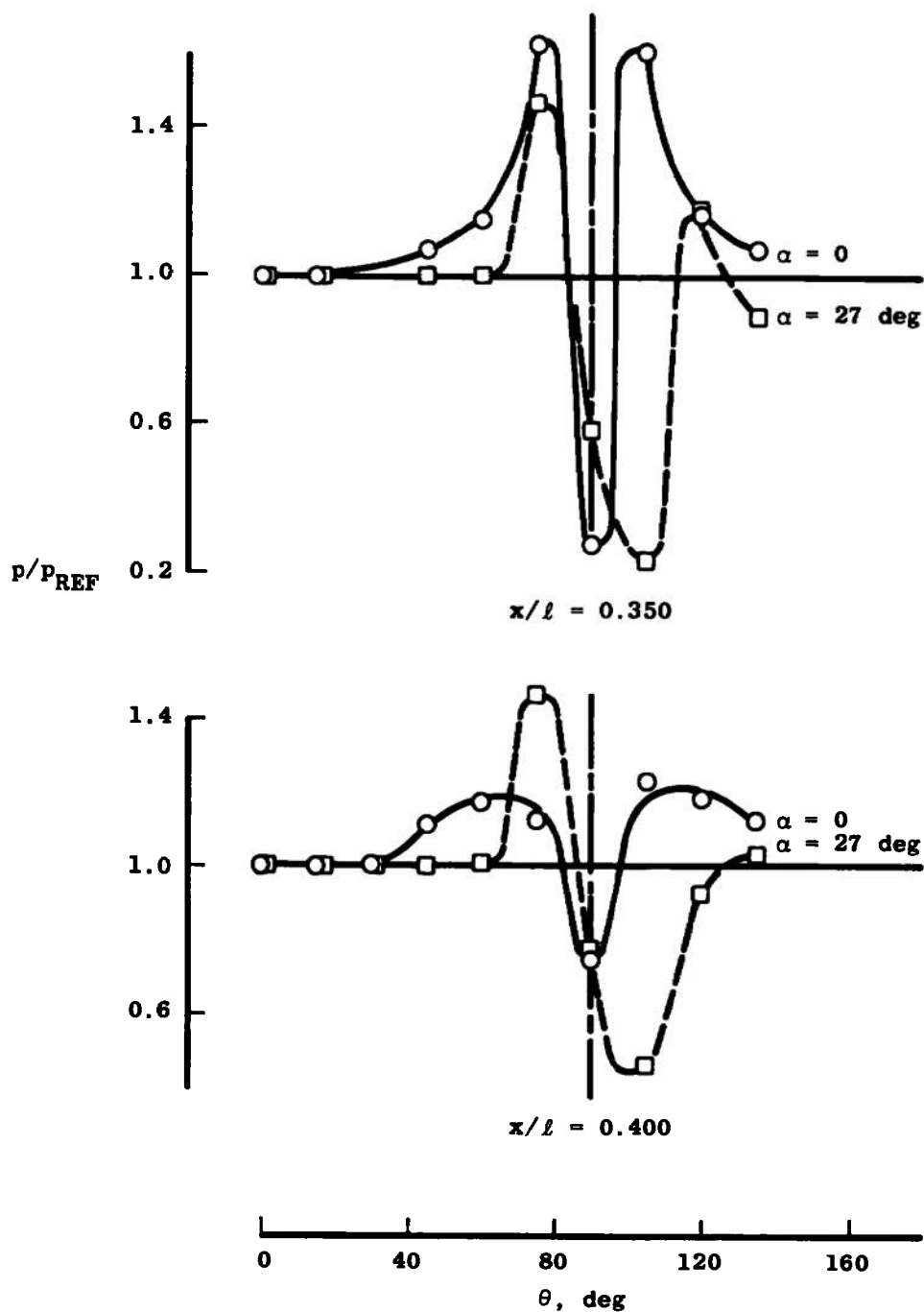


a. Upstream of Jet, $x/l = 0.20$ to 0.275

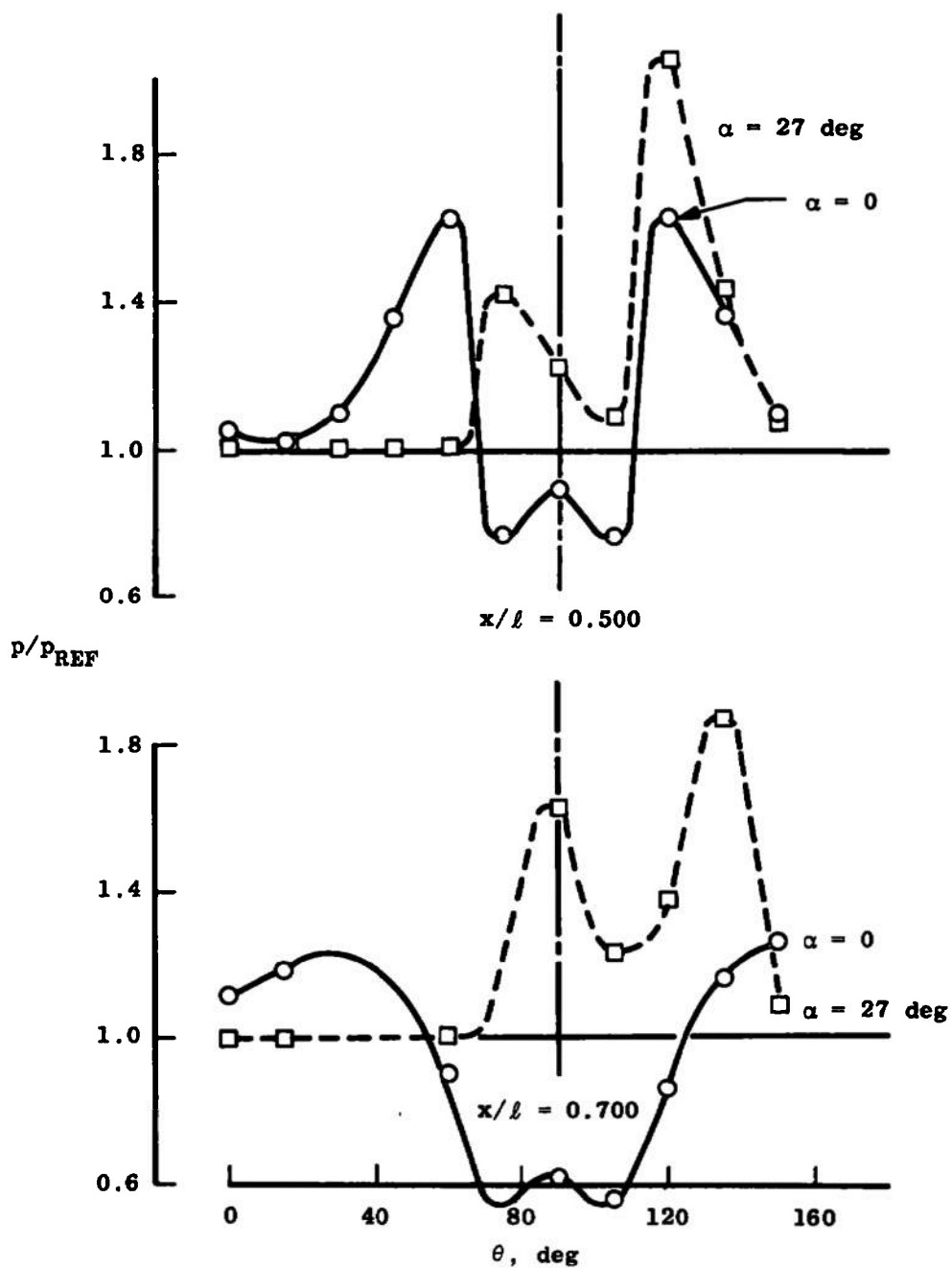
Fig. II-3 Circumferential Pressure Distributions on the 3-D Model in the Vicinity of the Air Jet from a Cluster of Four Supersonic Nozzles, $M_j = 2.54$, $d_j = 0.240$ in. Each, $p_{o_j}/q_\infty = 58$, $T_{o_j}/T_{o_\infty} \cong 0.4$, $M_\infty = 8.0$ and $Re_\ell = 1.9 \times 10^6$



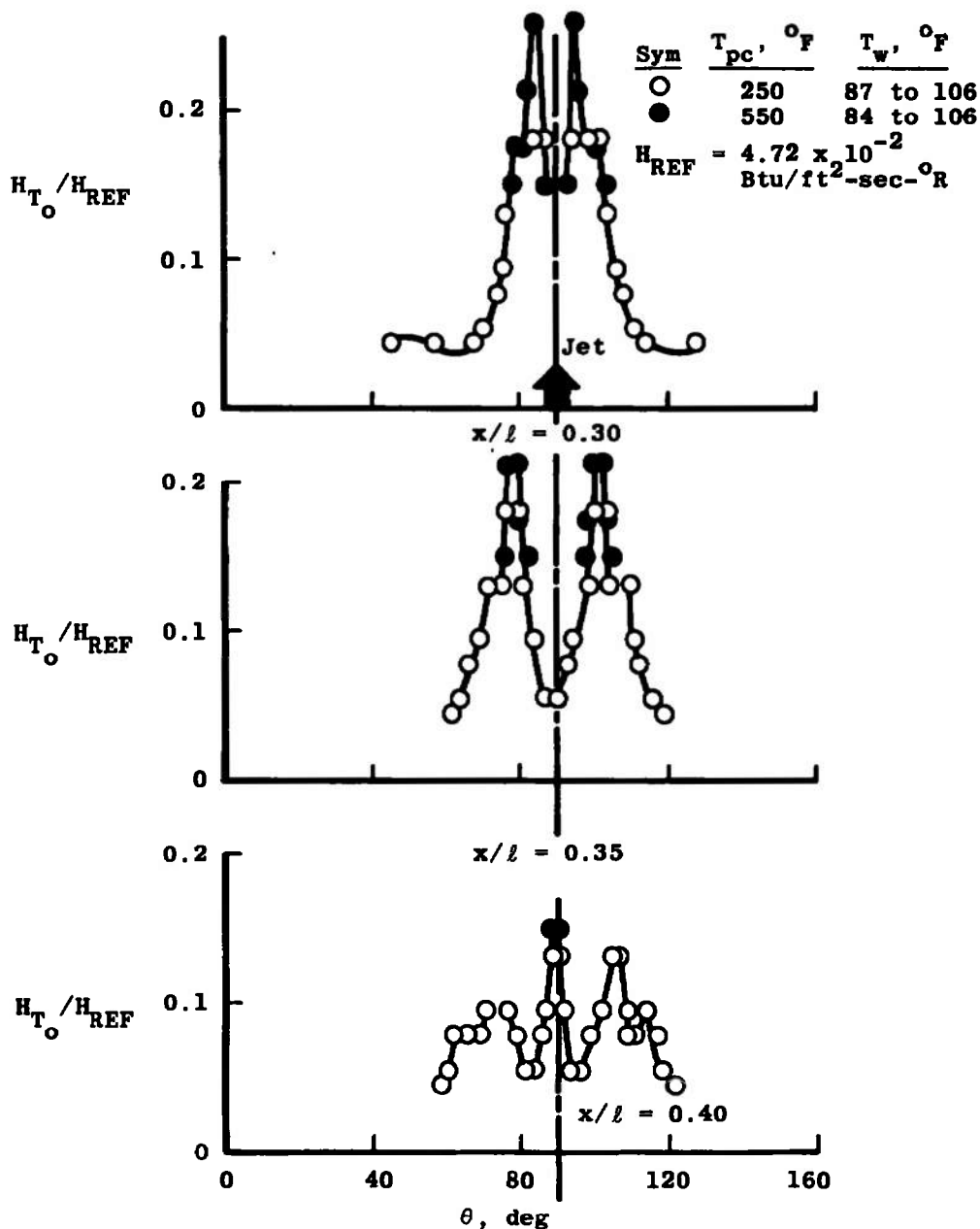
b. In the Vicinity of the Jet, $x/l = 0.30$ and 0.325
Fig. II-3 Continued



c. Downstream of Jet, $x/l = 0.35$ and 0.40
 Fig. II-3 Continued

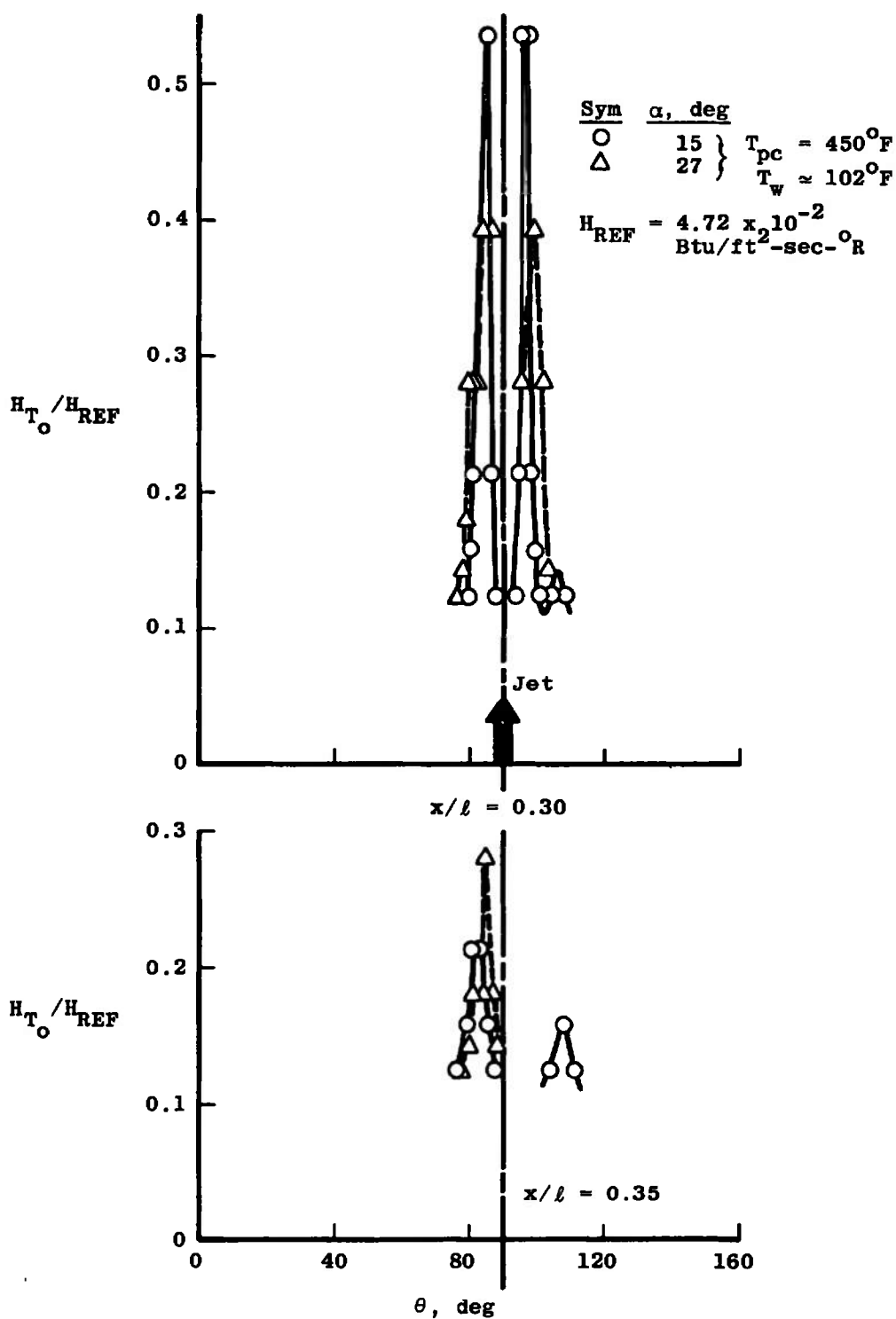


d. Downstream of Jet, $x/l = 0.50$ and 0.70
 Fig. II-3 Concluded



a. Zero Angle of Attack

Fig. II-4 Heat-Transfer-Rate Distributions on the 3-D Model Obtained from the Phase-Changing Paint Used in the Vicinity of the Air Jet from a Single Supersonic Nozzle, $M_j = 2.54$, $d_j = 0.240$ in., $p_{o_j}/q_\infty = 59$, $T_{o_j}/T_{o_\infty} \cong 0.4$, $M_\infty = 8.0$, and $Re_\ell = 1.9 \times 10^6$



b. Angles of Attack of 15 and 27 deg
 Fig. II-4 Concluded

UNCLASSIFIED

Security Classification

DOCUMENT CONTROL DATA - R & D

(Security classification of title, body of abstract and indexing annotation must be entered when the overall report is classified)

1. ORIGINATING ACTIVITY (Corporate author)		2a. REPORT SECURITY CLASSIFICATION	
Arnold Engineering Development Center Arnold Air Force Station, Tennessee 37389		UNCLASSIFIED	
3. REPORT TITLE		2b. GROUP	
NASA-CONVAIR ACS SPACE SHUTTLE STUDY AT MACH NUMBER 8.0		N/A	
4. DESCRIPTIVE NOTES (Type of report and inclusive dates)			
Final Report - May 10 to 17, 1972			
5. AUTHOR(S) (First name, middle initial, last name)			
W. T. Strike, Jr. and J. T. Best, Jr., ARO, Inc.			
6. REPORT DATE	7a. TOTAL NO. OF PAGES	7b. NO. OF REFS	
May 1973	161	9	
8a. CONTRACT OR GRANT NO.	9a. ORIGINATOR'S REPORT NUMBER(S)		
b. PROJECT NO.	AEDC-TR-73-40		
c. Program Element 921E-2	9b. OTHER REPORT NO(S) (Any other numbers that may be assigned this report)		
d.	ARO-VKF-TR-72-140		
10. DISTRIBUTION STATEMENT			
Approved for public release; distribution unlimited.			
11. SUPPLEMENTARY NOTES		12. SPONSORING MILITARY ACTIVITY	
Available in DDC		NASA-MSFC, S&E-AERO-AF Marshall Space Flight Center, AL 35812	
13. ABSTRACT Some aerothermodynamic design problems of the Space Shuttle attitude control system (ACS) were experimentally studied in a series of tests conducted at Mach number 8, at Reynolds numbers of 1×10^6 and 5×10^6 , using a flat plate containing interchangeable, flush-mounted nozzle cavities and lateral jet nozzles. The ACS configurations considered in this test program were a single supersonic nozzle and a cluster of four symmetrically located supersonic nozzles. Also, some preliminary results were obtained with nozzles similar to those on the flat plate used to simulate the yaw controls on a 2-percent-scaled nose section of the Convair Aerospace B-9U booster. The test data consist of pressure measurements, integrated pressure data to provide estimates of the jet interaction loading, heat-transfer-rate gage measurements, phase-change paint data, interferograms, and schlieren photographs. The flat plate was used to simulate the wing panel of a space shuttle vehicle. Interchangeable circular, contoured, nozzle cavities (no flow) of various sizes were mounted in the flat plate to determine the pressure and thermal loading generated within and around these cavities as the flat plate was inclined to the free-stream flow at angles of inclination from zero to nominally 30 deg.			

DD FORM 1473

1 NOV 65

UNCLASSIFIED

Security Classification

14.

KEY WORDS

LINK A

LINK B

LINK C

ROLE

WT

ROLE

WT

ROLE

WT

aerothermodynamic

design (problems)

tests

NASA-CONVAIR

attitude

control equipment

space (shuttle)

Mach number 8.0